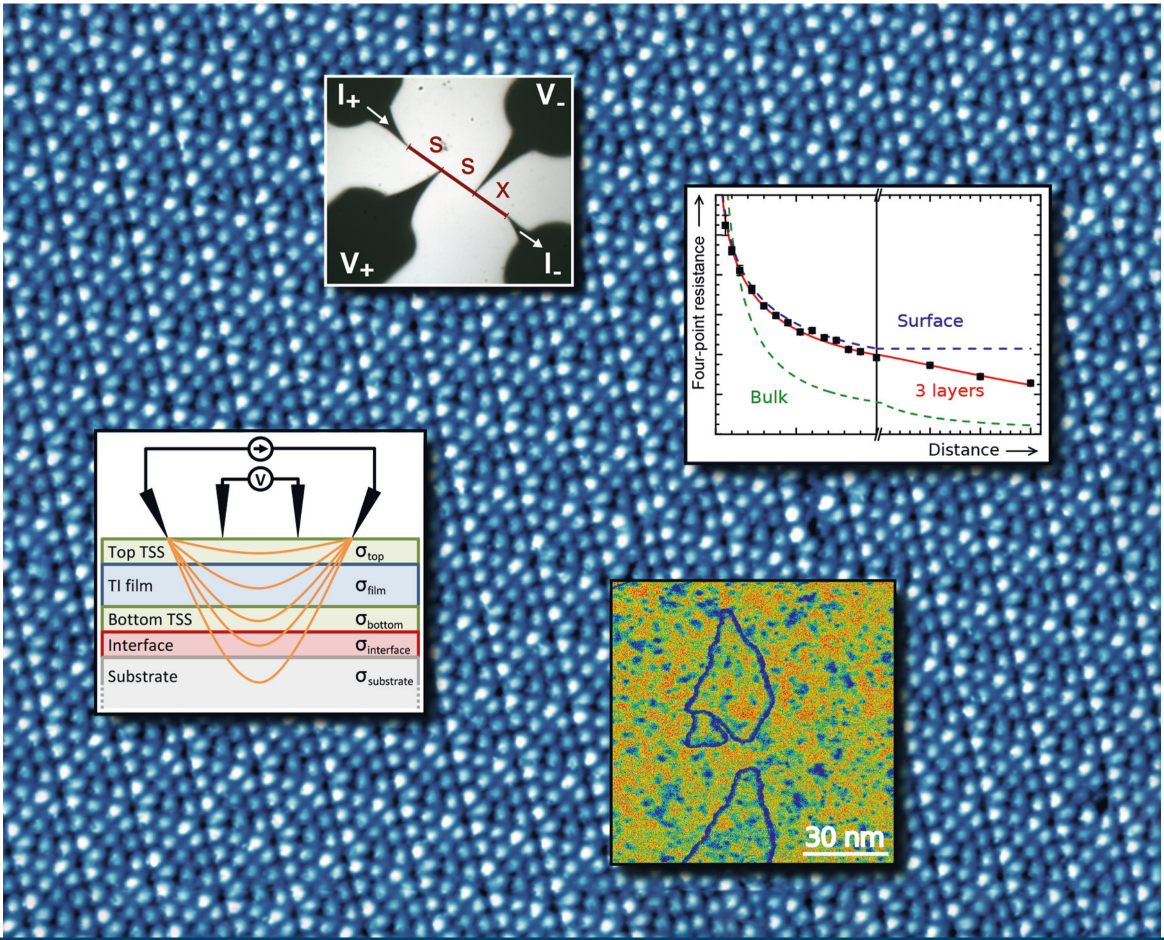

Disentangling parallel conduction channels by charge transport measurements on surfaces with a multi-tip scanning tunneling microscope

Sven Just

Information
Band / Volume 69
ISBN 978-3-95806-574-1

Mitglied der Helmholtz-Gemeinschaft

JÜLICH
Forschungszentrum

Schriften des Forschungszentrums Jülich
Reihe Information / Information Band / Volume 69

Forschungszentrum Jülich GmbH
Peter Grünberg Institut (PGI)
Quantum Nanoscience (PGI-3)

Disentangling parallel conduction channels by charge transport measurements on surfaces with a multi-tip scanning tunneling microscope

Sven Just

Schriften des Forschungszentrums Jülich
Reihe Information / Information Band / Volume 69

ISSN 1866-1777 ISBN 978-3-95806-574-1

Bibliografische Information der Deutschen Nationalbibliothek.
Die Deutsche Nationalbibliothek verzeichnet diese Publikation in der
Deutschen Nationalbibliografie; detaillierte Bibliografische Daten
sind im Internet über http://dnb.d-nb.de abrufbar.

Herausgeber und Vertrieb: Forschungszentrum Jülich GmbH
Zentralbibliothek, Verlag
52425 Jülich
Tel.: +49 2461 61-5368
Fax: +49 2461 61-6103
zb-publikation@fz-juelich.de
www.fz-juelich.de/zb

Umschlaggestaltung: Grafische Medien, Forschungszentrum Jülich GmbH

Druck: Grafische Medien, Forschungszentrum Jülich GmbH

Schriften des Forschungszentrums Jülich
Reihe Information / Information, Band / Volume 69

D 82 (Diss. RWTH Aachen University, 2021)

ISSN 1866-1777
ISBN 978-3-95806-574-1

Vollständig frei verfügbar über das Publikationsportal des Forschungszentrums Jülich (JuSER)
unter www.fz-juelich.de/zb/openaccess.

Abstract

Within this thesis, both position-dependent charge transport measurements with a multi-tip scanning tunneling microscope (STM) are performed, and theoretical models for describing these measured data are developed. Only a combination of both allows for actually disentangling multiple current transport channels present in parallel, in order to reveal the physical properties of the investigated systems, i.e. the conductivity of the individual channels. In chapter 2, the instrumental setup for the multi-tip STM is shown in general and the specific methods used for tip positioning are discussed. An introduction into the theory of distance-dependent four-point resistance measurements is given in chapter 3. Here, the relations between four-point resistance and conductivity influenced by the chosen probe geometry are discussed for both a pure two-dimensional and a pure three-dimensional system. Furthermore, also anisotropic conductance in two dimensions is considered. Chapters 4 – 7 depict actual measurements with the multi-tip STM on different sample systems, as semiconductors and topological insulators. First, in chapter 4 the conductivity of the Si(111)-(7×7) surface and the influence of atomic steps of the underlying substrate are investigated. In order to interpret the measured resistances, a 3-layer model is introduced which allows for a description by three parallel conductance channels, i.e. the surface, the space charge region and the bulk. Such a model enables to extract a value for the surface conductivity from the measurements. Moreover, by a measurement of the conductance anisotropy on the surface, the conductivity of a single atomic step can be disentangled from the conductivity of the step-free terraces. In chapter 5, the 3-layer model is extended to an N-layer model in order to model the strongly depth-dependent conductivity of the near-surface space charge region in semiconductors in a more precise way. In order to demonstrate the universal applicability of the N-layer model, it is used to extract values for the surface conductivity of Ge(100)-(2×1) and Si(100)-(2×1) reconstructions from data already published in the literature, but not evaluated in terms of the surface conductivity. Chapter 6 depicts a further combined experimental and theoretical approach in order to reveal parallel conductance channels in topological insulators thin films, i.e. the interface channel at the boundary to the substrate and the interior of the film itself, which are both in parallel to the transport channel through the topological surface states at top and bottom surface of the film. From measurements on specific surface reconstructions, the conductivity of the interface channel can be revealed, while the interior of the thin film is approached by band bending calculations in combination with results from angle-resolved photoemission spectroscopy measurements (ARPES). Here, it turns out that in the thin-film limit the charge carrier concentration inside the film is only governed by the position of the Fermi level at the surface, as it is revealed by ARPES, but not influenced by the actual dopant concentration inside the film material which is usually unknown, thus allowing for a reli-

able estimate of the film conductivity. Finally, in chapter 7, the weak topological insulator $Bi_{14}Rh_{3}I_{9}$ is investigated by means of scanning tunneling spectroscopy and scanning tunneling potentiometry, in order to reveal the presence and the transport properties of the one-dimensional edge state at step edges on the dark surface. From the spectroscopy and thermovoltage measurements, it turns out that the topological channel can indeed be found at step edges of the 2D TI-layer, as it has been already reported in literature, and additionally at artificially created scratches into the surface. However, it is not located directly at the Fermi energy, and thus cannot substantially contribute to current transport. Additionally, it turns out that the surrounding so-called dark surface is very conductive itself due to unintentional surface doping, as deduced from potentiometry with applied transport field and distance-dependent four-point measurements. Both facts prevent to directly reveal the transport properties of the edge channels for the studied $Bi_{14}Rh_{3}I_{9}$ crystals, but nevertheless in principle the depicted measurement method should be capable of revealing direct transport through an edge channel on more sophisticated samples.

Kurzfassung

Im Rahmen dieser Arbeit werden sowohl positionsabhängige Ladungstransportmessungen mit einem Multispitzen-Rastertunnelmikroskop durchgeführt, als auch theoretische Modelle für die Beschreibung der gemessenen Daten entwickelt. Nur eine Kombination aus beidem ermöglicht es, parallele Leitfähigkeitskanäle für Stromtransport voneinander zu trennen, um die grundlegenden physikalischen Eigenschaften in den untersuchten System aufzudecken, d.h. die spezifische Leitfähigkeit der einzelnen Kanäle zu bestimmen. In Kapitel 2 wird der allgemeine instrumentelle Aufbau des Multispitzen-Rastertunnelmikroskops gezeigt und Methoden für die Spitzenpositionierung werden besprochen. Eine Einführung in die Theorie zu abstandsabhängigen Vierpunktmessungen wird in Kapitel 3 gegeben. Hier werden die Beziehungen zwischen Vierpunktwiderstand und spezifischer Leitfähigkeit, welche durch die gewählte Spitzenanordnung beeinflusst werden, sowohl für zweidimensionale als auch für dreidimensionale Systeme hergeleitet. Zusätzlich wird auch anisotrope Leitfähigkeit in zwei Dimensionen betrachtet. Die Kapitel 4 – 7 zeigen Messungen mit dem Multispitzen-Rastertunnelmikroskop auf verschiedenen Probensystemen, wie Halbleitern und topologischen Isolatoren. Zunächst wird in Kapitel 4 die spezifische Leitfähigkeit der Oberfläche von Si(111)-(7×7) und der Einfluss von atomaren Stufenkanten des darunterliegenden Substrats untersucht. Um die gemessenen Vierpunktwiderstände interpretieren zu können, wird ein 3-Lagen-Modell eingeführt, welches eine Modellierung durch drei parallele Leitfähigkeitskanäle erlaubt, d.h. einen Oberflächenkanal, einen Kanal durch die Raumladungszone und einen Volumenkanal durch den Siliziumkristall. Solch ein Modell ermöglicht es, einen Wert für die spezifische Leitfähigkeit der Oberfläche aus den Messdaten zu extrahieren. Außerdem erlaubt eine Messung der Leitfähigkeitsanisotropie auf der Oberfläche, die Beiträge, welche durch die spezifische Leitfähigkeit einer einzelnen atomaren Stufe und der spezifischen Leitfähigkeit der stufenlosen Terrassen entstehen, voneinander zu trennen. In Kapitel 5 wird das 3-Lagen-Modell erweitert zu einem N-Lagen-Modell, um die in hohem Maße tiefenabhängige (bzgl. der Oberfläche) spezifische Leitfähigkeit der oberflächennahen Raumladungszone in Halbleitern präziser beschreiben zu können. Um die allgemeine Anwendbarkeit des N-Lagen-Modells zu demonstrieren, wird es zur Bestimmung der spezifischen Oberflächenleitfähigkeit der beiden Oberflächenrekonstruktionen Ge(100)-(2×1) und Si(100)-(2×1) verwendet, basierend auf bereits veröffentlichten Messdaten aus der Literatur, welche aber nicht unter Einbeziehung eines Oberflächenkanals für Stromtransport ausgewertet wurden. In Kapitel 6 wird ein weiterer kombinierter Ansatz aus Experiment und Theorie gezeigt, um parallele Leitfähigkeitskanäle in dünnen Filmen topologischer Isolatoren (TI) zu trennen, d.h. den Grenzflächenkanal an der Übergangsfläche zum Substrat und den Kanal durch das Innere des Films, welche beide parallel zu den Transportkanälen durch die topologischen Oberflächenzustän-

de auf der Ober- und Unterseite des Films verlaufen. Basierend auf Vierpunktmessungen von bestimmten Oberflächenrekonstruktionen lässt sich die spezifische Leitfähigkeit des Grenzflächenkanals ermitteln, wohingegen die Eigenschaften des Filminneren mit Hilfe von Berechnungen der Bandverbiegung in Verbindung mit Messdaten aus winkelaufgelöster Photoemissionsspektroskopie bestimmbar sind. Hierbei stellt sich heraus, dass im Grenzfall von dünnen Filmen die Ladungsträgerdichte im Inneren des Films nahezu nur von der Position der Fermienergie an der Oberfläche abhängt, wie sie aus winkelaufgelöster Photoemissionsspektroskopie ermittelt werden kann, aber nicht durch die tatsächliche Dotierkonzentration im Inneren des Filmmaterials beeinflusst wird, welche oftmals unbekannt ist, so dass letztendlich eine verlässliche Abschätzung der spezifischen Leitfähigkeit des Filminneren möglich ist. Schließlich wird in Kapitel 7 der schwache topologische Isolator $Bi_{14}Rh_3I_9$ mit Hilfe von Rastertunnelspektroskopie und Rastertunnelpotentiometrie untersucht, um die Existenz und die Transporteigenschaften von eindimensionalen Randzuständen an Stufenkanten auf der dunklen Oberfläche aufzudecken. Aus Spektroskopie und Messungen der Thermospannung ergibt sich, dass sich die topologischen Randkanäle tatsächlich an Stufenkanten auf der zweidimensionalen TI-Lage finden lassen, wie es auch in Übereinstimmung mit der Literatur ist, und zusätzlich auch an künstlich erzeugten Kratzern und Gräben in der Oberfläche auftreten. Allerdings stellt sich heraus, dass sich die Randzustände nicht unmittelbar an der Fermienergie befinden und daher nicht wesentlich zum Stromtransport beitragen können. Zusätzlich wird deutlich, dass auf Grund von unbeabsichtigter Oberflächendotierung die umgebende sogenannte dunkle Oberfläche selbst eine sehr hohe spezifische Leitfähigkeit aufweist, wie es sich aus Potentiometriemessungen mit angelegtem Transportfeld und abstandsabhängigen Vierpunktmessungen ableiten lässt. Diese beiden Tatsachen verhindern letztendlich, dass sich an den untersuchten $Bi_{14}Rh_3I_9$ Kristallen die Transporteigenschaften der Randkanäle unmittelbar aufdecken lassen, aber nichtsdestotrotz wäre es prinzipiell mit der verwendeten Messmethode möglich, direkten Transport durch die Randkanäle nachzuweisen, wenn ausgereiftere Proben zur Verfügung stünden.

Contents

1. Introduction

Due to the pronounced downscaling occurring in modern electronics and the progressing transition from microelectronics into nanoelectronics, the role of parasitic conductance channels in electronic devices becomes more and more important. Such parasitic channels which are present in parallel to the intended current paths, can have several undesired impacts, e.g. as an increased consumption of power or a pronounced heating of the devices, and therefore lead to a much less effective functionality. A simple example of such a parallel parasitic channel is a conductive surface present on a volume-based electronic component. In addition to the intended bulk channel whose properties are selected according to the desired specifications for current transport, e.g. for obtaining a diode or an ohmic resistor, such a surface conduction is always present in parallel, and therefore can lead to a substantial leakage current in the component. This is additionally emphasized, as the surface to volume ratio increases substantially with reducing the size of the element. So, it is an important task to reduce such undesired influences. However, in order to be able to design electronic devices in a way that such parallel parasitic channels are reduced as far as possible, one first has simply to *know* that such channels are present and, second, one needs to get some deeper insight into their specific properties. This means that is has to be possible to reveal the parallel channels from electrical measurements. In order to be able to judge their corresponding influence on current transport, also the conductivities of the individual channels need to be determined.

However, this task sounds more simple than it actually is. In principle, one may think that only a standard resistance measurement is required which can be performed easily, e.g. similar to a measurement with a multimeter. Nevertheless, if one stays in this picture and assumes that the device is accessible by a multimeter, even a standard resistance measurement would not lead to success, as only the total resistance can be measured including the contribution of all conduction channels in parallel, similar as it is the case for multiple resistors in a parallel circuit. So, a different method has to be found in order to measure each channel separately. One helpful fact is that the parasitic channels often have a different dimensionality than the main conductance channel. For example, in the common case of volume-based semiconductor components, as mentioned before, the surface conductance is obviously two-dimensional (2D), while the transport through the bulk semiconductor itself occurs along a three-dimensional (3D) channel. This also holds for other cases, e.g. a 2D conductive interface in between two 3D materials, or a (quasi 2D) thin film on top of a 3D bulk substrate. However, with the progressing development during the last decades, increasingly also exactly the opposite case applies, i.e. the intended current path of an electronic component is formed solely by a (quasi) 2D channel, e.g. along an interface or on a surface, which basically has been summarized by the Nobel laureate *Herbert Kroemer* with the famous statement that "the interface is the device" [1, 2]. A prominent example is the widely used silicon-based *metal-oxide-semiconductor field-effect transistor* (*MOSFET*), whose gate-controlled current channel has a vertical extension of only $\sim 10\,\mathrm{nm}$ beneath the gate oxide [3]. Nevertheless, also in such systems parasitic channels can exist, but beside the less common case of a parallel bulk channel, they are often of the same dimensionality as the intended current path, and thus more difficult to handle. An example from recent research is the GaN *high-electron-mobility transistor* (*HEMT*) intended for high frequency and power devices, where the presence of surface states in parallel to the 2D channel at the AlGaN/GaN boundary can lead to a substantial surface leakage current [4–7]. Another interesting material system, specifically for future electronic devices or various applications, e.g. as spintronics or quantum computing, are topological insulators. Here, due to their special topological properties [8, 9], a conductive surface with substantially reduced backscattering appears, while the bulk material still exhibits diffusive transport. Thus, it is the opposite now: One could benefit mostly from the topological properties, if the current transport occurs exclusively through the surface. Therefore, as now the surface is the desired conductance channel, one has to ensure that the current flows predominantly along the topological surface and not through the bulk itself. Nevertheless, from the measurement's point of view, as again different dimensionalities are involved, one still basically has to distinguish between 2D and 3D in order to separate both channels, at least for the case of a bulk topological insulator. The presence of thin films can complicate the proceeding much more, as it will be discussed later on in chapter 6.

So, if it turns out to be possible to distinguish the dimensionality of current transport, then one also could disentangle a considerable number of the different parallel conductance channels. The solution on this are position-dependent resistance measurements. Here, in contrast to one measurement with fixed contacts, multiple resistance measurements are performed subsequently, each of them with differently positioned contacts. So, in the end, from such measurements the specific distance-dependency of the resistance can be revealed. From theory it can be derived that the dimensionality of a charge transport channel directly affects the dependency of the resistance on the contact positions. Therefore, in principle it is possible to separate 2D and 3D channels from such position-dependent resistance measurements. While this can be done very easily for either pure 2D or 3D channels, it is more complex for mixed channels, i.e. a 2D channel and a 3D channel in parallel, as discussed before. Nevertheless, in combination with suitable theoretical models for the involved channels, i.e. which relate the measured resistance to the individual conductivities, it is possible to disentangle such composed systems and to determine separate conductivity values for each transport channel inside the system under study. In practice, usually four-point measurements are performed, i.e. four contacts are used in order to eliminate the influence of contact resistances. These four contacts are then subsequently placed at different positions and the corresponding four-point resistance is measured.

However, one fact still complicates the implementation of such position-dependent measurements, namely that everything is settled on the microscale or even nanoscale. Usually, for performing electrical measurement on these scales, metallic contacts are fabricated by lithography. Obviously, this does not work in the present case, as then no position-dependent measurements would be possible (or only very few for a very large amount of contacts). Another drawback of lithography is that no *in situ* measurements are possible, as the material always has to be exposed to ambient conditions in order to fabricate the contacts. However, this can substantially change the properties, e.g. of the surface, and therefore falsify the subsequently performed measurements. So, a better method is necessary. Nevertheless, a suitable tool for electrical measurements on the nanoscale with variable contact position on top of a surface already exists — the scanning tunneling microscope (STM). When the first STM has been developed in 1981 [10–12], it was used preferentially for imaging surfaces, but during the years the field of application shifted more and more to spectroscopic and electrical measurements on the nanoscale. However, it only exhibits one tip and for four-point measurements obviously four contacts are required. So, multi-tip scanning tunneling microscopy is the method of choice. A multi-tip STM is a very versatile tool, as it combines the full functionality of a single-tip STM with the possibility of performing multi-contact electrical measurements on surfaces. For example, a four-tip STM, i.e. in principle four single STMs in one setup, contains four separate tips which can be placed individually on a surface in order to establish electrical contacts to the sample. So, position-dependent resistance measurements are easily possible. Compared to lithography, no contacts have to be fabricated and all measurements are possible *in situ*. The first four-tip STM was introduced in 2001 [13] and since then several home-built designs have been developed [14–16]. Also an extension for including atomic force microscopy is possible [17–19] which can be used in order to access conductive structures on the nanoscale on top of non-conducting substrates. Up to now, it has been already applied for years in order to successfully reveal transport phenomena on the nanoscale. For example, studies dealt with conductance anisotropy on surfaces [20,21], step resistances [22,23], resistivities of nanowires [24–26], doping layers in semiconductors [27,28], topological insulators [29–31], resistances across grain boundaries [32,33], surface defects [34], ballistic transport channels [35,36] and spin-polarized transport [37,38]. This list is only an excerpt of the performed studies and does not claim for any completeness. However, it can be seen that the applicability of a four-tip STM is extended over a very broad range in the field of nanoscopic electrical conductance measurements.

So, it can be concluded here that with a multi-tip STM it is possible to perform position-dependent resistance measurements down to the nanoscale, as it is necessary in order to disentangle multiple parallel conduction channels. Such a multi-tip STM has been used for all four-point measurements presented within this thesis. In the next chapter 2, the instrumental setup of the four-tip STM is depicted which has been applied for obtaining the measurements on semiconductors and topological insulators presented in the chapters 4 – 7. An introduction into the theory of position-dependent four-point measurements will be given in chapter 3, while more sophisticated transport models considering multiple 2D and 3D channels in parallel are shown in chapters 4 and 5.

2. Experimental Setup

Within this chapter, the instrumental setup is presented which is used for all of the measurements throughout this thesis. Primarily, it is focussed on the multi-tip scanning tunneling microscope by showing an overview about its individual components and its functionality in order to perform position-dependent electrical conductance measurements. Specifically, this includes a discussion of the electronics, the method of controlling the tip positions by using an optical microscope, and the procedure for establishing a hard contact between the four tips and the sample in order to allow for four-point resistance measurements.

2.1. Multi-tip scanning tunneling microscope

The multi-tip scanning tunneling microscope (STM) exhibits four tips and operates under ultra-high vacuum (UHV) conditions, i.e. it is located inside a UHV chamber with a base pressure of $1 \times 10^{-10}\,\mathrm{mbar}$, as depicted in Fig. 2.1. Fig. 2.1(a) shows an overview of the complete chamber exhibiting several tools for *in situ* sample preparations, e.g. a high-current annealing stage, an optical and infrared pyrometer and multiple evaporators (Bi, Te, Si, Ge) with a quartz balance for controlling the flux. The part with the multi-tip STM inside is depicted in Fig. 2.1(b). A more detailed overview can be found in Fig. 2.2, where a top-view of the STM located on a CF160 flange with multiple cable feedthroughs is visible in Fig. 2.2(a) and a close-up of the four tips in the center is depicted in Fig. 2.2(b).

The multi-tip STM is rather small with a total outer diameter of only $50\,\mathrm{mm}$ [16]. It contains four separate STM tips arranged symmetrically, and each of them has the full functionality of a single-tip STM, i.e. an acquisition of STM images is possible with all

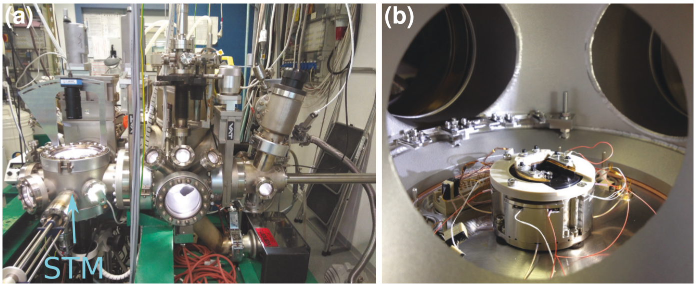

Figure 2.1.: (a) Overview of the ultra-high vacuum chamber, (b) Side-view of the multi-tip scanning tunneling microscope inside the UHV-chamber

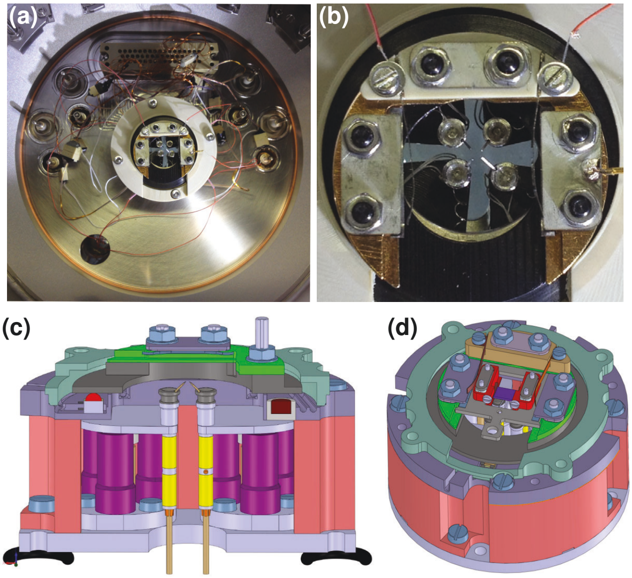

Figure 2.2.: (a) Top-view of the multi-tip STM in the UHV-chamber. It is positioned on a CF160 flange providing all cable feedthroughs for the wiring. (b) Enlarged image of the multi-tip STM showing the four tips inside the tip holders each positioned in the edge of a square. (c) Cross-section of the multi-tip STM. In the drawing, the three tube piezos (magenta) for the scanning movement below each of the four sliders, and the *Koala Drive* (yellow) for the z-approach below the tips are visible. (d) Drawing of the STM with inserted sample holder. The sample surface faces downwards towards the four tips. The drawings in (c) and (d) were produced by *Dr. Vasily Cherepanov*.

four tips. As visible in Fig. 2.2(b), the (tungsten) tips are mounted in tip holders with an elevation angle of $45°$ with respect to the surface plane, and are pointing towards the center of the STM. Each tip holder is fixed by a small magnet on top of a tip recipient, as visible in the cross-sectional view in Fig. 2.2(c). In turn, this tip recipient is attached to the end of a small nanopositioner along the z-direction (depicted as yellow), i.e. the so-called *KoalaDrive* [39]. Due to its special working principle, this positioner allows a very smooth and precise movement along its axis, so that it is used in the setup for the coarse approach of the tips towards the sample surface (z-direction). Each of the four positioners is fixed at the side of a plate [black triangles below the tips in Fig. 2.2(b)] which in turn is positioned on top of three tube-piezos arranged vertically and in parallel to each other (shown in magenta color). So, each set of such three piezos which are electrically connected in parallel, allows the scanning movement in x-, y- and z-direction of the corresponding STM tip. By driving the piezos with a saw-tooth signal, so that the plates on top act as inertial sliders, the in-plane coarse positioning is achieved.

A sample which is mounted inside a standard (*Omicron*) sample holder, can be inserted into the STM by using a wobble stick. The orientation of the sample itself is upside down, so that the surface points towards the tips below, as it is depicted in the drawing in Fig. 2.2(d)

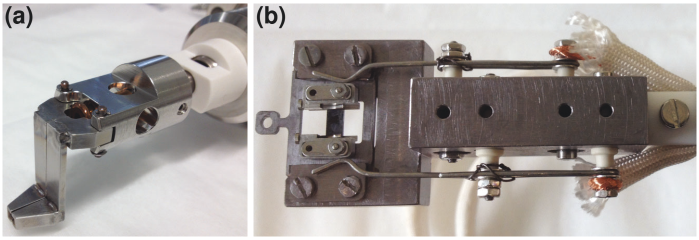

Figure 2.3.: (a) Wobble stick with a kinked pincer at the end. With this special pincer a transfer of samples between the STM and the transfer rod, which are both located in different parallel planes, is possible by only rotating the stick. (b) Top-view of the high-current annealing stage with a Si sample mounted inside a standard *Omicron* sample holder. The thick cables and the large size of the current contacts (springs) allow a reduced contact resistance in order to achieve high currents up to $10\,\mathrm{A}$.

which shows the STM with a mounted sample holder on top. The sample recipient of the STM is not fixed, but rotatable, as it is positioned on top of three (shear) piezo elements. So, the sample orientation can be changed in between measurements, without the need of directly touching the sample. In dependence of the type of the used sample holder, there are in total three possibilities for establishing electrical contacts to the sample, i.e. by the sample recipient itself or by two springs on top [indicated next to the two red blocks in Fig. 2.2(d)]. However, for indeed achieving three separated contacts, all of them have to be electrically insulated on the sample side.

As inside the UHV chamber the STM sample plane and the planes of the recipients at the transfer rods are not on the same height, it is necessary, in order to allow for a sample transfer in between, to use a wobble stick with a special pincer at the end, as depicted in Fig. 2.3(a). Such a pincer has a kinked shape, so that the height difference can be bridged by simply rotating the stick, i.e. the sample is first picked up, then rotated, and finally inserted upside-down in the STM. Prior to the measurements of this thesis the sample system of the multi-tip STM was not yet compatible to the *Omicron* standard, and thus it has been modified first. For this purpose, besides further parts for the UHV system, such a pincer was assembled. Additionally, also a new high-current annealing stage was designed for the *Omicron* sample holders, as depicted in Fig. 2.3(b). Such an annealing stage is used for flashing semiconductor materials, e.g. Si substrates, at high temperatures up to $1200\,^{\circ}\mathrm{C}$ by direct current heating, in order to achieve a clean surface without any oxide on top, enabling to prepare a specific surface reconstruction afterwards. The sample recipient of the stage exhibits two massive springs in order to allow for a stable electrical contact with the sample holder for injecting high currents up to $10\,\mathrm{A}$ through the sample. For this reason, also a large diameter of the cables is chosen. Both springs are electrically insulated from the body in between by using ceramic (*Macor*) washers. Furthermore, molybdenum is chosen as material of the very massive metallic body, in the same way as it applies for all other metal parts, so that degassing due to undesired excessive heating by thermal coupling during operation is mostly reduced, since such a heating would lead to an increased pressure inside the UHV chamber, which in turn is unfavourable for achieving a clean sample surface. A dimensioned drawing of the annealing stage can be found in Fig. C.1 in the appendix C. Obviously, in order to obtain a current flowing only through the sample substrate itself, and not through the holder surrounding it, also the contacts on the sample holder itself have to electrically insulated from the frame. This is similarly achieved by several ceramic plates positioned both below the two contact blocks and in between the screwed connections, as it is partly visible in Fig. 2.3(b). Since a high current results in a brightly glowing substrate, it is easily possible to monitor its temperature with an optical pyrometer.

The STM itself is directly mounted on the metal flange and does not have a mechanism for reducing vibrations, e.g. as a damping achieved by a spring suspension. However, the complete UHV chamber is mounted onto a passive air damping system which turned out to be sufficient for vibration isolation during STM measurement. An exchange of the tips in the STM is possible while maintaining UHV conditions. For this purpose, a special tip shuttle is used, consisting of a standard *Omicron* plate with a squared hole inside, so that four tip holders can be mounted at the same time, each positioned in one corner of the square. This tip shuttle can then be loaded similar to a standard sample. Within the STM the coarse positioning of the tips is used in order to deposit first the mounted tips in an empty shuttle and then pick up new tips from a second shuttle.

2.2. Electronics

The electronics used for the multi-tip STM is very similar to the one of a single-tip STM, but every component is required four times, e.g, as four high-voltage (HV) amplifiers for the tips. However, there are a few specific electrical components only used in the multi-tip setup which are discussed in the following. Basically, the cabling between the STM and the electronics is depicted in Fig. 2.4. The control unit (20 bit DSP-unit from *Createc*) exhibits four channels, each for controlling a single tip. The outputs from each channel, i.e. the digital-analogue converters (DACs), are used for the piezo signals (with a high-voltage amplifier in between) and the bias voltage of the controlled tip. The corresponding inputs, i.e. the analogue-digital converters (ADCs), measure the tip signals which are either the current or the voltage. So far, this setup is very similar to a single-tip STM. However, for the four-tip STM not only a bias voltage is applied at one tip, but at four tips at the same time. This implies that in order to reveal the current through each tip individually, the current cannot be acquired on the sample side, but has to be measured on the tip side separately for each tip. In general, for determining the current at the tunneling junction a transimpedance amplifier (*Femto* DLPCA-200), i.e. an amplifying current-to-voltage converter, is mostly used which allows a resolution down to the picoampere scale. However, a drawback is that it only can measure current with respect to ground (GND). But if the current has to be measured on the tip side, i.e. the side on which the bias voltage is applied, such a direct measurement with respect to GND is not possible. So, in order to further use the DLPCA-200, each of the four devices has to be set on a floating potential corresponding to the specific bias voltage applied to the attached tip. In order to achieve this, an

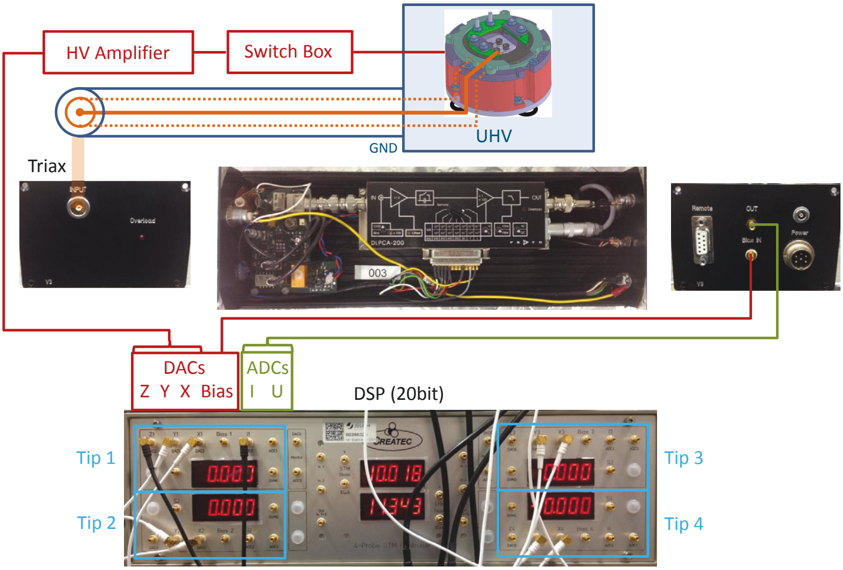

Figure 2.4.: Overview of the cabling between the electronics and the multi-tip STM. The control unit (lower part) has four channels for controlling the tips. The corresponding outputs (Z,Y,X,Bias) are each connected with a single tip with a high-voltage amplifier (and a switch box) in between. The inputs (I,U) of the channels measure the current or voltage from the tips which are both pre-processed by either a current preamplifier or a voltage follower in between (*Femto* box). The tips are connected to the *Femto* boxes by a triaxial cable.

additional electronic circuit is needed implemented together with the DLPCA-200 inside a box (shown in the center part of Fig. 2.4) which is in the following referred to as *Femto box*. Basically, the working principle of such a box is the following: The bias signal is used as reference for the DLPCA-200. The current signal from the tip is applied to the DLPCA-200 which measures the current with respect to the bias voltage. The converted output signal (voltage) is still shifted by the bias voltage, so that it first has to be subtracted by means of an operational amplifier (subtractor). Finally, the output signal can be forwarded to the STM control unit (I input). So, by using in total four *Femto* boxes, the current of each tip can be obtained separately.

Besides the current path, there exists another separated path inside the *Femto* boxes in order to measure a voltage at the tip. A switching between current and voltage mode is realized by a relay which can be controlled by the STM control unit. Within the voltage mode, the tip signal bypasses the DLPCA-200, and instead is forwarded directly to an operational amplifier (OP), i.e. a voltage follower, which basically only measures the applied voltage at the tip without any current flow due to the very high input impedance of the OP. Afterwards, the voltage signal is similarly forwarded to the STM control unit (U input) as before.

For the connection between the tips and the input of the *Femto* boxes, a triaxial cable is used. This has the advantage that especially for fast bias voltage ramps, e.g. as it is common for four-point transport measurements, no capacitive currents occur. If a standard coaxial cable with a grounded shield is used, the capacitance between core and shield would induce a substantial capacitive current due to the changing electric field during a voltage ramp. In turn, this leads to a falsification of the measurement of the actual (ohmic) current through the tips and sample, so that the capacitance effect should be avoided. In the case of the triaxial cable the outer shield is still on GND. However, the inner shield is set to the same potential as the signal at the core by using the voltage follower of the *Femto* boxes. Thus, no electric field is present between core and inner shield, so that also no capacitive current appears during fast voltage ramps. Within the UHV chamber, the type of cabling reduces to coaxial, as the chamber itself serves as surrounding GND. The inner shield is continued as far as possible towards the tip and only ends immediately before the contact to the tip recipient.

Another speciality of the setup is the usage of a switch box in between the HV amplifier and the piezo elements. Such a box just changes the assignment of the piezo electrodes to the HV amplifier signals, which can be controlled by the STM software. This is necessary for the present setup, as specifically the *KoalaDrives* need two separate channels for operation. So, in order to perform a coarse movement in z-direction, the switch box connects the *KoalaDrive* with the x- and y-signals used before for the tube piezos. After operation the channels are switched back. A drawback of this procedure is that the piezo offsets cannot be maintained during the operation of the *KoalaDrive*. However, this can be fixed by implementing additional HV amplifiers.

The operation of the STM is controlled by a software from *Createc*. This software is based on a version for a single-tip STM and contains several modifications specifically for the multi-tip setup. A screenshot of the STM software can be found in Fig. C.2 in the appendix C.

2.3. Control of the four tips

An exact control of the tip positions is crucial in order to perform any position-dependent electrical measurements with the four tips at the same time. In the following, it is discussed, how such a controlled positioning can be achieved, both in lateral and in vertical direction.

2.3.1. Lateral tip positioning

For a single-tip STM, the positioning of the tip is not a very difficult task, as only one tip is present. If a STM image has to be recorded, the tip can be initially placed everywhere on the sample without any restrictions. A specific structure on the sample can then be found by using the information from the recorded image. However, this is different for the multi-tip STM, as here all four tips are present at the same time on the sample surface. So, if the tips are moved laterally without knowing their relative positions, the risk of collisions arises, and obviously from a STM image recorded with one tip no direct information about

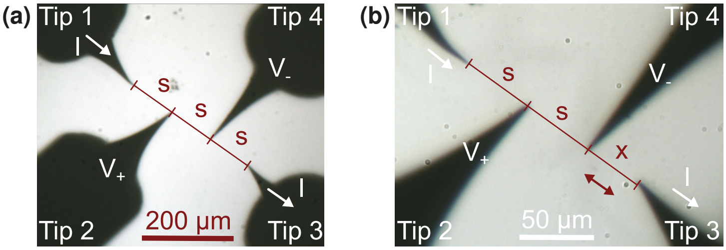

Figure 2.5.: (a) Optical microscope image of the four tips on the sample surface. As the light of the microscope is reflected by the sample surface, but not by the tips, the dark contrast allows to identify and control the tip position easily. In the shown image the tips are arranged in a equidistant linear configuration with equal spacing $s = 50\,\mu\text{m}$, whereby the outer tips are used as for current injection and the inner tips as voltage probes. (b) Optical image with larger magnification. The tips are now positioned in a non-equidistant linear configuration, where only three of the tips are spaced equally by $s = 50\,\mu\text{m}$, while the outer tip 3 used as current sink has a different distance of x.

the positions of the other tips can be gained. So, a further method has to be used to reveal the exact tip positions on the surface.

The method applied for the present setup is to use an optical microscope in order to view directly onto the sample surface. In the obtained optical image, the tips are directly visible by a dark contrast, as it is depicted in Fig. 2.5. The light inciding through the optics of the microscope gets reflected on the sample surface due to its planar shape, but not at the tips, resulting in a sharp contrast which identifies the actual tip positions. Different magnifications are possible, e.g. which allows to image linear tip arrangements with larger spacings, as shown in Fig. 2.5(a), as well as to obtain higher resolution images for smaller distances, as depicted in Fig. 2.5(b). The highest possible resolution is approximately $1.5\,\mu\text{m}$, i.e. two tips spaced by $1.5\,\mu\text{m}$ can still be distinguished, but for even smaller distances that is not possible anymore. However, the position of contact between two adjacent tips can still be obtained by monitoring the current. If a contact occurs, the current through both tips will be exactly equal with opposite sign, assuming that no further current paths exist, i.e. due to further tips or a grounding of the sample.

The tips are mounted with an elevation angle of $45°$ inside the tip holders, as already mentioned before. This is indeed necessary not only for enabling to approach their apices down to very small distances, but also in order to allow for an imaging of the tips by the optical microscope. If the tips were arranged perpendicular to the sample surface, the optical method would not work. However, this implies that in the optical images not directly the tip shape is visible, but only a projection of it into the sample plane. In general, this appears to be not a problem, as in most cases only the lateral positions are of interest. The vertical positions, i.e. the approach, can be controlled by the electronics using the tunneling current signal as feedback. One drawback of the tip geometry is that any deformation of the tips, e.g. caused by previous contacts, occurring particularly in the plane which is composed of the tip axis and the (sample) surface normal, might not be easily visible in the optical images. Thus, in this case there can be a small error in determining the tip position, as there is a deviation between the apparent point of contact, deduced from the projection in the optical image, and the actual position of contact. Nevertheless, some additional information about the z-direction can still be gained from the optical images. The actual position of the focal plane, in which the apices of the tips are sharply visible, indicates their distance with respect to the sample, if prior the focal plane of the sample itself has been determined. As with increasing magnification also the depth of focus reduces substantially, this method is quite precise.

A further method is to image the tip positions with an electron microscope. Such a microscope has a much better resolution so that even tip distances down to $< 100\,\mathrm{nm}$ can be resolved, but the setup in total is also much more complex. So, if for the measurements not specifically such a high resolution is necessary, the method with an optical microscope is also sufficient. Another substantial advantage of the optical microscope compared to an electron microscope is that the frequently observed influences of the electron beam on the surface properties of the sample can be completely avoided [40–42].

The tip positioning itself is performed with the lateral coarse positioning system. Each tip has its own coordinate system which is used for positioning, whereby the y-axis always points along the tip axis. However, for scanning all four tips use a collective coordinate system. Particularly, this is necessary in order to avoid any tip collisions, when two or more tips scan at the same time. Further more detailed information about the different coordinate systems of the tips can be found in the appendix C.2.

2.3.2. Approaching into hard contact

For actual transport measurements with the multi-tip STM, a tunneling contact between the tips and the surface is not sufficient, but a direct contact between both has to be established which is referred to as *hard* contact in the following. Indeed, for the two tips used for measuring the voltage on the sample surface, also a tunneling contact would be principally sufficient, if a setup similar to scanning tunneling potentiometry is chosen [43], as it will be discussed later on in section 7.5.1, but for the current injecting tips still a hard contact is required. However, for the four-point measurements presented in this thesis, such a potentiometry setup has not been used.

The procedure for establishing a hard contact with the sample surface for all tips is as follows: In a first step, the four tips are approached until a tunneling contact with a current in the low nA range is established. Then, after retracting the tips by several nm, the feedback of the STM is switched off, and the tips are manually approached further separately until an increase in the current up to $1\,\mu\mathrm{A}$ is observed. At this point, the tips are in hard contact with the sample, but they only touch the surface and have a penetration depth of only a few Å which is confirmed by separate experiments. One of such experiments is depicted in Fig. 2.6(a). Here, multiple hard contacts have been established subsequently along a straight line on a Si(111) surface. In the STM image, the distinct contact positions of the tip with the sample can be clearly identified by the appearance of small holes in the surface. In the corresponding height profile in Fig. 2.6(b), all tip indentations exhibit

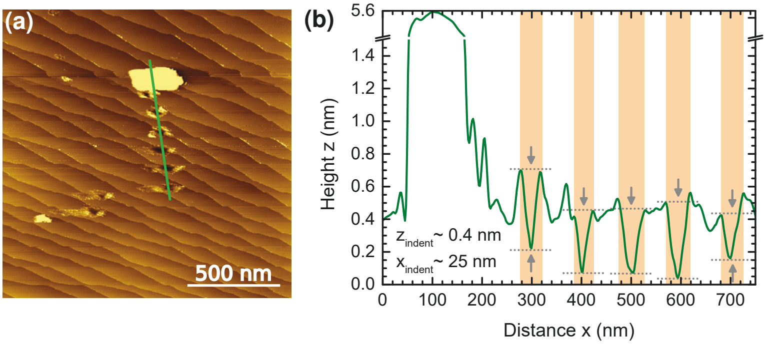

Figure 2.6.: (a) STM image of the tip contact positions on a Si(111) surface ($U = -1.3\,\mathrm{V}$, $I = 610\,\mathrm{pA}$). Multiple hard contacts with the surface were established and in between the tip was moved laterally along a straight line. At each contact position the tip indentation into the surface is clearly visible. (b) Profile line across the contact positions of the tip with the surface. All tip indentations (marked by the vertical red bars) are approximately equal in size exhibiting a depth of $z_{\mathrm{indent}} \approx 0.4\,\mathrm{nm}$ and a width of $x_{\mathrm{indent}} \approx 25\,\mathrm{nm}$.

nearly an identical shape with a width of $25\,\mathrm{nm}$ and a penetration depth of approximately $4\,\mathrm{\AA}$. The width coincides very well with the expected tip diameter [44]. The large adsorbate visible on the left most probably originates from residues at the tip deposited at the initial contact position. So, this measurement proves that the method presented before is suitable for establishing a very smooth contact to the sample surface with a penetration depth similar to the thickness of only one atomic layer. It should be noted additionally that the tips can act as a spring due to the mounting position with an angle of $45°$ with respect to the sample [44]. So, when pressed onto the sample surface, the tips can simply bend away. This implies that the vertical movement of the piezo is not equivalent to the actual penetration depth of the tips into the surface.

In principle, also a hard-contact established by using an enabled feedback with a very high current setpoint is possible, but indeed not favourable. It has turned out that in this case enhanced oscillations in the current appear due to an escalating feedback. So, without the feedback there are no oscillations, but instead the current can drift away from its initial value, as the tip might drift away with time. However, if the drifting is not too large, this does not have an effect on the four-point measurements, as shown briefly in the following section.

2.3.3. Electrical measurements

Each of the four tips in the multi-tip STM can be used as current or voltage probe, as indicated schematically in Fig. 2.7(a). In a four-point measurement setup, two tips inject a current into the sample, and the other two are used for measuring the resulting voltage drop. The basic procedure for performing such an electrical four-point measurement is as follows: For transport measurements, the sample is first set to floating potential, i.e. the

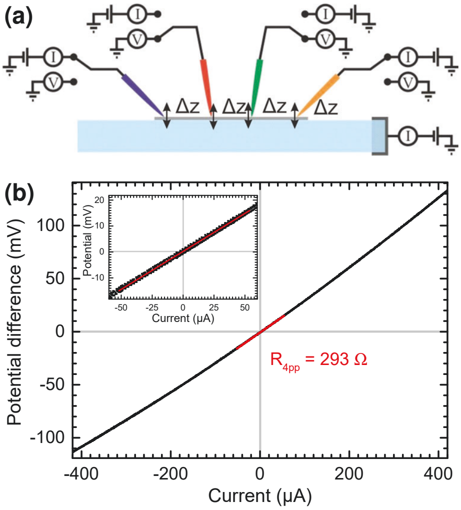

Figure 2.7.: (a) Schematic of the possible spectroscopic operations of the multi-tip STM. Each of the four tips can be approached individually towards the sample surface and used as a current or as a voltage probe. (b) Example of a measured voltage difference between two tips as function of the injected current by the other two tips. From such an I-V curve the four-point resistance can be extracted by a linear fit (red line). Due to non-linearity effects appearing at higher current values the linear fit is applied in the vicinity of the zero-crossing (inset).

connection to ground of the sample holder recipient in the STM is removed. By applying a symmetrical voltage ramp between two (current) tips, a corresponding ramped current (in the μA range) is injected into the sample. The voltage drop is measured in between the other two (voltage) tips. Since the voltage is measured as a function of the actual current, there is no influence of a potentially fluctuating contact resistance at the tip contacts, e.g. due to slight drift of the piezos towards or away from the surface with time. So, any variation in the sample current caused by the switched-off feedback does not have an effect on the measurement results. The four-point resistance $R^{4p} = \frac{I_{\text{injected}}}{U_{\text{measured}}}$ is finally obtained from the slope of the measured I/V curves in the vicinity of the origin, i.e. from a fit to the region close to zero, as it is depicted in Fig. 2.7(b) by the red line. The inset shows explicitly the linear region. Each obtained resistance value is averaged over three subsequently measured I/V curves.

So far, the fundamentals of the multi-tip STM and its general capability for performing *in situ* position-dependent four-point resistance measurements has been discussed. In the next chapter, an more mathematical overview is given about the relation between measured resistance and the conductivity of the material, and several specific tip configurations which are necessary for actual four-point measurements are presented.

3. Position-dependent transport measurements

With the multi-tip STM presented in the previous chapter, it is possible to perform position-dependent transport measurements down to the nanoscale. Thus, from an experiment a value for the four-point resistance can be obtained, in the same way as it is also applies for measurements on the macroscale, e.g. with a (four-terminal) multimeter. However, the measured value of *resistance* R only holds for the specific measurement situation and does not describe the intrinsic sample properties directly. For this purpose, a different quantity has to be determined, i.e. the *resistivity* ρ, which is an intrinsic material property. The same relation applies for the quantities *conductance* G and *conductivity* σ. So, it is not sufficient to perform only a conductance measurement, but in order to gain some deeper insight into the transport properties of the material under study, the intrinsic material parameters have to be determined from the measurement data.

In fact, it can be quite a challenging task to determine the conductivity (or resistivity), sometimes even more than the actual transport measurement itself. The problem is that a specific relation has to be found between the measured resistance R and the conductivity σ of the material. However, such a relation can depend on many factors, e.g. the dimensionality and size of the material, the arrangement and size of the measuring probes, the number of current paths, etc. While it is quite easy to derive analytical relations $R(\sigma)$ for homogeneous materials which are either one-dimensional, i.e. a conducting line, two-dimensional, i.e. a conducting sheet, or three-dimensional, i.e. a conducting bulk, it can be much more complicated for composed materials exhibiting multiple current paths. Particularly, for systems containing conductance channels of different dimensionality, i.e. a conducting surface on top of a conductive bulk, there indeed exist analytic expressions but due to their complexity numerical solution methods are necessary. The derivation and applicability of such models is a main topic of this thesis and will be discussed later on in the chapters 4 and 5.

Within this chapter, the derivations of the analytical solutions for the two simplest cases, i.e. the two-dimensional sheet and the three-dimensional bulk, are presented for isotropic samples. Furthermore, the two-dimensional case is also discussed for anisotropic materials, i.e. the conductivity is not a scalar value but a tensor. For all three cases, the influence of the specific measurement geometry, i.e. the tip arrangement, is considered and the corresponding analytical equations are presented.[1]

---

[1] These equations are all well-known in literature, but often shown without any derivation; thus, it is included here for the sake of completeness and as basis for the subsequently discussed multi-layer models.

3.1. Principle of four-point measurements

The most common method for measuring electrical transport is by using four-point measurements. Here, a current I is injected into the sample by applying a bias voltage U_{bias} with two probes, while the voltage drop ΔU is measured by two different probes, as it is depicted schematically in Fig. 3.1(a). One may ask, why it is necessary to actually measure the voltage drop with two more probes, as it seems to be equal to the applied bias voltage between both injecting tips. So, a two-point measurement would be sufficient, as shown by the setup in Fig. 3.1(c). However, this is not true, if the contact resistance is considered. For a two-point setup, the measured resistance $R^{2\mathrm{p}}$ is a composition of the actual sample resistance R_{sample} with the contact resistances R_{contact} present at the contacts of the two probes in series and it reads

$$R^{2\mathrm{p}} = \frac{U_{\mathrm{bias}}}{I} = R_{\mathrm{contact},1} + R_{\mathrm{sample}} + R_{\mathrm{contact},2} \tag{3.1}$$

which is shown by the circuit diagram in Fig. 3.1(d). So, R_{sample} cannot be separated as it is intended by the measurement. A solution is to perform a four-point measurement. Here, due to the separation of current injecting and voltage measuring probes, no current flows actually through the inner two probes because of the high input resistance of the voltmeter. This implies that also no voltage drop appears due to the contact resistances which are equally present as before. So, the measured voltage drop ΔU is exactly equivalent to the

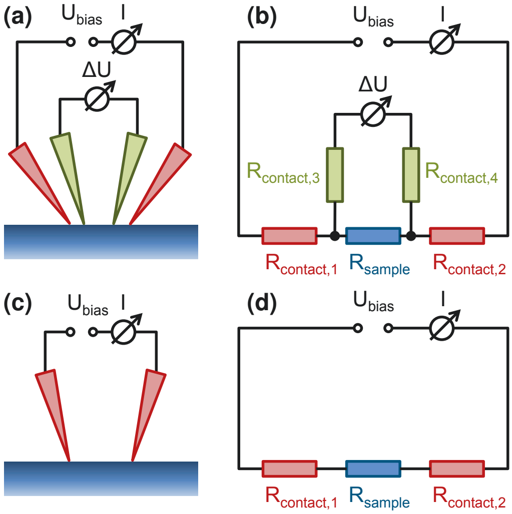

Figure 3.1.: Basic principle of four-point measurements [(a),(b)], compared to the setup with only two probes [(c),(d)]. In (a) and (c) the probe arrangements for four-point and two-point measurements are depicted, respectively. In (b) and (d) the circuit diagrams corresponding to four-point (b) and two-point (d) setup are depicted.

one on the sample surface and the obtained resistance $R^{4\mathrm{p}}$ reads

$$R^{4\mathrm{p}} = \frac{\Delta U}{I} = R_{\mathrm{sample}} \tag{3.2}$$

which is visualized in the circuit diagram in Fig. 3.1(b). Thus, by using four probes it is possible to reveal the sample resistance from the measurement.

First, four-point measurements were applied in 1915 by *Frank Wenner* in the field of geophysics in order to measure the conductivity of earth by equidistantly spaced four probes [45], and today this method is referred to as the *Wenner* method [46, 47]. Also a non-equidistant method had been established and used for geophysics [48]. However, only in 1954, the four-point method was first used in order to reveal the conductivity of semiconductor wafers [49]. Since 1975, it has been finally established as a standard measurement method in the field of microelectronics [50, 51].

3.2. Isotropic conductivity

In this section, the relations $R(\sigma)$ for both two-dimensional and three-dimensional materials are derived for the isotropic case, i.e. the conductivity σ is a scalar quantity, and linear tip configurations are discussed.

3.2.1. Two-dimensional surface conductivity

In two dimensions (2D), a current can flow within a plane, e.g. as it occurs for a thin conducting sheet. The conductivity describing such a 2D system is termed as $\sigma_{2\mathrm{D}}$ with the unit *Siemens*, i.e. $[\sigma_{2\mathrm{D}}] = \mathrm{S}$. For a rectangular sheet of length L with electrodes along its width W, it is defined as [52]

$$R_{2\mathrm{D}}^{\mathrm{ext}} = \frac{1}{\sigma_{2\mathrm{D}}} \frac{L}{W}. \tag{3.3}$$

which gives a relation between the measured quantity ($R_{2\mathrm{D}}^{\mathrm{ext}}$) and the intrinsic quantity ($\sigma_{2\mathrm{D}}$), however only for the case of extended contacts. It should be noted that, as also the measured quantity conductance G has the same unit *Siemens*, a given value can be ambiguous. For this reason, it is common to add the suffix $/\square$, meaning *per square*, to the unit of the 2D conductivity, resulting in $[\sigma_{2\mathrm{D}}] = \mathrm{S}/\square$. However, there is no additional physical meaning in the added symbol and, technically, it is not included in the regulations for the international system of units (SI) [53, 54]. Nevertheless, it leads to a much easier identification of a 2D conductivity value, and therefore it is used throughout this thesis.

The relation given above in Eq. (3.3) does not hold for point contacts on top of a surface, as it applies for measurements with a multi-tip STM. So, the corresponding relation for such a geometry has to be derived, which will be shown in the following. It should be noted that in this chapter only point contacts with no lateral extension are considered, as it turned out

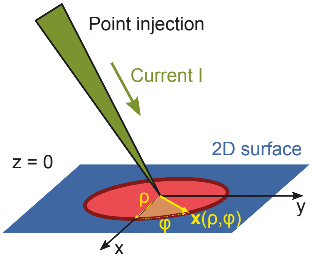

Figure 3.2.: Geometry for a point injection of current I by a tip positioned at $z = 0$ into an infinite 2D sheet. According to the symmetry, polar coordinates $\boldsymbol{x}(\rho, \varphi)$ can be chosen with the coordinate system as indicated.

that for STM tips with typical diameters of $\sim 25\,\mathrm{nm}$ the influence of the contact size is negligible small (cf. section 4.2), so that it is reasonable to simplify the equations by using the approximation of point contacts.

The geometry for such a point injection of current I on top of an infinitely extended sheet, i.e. a 2D system, is depicted in Fig. 3.2. Here, initially only one tip is considered, which is positioned at the origin of the coordinate system and acts as current source[2], while any current sinks are assumed to be located at infinity. First, for such a single-tip arrangement the corresponding potential distribution $\Phi(x, y)$ in the 2D sheet is calculated. Then, in a second step, the potential arising from a current I between two adjacent tips, i.e. a source and a sink, can be obtained by a superposition of the solutions for two correspondingly located single tips. Finally, in order to take into account a four-point probe setup, the potential difference between two voltage probing tips is evaluated, based on the prior solutions, so that in combination with the known current a relation for $R^{4\mathrm{p}}_{2\mathrm{D}}(\sigma_{2\mathrm{D}})$ results. Such a basic approach applies to all derivations of $R(\sigma)$ presented in the following, but obviously, the obtained solutions for each case depend strongly on the dimensionality (and number) of the conducting channels and the specific tip arrangement.

In order to obtain the potential distribution for the single-tip setup depicted in Fig. 3.2, one starts with the relation $\nabla \cdot \boldsymbol{j} = 0$, i.e. the vanishing divergence of current density $\boldsymbol{j}$ due to missing additional sources (sinks) apart from the one at the position of the single tip. This relation immediately follows from Maxwell's equations and holds for the current density $\boldsymbol{j}(x, y)$ in the 2D plane excluding the injection point at the origin. The current density $\boldsymbol{j}$ can be expressed by

$$\boldsymbol{j}(x, y) = \sigma_{2\mathrm{D}} \boldsymbol{E}(x, y) = -\sigma_{2\mathrm{D}} \nabla \Phi(x, y) \tag{3.4}$$

with the electric field $\boldsymbol{E}(x, y)$ and the potential $\Phi(x, y)$, respectively. It follows that

$$\nabla \cdot \boldsymbol{j}(x, y) = \nabla \cdot [-\sigma_{2\mathrm{D}} \nabla \Phi(x, y)] = -\sigma_{2\mathrm{D}} \underbrace{\nabla \cdot \nabla}_{=\Delta} \Phi(x, y) = 0 \tag{3.5}$$

---

[2] The same holds for a current sink with sources at infinity, except that the direction of current is reversed, i.e. the sign of the current density is changed.

$$\Leftrightarrow \qquad \Delta\Phi(x,y) = 0 \qquad\qquad (\sigma_{2D} \neq 0) \tag{3.6}$$

with the Laplace operator $\Delta = \frac{\partial^2}{\partial x^2} + \frac{\partial^2}{\partial y^2}$. Eq. (3.6) represents a homogeneous Laplace equation in two dimensions and has to be solved in order to determine the potential $\Phi(x, y)$. Due to the symmetry of the problem which is visible in Fig. 3.2, the current density has to be angle-independent, i.e. it depends only on the radial distance from the origin while pointing in radial direction ($\boldsymbol{j} = j_\rho(\rho)\hat{\boldsymbol{e}}_{\boldsymbol{\rho}}$)[3]. As a result, also the potential distribution has to be radially symmetric ($\Phi = \Phi(\rho)$). Therefore, it is useful to introduce polar coordinates $\boldsymbol{x}(\rho, \varphi)$ with

$$\boldsymbol{x}(\rho,\varphi) = \begin{pmatrix} x \\ y \end{pmatrix} = \begin{pmatrix} \rho\cos(\varphi) \\ \rho\sin(\varphi) \end{pmatrix} \qquad \text{and} \qquad \rho = \sqrt{x^2 + y^2}. \tag{3.7}$$

The Laplace operator expressed in polar coordinates reads $\Delta = \frac{1}{\rho}\frac{\partial}{\partial\rho}\rho\frac{\partial}{\partial\rho} + \frac{1}{\rho^2}\frac{\partial^2}{\partial\varphi^2}$. However, as $\Phi = \Phi(\rho)$ due to symmetry, the second term immediately vanishes ($\frac{\partial\Phi}{\partial\varphi} = 0$). So, by using the abbreviation $\partial_\rho := \frac{\partial}{\partial\rho}$, it follows that

$$\Delta\Phi(\rho) = 0 \tag{3.8}$$

$$\Leftrightarrow \qquad \frac{1}{\rho}\,\partial_\rho\,\rho\,\partial_\rho\Phi(\rho) = 0 \qquad\qquad \rho > 0 \tag{3.9}$$

$$\Leftrightarrow \qquad \rho\,\partial_\rho\Phi(\rho) = c_1 \tag{3.10}$$

$$\Leftrightarrow \qquad \partial_\rho\Phi(\rho) = \frac{c_1}{\rho} \tag{3.11}$$

$$\Leftrightarrow \qquad \Phi(\rho) = c_1\ln(\rho) + c_2 \tag{3.12}$$

with the two integration constants c_1 and c_2 which have to be determined from boundary conditions. The constant c_2 in Eq. (3.12) forms only an additive term, so that it can be set to zero, i.e. $c_2 = 0$, as the electrostatic potential Φ is physically only defined except for an additive constant. The second condition arises from the basic definition of current density, i.e. $I = \int_F \boldsymbol{j} \cdot d\boldsymbol{F}$, relating the total current I to the integral over the current densities along all surface elements $d\boldsymbol{F}$ of the surface F [4]. In the case of the 2D system with a point injection of current I at the origin, this 'surface' is one-dimensional and corresponds to the path of a closed circle around the origin. So, the current density can be written as

$$I = \oint_F \boldsymbol{j}\cdot d\boldsymbol{F} \overset{\boldsymbol{j}=j_\rho(\rho)\hat{\boldsymbol{e}}_\rho}{=} \oint_F j_\rho(\rho)dF^\rho \overset{dF^\rho=\rho d\varphi}{=} \int_0^{2\pi} \rho\, j_\rho(\rho)d\varphi. \tag{3.13}$$

By using $j_\rho(\rho) = -\sigma_{\text{2D}}\,\partial_\rho\Phi(\rho)$ and inserting Eq. (3.12), it follows for the constant c_1 that

$$I = -\int_0^{2\pi} d\varphi\,\rho\,\sigma_{\text{2D}}\,\underbrace{\partial_\rho\big(c_1\ln(\rho)\big)}_{=\frac{c_1}{\rho}} = -\sigma_{\text{2D}}\,\rho\,\frac{c_1}{\rho}\underbrace{\int_0^{2\pi} d\varphi}_{=2\pi} = -2\pi\sigma_{\text{2D}}\,c_1 \tag{3.14}$$

---

[3] The normalized unity vectors $\hat{\boldsymbol{e}}_{\boldsymbol{i}}$ form a basis of the coordinate system, e.g. with $i \in \{1, 2, 3\}$ for 3D.

[4] The surface element $d\boldsymbol{F}$ is normal to the surface F and in 3D in general given for orthogonal coordinates ξ_i by $d\boldsymbol{F} = dF^i\hat{\boldsymbol{e}}_{\boldsymbol{i}}$ with $dF^i = h_j h_k d\xi_j d\xi_k$, $(i, j, k) \in \{1, 2, 3\}$ and the metric coefficients h_1, h_2, h_3.

$$\Leftrightarrow \qquad c_1 = -\frac{I}{2\pi\sigma_{2D}}. \tag{3.15}$$

So, after back transformation into Cartesian coordinates by using Eq. (3.7), the potential distribution in the 2D sheet can finally be expressed by

$$\Phi(x,y) = -\frac{I}{2\pi\sigma_{2D}} \ln\left(\sqrt{x^2+y^2}\right) = -\frac{I}{4\pi\sigma_{2D}} \ln\left(x^2+y^2\right) \qquad (x,y) \neq (0,0). \tag{3.16}$$

If the current injection is shifted from the origin to the position $\boldsymbol{x}_A = \binom{x_A}{y_A}$, Eq. (3.16) changes into

$$\Phi^A(x,y) = -\frac{I}{4\pi\sigma_{2D}} \ln\left[(x-x_A)^2 + (y-y_A)^2\right] \qquad (x,y) \neq (x_A,y_A). \tag{3.17}$$

The potential arising from a current source $(+I)$ at $\boldsymbol{x}_A$ and an additional current sink $(-I)$ at position $\boldsymbol{x}_B = \binom{x_B}{y_B}$ can be expressed by a superposition as

$$\Phi^{AB}(x,y) = \Phi^A(x,y) + \Phi^B(x,y) \tag{3.18}$$

$$\Leftrightarrow \quad \Phi^{AB}(x,y) = \frac{I}{4\pi\sigma_{2D}}\left[-\ln\left[(x-x_A)^2+(y-y_A)^2\right] + \ln\left[(x-x_B)^2+(y-y_B)^2\right]\right] \tag{3.19}$$

$$\Leftrightarrow \quad \Phi^{AB}(x,y) = \frac{I}{4\pi\sigma_{2D}} \ln\left[\frac{(x-x_B)^2+(y-y_B)^2}{(x-x_A)^2+(y-y_A)^2}\right]. \tag{3.20}$$

In order to obtain the potential difference between two probes at $\boldsymbol{x}_C = \binom{x_C}{y_C}$ and $\boldsymbol{x}_D = \binom{x_D}{y_D}$, Eq. (3.20) has to be evaluated at these positions, resulting in

$$\Phi^{AB}_{CD} = \Phi^{AB}(x_D,y_D) - \Phi^{AB}(x_C,y_C) \tag{3.21}$$

$$\Leftrightarrow \quad \Phi^{AB}_{CD} = \frac{I}{4\pi\sigma_{2D}}\left[\ln\left[\frac{(x_D-x_B)^2+(y_D-y_B)^2}{(x_D-x_A)^2+(y_D-y_A)^2}\right] - \ln\left[\frac{(x_C-x_B)^2+(y_C-y_B)^2}{(x_C-x_A)^2+(y_C-y_A)^2}\right]\right] \tag{3.22}$$

$$\Leftrightarrow \quad \Phi^{AB}_{CD} = \frac{I}{4\pi\sigma_{2D}} \ln\left[\frac{\left[(x_D-x_B)^2+(y_D-y_B)^2\right]\left[(x_C-x_A)^2+(y_C-y_A)^2\right]}{\left[(x_D-x_A)^2+(y_D-y_A)^2\right]\left[(x_C-x_B)^2+(y_C-y_B)^2\right]}\right]. \tag{3.23}$$

Eq. (3.23) gives a general expression for the potential drop in a 2D sheet, arising from a four-point setup with tips at $\boldsymbol{x}_A$, $\boldsymbol{x}_B$ (current injection) and $\boldsymbol{x}_C$, $\boldsymbol{x}_D$ (voltage probes). With $R^{\mathrm{4pp}}_{AB,CD} = \frac{\Phi^{AB}_{CD}}{I}$ the corresponding four-point resistance is obtained[5]. However, for specific tip arrangements Eq. (3.23) simplifies significantly, which will be discussed in section 3.2.3.

---

[5] This index notation ij, kl with (i,j,k,l) being a permutation of (A,B,C,D) is always used in the following in order to label four-point resistances with a non-specific geometrical tip arrangement. The first pair ij denotes the two current injecting tips, while the second pair kl describes the voltage probing tips.

3.2.2. Three-dimensional bulk conductivity

In three dimensions (3D), a current can flow in the entire space, e.g. through an (infinitely extended) bulk crystal. The conductivity describing such a 3D system is termed as $\sigma_{3\mathrm{D}}$ with the unit $[\sigma_{3\mathrm{D}}] = \mathrm{S/m}$. For a cuboidal bulk of length L with electrodes on its opposite surfaces with area A, it is defined as [52]

$$R_{3\mathrm{D}}^{\mathrm{ext}} = \frac{1}{\sigma_{3\mathrm{D}}} \frac{L}{A} \tag{3.24}$$

which gives a relation between the measured quantity ($R_{3\mathrm{D}}^{\mathrm{ext}}$) and the intrinsic quantity ($\sigma_{3\mathrm{D}}$). However, Eq. (3.24) only holds for the case of extended contacts, so that for point contacts on top of a bulk crystal, e.g. as present in a multi-tip STM setup, again a modified expression has to be derived which is shown in the following.

In Fig. 3.3, the geometry of the 3D case with a point injection of current I on top of a semi-infinite bulk is depicted. The coordinate system is chosen in such a way that the surface is located at $z = 0$ with the injection point at the origin, while the z-axis points downwards into the half-space with the bulk material ($z \geq 0$). With similar considerations as shown before for the 2D case in Eqs. (3.4) – (3.6), except for using 3D coordinates and $\sigma_{3\mathrm{D}}$ now, one obtains the homogeneous Laplace equation in three dimensions, i.e.

$$\Delta\Phi(x, y, z) = 0 \qquad\qquad (\sigma_{3\mathrm{D}} \neq 0) \tag{3.25}$$

with the Laplace operator $\Delta = \frac{\partial^2}{\partial x^2} + \frac{\partial^2}{\partial y^2} + \frac{\partial^2}{\partial z^2}$. In order to solve this equation, it is again useful to take advantage of the symmetry of the problem. From Fig. 3.3 it is visible that for the half-space of the bulk ($z \geq 0$) the current density has to point in radial direction and does not have any angular dependence, i.e. $\boldsymbol{j} = j_r(r)\hat{\boldsymbol{e}}_{\boldsymbol{r}}$, which implies that this also holds for the potential $\Phi = \Phi(r)$. Therefore, spherical coordinates $\boldsymbol{x}(r, \theta, \varphi)$ are introduced with

$$\boldsymbol{x}(r, \theta, \varphi) = \begin{pmatrix} x \\ y \\ z \end{pmatrix} = \begin{pmatrix} r\sin(\theta)\cos(\varphi) \\ r\sin(\theta)\sin(\varphi) \\ r\cos(\theta) \end{pmatrix} \qquad \text{and} \qquad r = \sqrt{x^2 + y^2 + z^2}. \tag{3.26}$$

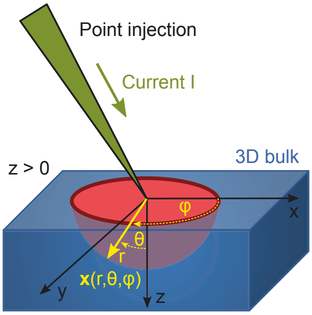

Figure 3.3.: Geometry for a point injection of current I by a tip positioned at $z = 0$ into a semi-infinite 3D bulk material. According to the symmetry, spherical coordinates $\boldsymbol{x}(r, \theta, \varphi)$ can be chosen with the coordinate system as indicated.

The Laplace operator for spherical coordinates reads $\Delta = \frac{1}{r^2}\frac{\partial}{\partial r}r^2\frac{\partial}{\partial r} + \frac{1}{r^2\sin(\theta)}\frac{\partial}{\partial \theta}\sin(\theta)\frac{\partial}{\partial \theta} + \frac{1}{r^2\sin^2(\theta)}\frac{\partial^2}{\partial \varphi^2}$, but when applied only the first term survives, as due to symmetry $\frac{\partial}{\partial\theta}\Phi(r) = 0$ and $\frac{\partial}{\partial\varphi}\Phi(r) = 0$. So, it follows with $\partial_r := \frac{\partial}{\partial r}$ that

$$\Delta\Phi(r) = 0 \tag{3.27}$$

$$\Leftrightarrow \quad \frac{1}{r^2}\,\partial_r\, r^2\partial_r\Phi(r) = 0 \qquad r > 0 \tag{3.28}$$

$$\Leftrightarrow \quad r^2\partial_r\Phi(r) = c_1 \tag{3.29}$$

$$\Leftrightarrow \quad \partial_r\Phi(r) = \frac{c_1}{r^2} \tag{3.30}$$

$$\Leftrightarrow \quad \Phi(r) = -\frac{c_1}{r} + c_2 \tag{3.31}$$

with the two integration constants c_1 and c_2. With the same argument as presented in section 3.2.1, it is reasonable to set $c_2 = 0$, thus the potential vanishes at infinity, i.e. $\Phi(r \to \infty) = 0$. The constant c_1 is again determined from the boundary condition at the injection point, i.e. the injected current I, as

$$I = \int_F \boldsymbol{j}\cdot d\boldsymbol{F} \overset{\boldsymbol{j}=j_r(r)\hat{\boldsymbol{e}}_r}{=} \int_F j_r(r)dF^r \overset{dF^r=r^2\sin(\theta)d\theta d\varphi}{=} \iint_F r^2\sin(\theta)j_r(r)d\theta d\varphi. \tag{3.32}$$

The area F is given by the surface of the hemisphere inside the bulk material with its centre at the injection point. Thus, this implies that the following solution for $\Phi(r)$ will be only valid for a half-space with the injection at the boundary. By using $j_r(r) = -\sigma_{3\mathrm{D}}\,\partial_r\Phi(r)$ and inserting Eq. (3.31), it follows that

$$I = -\int_0^\pi d\theta \int_0^\pi d\varphi\, r^2\sin(\theta)\sigma_{3\mathrm{D}}\, \underbrace{\partial_r\left(\frac{-c_1}{r}\right)}_{=\frac{c_1}{r^2}} \tag{3.33}$$

$$\Leftrightarrow \quad I = -\sigma_{3\mathrm{D}}\, r^2\,\frac{c_1}{r^2}\int_0^\pi d\theta\,\sin(\theta)\underbrace{\int_0^\pi d\varphi}_{=\pi} \tag{3.34}$$

$$\Leftrightarrow \quad I = -\pi\sigma_{3\mathrm{D}}\, c_1 \underbrace{\Big[-\cos(\theta)\Big]_0^\pi}_{=-\cos(\pi)+\cos(0)=2} \tag{3.35}$$

$$\Leftrightarrow \quad c_1 = -\frac{I}{2\pi\sigma_{3\mathrm{D}}}. \tag{3.36}$$

With a back transformation into Cartesian coordinates according to Eq. (3.26), the potential $\Phi(x, y, z)$ for a current injection at the origin is given by

$$\Phi(x,y,z) = \frac{I}{2\pi\sigma_{3\mathrm{D}}\sqrt{x^2+y^2+z^2}} \qquad z \geq 0, (x,y,z) \neq (0,0,0) \tag{3.37}$$

In general, for an injection at position $\boldsymbol{x}_A = \left(\begin{smallmatrix} x_A \\ y_A \\ 0 \end{smallmatrix}\right)$ on top of the surface, it follows correspondingly

$$\Phi^A(x,y,z) = \frac{I}{2\pi\sigma_{3\mathrm{D}}\sqrt{(x-x_A)^2+(y-y_A)^2+z^2}}, \qquad z \geq 0, (x,y,z) \neq (x_A, y_A, 0). \tag{3.38}$$

The potential from a current source at $\boldsymbol{x}_A$ and a current sink at $\boldsymbol{x}_B = \left(\begin{smallmatrix} x_B \\ y_B \\ 0 \end{smallmatrix}\right)$ results in

$$\Phi^{AB}(x,y,z) = \Phi^A(x,y,z) + \Phi^B(x,y,z) \tag{3.39}$$

$$\Leftrightarrow \quad \Phi^{AB}(x,y,z) = \frac{I}{2\pi\sigma_{3\mathrm{D}}}\left[\frac{1}{\sqrt{(x-x_A)^2+(y-y_A)^2+z^2}} - \frac{1}{\sqrt{(x-x_B)^2+(y-y_B)^2+z^2}}\right]. \tag{3.40}$$

The potential difference between two probes at $\boldsymbol{x}_C = \left(\begin{smallmatrix} x_C \\ y_C \\ 0 \end{smallmatrix}\right)$ and $\boldsymbol{x}_D = \left(\begin{smallmatrix} x_D \\ y_D \\ 0 \end{smallmatrix}\right)$ on top of the 3D bulk material can then be expressed by

$$\Phi^{AB}_{CD} = \Phi^{AB}(x_D, y_D, 0) - \Phi^{AB}(x_C, y_C, 0) \tag{3.41}$$

$$\begin{aligned} \Leftrightarrow \quad \Phi^{AB}_{CD} = \frac{I}{2\pi\sigma_{3\mathrm{D}}}\Bigg[&\frac{1}{\sqrt{(x_D-x_A)^2+(y_D-y_A)^2}} - \frac{1}{\sqrt{(x_D-x_B)^2+(y_D-y_B)^2}} \\ &- \frac{1}{\sqrt{(x_C-x_A)^2+(y_C-y_A)^2}} + \frac{1}{\sqrt{(x_C-x_B)^2+(y_C-y_B)^2}}\Bigg]. \end{aligned} \tag{3.42}$$

In the next section, specific tip arrangements commonly used for four-tip measurements are discussed in more detail.

3.2.3. Linear tip configurations

From Eqs. (3.23) and (3.42), general expressions for the 2D and 3D cases are obtained, respectively, which describe the potential drop on the surface as function of the (arbitrary) position $\boldsymbol{x}_i = \left(\begin{smallmatrix} x_i \\ y_i \end{smallmatrix}\right)$ with $i \in \{A, B, C, D\}$ of both current injecting probes (A, B) and voltage measuring probes (C, D). However, in an actual four-point measurement setup, usually a specific probe arrangement is used which substantially simplifies the equations. A common setup is a linear equidistant tip configuration, i.e. all probes are arranged in a straight line and equally spaced by a distance x, as depicted schematically in Fig. 3.4(a). Here, the tips are arranged symmetrically with respect to the origin resulting in the respective positions (without loss of generality is $y_i = 0$) $\boldsymbol{x}_A = -\frac{3}{2}s\,\hat{\boldsymbol{e}}_{\boldsymbol{x}}$, $\boldsymbol{x}_B = \frac{3}{2}s\,\hat{\boldsymbol{e}}_{\boldsymbol{x}}$, $\boldsymbol{x}_C = -\frac{1}{2}s\,\hat{\boldsymbol{e}}_{\boldsymbol{x}}$ and $\boldsymbol{x}_D = \frac{1}{2}s\,\hat{\boldsymbol{e}}_{\boldsymbol{x}}$ with the unity vector $\hat{\boldsymbol{e}}_{\boldsymbol{x}} = \left(\begin{smallmatrix} 1 \\ 0 \end{smallmatrix}\right)$ along the x-axis. Inserting these positions

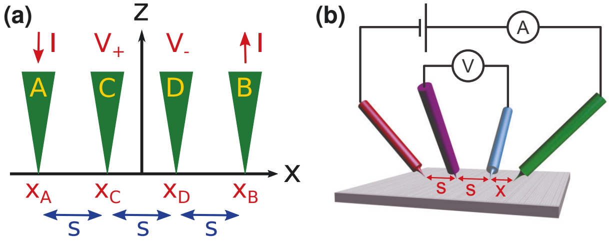

Figure 3.4.: Four-point measurements with a linear probe configuration, in which the current is injected by the outer tips and the voltage is measured by the inner tips. (a) Equidistantly arranged probes with a spacing s in between and the electrical configuration (AB, DC). (b) Non-equidistant setup, in which 3 tips have a spacing s, while the distance between one current injecting tip and the adjacent voltage measuring tip is changed to x.

into Eq. (3.23) and calculating the four-point resistance by $R_{AB,DC} = \frac{-\Phi_{CD}^{AB}}{I}$ leads to[6]

$$R_{\text{lin}}^{\text{2D}}(\sigma_{\text{2D}}) = -\frac{1}{4\pi\sigma_{\text{2D}}} \underbrace{\ln\left[\frac{\left(\frac{1}{2}s - \frac{3}{2}s\right)^2 \left(-\frac{1}{2}s + \frac{3}{2}s\right)^2}{\left(\frac{1}{2}s - \frac{3}{2}s\right)^2 \left(-\frac{1}{2}s - \frac{3}{2}s\right)^2}\right]}_{=\ln\left[\frac{s^4}{(2s)^4}\right]=\ln\left(2^{-4}\right)=-4\ln(2)} \tag{3.43}$$

$$\Leftrightarrow \quad R_{\text{lin}}^{\text{2D}}(\sigma_{\text{2D}}) = \frac{1}{\pi\sigma_{\text{2D}}} \ln(2). \tag{3.44}$$

Similarly, by inserting the probe positions into Eq. (3.42), for the 3D case follows

$$R_{\text{lin}}^{\text{3D}}(\sigma_{\text{3D}}, s) = -\frac{1}{2\pi\sigma_{\text{3D}}} \underbrace{\left[\frac{1}{\left|\frac{1}{2}s+\frac{3}{2}s\right|} - \frac{1}{\left|\frac{1}{2}s-\frac{3}{2}s\right|} - \frac{1}{\left|-\frac{1}{2}s+\frac{3}{2}s\right|} + \frac{1}{\left|-\frac{1}{2}s-\frac{3}{2}s\right|}\right]}_{=\frac{1}{2s}-\frac{1}{s}-\frac{1}{s}+\frac{1}{2s}=-\frac{1}{s}} \tag{3.45}$$

$$\Leftrightarrow \quad R_{\text{lin}}^{\text{3D}}(\sigma_{\text{3D}}, s) = \frac{1}{2\pi\sigma_{\text{3D}}s}. \tag{3.46}$$

By comparing the results in Eqs. (3.44) and (3.46), it is apparent that the four-point resistance in the 2D case does not at all depend on the spacing of the probes, while the resistance in the 3D case is proportional to the inverse of the spacing s. A plot of both functions, as shown by the blue lines in Fig. 3.5(a) and 3.5(b), makes the hallmark of the 2D case even more obvious, namely that the four-point resistance is constant, while the 3D resistance exhibits a strong distance dependency. So by measuring this distance-dependence, a material with a 2D conductance channel can be unambiguously distinguished from a material exhibiting a 3D conductance channel.

So far, only infinitely extended materials have been considered, but obviously in a measurement situation all samples have a finite size. However, if the four-point measurement

---

[6] The negative sign is added, as $\Phi_{CD}^{AB} = \Phi_D^{AB} - \Phi_C^{AB} < 0$ for a current I flowing from A to B with a tip labelling according to Fig. 3.4(a). Thus, e.g. by reversing the voltage measurement, one obtains $-\Phi_{CD}^{AB} = \Phi_{DC}^{AB} = \Phi_C^{AB} - \Phi_D^{AB} > 0$, so that finally $R_{AB,DC} \geq 0$.

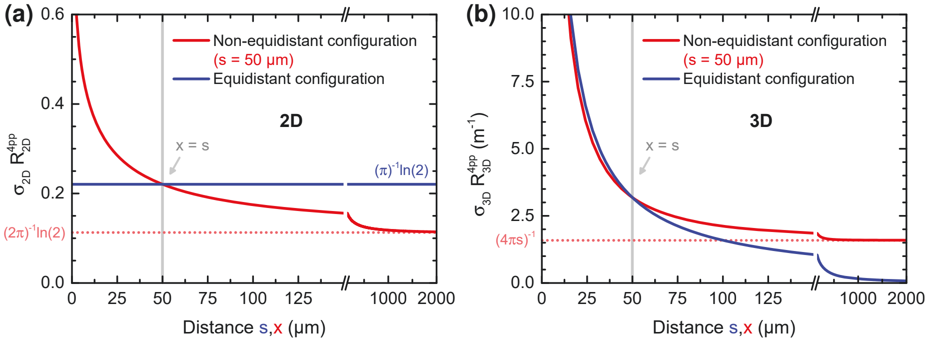

Figure 3.5.: Comparison of the distance dependency of the four-point resistance between the equidistant (blue line) and the non-equidistant (red line) configuration, both for the 2D case (a) and 3D case (b) ($s = 50\,\mu\mathrm{m}$ for the non-equidistant setup). The normalized products $\sigma_{2\mathrm{D}} R_{2\mathrm{D}}^{4\mathrm{pp}}$ (a) and $\sigma_{3\mathrm{D}} R_{3\mathrm{D}}^{4\mathrm{pp}}$ (b) are plotted as function of distance s (equidistant) and x (non-equidistant). (a) For 2D, in the equidistant setup, there is constant value at $\frac{\ln(2)}{\pi}$, while in the non-equidistant setup the resistance approaches $\frac{\ln(2)}{2\pi}$ for $x \to \infty$. (b) For 3D, in the equidistant setup, the resistance is proportional to s^{-1}, while in the non-equidistant case it approaches $\frac{1}{4\pi s}$ for $x \to \infty$.

is not performed in the direct vicinity of the sample boundaries or if the spacing of the probes itself is not on the order of the sample size, the approximation by an infinite geometry is applicable in the most cases. Nevertheless, if necessary, there can be several correction factors applied for the relations $R(\sigma)$ in order to take into account such geometric effects. Most commonly, three factors are used, i.e. F_1 for the sample thickness, F_2 for influence of sample boundaries and F_3 for a sample size comparable to the tip spacings. Such factors can be determined by several mathematical approaches or numerical calculations, for all of which the actual sample and measurement geometry has to be considered [49, 55–60]. Particularly, the thickness of a sample is an important parameter, as it can induce a transition between 2D and 3D conductance behavior. For example, if a thin film is considered with a thickness t, then the measured four-point resistance appears to be two-dimensional if for the ratio between film thickness t and probe spacing s holds $\frac{t}{s} \leq 0.2$, but three-dimensional, if $\frac{t}{s} \geq 4$, while in between a transition exists. This shows that an appropriately chosen probe spacing is very important for revealing the nature of conductance channels, as, e.g. for a too large probe spacing also a substantially thick film can appear as two-dimensional.

Another common linear tip configuration results directly from the equidistant setup by a simple modification, i.e. by varying the distance x between the two outer adjacent probes, while maintaining all the other spacings s. Such a setup is depicted in Fig. 3.4(b), and referred to as *non*-equidistant probe configuration in the following. The big advantage of such a measurement geometry is that, in order to perform a distance-dependent measurement, only the spacing x has to be varied, implying that only one tip has to be moved, while all others remain fixed. So, one can benefit twice, as both a faster measurement is possible and the influence of tip positioning errors on the results is much less. For this reasons, such a probe setup is used preferentially for nearly all four-point resistance measurements presented in the following chapters. In order to get a relation $R(\sigma)$, first the modified tip positions are expressed as $\boldsymbol{x}_A = -\frac{3}{2}s\,\hat{\boldsymbol{e}}_{\boldsymbol{x}}$, $\boldsymbol{x}_B = \left(\frac{1}{2}s + x\right)\hat{\boldsymbol{e}}_{\boldsymbol{x}}$, $\boldsymbol{x}_C = -\frac{1}{2}s\,\hat{\boldsymbol{e}}_{\boldsymbol{x}}$ and $\boldsymbol{x}_D = \frac{1}{2}s\,\hat{\boldsymbol{e}}_{\boldsymbol{x}}$, which are then inserted into Eqs. (3.23) and (3.42). For the 2D case follows that

$$R^{\mathrm{2D}}_{\mathrm{lin,ne}}(\sigma_{\mathrm{2D}}, s, x) = -\frac{1}{4\pi\sigma_{\mathrm{2D}}} \underbrace{\ln\left[\frac{\left(\frac{1}{2}s - \frac{1}{2}s - x\right)^2\left(-\frac{1}{2}s + \frac{3}{2}s\right)^2}{\left(\frac{1}{2}s - \frac{3}{2}s\right)^2\left(-\frac{1}{2}s - \frac{1}{2}s - x\right)^2}\right]}_{=\ln\left[\frac{x^2s^2}{(2s)^2(s+x)^2}\right]=2\ln\left[\frac{x}{2(s+x)}\right]=-2\ln\left[\frac{2(s+x)}{x}\right]} \tag{3.47}$$

$$\Leftrightarrow R^{\mathrm{2D}}_{\mathrm{lin,ne}}(\sigma_{\mathrm{2D}}, s, x) = \frac{1}{2\pi\sigma_{\mathrm{2D}}} \ln\left[\frac{2(s+x)}{x}\right]. \tag{3.48}$$

and correspondingly for the 3D case results

$$R^{\mathrm{3D}}_{\mathrm{lin,ne}}(\sigma_{\mathrm{3D}}, s, x) = -\frac{1}{2\pi\sigma_{\mathrm{3D}}} \underbrace{\left[\frac{1}{\left|\frac{1}{2}s+\frac{3}{2}s\right|} - \frac{1}{\left|\frac{1}{2}s-\frac{1}{2}s-x\right|} - \frac{1}{\left|-\frac{1}{2}s+\frac{3}{2}s\right|} + \frac{1}{\left|-\frac{1}{2}s-\frac{1}{2}s-x\right|}\right]}_{=\frac{1}{2s}-\frac{1}{x}-\frac{1}{s}+\frac{1}{s+x}=-\left[\frac{1}{2s}+\frac{1}{x}-\frac{1}{s+x}\right]} \tag{3.49}$$

$$\Leftrightarrow R^{\mathrm{3D}}_{\mathrm{lin,ne}}(\sigma_{\mathrm{3D}}, s, x) = \frac{1}{2\pi\sigma_{\mathrm{3D}}} \left[\frac{1}{2s} + \frac{1}{x} - \frac{1}{s+x}\right]. \tag{3.50}$$

It is obvious that now both relations depend on the tip distances s and x, so that the constant behavior for 2D systems has been lost. But, as visible from a comparison of the red-coloured plots in Fig. 3.5(a) and 3.5(b), the resistances for the 2D and the 3D case are still distinguishable by their specific distance dependency, which is especially pronounced for small probe spacings $x \leq s$. Moreover, this difference can be additionally emphasized by a scaling due to very different values for the 2D and 3D conductivity.

In the literature, an expression can be found in order to relate the results from the non-equidistant setup directly to the equidistant setup [61,62]. Here, two factors are introduced, i.e. the *2D sensitivity* and the *effective spacing*, which allow to express Eqs. (3.48) and (3.50) by a modified version of Eqs. (3.44) and (3.46) for the equidistant arrangement. These modified equations are for the 2D case and 3D case

$$R^{\mathrm{2D}}_{\mathrm{lin}}(\sigma_{\mathrm{2D}}, s, x) = \frac{1}{\chi_{\mathrm{2D}}}(s, x)\frac{\ln(2)}{\pi\sigma_{\mathrm{2D}}} \quad \text{and} \quad R^{\mathrm{3D}}_{\mathrm{lin}}(\sigma_{\mathrm{3D}}, s, x) = \frac{1}{2\pi\sigma_{\mathrm{3D}}} {s^{\mathrm{eff}}_{3D}}^{-1}(s, x), \tag{3.51}$$

respectively, with the 2D sensitivity χ_{2D}

$$\frac{1}{\chi_{\mathrm{2D}}}(s, x) = \frac{1}{2\ln(2)}\left[\ln\left(\frac{2s}{x}\right) + \ln\left(\frac{s+x}{s}\right)\right] \tag{3.52}$$

and the effective spacing $s^{\mathrm{eff}}_{\mathrm{3D}}$

$$\frac{1}{s^{\mathrm{eff}}_{\mathrm{3D}}}(s, x) = \frac{1}{x} + \frac{1}{2s} - \frac{1}{s+x}\,. \tag{3.53}$$

3.3. Anisotropic conductivity

In this section, the case of anisotropic conductivity is considered for two-dimensional materials, i.e. the conductivity $\underline{\underline{\boldsymbol{\sigma}}}$ is a tensor. The relation $R(\underline{\underline{\boldsymbol{\sigma}}})$ will be derived and the square tip configurations is discussed.

3.3.1. Two-dimensional anisotropy

If the conductivity is not completely homogeneous inside a material, but different for different directions of current transport, it can be termed as anisotropic. Such an anisotropy is a fundamental property of a specific system, e.g. caused by crystal symmetry, and in general can occur in multiple directions. However, in the following only a two-fold anisotropy is considered, i.e. it appears in terms of two separate conductivity values along two distinct directions. For two-dimension, such a type of anisotropy leads to different conductivities along a basis , i.e. two perpendicular axes, of a 2D sheet. This means mathematically that the conductivity σ is no longer a scalar quantity, but now a two-dimensional tensor $\underline{\underline{\boldsymbol{\sigma}}}$. If the basis of this tensor is chosen equally to the principal axes of the 2D system, i.e. the axes along which the different conductivities occur[7], the tensor exhibits a diagonalized form and reads

$$\underline{\underline{\boldsymbol{\sigma}}} = \begin{pmatrix} \sigma_x & 0 \\ 0 & \sigma_y \end{pmatrix} \tag{3.54}$$

with the two conductivity components σ_x and σ_y along the x- and y-direction, respectively. In order to derive an expression for $R(\underline{\underline{\boldsymbol{\sigma}}})$ for such an anisotropic 2D system, one starts again with the relation $\nabla \cdot \boldsymbol{j} = 0$ for the current density $\boldsymbol{j}(x, y)$ in the 2D plane (excluding the injection point at the origin), in the same way as it has been shown before in section 3.2 for isotropic systems. However, in the anisotropic case the current density has to be expressed by the conductivity tensor $\underline{\underline{\boldsymbol{\sigma}}}$, so that it now reads $\boldsymbol{j} = \underline{\underline{\boldsymbol{\sigma}}} \cdot \boldsymbol{E}(x, y) = -\underline{\underline{\boldsymbol{\sigma}}} \cdot \nabla\Phi(x, y)$ with the electric field $\boldsymbol{E}(x, y)$ and the potential $\Phi(x, y)$, respectively. Explicitly, for two dimensions it follows that

$$\boldsymbol{j} = \begin{pmatrix} j_x \\ j_y \end{pmatrix} = \begin{pmatrix} \sigma_x & 0 \\ 0 & \sigma_y \end{pmatrix} \cdot \begin{pmatrix} E_x \\ E_y \end{pmatrix} = \begin{pmatrix} \sigma_x E_x \\ \sigma_y E_y \end{pmatrix} = \begin{pmatrix} -\sigma_x \partial_x \Phi(x, y) \\ -\sigma_y \partial_y \Phi(x, y) \end{pmatrix} \tag{3.55}$$

with the short form of the partial derivations defined as $\partial_x := \frac{\partial}{\partial x}$ and $\partial_y := \frac{\partial}{\partial y}$, respectively. So, from the condition of a vanishing divergence of the current density, one obtains

$$\nabla \cdot \boldsymbol{j} = \begin{pmatrix} \partial_x \\ \partial_y \end{pmatrix} \cdot \begin{pmatrix} -\sigma_x \partial_x \Phi(x, y) \\ -\sigma_y \partial_y \Phi(x, y) \end{pmatrix} = 0 \tag{3.56}$$

$$\Leftrightarrow \qquad \sigma_x \partial^2_{xx} \Phi(x, y) + \sigma_y \partial^2_{yy} \Phi(x, y) = 0 \tag{3.57}$$

with the second partial derivations abbreviated by $\partial^2_{xx} := \frac{\partial^2}{\partial x^2}$ and $\partial^2_{yy} := \frac{\partial^2}{\partial y^2}$, respectively. Eq. (3.57) corresponds to an anisotropic homogeneous Laplace equation and has to be solved in order to obtain the potential distribution $\Phi(x, y)$ in the anisotropic 2D system.

---

[7] This basis is also considered as the basis of the Cartesian coordinate system for the 2D sheet in the following.

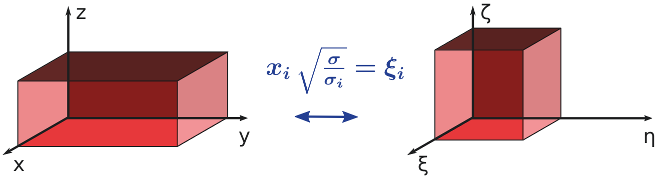

Figure 3.6.: Visualization of the linear coordinate transformation used in Eqs. (3.58) and (3.59) for the general case of three dimensions. It transforms between an anisotropic cuboid with different σ_i along each axis x_i (left part) and an isotropic cube with $\sigma = \sqrt[3]{\sigma_x\sigma_y\sigma_z}$ along all three axes ξ_i (right part).

First, a coordinate transformation $(x, y) \to (\xi, \eta)$ is performed as [63–65]

$$x = \xi\left(\frac{\sigma_x}{\sqrt{\sigma_x\sigma_y}}\right)^{\frac{1}{2}} \quad\Leftrightarrow\quad \xi = x\left(\frac{\sqrt{\sigma_x\sigma_y}}{\sigma_x}\right)^{\frac{1}{2}} \quad\Leftrightarrow\quad \frac{\partial\xi}{\partial x} = \left(\frac{\sqrt{\sigma_x\sigma_y}}{\sigma_x}\right)^{\frac{1}{2}} \tag{3.58}$$

$$y = \eta\left(\frac{\sigma_y}{\sqrt{\sigma_x\sigma_y}}\right)^{\frac{1}{2}} \quad\Leftrightarrow\quad \eta = y\left(\frac{\sqrt{\sigma_x\sigma_y}}{\sigma_y}\right)^{\frac{1}{2}} \quad\Leftrightarrow\quad \frac{\partial\eta}{\partial y} = \left(\frac{\sqrt{\sigma_x\sigma_y}}{\sigma_y}\right)^{\frac{1}{2}} \tag{3.59}$$

which is visualized in Fig. 3.6 for the general case of three dimensions. The linear transformation simply scales the axes of the system, so that an (anisotropic) cuboid with σ_i along its individual axes x_i is transformed into an (isotropic) cube with $\sigma = \sqrt[i]{\prod_i \sigma_i}$ along all axes ξ_i. If this transformation is applied to Eq. (3.57), i.e. $\Phi(x, y)$ is substituted by $\Phi(\xi, \eta)$, it follows that

$$\sigma_x\partial^2_{xx}\Phi\big(\xi(x),\eta(y)\big) + \sigma_y\partial^2_{yy}\Phi\big(\xi(x),\eta(y)\big) = 0 \tag{3.60}$$

$$\Leftrightarrow\quad \sigma_x\partial_x\left[\frac{\partial\xi(x)}{\partial x}\partial_\xi\Phi\big(\xi(x),\eta(y)\big)\right] + \sigma_y\partial_y\left[\frac{\partial\eta(y)}{\partial y}\partial_\eta\Phi\big(\xi(x),\eta(y)\big)\right] = 0 \tag{3.61}$$

$$\overset{\substack{\partial^2_{xx}\xi=0\\ \partial^2_{yy}\eta=0}}{\Leftrightarrow}\quad \sigma_x\frac{\partial\xi(x)}{\partial x}\underbrace{\partial_x\Big[\partial_\xi\Phi\big(\xi(x),\eta(y)\big)\Big]}_{=\frac{\partial\xi(x)}{\partial x}\partial^2_{\xi\xi}\Phi\left(\xi(x),\eta(y)\right)} + \sigma_y\frac{\partial\eta(y)}{\partial y}\underbrace{\partial_y\Big[\partial_\eta\Phi\big(\xi(x),\eta(y)\big)\Big]}_{=\frac{\partial\eta(y)}{\partial y}\partial^2_{\eta\eta}\Phi\left(\xi(x),\eta(y)\right)} = 0 \tag{3.62}$$

$$\Leftrightarrow\quad \sigma_x\underbrace{\left[\frac{\partial\xi(x)}{\partial x}\right]^2}_{\overset{(3.58)}{=}\frac{\sqrt{\sigma_x\sigma_y}}{\sigma_x}}\partial^2_{\xi\xi}\Phi\big(\xi(x),\eta(y)\big) + \sigma_y\underbrace{\left[\frac{\partial\eta(y)}{\partial y}\right]^2}_{\overset{(3.59)}{=}\frac{\sqrt{\sigma_x\sigma_y}}{\sigma_y}}\partial^2_{\eta\eta}\Phi\big(\xi(x),\eta(y)\big) = 0 \tag{3.63}$$

$$\Leftrightarrow\quad \underbrace{\sqrt{\sigma_x\sigma_y}}_{=\sigma}\partial^2_{\xi\xi}\Phi(\xi,\eta) + \underbrace{\sqrt{\sigma_x\sigma_y}}_{=\sigma}\partial^2_{\eta\eta}\Phi(\xi,\eta) = 0 \tag{3.64}$$

$$\overset{\sigma\neq 0}{\Leftrightarrow}\quad \partial^2_{\xi\xi}\Phi(\xi,\eta) + \partial^2_{\eta\eta}\Phi(\xi,\eta) = 0 \tag{3.65}$$

$$\Leftrightarrow\quad \Delta\Phi(\xi,\eta) = 0 \tag{3.66}$$

with the partial derivations $\partial_\xi := \frac{\partial}{\partial \xi}$, $\partial_\eta := \frac{\partial}{\partial \eta}$, $\partial^2_{\xi\xi} := \frac{\partial^2}{\partial \xi^2}$, $\partial^2_{\eta\eta} := \frac{\partial^2}{\partial \eta^2}$, respectively, and the Laplace operator $\Delta = \partial^2_{\xi\xi} + \partial^2_{\eta\eta}$. From Eq. (3.66) it is obvious that the mapping procedure has resulted in an isotropic Laplace equation for the potential $\Phi(\xi, \eta)$. Such an equation has already been found before for the isotropic case [Eq. (3.6)] with the corresponding solution derived in Eq. (3.16). Based on this result, and by using $\sigma = \sqrt{\sigma_x \sigma_y}$ the solution for Eq. (3.66) case can be expressed by

$$\Phi(\xi, \eta) = -\frac{I}{4\pi\sqrt{\sigma_x\sigma_y}} \ln\left(\xi^2 + \eta^2\right) \qquad (\xi, \eta) \neq (0, 0). \tag{3.67}$$

In order to return to the anisotropic coordinate system, the Eqs. (3.58) and (3.59) have to be inserted into Eq. (3.67), resulting in

$$\tilde{\Phi}(x, y) = -\frac{I}{4\pi\sqrt{\sigma_x\sigma_y}} \ln \underbrace{\left[x^2 \frac{\sqrt{\sigma_x\sigma_y}}{\sigma_x} + y^2 \frac{\sqrt{\sigma_x\sigma_y}}{\sigma_y}\right]}_{= \frac{x^2\sigma_y\sqrt{\sigma_x\sigma_y} + y^2\sigma_x\sqrt{\sigma_x\sigma_y}}{\sigma_x\sigma_y}} \tag{3.68}$$

$$\Leftrightarrow \quad \tilde{\Phi}(x, y) = -\frac{I}{4\pi\sqrt{\sigma_x\sigma_y}} \ln\left[\frac{\sigma_y x^2 + \sigma_x y^2}{\sqrt{\sigma_x\sigma_y}}\right] \tag{3.69}$$

$$\Leftrightarrow \quad \tilde{\Phi}(x, y) = -\frac{I}{4\pi\sqrt{\sigma_x\sigma_y}} \ln\left[\sigma_y x^2 + \sigma_x y^2\right] + \underbrace{\frac{I \ln\left[\sqrt{\sigma_x\sigma_y}\right]}{4\pi\sqrt{\sigma_x\sigma_y}}}_{=:\tilde{c}_2 = const} \tag{3.70}$$

The constant additive term $\tilde{c}_2$ in Eq. (3.70) can be removed by choosing a different gauging[8] as $\tilde{\Phi} \rightarrow \Phi = \tilde{\Phi} - \tilde{c}_2$. So, more generally it follows for the potential $\Phi^A(x, y)$ for a current source at position $\boldsymbol{x}_A = \left(\begin{smallmatrix} x_A \\ y_A \end{smallmatrix}\right)$ that

$$\Phi^A(x, y) = -\frac{I}{4\pi\sqrt{\sigma_x\sigma_y}} \ln\left[\sigma_y(x - x_A)^2 + \sigma_x(y - y_A)^2\right]. \tag{3.71}$$

With the same considerations as in section 3.2.1, i.e. by adding a current sink at $\boldsymbol{x}_B = \left(\begin{smallmatrix} x_B \\ y_B \end{smallmatrix}\right)$ and evaluating the potential drop between $\boldsymbol{x}_C = \left(\begin{smallmatrix} x_C \\ y_C \end{smallmatrix}\right)$ and $\boldsymbol{x}_D = \left(\begin{smallmatrix} x_D \\ y_D \end{smallmatrix}\right)$, the potential measured on a 2D anisotropic sheet by a four point-probe setup can finally be expressed by

$$\Phi^{AB}_{CD} = \underbrace{\left[\Phi^A(x_D, y_D) + \Phi^B(x_D, y_D)\right]}_{=\Phi^{AB}(x_D, y_D)} - \underbrace{\left[\Phi^A(x_C, y_C) + \Phi^B(x_C, y_C)\right]}_{=\Phi^{AB}(x_C, y_C)} \tag{3.72}$$

$$\Leftrightarrow \quad \Phi^{AB}_{CD} = \frac{I}{4\pi\sqrt{\sigma_x\sigma_y}} \ln\left[\frac{\left[\sigma_y(x_D - x_B)^2 + \sigma_x(y_D - y_B)^2\right]\left[\sigma_y(x_C - x_A)^2 + \sigma_x(y_C - y_A)^2\right]}{\left[\sigma_y(x_D - x_A)^2 + \sigma_x(y_D - y_A)^2\right]\left[\sigma_y(x_C - x_B)^2 + \sigma_x(y_C - y_B)^2\right]}\right]. \tag{3.73}$$

---

[8] Such a gauging process is equal to the selection of a specific value for the integration constants c_2, as performed before for Eqs. (3.12) and (3.31).

3.3.2. Square tip configuration

From the potential distribution in Eq. (3.73) for anisotropic systems, an expression for a specific probe arrangement can be obtained, similar as it has been shown before. For example, a very simple measurement setup would be to use again a non-equidistant linear tip configuration. If the corresponding tip positions for such a setup assumed to be aligned along the x-axis, as expressed before in section 3.2.3, are inserted into Eq. (3.73), one obtains for the four-point resistance

$$R^{\text{2D,anisotropic}}_{\text{lin,ne}} = -\frac{1}{4\pi\sqrt{\sigma_x\sigma_y}} \underbrace{\ln\left[\frac{\sigma_y\left(\frac{1}{2}s-\frac{1}{2}s-x\right)^2\sigma_y\left(-\frac{1}{2}s+\frac{3}{2}s\right)^2}{\sigma_y\left(\frac{1}{2}s-\frac{3}{2}s\right)^2\sigma_y\left(-\frac{1}{2}s-\frac{1}{2}s-x\right)^2}\right]}_{=\ln\left[\frac{x^2s^2}{(2s)^2(s+x)^2}\right]=2\ln\left[\frac{x}{2(s+x)}\right]=-2\ln\left[\frac{2(s+x)}{x}\right]} \tag{3.74}$$

$$\Leftrightarrow\quad R^{\text{2D,anisotropic}}_{\text{lin,ne}} = \frac{1}{2\pi\sqrt{\sigma_x\sigma_y}}\ln\left[\frac{2(s+x)}{x}\right]. \tag{3.75}$$

If compared to Eq. (3.48) for an isotropic systems, it is obvious that only a difference occurs for the prefactor, namely that the expression $\sqrt{\sigma_x\sigma_y}$ replaces the σ_{2D} present before. So, in the actual distance-dependency the anisotropy components are not included which directly implies that they cannot be extracted from a corresponding measurement. For this reason, it turns out that a linear tip arrangement is insensitive for anisotropic conductance, as only the geometric mean $\sqrt{\sigma_y\sigma_y} = \sigma_{\text{2D}}$ of both conductivity components can be measured. This also applies, if the in-line tip arrangement is not aligned along one of the principal axes of the system, as assumed before by selecting the x-axis, but rotated arbitrarily by an angle θ on the surface, as it is more generally derived in the appendix A.1.1.

In order to indeed reveal the two conductivity components σ_x and σ_y, a different tip configuration has to be chosen. A suitable arrangement is a square configuration, in which both the current injecting probes and voltage measuring probes are located next to each other at the corners of a square with side length s, as it is visualized in Fig. 3.7. In this

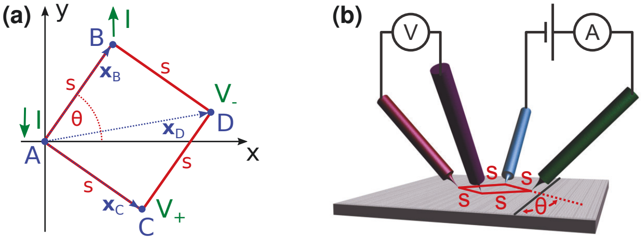

Figure 3.7.: Square tip configuration with the probes positioned at the corners of a square with side length s. (a) Layout of a (AB, DC) tip configuration. The current injecting tip are at positions A and B, while the voltage measuring tips are located at C and D, with the position vectors as indicated. The square can be rotated by the angle θ with respect to the principal axes of the anisotropic system. (b) Visualization of the tip setup for the rotational square method.

case, no longer a distance-dependent measurement is performed, but an angle-dependent, as the square is rotated successively by the angle θ with respect to the principal axes of the system. So, the angle dependence of the four-point resistance is recorded. According to the drawing in Fig. 3.7(a), the positions of the four tips can be expressed as

$$\boldsymbol{x}_A = \begin{pmatrix} 0 \\ 0 \end{pmatrix},\ \boldsymbol{x}_B = s\begin{pmatrix} \cos(\theta) \\ \sin(\theta) \end{pmatrix},\ \boldsymbol{x}_C = s\begin{pmatrix} \sin(\theta) \\ -\cos(\theta) \end{pmatrix},\ \boldsymbol{x}_D = \underbrace{s\begin{pmatrix} \sin(\theta)+\cos(\theta) \\ \sin(\theta)-\cos(\theta) \end{pmatrix}}_{=\boldsymbol{x}_B+\boldsymbol{x}_C}. \tag{3.76}$$

After inserting these position vectors into Eq. (3.73) and calculating the four-point resistance according to $R_{AB,DC} = \frac{-\Phi_{CD}^{AB}}{I}$, it follows with the prefactor $A := \frac{1}{4\pi\sqrt{\sigma_x\sigma_y}}$ that

$$\begin{aligned}
R_{\text{sq}}^{\text{2D}} &= -A\ln\Bigg[\frac{\sigma_y\left(s[\sin(\theta)+\cos(\theta)]-s\cos(\theta)\right)^2+\sigma_x\left(s[\sin(\theta)-\cos(\theta)]-s\sin(\theta)\right)^2}{\sigma_y\left(s[\sin(\theta)+\cos(\theta)]\right)^2+\sigma_x\left(s[\sin(\theta)-\cos(\theta)]\right)^2} \\
&\qquad\times\frac{\sigma_y\left(s\sin(\theta)\right)^2+\sigma_x\left(-s\cos(\theta)\right)^2}{\sigma_y\left(s\sin(\theta)-s\cos(\theta)\right)^2+\sigma_x\left(-s\cos(\theta)-s\sin(\theta)\right)^2}\Bigg] \qquad (3.77) \\
&= -A\ln\Bigg[\frac{\sigma_y\sin^2(\theta)+\sigma_x\cos^2(\theta)}{\sigma_y\left(\sin(\theta)+\cos(\theta)\right)^2+\sigma_x\left(\sin(\theta)-\cos(\theta)\right)^2} \\
&\qquad\times\frac{\sigma_y\sin^2(\theta)+\sigma_x\cos^2(\theta)}{\sigma_y\left(\sin(\theta)-\cos(\theta)\right)^2+\sigma_x\left(\cos(\theta)+\sin(\theta)\right)^2}\Bigg] \qquad (3.78) \\
&\overset{\sin^2(\theta)+\cos^2(\theta)=1}{=} -A\ln\left[\underbrace{\frac{\left(\sigma_y\sin^2(\theta)+\sigma_x\cos^2(\theta)\right)^2}{\left[\sigma_y\left(1+2\sin(\theta)\cos(\theta)\right)+\sigma_x\left(1-2\sin(\theta)\cos(\theta)\right)\right]\times\left[\sigma_y\left(1-2\sin(\theta)\cos(\theta)\right)+\sigma_x\left(1+2\sin(\theta)\cos(\theta)\right)\right]}}_{=\frac{\left(\sigma_y\sin^2(\theta)+\sigma_x\cos^2(\theta)\right)^2}{\sigma_y^2\left(1-4\sin^2(\theta)\cos^2(\theta)\right)+2\sigma_x\sigma_y\left(1+4\sin^2(\theta)\cos^2(\theta)\right)+\sigma_x^2\left(1-4\sin^2(\theta)\cos^2(\theta)\right)}}\right] \qquad (3.79) \\
&= -A\ln\left[\frac{\left(\sigma_y\sin^2(\theta)+\sigma_x\cos^2(\theta)\right)^2}{\left(\sigma_x^2+\sigma_y^2\right)\left(1-4\cos^2(\theta)\sin^2(\theta)\right)+2\sigma_x\sigma_y\left(1+4\cos^2(\theta)\sin^2(\theta)\right)}\right] \qquad (3.80) \\
&= -A\ln\left[\frac{\left(\sigma_y\sin^2(\theta)+\sigma_x\cos^2(\theta)\right)^2}{\underbrace{\sigma_x^2+\sigma_y^2+2\sigma_x\sigma_y}_{=(\sigma_x+\sigma_y)^2}-4\cos^2(\theta)\sin^2(\theta)\underbrace{\left(\sigma_x^2+\sigma_y^2-2\sigma_x\sigma_y\right)}_{=(\sigma_x-\sigma_y)^2}}\right] \qquad (3.81) \\
&= -A\ln\left[\frac{\sigma_y^2\left(\sin^2(\theta)+\frac{\sigma_x}{\sigma_y}\cos^2(\theta)\right)^2}{\sigma_y^2\left(\frac{\sigma_x}{\sigma_y}+1\right)^2-4\cos^2(\theta)\sin^2(\theta)\sigma_y^2\left(\frac{\sigma_x}{\sigma_y}-1\right)^2}\right]. \qquad (3.82)
\end{aligned}$$

Thus, after further rearrangement by using the relation $\ln(a^{-1}) = -\ln(a)$, the four-point

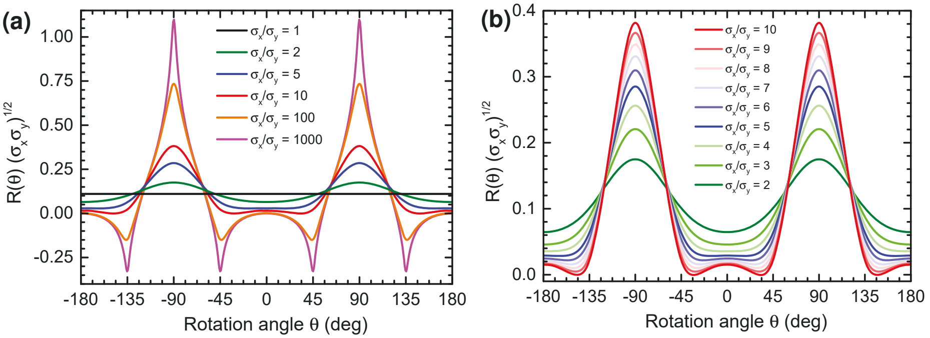

Figure 3.8.: Normalized plots of the relations $R(\theta)\sqrt{\sigma_x\sigma_y}$ for a square tip configuration as function of the rotation angle θ with the anisotropy ratio σ_x/σ_y as additional parameter. (a) Overview of the π-periodic function for a large range of anisotropy ratios σ_x/σ_y. Also negative values can appear which means physically that the voltage drops in the reverse direction. (b) For smaller anisotropy ratios $\sigma_x/\sigma_y \leq 10$, the curve is positive. For $\sigma_x/\sigma_y \geq 5$ it exhibits two local maxima directly indicating the two principal axes of the system, i.e. the directions of high (σ_x) and low (σ_y) conductivity.

resistance can finally be written as [20]

$$R^{2\text{D}}_{\text{square}}(\sigma_x,\sigma_y,\theta) = \frac{1}{4\pi\sqrt{\sigma_x\sigma_y}} \ln\left[\frac{\left(\frac{\sigma_x}{\sigma_y}+1\right)^2 - 4\cos^2(\theta)\sin^2(\theta)\left(\frac{\sigma_x}{\sigma_y}-1\right)^2}{\left(\sin^2(\theta)+\frac{\sigma_x}{\sigma_y}\cos^2(\theta)\right)^2}\right]. \tag{3.83}$$

From Eq. (3.83), it can be seen that for the square configuration, the four-point resistance is strongly dependent on the rotation angle θ, while indeed no distance-dependency appears, i.e. the resistance is independent of the actual size s of the square. Now, the anisotropy is included both in the prefactor as well as in the angle-dependent part, so that a determination of both components σ_x and σ_y is possible, as the specific shape of the angle-dependent function reveals the anisotropy ratio σ_x/σ_y and from the absolute resistance values the geometric mean $\sqrt{\sigma_x\sigma_y}$ is obtained. In Fig. 3.8, the angle dependence of Eq. (3.83) is plotted for different anisotropy ratios. In order to remove the additional scaling resulting from the prefactor, the normalized expression $R(\theta)\sqrt{\sigma_x\sigma_y}$ is chosen. In Fig. 3.8(a), the function is depicted for anisotropy ratios in the range $1 \leq \frac{\sigma_x}{\sigma_y} \leq 1000$. It is visible that the shape of the π-periodic resistance function is strongly dependent on the anisotropy ratio and that for several values even a negative resistance can be obtained, which physically only means that the voltage drop occurs in the reverse direction. Fig. 3.8(b) depicts the behavior in a smaller range of $1 \leq \frac{\sigma_x}{\sigma_y} \leq 10$ which is more relevant for measurements on actual sample systems. Here, for very small anisotropies (< 5) the shape of the function appears similar to sine, but with half periodicity, while for larger ratios (≥ 5) two local maxima occur which directly indicate the two principal axes of the systems, i.e. the direction of high (σ_x) and low (σ_y) conductivity. For a vanishing anisotropy, i.e. $\frac{\sigma_x}{\sigma_y} = 1$, the function approaches $\frac{\ln(2)}{2\pi\sigma}$, as visible from Eq. (3.83), and correspondingly also the angle dependence vanishes.

In practice, for performing a four-point measurement using such a rotational square setup, it is sufficient to rotate the square with the tips only by in total $90°$. For each angular position, the assignment of the probes, i.e. current or voltage mode, can then be rotated further by $90°$. So, the tips remain at a fixed position, and only the cabling has to be interchanged, which allows to simultaneously record two separate resistance values, i.e. $R(\theta)$ and $R(\theta + \pi/2)$, for a fixed rotation angle θ of the setup. So, in total the complete range of the π-periodic resistance function is measured. This procedure reduces the sources of errors due to a misalignment of the tips and allows a faster measurement. In principle, even a further rotation in multiples of 90° is possible for recording the complete angular space of 2π, but for $\theta > 180°$, basically only the current and voltage tips are interchanged. For such an exchange, the measured four-point resistance stays the same, which is at the same time also the reason for only the π-periodicity of Eq. (3.83). The explanation for this rather fundamental behavior will be discussed briefly in the next section.

3.4. Permutability of tip positions

For a four-tip measurement setup with four probes fixed at the positions $(\boldsymbol{x}_A, \boldsymbol{x}_B, \boldsymbol{x}_C, \boldsymbol{x}_D)$ it results that in total $4! = 24$ different tip permutations (ij, kl) with (i, j, k, l) being a permutation of (A, B, C, D) are possible, either realized by tip interchangement or by different electrical assignment of the tips. Thus, at first glance one might think that there exist a large number of different values for the four-point resistance measured by these individual tip arrangements. However, if first either both current injecting tips or both voltage measuring tips are interchanged with each other, this only leads to a reversed current direction or a voltage drop occurring in the reverse direction, respectively, so that only the sign of the measured four-point resistance changes as $R_{ij,kl} = -R_{ji,kl} = -R_{ij,lk} = R_{ji,lk}$. Thus, the absolute value of the resistance remains unchanged. As a result, there are only $\frac{24}{4} = 6$ remaining combinations which still can be different for the obtained resistance. Secondly, if now the pairs of current tips and voltage tips are exchanged with each other, the measured four-point resistance stays again the same, as this is a fundamental property predicted by the reciprocity theorem for electrical networks. This theorem states that for a linear time-invariant resistive network with no independent sources inside, the ratio between the voltage measured at one pair of terminals and the excitation current applied to another pair of terminals is invariant to an interchange of both pairs of terminals [66–68].[9] Specifically for a four-point setup this implies that the actual tip arrangement does not play a role, as the theorem is independent of the geometry. So, as $R_{ij,kl} = R_{kl,ij}$, the number of possibly different tip configuration has reduced to $\frac{6}{2} = 3$ [69]. Indeed, these three remaining combinations result in different four-point resistances, as they are based on locally distinct current paths due to different tips used for the injection, e.g. the tip pairs (A, B), (A, C) and (A, D) [70, 71]. Further on, it turns out that only two linear independent tip arrangements exist, i.e. the four-point resistance of the third one can be expressed by a

---

[9] It should be noted that for systems with a broken time-invariance, e.g. due to a magnetic field, this might not apply.

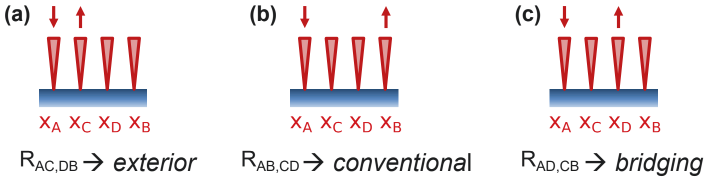

Figure 3.9.: The three different arrangements of the current (indicated by arrows) and voltage tips for a linear equidistant tip setup with the correspondingly labelled four-point resistance as indicated. (a) In the *exterior* configuration, the two injecting tips are located both on one side (A,C) next to the voltage measuring tips (D,B). (b) In the *conventional* setup, the current tips (A,B) surround the voltage tips located in the center position (C,D). (c) In the *bridging* configuration, the current tips (A,D) and voltage tips (C,B) are alternatingly arranged.

combination of the resistances from the other two configurations [71]. A specific relation depends on the actual tip positions and cannot be expressed in general. However, if as an example a linear tip configuration is considered, the three different tip arrangements are referred to as *exterior* ($R_{AC,DB}$), *conventional* ($R_{AB,CD}$) and *bridging* ($R_{AD,CB}$) configuration, as depicted in Fig. 3.9.[10] In this case, it can be written that [72–74]

$$\underbrace{|R_{AC,DB}|}_{exterior} = \underbrace{|R_{AB,CD}|}_{conventional} - \underbrace{|R_{AD,CB}|}_{bridging} . \tag{3.84}$$

As a quantitative example, the four-point resistance for a 3D geometry obtained by an equidistant linear tip setup is calculated for these three different tip arrangements. By exchanging the tip coordinates in Eq. (3.42) correspondingly, it immediately follows that

$$\left|R^{3\mathrm{D}}_{AC,DB}\right| = \frac{1}{2\pi\sigma_{3\mathrm{D}}}\left|\frac{1}{3s} - \frac{1}{2s} - \frac{1}{2s} + \frac{1}{s}\right| = \frac{1}{6\pi\sigma_{3\mathrm{D}}s}, \tag{3.85}$$

$$\left|R^{3\mathrm{D}}_{AB,CD}\right| = \frac{1}{2\pi\sigma_{3\mathrm{D}}}\left|\frac{1}{2s} - \frac{1}{s} - \frac{1}{s} + \frac{1}{2s}\right| = \frac{1}{2\pi\sigma_{3\mathrm{D}}s}, \tag{3.86}$$

$$\left|R^{3\mathrm{D}}_{AD,CB}\right| = \frac{1}{2\pi\sigma_{3\mathrm{D}}}\left|\frac{1}{3s} - \frac{1}{s} - \frac{1}{s} + \frac{1}{s}\right| = \frac{1}{3\pi\sigma_{3\mathrm{D}}s}. \tag{3.87}$$

It is obvious that the relation from Eq. (3.84) is fulfilled and that $|R_{AC,DB}| \ll |R_{AB,CD}| \sim |R_{AD,CB}|$ which also holds in general. For this reason, in four-point measurements more often the conventional and bridging configurations are used, as the absolute value of the measured resistance is simply larger implying that a better resolution can be obtained.

If a square tip arrangement is considered, the configurations *conventional* and *exterior* are not well defined. Nevertheless, in principle the relation from Eq. (3.84) is still valid, but without taking the absolute values, as due to the periodicity the sign of the four-point resistances depend on the rotation angle. The configurations $R_{AB,CD}$ and $R_{AC,DB}$ (with

---

[10] The same tip labelling is used as before in Fig. 3.4, i.e. the tips C and D are physically located in between the tips A and B.

the tips marked according to Fig. 3.7) directly follow from Eq. (3.83) for θ and $\theta + \frac{\pi}{2}$ as argument, respectively. The *bridging* setup $R_{AD,CB}$ is referred to as *rhombic* configuration [63], as the current and voltage tips are positioned along the diagonal at the opposite corners of the square. A derivation is given in the appendix A.1.2. Due to the rotated current direction compared to the square tip arrangement, a different rotation angle α is introduced with $\theta = \alpha + \frac{\pi}{4}$. From Eq. (3.84) in combination with Eq. (3.83), it follows that

$$R_{AD,CB} = R_{AB,CD} - R_{AC,DB} = R^{\text{2D}}_{\text{square}}\left(\theta\right) - R^{\text{2D}}_{\text{square}}\left(\theta + \frac{\pi}{2}\right) \tag{3.88}$$

$$= \frac{1}{4\pi\sqrt{\sigma_x\sigma_y}} \ln\left[\frac{\left(\frac{\sigma_x}{\sigma_y}+1\right)^2 - 4\cos^2(\theta)\sin^2(\theta)\left(\frac{\sigma_x}{\sigma_y}-1\right)^2}{\left[\sin^2(\theta) + \frac{\sigma_x}{\sigma_y}\cos^2(\theta)\right]^2} \right.$$
$$\left. \times \frac{\left[\sin^2\left(\theta+\frac{\pi}{2}\right) + \frac{\sigma_x}{\sigma_y}\cos^2\left(\theta+\frac{\pi}{2}\right)\right]^2}{\left(\frac{\sigma_x}{\sigma_y}+1\right)^2 - 4\underbrace{\cos^2\left(\theta+\frac{\pi}{2}\right)}_{=\sin^2(\theta)}\underbrace{\sin^2\left(\theta+\frac{\pi}{2}\right)}_{=\cos^2(\theta)}\left(\frac{\sigma_x}{\sigma_y}-1\right)^2}\right] \tag{3.89}$$

$$\overset{\ln\left[a^2\right]=2\ln[a]}{=} \frac{1}{2\pi\sqrt{\sigma_x\sigma_y}} \ln\left[\frac{\cos^2(\theta) + \frac{\sigma_x}{\sigma_y}\sin^2(\theta)}{\sin^2(\theta) + \frac{\sigma_x}{\sigma_y}\cos^2(\theta)}\right] \tag{3.90}$$

$$\overset{\theta=\alpha+\frac{\pi}{4}}{=} \frac{1}{2\pi\sqrt{\sigma_x\sigma_y}} \ln\left[\frac{\cos^2\left(\alpha+\frac{\pi}{4}\right) + \frac{\sigma_x}{\sigma_y}\sin^2\left(\alpha+\frac{\pi}{4}\right)}{\underbrace{\sin^2\left(\alpha+\frac{\pi}{4}\right)}_{\substack{\overset{(A.10)}{=}\left[\frac{1}{\sqrt{2}}[\sin(\alpha)+\cos(\alpha)]\right]^2 \\ = \frac{1}{2}[1+2\sin(\alpha)\cos(\alpha)]}} + \frac{\sigma_x}{\sigma_y}\underbrace{\cos^2\left(\alpha+\frac{\pi}{4}\right)}_{\substack{\overset{(A.11)}{=}\left[\frac{1}{\sqrt{2}}[\cos(\alpha)-\sin(\alpha)]\right]^2 \\ = \frac{1}{2}[1-2\sin(\alpha)\cos(\alpha)]}}}\right] \tag{3.91}$$

$$= \frac{1}{2\pi\sqrt{\sigma_x\sigma_y}} \left[\frac{1-2\sin(\alpha)\cos(\alpha) + \frac{\sigma_x}{\sigma_y}[1+2\sin(\alpha)\cos(\alpha)]}{1+2\sin(\alpha)\cos(\alpha) + \frac{\sigma_x}{\sigma_y}[1-2\sin(\alpha)\cos(\alpha)]}\right] \tag{3.92}$$

$$= \frac{1}{2\pi\sqrt{\sigma_x\sigma_y}} \left[\frac{1+\frac{\sigma_x}{\sigma_y}+2\sin(\alpha)\cos(\alpha)\left(\frac{\sigma_x}{\sigma_y}-1\right)}{1+\frac{\sigma_x}{\sigma_y}-2\sin(\alpha)\cos(\alpha)\left(\frac{\sigma_x}{\sigma_y}-1\right)}\right] = R^{\text{2D}}_{\text{rhombic}}(\alpha). \tag{3.93}$$

Obviously, the result corresponds to Eq. (A.20). Thus, the angle-dependent four-point resistance of the rhombic configuration can be calculated from a rotational square measurement, if it has not been measured directly. An advantage of the rhombic arrangement is that the four-point resistance vanishes completely along the two principal axes of the system. So, from the zero-crossings it is quite easy to determine the orientations for the conductivity components σ_x and σ_y inside the sample. More details can be found in the appendix A.1.2.

It is also possible to take explicitly advantage of the fact that two linear independent tip configurations exist, since measuring the four-point resistance separately with both arrangements provides more information about the sample than only using one setup. For example, this can be utilized in 2D systems by the *van der Pauw* geometry, which is frequently used in literature for lithographically-based four-point measurements. Here, the four tips have to be placed at the boundary of a singly-connected domain, e.g. at the edges of a limited 2D sheet with isotropic conductivity. Subsequently, the four-point resistances arising from current paths through neighbouring tips have to be measured,[11] e.g. as it is realized by the tip configurations (AB, CD) and (AC, DB) with a labelling of the tips according to Fig. 3.9. It has been shown for 2D systems that both resistance values $R_{AB,CD}$ and $R_{AC,DB}$ fulfill the relation [75, 76]

$$e^{-\pi\sigma_{2\mathrm{D}}\left|R_{AB,CD}\right|}+e^{-\pi\sigma_{2\mathrm{D}}\left|R_{AC,DB}\right|}=1, \tag{3.94}$$

so that the sheet conductivity $\sigma_{2\mathrm{D}}$ can be calculated from such a measurement. Hereby, the individual positions of the tips are not of importance, as long as they are all positioned on the boundary. So, in contrast to a measurement of both the resistance and the tip positions, as it is essential while using only one specific tip configuration, now two separate resistances are measured, so that further knowledge about the tip positions is not necessary which reduces positioning errors. However, for multi-tip STM such a measurement geometry with contacts at the boundary of the sample is not really useful, as it is particularly the purpose of the STM to bring the tips together at small distances, and not to position them widely spaced at the edges of a sample. Thus, the original *van der Pauw* geometry is basically not used for multi-tip STM. Nevertheless, there exists an extension of the theorem which allows also measurements in the interior of a 2D sheet [77]. If a sample exhibits a mirror plane, then it is sufficient to place all four tips in a linear setup along the intersecting line with this mirror plane, in order to satisfy the modified relation

$$e^{-2\pi\sigma_{2\mathrm{D}}\left|R_{AB,CD}\right|}+e^{-2\pi\sigma_{2\mathrm{D}}\left|R_{AC,DB}\right|}=1 \tag{3.95}$$

in which an additional factor 2 has been introduced. The reason is that, if the tips are placed at the mirror plane, the current density perpendicular to the mirror plane vanishes completely due to symmetry. Thus, the mirror plane can be theoretically replaced by an insulating boundary implying that only half of the sample is considered, so that the *van der Pauw* condition with contacts at the boundary is again fulfilled. As a result of the reduced current paths the resistance increases correspondingly by a factor of 2. The individual spacing of the tips is again irrelevant, as long as they are located at the mirror plane. If very large samples are considered which can be approximated inside to be infinitely extended, then basically every plane is a mirror plane. Thus, the linear tip arrangement can be placed arbitrarily, as long as the in-line geometry is maintained. It can be easily shown that in this case Eq. (3.95) is still fulfilled, as it is done in the appendix A.1.3. Nevertheless, major drawbacks are that this method is only applicable to pure 2D systems, and that due to the missing position-dependency it is not even possible to conclude, if the sample under study is 2D or not. Thus, this method can be useful for determining the conductivity of obviously 2D materials, but not to investigate unknown sample systems. Here, the acquisition of the distance-dependency, described by the formulas presented before in this chapter, is more useful.

---

[11] On a closed boundary of a 2D domain, every tip has two neighbouring tips. Thus, only a measurement with a *bridging* configuration is not allowed to be used.

3.5. Summary

Within this chapter, the analytical relations between the measured four-point resistance and the conductivity of the material itself, i.e. $R(\sigma)$, have been derived, both generally for the case of pure 2D and pure 3D systems, and for specific tip arrangements used in actual four-tip measurements, i.e. the linear equidistant and non-equidistant setup. Furthermore, the anisotropic conductivity has been discussed for 2D materials and the rotational square method for performing angular-dependent measurements has been presented. Moreover, it has been shown that for a measurement with four fixed tips only three substantially different four-point resistances can exist which are accessible by different electrical assignment of the tips.

So far, different dimensionality has been considered only in separated systems. However, if the system under study exhibits multiple conductance channels with a mixed geometry, i.e. a conductive surface on a bulk crystal, the equations presented above do not hold. For this purpose, different models have to be developed, which will be discussed in the framework of multi-layer models for charge transport, i.e. a 3-layer and N-layer model, in the following chapters in combination with measurements on such composed systems.

4. Surface and step conductivities on Si(111) surfaces

Within this chapter, the appearance of multiple conducting channels in parallel is addressed, i.e. basically a system with a highly conductive two-dimensional surface channel on top of a three-dimensional bulk crystal is considered. More specifically, the doped semiconductor Si(111) is investigated, whose surface states arising from certain surface terminations, e.g. as the 7×7 reconstruction, can contribute significantly to lateral current transport. Thus, the crucial task is to find a method for reliably determining this surface conductivity. For this purpose, a combined approach is presented in the following which is based both on experimental four-point resistance measurements performed with a multi-tip STM, as well as on the additional support by a theoretical model taking into account the specific conductance channels inside the sample. The combination of both allows for a separation of the surface conductance from the bulk contribution and, for example, enables the measurement of the Si(111)-(7×7) surface conductivity.

4.1. The Si(111)-(7×7) surface

In modern nanoelectronic devices, the importance of surface conductance compared to conductance through the bulk increases continuously. This calls for a reliable determination of the surface conductivity in order to minimize the influence of undesired leakage currents on the device performance or to use surfaces as functional units. Due to the common standard in the field of semiconductor devices, a model system for corresponding investigations is the Si(111)-(7×7) surface. Over the years a wide range of values for the conductivity of this surface has been reported, spanning several orders of magnitude [78], and the latest measurements deviate still by a factor of 2 to 3 [23, 79]. From the used methods, it turned out that the main difficulty in measuring the surface conductivity is to separate the 2D conductance at the surface from the simultaneously existing conductance through other channels, as the bulk and the space charge layer.

Here, an alternative approach is used, namely performing linear distance-dependent four-probe measurements with a multi-tip STM. In order to model the measured four-point resistance with regard to the presence of multiple conductance channels, an analytical 3-layer model for charge transport is developed. The formalism for this model is presented in section 4.2. Such a combined method allows to disentangle the surface conductivity from other non-surface contributions due to the characteristic probe-spacing dependency of the involved 2D and 3D conductance channels. In section 4.1.4, this will be shown specifically for the Si(111)-(7×7) surface. Moreover, it turns out that the conductance channels present in the Si(111) can be substantially changed by a termination of the surface with either bismuth or hydrogen. As a result, the two limiting cases of a pure 2D or 3D conductance are obtained, respectively.

Further on, as depicted in section 4.3, the anisotropy of the surface conductance caused by the influence of atomic steps is analysed. Here, in order to further disentangle the surface conductivity of the step-free surface from the contributions due to atomic steps, a square four-probe configuration is applied as function of the rotation angle. With the support of the results obtained before from the linear measurements, the conductivity of a single step on the Si(111)-(7×7) surface is obtained as well as the 2D surface conductivity of the step-free terraces.

In order to verify the obtained values, further measurements are performed on Si(111) substrates with different type and concentration of doping, as shown in section 4.4. Also, the influences of the step density and the quality of the 7×7 reconstruction on the surface conductivity are investigated.

4.1.1. Measurement details

The distance-dependent measurements of the four-point resistance on Si(111) are performed with the four-tip STM described in section 2.1. A linear arrangement of the four probes is applied, as it is shown in the inset in Fig. 4.3. In order to obtain the four-point resistance in this this linear setup, a *conventional* tip arrangement is used, i.e. the voltage between the inner two tips is measured as a function of the current injected by the outer tips. As derived in detail in the previous chapter in section 3.2.3, for equidistant tips the relations between four-point resistance and conductivity can be expressed analytically for both a 2D sheet (surface) and a 3D bulk crystal (half space) by Eqs. (3.44) and (3.46), respectively. The hallmark of the 2D channel is that the measured resistance is independent of the probe spacing, while for the 3D channel it depends on the distance s of the four probes. In order to minimize the number of tips to be repositioned, the non-equidistant spacing is preferentially used. Here, three tips remain at a mutual distance of $s = 50\,\mu\mathrm{m}$, while only the distance x between tip 1 and tip 2 is varied, as it is visualized in the inset of Fig. 4.3. However, in this non-equidistant setup, the Eqs. (3.48) and (3.50) describe the four-point resistances for the 2D and 3D case, respectively, implying that the hallmark of the constant 2D behaviour is lost.

4.1.2. The 7×7 surface reconstruction

At the boundary to vacuum the symmetry of a bulk crystal is broken, and due to the missing subsequent atomic layer at the crystal surface a substantial amount of unsaturated dangling bonds results in the topmost atomic layer. However, this dangling bonds are energetically not favoured so that a rearrangement of atoms occurs exactly at the surface in order to reduce the total number of dangling bonds. The resulting lattice structure at the surface

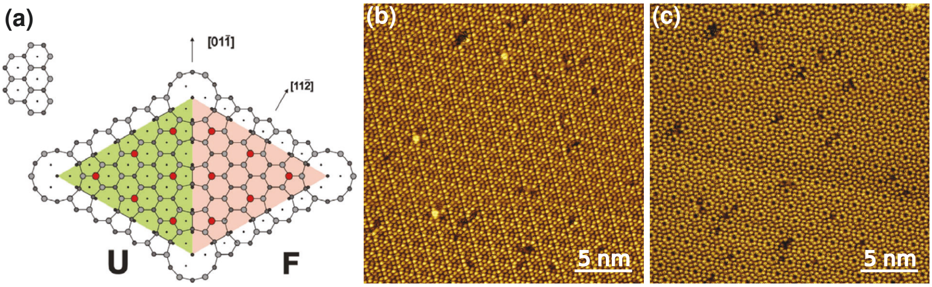

Figure 4.1.: (a) Top-view of the unit cell of the Si(111)-(7×7) surface reconstruction [81, 82]. Adatoms (red points), and the two parts with (F, red area) and without (U, green area) stacking fault are indicated. Smaller atoms are located in the subsurface layers. Inset: Top-view of the structure of the underlying bulk (diamond lattice). The drawing is taken from Ref. [81]. (b,c) STM images of the Si(111)-(7×7) surface reconstruction for (b) positive tip bias voltage ($U = 640\,\mathrm{mV}$, $I = 100\,\mathrm{pA}$) and (c) negative tip bias voltage ($U = -640\,\mathrm{mV}$, $I = 100\,\mathrm{pA}$).

caused by this local rearrangement is termed as surface reconstruction.

A common surface reconstruction on Si(111) is the (7×7) structure, i.e. Si(111)-(7×7), which also was the first semiconductor reconstruction imaged by STM [80]. It exhibits a rather large rhombic unit cell with a width of $26.9\,\text{Å}$, and, as already indicated by the term *7×7*, it is by a factor of 49 larger than the unit cell of the (1×1) surface, i.e. the unreconstructed Si(111) surface [81]. The reconstruction occurs in the topmost bilayer, i.e. a pair of two planes with sp^3-hybridized Si atoms, of the diamond lattice of the Si(111) bulk crystal. By formation of several dimers, adatoms and a stacking fault, according to the DAS model [82], the total number of dangling bonds is reduced to 9 per 7×7 unit cell, while the unreconstructed 1×1 unit cell exhibits 49 dangling bonds. In Fig. 4.1(a), the lattice structure of the 7×7 surface is visualized. The adatoms (red points), and both the faulted stacking (F) with respect to the underlying bulk stacking order (shown in the inset) in one half of the unit cell (red area) as well as the correct stacking (U) in the other half (green area) are indicated. The depicted size of the atoms inside the structure corresponds to their vertical position, i.e. the smaller the atom appears the further away is its position from the surface. A further characteristic structure are the corner holes which appear at the connection points between multiple neighbouring unit cells.

The 7×7 reconstruction introduces additional electronic states exactly at the crystal surface, which exhibit substantially different electronic properties than the bulk. In contrast to a semiconductor these states show a metallic behavior, i.e. in the density of states no gap appears in the region around the Fermi energy E_F, as it has been deduced from measurements and DFT calculations [83, 84]. For this reason, the surface states significantly contribute in current transport and, therefore, a second current path along the surface is established in parallel to the one through the bulk material.

A 7×7 reconstruction can be achieved by a heat treatment of the Si(111) substrate under ultra-high vacuum (UHV) conditions with a base pressure of $\sim 1\times10^{-10}\,\mathrm{mbar}$. First,

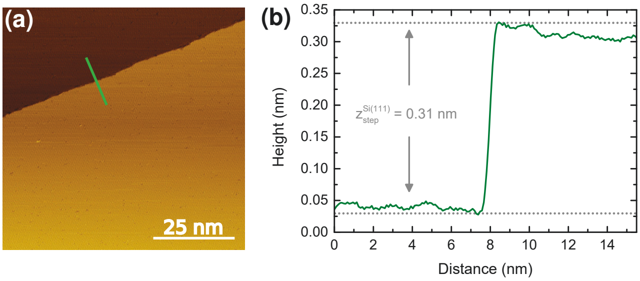

Figure 4.2.: (a) STM image of a single step edge on a Si(111) surface ($U = -1.2\,\mathrm{mV}$, $I = 100\,\mathrm{pA}$). On the flat terraces the (7×7)-reconstruction is slightly visible. (b) Height profile of the step edge shown in (a), indicating the height of a single atomic step on Si(111) of $z_{\mathrm{step}}^{\mathrm{Si(111)}} = 310\,\mathrm{pm}$.

for a cleaning process the Si(111) is annealed by direct current heating to $1230\,^{\circ}\mathrm{C}$. Subsequently, the substrate is cooled down slowly, so that around the transition temperature of $\sim 800\,^{\circ}\mathrm{C}$ the 7×7 surface reconstruction establishes. Afterwards, the 7×7 reconstruction is imaged *in situ* by STM, as shown in the Figs. 4.1(b) and 4.1(c). For the image in Fig. 4.1(b) a positive bias voltage at the tip is chosen, while the bias voltage for Fig. 4.1(c) is negative, and from comparing both measurements it is visible that the 7×7 structure appears differently. In both cases, mainly the adatoms of the reconstruction are imaged, and in both the characteristic corner holes are directly visible. However, in Fig. 4.1(b) there is a brightness contrast between adatoms positioned on the two halves of the unit cell (either on the one with or without stacking fault), while in Fig. 4.1(c) all adatoms appear equally bright. The reason is that the tunneling probability for electrons tunneling from the occupied states [Fig. 4.1(b)] is different for the both halves of the unit cell [85], as due to the stacking fault the energy levels are shifted with respect to each other, while for the tunneling process into the unoccupied states no difference appears [Fig. 4.1(c)]. Additionally, it is visible that some defects (holes) in the 7×7 structure appear, but when compared to the total area of the reconstructed surface, the fraction of defects is small. However, a large amount of such defects can significantly alter the properties of the reconstruction, e.g. the conductivity, as it will be discussed in more detail later in section 4.4.3.

Underneath the 7×7 reconstruction at the surface, the step edges of the Si(111) substrate are still present. This can be seen in Fig. 4.2(a), where on the terraces the 7×7 structure is slightly visible. From a profile line [Fig. 4.2(b)] the apparent step height can be identified to be $z_{\mathrm{step}}^{\mathrm{Si(111)}} = 310\,\mathrm{pm}$. This value corresponds to the distance of two neighbouring bilayers in the bulk crystal, which is the smallest observable step height on Si(111).

4.1.3. Bi passivation — Bi/Si(111)-($\sqrt{3} \times \sqrt{3}$)

As there are still some remaining dangling bonds on the Si(111)-(7×7) surface, it is chemical reactive and can easily be passivated by another material. Here, for the first experiment Bi is chosen in order to obtain a different reconstructed surface, i.e. Bi/Si(111)-($\sqrt{3} \times \sqrt{3}$).

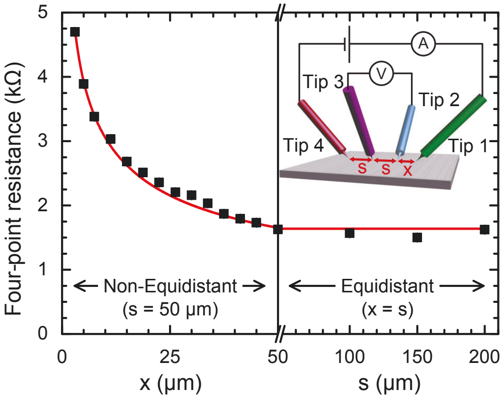

Figure 4.3.: Four-point resistance of a Bi-terminated Si(111)-($\sqrt{3} \times \sqrt{3}$)R30° sample as function of the probe distances s and x for the equidistant (right part) and the non-equidistant configuration (left part). The red solid line correspond to a fit resulting a pure 2D conductance with $\sigma_{\mathrm{Bi}} = (1.4 \pm 0.1) \times 10^{-4}\,\mathrm{S}/\square$. In the inset, the linear measurement configuration is shown. (Sample preparation and measurement have been performed by *Marcus Blab* [87]).

First, the 7×7 reconstruction is established, as described in the previous section 4.1.2. Afterwards the surface is passivated by $1\,\mathrm{ML}$ bismuth, as described in Ref. [86], which results in the $(\sqrt{3} \times \sqrt{3})$R30° surface.

Subsequently, four-point measurements are carried out *in situ* under ultra-high vacuum conditions at a base pressure of $\sim\ 1 \times 10^{-10}\,\mathrm{mbar}$, which is the case for all measurements presented in this chapter. In Fig. 4.3, the obtained four-point resistance is shown for the Bi/Si(111)-($\sqrt{3} \times \sqrt{3}$) surface of an n-doped Si bulk crystal $(2\,\mathrm{k}\Omega\,\mathrm{cm})$. Both the non-equidistant tip configuration with distances $x \leq s = 50\,\mu\mathrm{m}$ and the equidistant configuration with distances $x = s \geq 50\,\mu\mathrm{m}$ have been used for the measurement, as depicted on the axis (the sample preparation and the measurement itself have been performed by *Marcus Blab*, as described in [87]). The constant behavior in the equidistant range $s \geq 50\,\mu\mathrm{m}$ indicates a pure 2D character of conductance. Another indicator for 2D surface transport is the fact that the four-point resistance, which is expected considering only the bulk conductivity, is several orders of magnitude larger than the observed one. Therefore, the experimental data are compared to a 2D model, and a good correspondence is obtained for $\sigma_{\mathrm{Bi}} = (1.4 \pm 0.1) \times 10^{-4}\,\mathrm{S}/\square$ (solid red line) confirming that the charge transport in the Bi-terminated Si(111) sample occurs almost exclusively through the 2D surface channel. Similar results were found for two differently doped samples.

4.1.4. Multiple conductance channels of Si(111)-(7×7)

Subsequently, the distance dependence of the four-point resistance has been measured on a clean Si(111)-(7×7) sample. The results for an n-doped sample $(700\,\Omega\,\mathrm{cm})$ are shown in Fig. 4.4. (The sample preparation and measurement have been performed together with

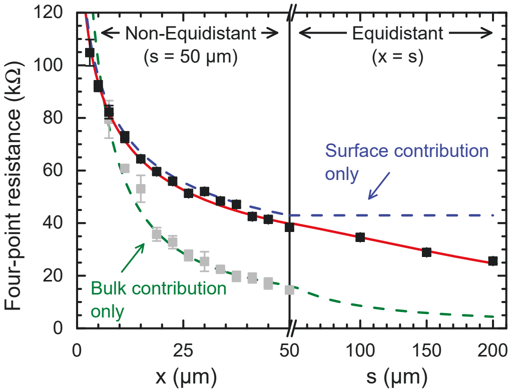

Figure 4.4.: Four-point resistance of an n-doped Si(111)-(7×7) sample as function of the probe distances s and x for the equidistant and the non-equidistant configuration. A 3-layer model for charge transport yields the solid red line with $\sigma_{2D} = (5.1 \pm 0.7) \times 10^{-6}\,\mathrm{S}/\square$ located between the two limiting contributions to the fit, i.e. a pure surface conductance (dashed blue line, as obtained from the 3-layer fit) and a pure bulk conductance (dashed green line). If the Si(111) surface is hydrogen-terminated, the surface contribution vanishes completely and the remaining bulk conductance can directly be measured (gray data points). (The sample preparation and measurement have been performed together with *Marcus Blab* [87]).

Marcus Blab [87]). The observed decreasing four-point resistance for increasing equidistant probe spacing s indicates that a non-surface channel contributes to the charge transport, since a pure 2D conduction exhibits a constant behavior in the equidistant region (cf. Fig. 4.3). Thus, the measured four-point resistance should be modelled by a conductance channel through the surface states as well as additional contributions from the bulk and a near-surface space charge layer. However, this implies that in this case the Eqs. (3.44) and (3.46) for pure 2D and 3D geometries, respectively, cannot be applied.

Often an approximation of a parallel circuit consisting of the four-point resistance of the surface and the bulk (plus space charge layer) is used [62], but this approach has several shortcomings, i.e. a separation between surface and bulk, and equal current injection into both, as it will be discussed in more detail in the next chapter in section 5.2. If multiple current paths exist in parallel, the four-point resistance, which is measured on the surface, can depend on both transitions between the conducting channels for transport, as well as on the properties of the current injecting contacts. Therefore, in general the well-known statement that the four-point resistance is independent of the contact resistances is not completely true in this case.

In order to describe the charge transport through the different channels more accurately, an analytically derived 3-layer model for conductance is used (cf. section 4.2). In this model, the bulk enters with its known conductivity, while the surface conductivity is the parameter to be determined by a fit to the data. The space charge layer is approximated by an intermediate layer with a certain thickness and conductivity. These two values can be obtained by the solution of the Poisson equation, which considers the known Fermi level pinning of the Si(111)-(7×7) surface [88, 89]. Nevertheless, the use of the bulk doping concentration as parameter in this calculation turns out to be not sufficient in the present case, since with the resulting width and average conductivity the space charge layer is too highly conductive in order to be able to describe the data in Fig. 4.4. However, it is known that high-temperature annealing up to $1200\,^{\circ}\mathrm{C}$ performed for cleaning the Si(111) surface causes a dopant redistribution and an additional p-type doping in the near-surface region due to boron in-diffusion [90–93] or possible formation of near-surface single vacancies [94]. These effects can lead to a reduced carrier concentration in the space charge layer, similar as it is observed. Generally, the details of the modification of the near-surface doping depend highly on the specific method and setup used for sample preparation [95]. It turns out that the experimental data can be described well for a conductivity of $2.5 \times 10^{-4}\,\mathrm{S/m}$ and a thickness of $3.1\,\mu\mathrm{m}$ for the intermediate layer representing the space charge layer. This quite approximate modelling of the space charge region as only one layer with constant conductivity seems to be sufficient, as the surface conductivity obtained from the fit to the measured data turns out to be insensitive to the specific properties of the intermediate layer.

Overall, the 3-layer model results in a much more accurate description of the measured four-point resistance than the simple parallel-circuit model, since it avoids the artificial separation between the surface and the non-surface channels and takes into account the injection geometry giving rise to a charge transport inside and between the layers according to their properties. The analytical derivation of the model is described in detail in section 4.2.

The best fit to the measured four-point resistance using the 3-layer model is shown as a solid red line in Fig. 4.4 and results in a surface conductivity of $\sigma_{2D} = (5.1 \pm 0.7) \times 10^{-6}\,\mathrm{S}/\square$. For comparison the two limiting cases, which contribute to the fit, are marked in Fig. 4.4: The four-point resistance arising from a pure 2D conductivity σ_{2D} is shown as dashed blue line, while the four-point resistance induced by a pure 3D conductance, with its $1/s$ behavior in the equidistant configuration, is indicated as dashed green line, which features the bulk conductivity value of the Si(111). This value for the bulk is confirmed by an additional experiment which is described below. In the non-equidistant region the measured four-point resistance is close to the one expected from a pure surface conductance (less than $6\,\%$ deviation for $x \leq 50\,\mu\mathrm{m}$), but for larger probe spacing an increasing deviation from the 2D behavior is observed. This reflects the well-known general tendency that the conductance is more surface-dominated for small probe distances, while a non-surface contribution develops more significantly for larger distances [78]. However, the observed four-point resistance does not approach the $1/s$ bulk behavior for $s \geq 50\,\mu\mathrm{m}$, because the space charge layer blocks the charge transport into the bulk due to the low conductivity of the depletion zone. So, the four-point resistance in the equidistant range particularly reflects the properties of the space charge layer and the bulk, while the non-equidistant region is more suitable for the determination of the surface conductivity. In total, the 3-layer model including the intermediate layer describes the experimentally observed behavior very well. Results obtained for other doping levels are shown in section 4.4.1 and confirm the results presented above.

An additional experiment is used to explore, if the bulk conductivity can be measured directly with the four-probe setup after removing the surface conductance channel. A hydrogen termination of the Si(111) surface resulting in the formation of the Si(111)-(1×1)-H, is known to remove the surface states present on the 7×7 surface [96]. In order to achieve this H-termination, a treatment of the Si(111) in a $1\,\%$ solution of HF acid is used, and after an additional cleaning step in deionized water the sample is transferred to the UHV within a time of $10\,\mathrm{min}$. The gray data points in Fig. 4.4 show the distance dependence of the four-point resistance in the non-equidistant region measured afterwards on such a hydrogen-terminated Si(111) sample. The dashed green line corresponds to a fit using a pure 3D bulk behavior with a resistivity of $\rho_{3D} = (580 \pm 70)\,\Omega\,\mathrm{cm}$, which is close to the macroscopically measured nominal bulk resistivity of $(700 \pm 50)\,\Omega\,\mathrm{cm}$ and therefore confirms that without surface states a pure 3D bulk conductance is obtained.

4.2. The 3-layer conductance model

In this section, the analytical derivation of the 3-layer conductance model is presented and its applicability is discussed. The 3-layer model assumes a layered sample structure shown in Fig. 4.5 consisting of a thin surface layer, an intermediate layer and a semi-infinite bulk characterized by their respective conductivities σ_1, σ_2 and σ_3, and positions of the interfaces z_1 and z_2. At the surface a current I is injected by a cylindrical tip with radius r_t. Due to calculation requirements, the surface layer cannot be two-dimensional, so that a finite thickness of one atomic layer ($3\,\text{Å}$) is assumed. In the same way as shown in section 3.2, based on $\nabla \cdot \boldsymbol{j} = 0$ for the current density $\boldsymbol{j} = \sigma \boldsymbol{E} = -\sigma\,\nabla\Phi$ inside the sample (excluding the injection point), the electrical potential Φ can be determined by solving the Laplace equation

$$\Delta\Phi = 0 \tag{4.1}$$

in cylindrical coordinates $\boldsymbol{x}(\rho, \varphi, z)$ with

$$\boldsymbol{x}(\rho,\varphi,z) = \begin{pmatrix} x \\ y \\ z \end{pmatrix} = \begin{pmatrix} \rho\cos(\varphi) \\ \rho\sin(\varphi) \\ z \end{pmatrix} \qquad \text{and} \qquad \rho = |\boldsymbol{x}| = \sqrt{x^2 + y^2}. \tag{4.2}$$

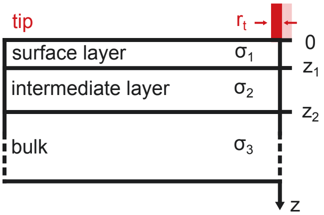

Figure 4.5.: The 3-layer model consists of a thin surface layer, an intermediate layer and the semi-infinite bulk described by their respective conductivities σ_1, σ_2 and σ_3, and their positions z_1 and z_2. The current I is injected by a cylindrical tip of radius r_t at the surface layer.

Taking account of the angle-independent polar symmetry for one current injecting tip, a solution for the potential in the individual layers can be generally expressed by [97]

$$\Phi_1(\rho, z) = \int_0^\infty \left[a(k)\, e^{kz} + b(k)\, e^{-kz}\right] J_0(k\rho)\, dk, \qquad \text{for } 0 \le z \le z_1 \tag{4.3a}$$

$$\Phi_2(\rho, z) = \int_0^\infty \left[c(k)\, e^{kz} + d(k)\, e^{-kz}\right] J_0(k\rho)\, dk, \qquad \text{for } z_1 \le z \le z_2 \tag{4.3b}$$

$$\Phi_3(\rho, z) = \int_0^\infty f(k)\, e^{-kz}\, J_0(k\rho)\, dk, \qquad \text{for } z_2 \le z \tag{4.3c}$$

with J_0 denoting the *Bessel* function of the first kind. The corresponding boundary conditions determining the coefficients are

$$-\sigma_1 \frac{\partial}{\partial z} \Phi_1(\rho, 0) = j_1\, H(r_t - \rho) \tag{4.4a}$$

$$\sigma_1 \frac{\partial}{\partial z} \Phi_1(\rho, z_1) = \sigma_2 \frac{\partial}{\partial z} \Phi_2(\rho, z_1) \tag{4.4b}$$

$$\Phi_1(\rho, z_1) = \Phi_2(\rho, z_1) \tag{4.4c}$$

$$\sigma_2 \frac{\partial}{\partial z} \Phi_2(\rho, z_2) = \sigma_3 \frac{\partial}{\partial z} \Phi_3(\rho, z_2) \tag{4.4d}$$

$$\Phi_2(\rho, z_2) = \Phi_3(\rho, z_2) \tag{4.4e}$$

which result from the current injection [Eq. (4.4a)], as well as from the continuous transitions of the potential [Eq. (4.4c) and Eq. (4.4e)] and the current density [Eq. (4.4b) and Eq. (4.4d)] between the layers. In Eq. (4.4a), the expression $H(r_t - \rho)$ denotes the *Heaviside* step function. With the assumption of a uniform current flux beneath the tip contact the injected current density can be described by $j_1 = \frac{I}{\pi r_t^2}$ assuming a cylindrical tip with a tip radius of $r_t \approx 25\,\mathrm{nm}$, which seems reasonable for an STM tip. Nevertheless, it turns out that also other values for the tip radius in the range of $5\,\mathrm{nm}$ to $100\,\mathrm{nm}$ do not influence the results of the calculations in a considerable manner.

Besides the uniform flux condition [98], several other assumptions for the current density at the injection point have been presented in the literature, i.e. the variable flux condition based on the exact solution for a circular contact on an infinitely thick slab [99] and the *Dirac delta* current distribution leading to a ring current density [100, 101]. All approaches are used to approximate the exact surface boundary condition of constant potential beneath the probe, which would lead to a more difficult mixed boundary value problem. However, the differences between the three conditions are rather small [100–102], and especially for small layer thicknesses compared to the radius of the probe contacts, as it applies for the highly conductive surface layer with a thickness of $3\,\text{Å}$, the uniform flux condition is the best approximation [102], so that this condition is used for the calculation.

Based on Eqs. (4.4a) – (4.4e), in combination with the corresponding potentials from Eqs. (4.3a) – (4.3c), a system of five equations for the coefficients $a(k), \ldots, f(k)$ can be derived as

$$-\sigma_1 \int_0^\infty [a(k) - b(k)]\, k J_0(k\rho) dk = j_1\, H(r_t - \rho) \tag{4.5a}$$

$$\sigma_1\int_0^\infty\left[a(k)e^{kz_1}-b(k)e^{-kz_1}\right]kJ_0(k\rho)dk=\sigma_2\int_0^\infty\left[c(k)e^{kz_1}-d(k)e^{-kz_1}\right]kJ_0(k\rho)dk \tag{4.5b}$$

$$\int_0^\infty\left[a(k)e^{kz_1}+b(k)e^{-kz_1}\right]J_0(k\rho)dk=\int_0^\infty\left[c(k)e^{kz_1}+d(k)e^{-kz_1}\right]J_0(k\rho)dk \tag{4.5c}$$

$$\sigma_2\int_0^\infty\left[c(k)e^{kz_2}-d(k)e^{-kz_2}\right]kJ_0(k\rho)dk=-\sigma_3\int_0^\infty f(k)e^{-kz_2}kJ_0(k\rho)dk \tag{4.5d}$$

$$\int_0^\infty\left[c(k)e^{kz_2}+d(k)e^{-kz_2}\right]J_0(k\rho)dk=\int_0^\infty f(k)e^{-kz_2}J_0(k\rho)dk. \tag{4.5e}$$

After an rearrangement of Eqs. (4.5a) – (4.5e), one obtains

$$\int_0^\infty\sigma_1\left[a(k)-b(k)\right]kJ_0(k\rho)dk=-j_1\,H(r_t-\rho) \tag{4.6a}$$

$$\int_0^\infty\left[\left(\sigma_1a(k)-\sigma_2c(k)\right)e^{kz_1}-\left(\sigma_1b(k)-\sigma_2d(k)\right)e^{-kz_1}\right]kJ_0(k\rho)dk=0 \tag{4.6b}$$

$$\int_0^\infty\left[\left(a(k)-c(k)\right)e^{kz_1}+\left(b(k)-d(k)\right)e^{-kz_1}\right]J_0(k\rho)dk=0 \tag{4.6c}$$

$$\int_0^\infty\left[\sigma_2c(k)e^{kz_2}-\left(\sigma_2d(k)-\sigma_3f(k)\right)e^{-kz_2}\right]kJ_0(k\rho)dk=0 \tag{4.6d}$$

$$\int_0^\infty\left[c(k)e^{kz_2}+\left(d(k)-f(k)\right)e^{-kz_2}\right]J_0(k\rho)dk=0. \tag{4.6e}$$

In order to separate the coefficients $a(k),\ldots,f(k)$ in Eqs. (4.6a) – (4.6e), the *Hankel* transform can be calculated and the orthogonality of the *Bessel* functions $\int_0^\infty\rho J_0(k\rho)J_0(k'\rho)d\rho=\frac{1}{k}\delta(k-k')$ can be used [97], whereby $\delta(k)$ denotes the *Delta* distribution. The application of the *Hankel* transformation is shown exemplarily for the case of Eq. (4.6a) in the appendix A.2.1. So, afterwards one obtains for the coefficients

$$\sigma_1\left[a(k)-b(k)\right]=-j_1\int_0^{r_t}\rho J_0(k\rho)d\rho \tag{4.7a}$$

$$\left[\sigma_1a(k)-\sigma_2c(k)\right]e^{kz_1}-\left[\sigma_1b(k)-\sigma_2d(k)\right]e^{-kz_1}=0 \tag{4.7b}$$

$$\left[a(k)-c(k)\right]e^{kz_1}+\left[b(k)-d(k)\right]e^{-kz_1}=0 \tag{4.7c}$$

$$\sigma_2c(k)e^{kz_2}-\left[\sigma_2d(k)-\sigma_3f(k)\right]e^{-kz_2}=0 \tag{4.7d}$$

$$c(k)e^{kz_2}+\left[d(k)-f(k)\right]e^{-kz_2}=0. \tag{4.7e}$$

Eqs. (4.7a) – (4.7e) can be rewritten in matrix notation as

$$\begin{pmatrix}1 & -1 & 0 & 0 & 0\\ e^{kz_1} & -e^{-kz_1} & -\frac{\sigma_2}{\sigma_1}e^{kz_1} & \frac{\sigma_2}{\sigma_1}e^{-kz_1} & 0\\ e^{kz_1} & e^{-kz_1} & -e^{kz_1} & -e^{-kz_1} & 0\\ 0 & 0 & e^{kz_2} & -e^{-kz_2} & \frac{\sigma_3}{\sigma_2}e^{-kz_2}\\ 0 & 0 & e^{kz_2} & e^{-kz_2} & -e^{-kz_2}\end{pmatrix}\cdot\begin{pmatrix}a(k)\\ b(k)\\ c(k)\\ d(k)\\ f(k)\end{pmatrix}=\begin{pmatrix}I(k,\sigma_1)\\ 0\\ 0\\ 0\\ 0\end{pmatrix} \tag{4.8}$$

with

$$I(k,\sigma_1) := -\frac{j_1}{\sigma_1}\int_0^{r_t} \rho\, J_0(k\rho)\, d\rho \tag{4.9}$$

The matrix equation (4.8) can be solved by means of matrix inversion in order to obtain the coefficients $a(k), \dots, f(k)$. As the potential at the surface ($z = 0$) directly follows from Eq. (4.3a) as

$$\Phi_{\text{surf}}(\rho) = \Phi_1(\rho, 0) = \int_0^{\infty} [a(k) + b(k)]\, J_0(k\rho)\, dk, \tag{4.10}$$

only the sum $a(k) + b(k)$ of the coefficients is relevant for the calculation. As shown in the appendix A.2.2, from Eq. (4.8) an expression for the sum can be derived as

$$a(k) + b(k) = \frac{j_1}{\sigma_1}\int_0^{r_t} \rho J_0(k\rho)\, d\rho\; \frac{\dfrac{\frac{\sigma_3}{\sigma_2}\tanh[k(z_2 - z_1)] + 1}{\tanh[k(z_2 - z_1)] + \frac{\sigma_3}{\sigma_2}} + \frac{\sigma_2}{\sigma_1}\tanh[kz_1]}{\dfrac{\frac{\sigma_3}{\sigma_2}\tanh[k(z_2 - z_1)] + 1}{\tanh[k(z_2 - z_1)] + \frac{\sigma_3}{\sigma_2}}\tanh[kz_1] + \frac{\sigma_2}{\sigma_1}}. \tag{4.11}$$

Thus, by insertion into Eq. (4.10) and numerical evaluation of the integral, the surface potential arising from one current injecting tip can be calculated.

In order to take into account more than one tip, it is useful to transform back into Cartesian coordinates [cf. Eq. (4.2)]. However, as based on Eq. (4.10) only the surface is considered, two-dimensional coordinates are sufficient, i.e. $\boldsymbol{x} = \left(\begin{smallmatrix} x \\ y \end{smallmatrix}\right)$. Thus, for an injecting tip positioned at $\boldsymbol{x}_A = \left(\begin{smallmatrix} x_A \\ y_A \end{smallmatrix}\right)$, Eq. (4.10) changes into

$$\Phi^A_{\text{surf}}(\boldsymbol{x}) = \int_0^{\infty} [a(k) + b(k)]\, J_0(k\,|\boldsymbol{x} - \boldsymbol{x}_A|)\, dk. \tag{4.12}$$

The combined potential arising from a current source at $\boldsymbol{x}_A$ and a current sink at $\boldsymbol{x}_B$ is correspondingly expressed by the superposition

$$\Phi^{AB}_{\text{surf}}(\boldsymbol{x}) = \Phi^A_{\text{surf}}(\boldsymbol{x}) - \Phi^B_{\text{surf}}(\boldsymbol{x}) = \int_0^{\infty} [a(k)+b(k)] \Big[J_0(k\,|\boldsymbol{x}-\boldsymbol{x}_A|) - J_0(k\,|\boldsymbol{x}-\boldsymbol{x}_B|)\Big]\, dk. \tag{4.13}$$

Evaluating the potential difference between two probes positioned at $\boldsymbol{x}_C$ and $\boldsymbol{x}_D$, respectively, finally results in

$$\Phi^{AB}_{CD} = \Phi^{AB}_{\text{surf}}(\boldsymbol{x}_D) - \Phi^{AB}_{\text{surf}}(\boldsymbol{x}_C) \tag{4.14}$$

$$\begin{aligned}\Leftrightarrow\ \Phi^{AB}_{CD} = \int_0^{\infty} \Big[a(k)+b(k)\Big] \Big[& J_0\big(k|\boldsymbol{x}_D-\boldsymbol{x}_A|\big) - J_0\big(k|\boldsymbol{x}_D-\boldsymbol{x}_B|\big) \\ & - J_0\big(k|\boldsymbol{x}_C-\boldsymbol{x}_A|\big) + J_0\big(k|\boldsymbol{x}_C-\boldsymbol{x}_B|\big)\Big]\, dk\,.\end{aligned} \tag{4.15}$$

If a linear equidistant probe configuration with a spacing s is considered, as it is depicted in Fig. 3.4(a), the four-point resistance $R = \frac{-\Phi_{CD}^{AB}}{I}$ measured on the surface for an injected current I can be expressed by

$$R_{\mathrm{lin}}^{3-\mathrm{lay}}(s) = \frac{2}{I}\int_0^\infty \Big[a(k)+b(k)\Big]\Big[J_0\big(ks\big) - J_0\big(2ks\big)\Big]\,dk\,. \tag{4.16}$$

For a non-equidistant linear setup [cf. Fig. 3.4(b)] with the spacings x and s, one obtains with the same considerations as in section 3.2.3 that

$$R_{\mathrm{lin,ne}}^{3-\mathrm{lay}}(s,x) = \frac{1}{I}\int_0^\infty \Big[a(k)+b(k)\Big]\Big[J_0\big(ks\big) - J_0\big(k[s+x]\big) - J_0\big(2ks\big) + J_0\big(kx\big)\Big]\,dk\,. \tag{4.17}$$

So, the equidistant measurement range in Fig. 4.4, i.e. $s = x \geq 50\,\mu\mathrm{m}$, can be described by Eq. (4.16), while for the non-equidistant region, i.e. $x \leq s = 50\,\mu\mathrm{m}$, Eq. (4.17) has to be used. The integral over the Bessel functions can be evaluated numerically and the result can be fitted to the measurement data with the free parameters σ_1, σ_2 and z_2, which define the properties of the surface layer and the intermediate layer used as approximation for the space charge region in the sample. The value for σ_3 is known from macroscopic measurements of the bulk resistivity and is in agreement with the nominal doping concentration.

The surface conductance channel has the largest influence on the four-point resistance for small distances, i.e. $x \leq 50\,\mu\mathrm{m}$ (region of non-equidistant probe spacing), while the properties of the intermediate layer (conductivity and thickness) have the largest influence on the four-point resistance in the region of larger distances (equidistant spacing region). This is illustrated in Fig. 4.6, in which the measured four-point resistance from Fig. 4.4 (n-doped Si(111)-(7×7) sample, bulk resistivity $700\,\Omega\,\mathrm{cm}$) is compared to theoretical curves resulting from the 3-layer model for different input parameters (colored curves). For the constant nominal bulk resistivity of the sample and a varying conductivity for the intermediate layer (space charge layer) over three orders of magnitude from $1 \times 10^{-3}\,\mathrm{S/m}$ (magenta curve) to $1 \times 10^{-6}\,\mathrm{S/m}$ (green curve), the measured data are fitted to determine the surface conductivity. If the space charge layer conductivity is enhanced above a value of $1 \times 10^{-3}\,\mathrm{S/m}$, the measured data cannot be described any more by the model and a fit is not possible. So, the space charge layer should be described by a conductivity value in the chosen region. Although there is a very large spread in the space charge layer conductivity, the results show a very minor spread of the surface conductivity with a deviation of less than $10\,\%$ from $\sigma_{2D} = 4.8 \times 10^{-6}\,\mathrm{S}/\Box$ (magenta curve) to $\sigma_{2D} = 5.4 \times 10^{-6}\,\mathrm{S}/\Box$ (green curve). All fit curves describe the data very well in the region of small probe spacing ($x \leq 50\,\mu\mathrm{m}$), while there are considerable deviations from the data points for larger probe spacing ($s \geq 50\,\mu\mathrm{m}$). This confirms the influence of surface conductivity and space charge layer conductivity in different regions of the used probe distances. Thus the surface conductivity can be determined very precisely from the non-equidistant probe spacing region, even if the properties of the space charge layer are taken into account only very approximately. On the other hand, the parameters of the space charge layer can be further approximated from the measurement data in the equidistant region. In total, this justifies the crude approximation of

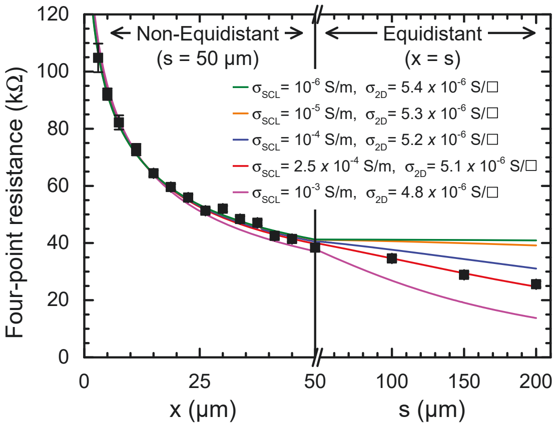

Figure 4.6.: Description of the measured four-point resistance from Fig. 4.4 (n-doped Si(111)-(7×7) sample, bulk resistivity $700\,\Omega\,\mathrm{cm}$) by the 3-layer model for different input parameters (colored curves). For the nominal bulk conductivity and a space charge layer conductivity varying over three orders of magnitude from $1 \times 10^{-3}\,\mathrm{S/m}$ (magenta curve) to $1 \times 10^{-6}\,\mathrm{S/m}$ (green curve) the measured data are fitted with the surface conductivity as free parameter. All curves can describe the data in the region of small probe spacings ($x \leq 50\,\mu\mathrm{m}$) very well, while there are considerable deviations from the data in the region of larger probe distances ($s \geq 50\,\mu\mathrm{m}$). Nevertheless, the obtained surface conductivity shows only a very minor spread and varies less than $10\,\%$ from $\sigma_{2D} = 4.8 \times 10^{-6}\,\mathrm{S}/\square$ (magenta curve) to $\sigma_{2D} = 5.4 \times 10^{-6}\,\mathrm{S}/\square$ (green curve). This indicates that the measured four-point resistance in the small probe spacing region does not depend on the details of the space charge layer, and so the surface conductivity can be determined very precisely, even if the exact properties of the space charge layer are not known.

the space charge region as only one layer with constant conductivity, as the quantity to be determined, the surface conductivity σ_1, does not depend significantly on the values of the conductivity σ_2 and width z_2 used to describe the intermediate layer.

In principle, the 3-layer model described above can be extended to a multi-layer model consisting of N separate layers, as it will be shown in the next chapter 5. In this case, the boundary conditions in Eqs. (4.4a) – (4.4e) have to be modified to include the transitions between layer $n - 1$ and n [for $n = 1, \ldots, N - 1$] and the size of the matrix in Eq. (4.8) becomes $(2N - 1) \times (2N - 1)$.

In contrast to the analytical model, one other way to simulate the contributions of the different charge transport channels to the four-point resistance is to invoke finite element calculations. This has not been done, since the distances involved range from a few nanometers (radius of the current injection) to $200\,\mu\mathrm{m}$ (maximum probe distance) and such a large range of length scales is difficult to include in finite element calculations. Nevertheless, as the exact analytical solution of the potential problem in a layered sample has quite an elementary form, the 3-layer model is easier to apply and provides a more accurate computation than a finite element simulation.

4.3. Step conductivity of Si(111)-(7×7)

While the distance-dependent four-point measurements in combination with the 3-layer model could disentangle the surface conductivity from non-surface contributions to charge transport, the influence of atomic steps located on the (7×7)-reconstructed Si surface has not been considered up to now. The conductivity arising from a single step for a current passing through it can be treated as scalar quantity. However, if a larger surface area is taken into account, the step array leads on average to an anisotropic conductivity described by the tensor components $\sigma^{\|}$ along the step edges and $\sigma^{\perp}$ perpendicular to the step edges [22]. So, the anisotropic conductance is a macroscopic (mean field) result of the different number of step edges per unit length along different current paths. As already discussed in chapter 3, the linear four-point measurement configuration applied before (Fig. 4.4) is not sensitive to a two-dimensional conductance anisotropy [20]. So, a square arrangement of the four probes, as shown in Fig. 4.7(c), has to be used instead. For such a setup, an angle-dependent four-point resistance is expected [20, 63], as it has been derived previously in section 3.3. In the present case, the components of high and low conductivity are $\sigma_x = \sigma^{\|}$ and $\sigma_y = \sigma^{\perp}$, respectively. Thus, Eq. (3.83) reads

$$R^{\mathrm{2D}}_{\mathrm{square}}(\theta) = \frac{1}{4\pi\sqrt{\sigma^{\|}\sigma^{\perp}}} \ln\left[\frac{\left(\frac{\sigma^{\|}}{\sigma^{\perp}}+1\right)^2 - 4\cos^2(\theta)\sin^2(\theta)\left(\frac{\sigma^{\|}}{\sigma^{\perp}}-1\right)^2}{\left(\sin^2(\theta)+\frac{\sigma^{\|}}{\sigma^{\perp}}\cos^2(\theta)\right)^2}\right]. \tag{4.18}$$

It should be noted that, in contrast to the 3-layer model used before, Eq. (4.18) can only describe a pure 2D conductance channel. A derivation of an more exact equation which considers besides the 2D surface also an 3D channel, i.e. an anisotropic 3-layer model, is quite complicated, if the anisotropy applies only for the surface channel, while the bulk remains isotropic. However, as an approximation, by comparing with the linear measurements shown before, which are describable by the 3-layer model, a correction factor for a fixed tip spacing can be obtained between the four-point resistance, which is observable in the measurement and the one which would appear, if only the 2D conductance channel is present in the sample. As it turns out that the correction factors are quite small for the discussed samples, this method is applied in the following in order to increase the precision of the obtained anisotropic conductivity values.

Results for the measured anisotropic four-point resistance on an n-doped Si(111)-(7×7) sample ($700\,\Omega\,\mathrm{cm}$) for a probe spacing of $s = 50\,\mu\mathrm{m}$ are shown in Fig. 4.7(a) as a function of the rotation angle θ relative to the step direction. For such a square configuration, the voltage probes and current probes are located at the corners of opposite sides of the square. The four sets of differently colored data points in angle increments of $5°$ arise from the fact that for one fixed orientation of the probes four different rotation angles can be realized by successively assigning different probes as current and voltage probes.

A fit of Eq. (4.18) to the experimental data is shown as a dotted blue line in Fig. 4.7(a) describing the angle dependence quite well.[1] Nevertheless, the mean field approach applied so far assumes only straight step edges. However, the typical step structure present

---

[1] Since Eq. (4.18) considers exclusively a 2D conductivity, a correction factor for the $6\,\%$ non-surface con-

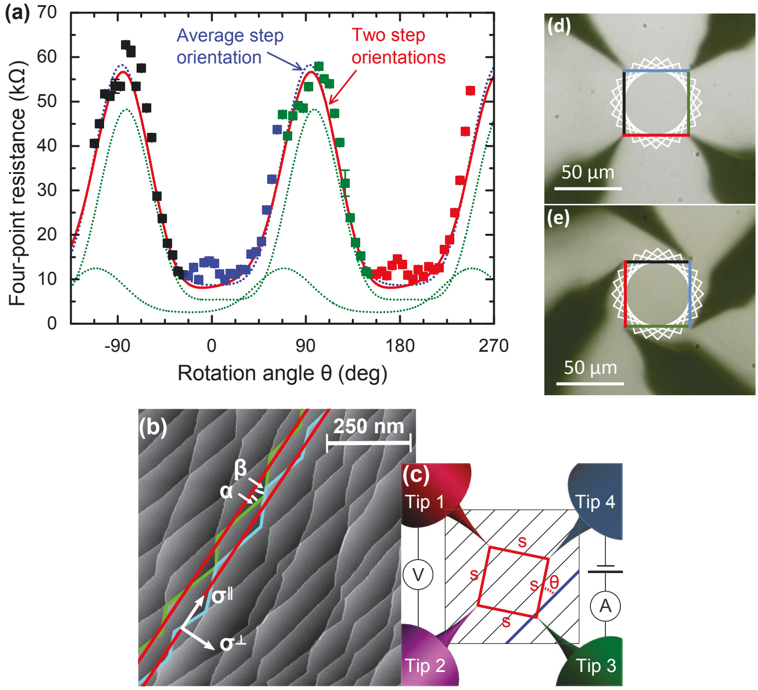

Figure 4.7.: (a) Four-point resistance measured on a Si(111)-(7×7) surface in the square configuration [shown in (c)] with $s = 50\,\mu\text{m}$ as a function of rotation angle θ between the average step orientation and the line connecting the current injecting tips (colored data points). The fits to the data using either only one average step direction or a superposition of two step orientations (respective parts are shown as green dotted lines) are indicated as dotted blue line and solid red line, respectively. (b) STM image of the Si(111)-(7×7) surface showing the representative step arrangement on the sample with a step density of $\sim 14\,\text{steps}/\mu\text{m}$. Two adjacent step edges are highlighted (solid green and blue line) consisting of two main step directions indicated by the angles α and β relative to the average step orientation (solid red lines). (d),(e) Optical microscope images of the four STM tips positioned at the corners of the square. From (d) to (e) the total rotation is 90° with multiple steps in between (white squares). For each step, by rotating the tip assignment (voltage or current probe) four data points in multiples of 90° can be recorded, as indicated by the four colored lines in (d) and (e), and the correspondingly colored data points in (a).

on the $0.25°$ misoriented Si(111)-(7×7) sample surface shown in Fig. 4.7(b) consists of steps aligned mainly along two directions with average angles of $\alpha \approx 8°$ and $\beta \approx 21°$ with respect to the average step orientation (indicated as red lines), which now defines $\sigma^{\parallel}$ and $\sigma^{\perp}$. This average step orientation ($\sim 14\,\text{steps}/\mu\text{m}$) arises from the macroscopic azimuthal direction of the sample miscut and is not aligned with the low-index orientations of the step edges. To model this more complicated non-parallel step pattern, as first-order

---

tribution (at $50\,\mu\text{m}$) to charge transport determined by the linear probe measurements has been taken into account.

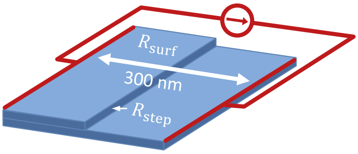

Figure 4.8.: Relation between the resistivities of the step-free surface and the single atomic step on Si(111)-(7×7): The resistance (per unit length) of an atomic step is equal to the resistance (per unit length) of a segment of the step-free terrace with a width of $300\,\mathrm{nm}$.

approximation a superposition of two step orientations is considered with angles α and β relative to the average step orientation weighted with their respective portion extracted from Fig. 4.7(b). This leads to a slightly skewed curve shown as solid red line in Fig. 4.7(a), which consists of an amount of $70\,\%$ and $30\,\%$ of the two single contributions, respectively (dotted green lines). The model including the two step orientations describes the data as well as Eq. (4.18), but contains a better approximation of the sample step structure, and results in $\sigma_{\|} = (9 \pm 2) \times 10^{-6}\,\mathrm{S}/\square$ and $\sigma_{\perp} = (1.7 \pm 0.4) \times 10^{-6}\,\mathrm{S}/\square$ with an anisotropy ratio of $\sigma_{\|}/\sigma_{\perp} \approx 5$. The geometric mean $\sqrt{\sigma^{\|}\sigma^{\perp}} = (3.9 \pm 0.6) \times 10^{-6}\,\mathrm{S}/\square$ has nearly the same value within the error tolerances as the surface conductivity $\sigma_{2\mathrm{D}}$ obtained in the linear configuration. Thus, the two independent methods, the distance-dependent linear configuration and the angle-dependent square configuration, yield the same results for the surface conductivity.

In a last step, the measured mean field anisotropic conductivity is approximated by the scalar resistivities of a step-free terrace ρ_{surf} and a single step ρ_{step}. Considering first the direction parallel to the steps, no step edges have to be crossed by the current, which results in the relation

$$1/\sigma^{\|} = \rho^{\|} = \rho_{\text{surf}}\,. \tag{4.19}$$

Second, the resistivity perpendicular to the step edges is composed of additive contributions from the steps and the step-free terraces and can be expressed as series resistance, resulting in [22]

$$1/\sigma^{\perp} = \rho^{\perp} = \rho_{\text{surf}} + \rho_{\text{step}}/d^{\perp}_{\text{step}} \tag{4.20}$$

with $d^{\perp}_{\text{step}}$ denoting the average distance between the steps. From the two relations in Eq. (4.19) and Eq. (4.20) finally the conductivity of the step-free Si(111)-(7×7) surface can be disentangled from the influence of the step conductivity as $\sigma_{\text{surf}} = (9 \pm 2) \times 10^{-6}\,\mathrm{S}/\square$, and $\sigma_{\text{step}} = (29 \pm 9)\,\mathrm{S/m}$. The value of the surface conductivity σ_{surf} is a factor of 2 to 6 larger than the values obtained in recent experiments [23, 79]. Such smaller values may be explained, as these experiments are based on a more indirect comparison of the conductivity before and after quenching the surface states by adsorption of atoms or molecules. However, since there are several experimental requirements for such a differential measurement, particularly these indirect methods can exhibit a couple of shortcomings, as it will be discussed in more detail later on in section 5.1.

From a comparison of the surface resistivity and the step resistivity, the following relation is obtained, which is visualized in Fig. 4.8: The resistance of one step (per unit length) corresponds to the resistance of a segment of the step-free Si(111)-(7×7) surface (per unit length) of a width of $300\,\mathrm{nm}$. For the sample with a step density of $14\,\mathrm{steps}/\mu\mathrm{m}$, the contribution of the step resistance to the total resistance has a substantial amount of $80\,\%$ for a current flowing in the perpendicular direction. In general, the presence of steps will reduce the surface conductivity of the Si(111)-(7×7) considerably, however, in a well predictable manner.

4.4. Influence of substrate properties

In this section, it is investigated, in which way the the substrate properties can influence the surface conductivity of the 7×7 reconstruction. For this purpose, both the doping concentration and character is varied, as well as the miscut angle which lead to a different amount of step edges of the substrate. Additional four-point resistance measurements are performed on these different Si(111) substrates in order to verify the values for the surface and step conductivities of Si(111)-(7×7) obtained before. Furthermore, the consequences of an increased density of surface defects in the 7×7 structure on its conductivity are investigated.

4.4.1. Variation of concentration and type of doping in Si(111)

In a first step, several Si(111) substrates with different type and concentration of doping are used, as shown in the following sections.

4.4.1.1. n-doped Si(111)

On differently n-doped Si(111)-(7×7) samples with bulk resistivities ranging over two orders of magnitude, further four-point resistance measurements in the linear probe configuration are carried out The results for the non-equidistant probe spacing with $x \leq 50\,\mu\mathrm{m}$ and $s = 50\,\mu\mathrm{m}$, as well as the equidistant spacing with distances $x = s \geq 50\,\mu\mathrm{m}$ are shown in Fig. 4.9 for three different Si(111) samples with resistivities of (a) $20\,\Omega\,\mathrm{cm}$, (b) $2000\,\Omega\,\mathrm{cm}$ and (c) $4100\,\Omega\,\mathrm{cm}$. (The sample preparation and the measurement itself has been performed by *Marcus Blab*, as described in [87]). From the best fits according to the used 3-layer model (solid red line), the surface conductivities for the three different samples can be determined to $\sigma_{(a)} = (4.2 \pm 0.6) \times 10^{-6}\,\mathrm{S}/\square$, $\sigma_{(b)} = (4.7 \pm 0.6) \times 10^{-6}\,\mathrm{S}/\square$ and $\sigma_{(c)} = (5.3 \pm 0.8) \times 10^{-6}\,\mathrm{S}/\square$.

As the measured surface conductivity in the linear configuration is a combination of contributions due to step edges and the step-free surface, these values can differ slightly from each other for the three differently doped Si samples because of slightly different miscut angles of the substrates and resulting different step densities at the surfaces. Neverthe-

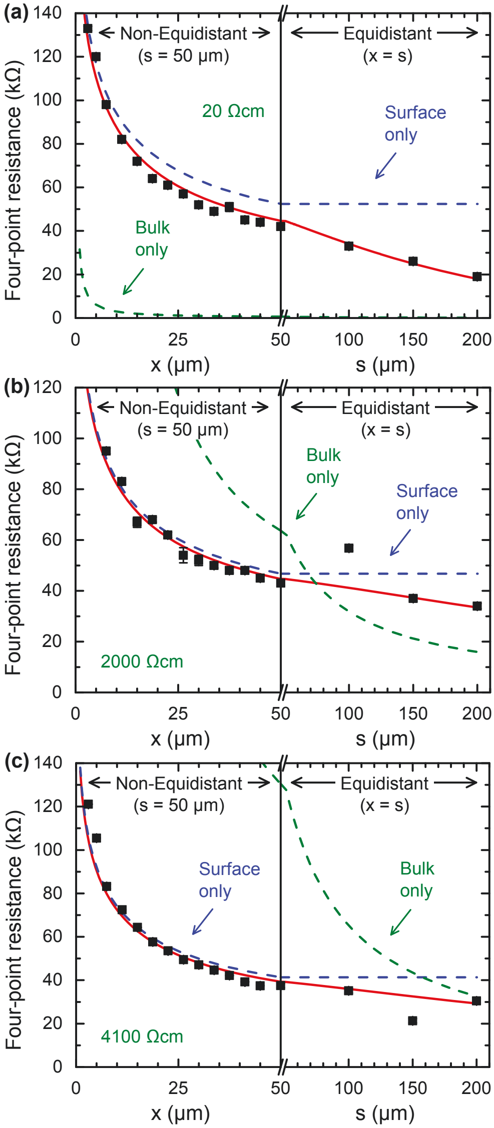

Figure 4.9.: Measured four-point resistances of n-doped Si(111)-(7×7) samples with bulk resistivities of (a) $20\,\Omega\,\mathrm{cm}$, (b) $2000\,\Omega\,\mathrm{cm}$ and (c) $4100\,\Omega\,\mathrm{cm}$ as function of the probe distances s and x for the equidistant configuration as well as the non-equidistant configuration with $s = 50\,\mu\mathrm{m}$. The decreasing four-point resistances in the equidistant region indicate a non-surface contribution to conductance due to bulk and space charge layer. Applying a 3-layer model for transport in the samples yields the solid red lines, which are composed out of the limiting cases [varying contributions from (a) to (c)] of a pure surface conductance (dashed blue line) and a pure bulk conductance (dashed green line). (Sample preparation and measurement have been performed by *Marcus Blab* [87]).

less, all obtained surface conductivities (including the $700\,\Omega\,\mathrm{cm}$ sample discussed before with $\sigma_{\mathrm{2D}} = (5.1 \pm 0.7) \times 10^{-6}\,\mathrm{S}/\square$) are very close to each other and still compatible within the error tolerances indicating that the step contributions are similar for all samples ($\sim 14\,\mathrm{steps}/\mu\mathrm{m}$).

By comparing the measured data to the two limiting cases of a pure 2D conductivity (with the above values) and a pure 3D conductivity arising only from the bulk, which are both shown as dashed blue and green lines in Fig. 4.9, respectively, one can see that the observed resistance behavior for $x \leq 50\,\mu\mathrm{m}$ is very close to the 2D case for all of the three differently doped Si(111) samples, although the bulk resistance varies over several orders of magnitude. This indicates a separation of the surface layer from the bulk arising from the space charge region with low conductivity due to a depletion zone preventing an enhanced charge transport through the bulk, which especially becomes important for high bulk doping concentrations. For larger probe distances, the measured four-point resistance increasingly deviates from the 2D case and shows a pronounced non-surface contribution resulting from additional charge transport through space charge layer and bulk. This non-surface contribution decreases for lower bulk doping levels, as it is expected in comparison with the large increase in bulk resistance in the limiting case of a pure 3D conductivity. Within the 3-layer model, the space charge region is approximated by one intermediate layer with thicknesses of (a) $0.9\,\mu\mathrm{m}$, (b) $4.8\,\mu\mathrm{m}$ and (c) $5.3\,\mu\mathrm{m}$, and with constant conductivities of (a) $1.5 \times 10^{-4}\,\mathrm{S/m}$, (b) $1.8 \times 10^{-4}\,\mathrm{S/m}$ and (c) $3.2 \times 10^{-4}\,\mathrm{S/m}$, respectively, for the three differently doped samples in Figs. 4.9(a) – 4.9(c).

4.4.1.2. p-doped Si(111)

A similar four-point measurements has been performed on a p-doped Si(111)-(7×7) sample with a bulk resistivity of $22.5\,\mathrm{k}\Omega\,\mathrm{cm}$, as it is shown in Fig. 4.10(a). The advantage of a p-doped substrate is that additional p-type doping due to the preparation process [90–93], as discussed before, has not such a strong effect on the doping profile in the space charge region than it is the case for an n-type substrate, where an unexpected near-surface inversion layer may arise. So, the space charge region in the p-type sample can be much better modelled and, as it is depicted in Fig. 4.10(b), a conductivity profile for the near-surface region (red curve) can be obtained from the calculated band bending [inset of Fig. 4.10(b)], which uses specific material parameters as input, e.g. bulk resistivity and Fermi level pinning at the surface. A more detailed overview about the calculation and usage of such conductivity profiles will be given in the next chapter 5. In order to describe the space charge layer with a fixed width and conductivity, as it is necessary for the 3-layer model, the strongly z-dependent profile can be approximated in first order by a single step ($1.3 \times 10^{-3}\,\mathrm{S/m}$, width $22\,\mu\mathrm{m}$), as indicated by the green line in Fig. 4.10(b).[2] These two values can then be used as input for the 3-layer model in order to obtain only the surface conductivity from a fit to the data. This is a conceptual difference compared to the case of the n-type samples

---

[2] As such a approximation seems quite rough, the same measurement data will be evaluated again with the N-layer model in section 5.4.3, in order to reveal, if a more accurate description of the space charge region increases the precision of the obtained surface conductivity.

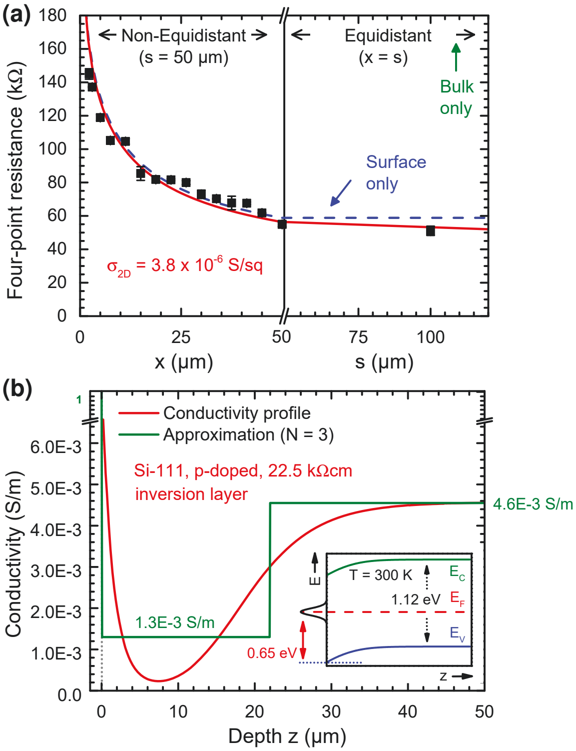

Figure 4.10.: (a) Four-point resistance of Si(111)-(7×7) measured on a p-type Si(111) substrate ($22.5\,\mathrm{k\Omega\,cm}$). A fit (red line) according to the 3-layer model results in a surface conductivity of $\sigma_{2\mathrm{D}} = (3.8 \pm 0.3) \times 10^{-6}\,\mathrm{S}/\square$, with the limiting case of pure 2D conductance as major contribution (dashed blue line), while the contribution of the bulk is only marginal (green arrow). For the fit, the space charge region enters with fixed values ($1.3 \times 10^{-3}\,\mathrm{S/m}$, layer width $22\,\mu\mathrm{m}$), as deduced from the calculation in (b). (b) Calculated conductivity profile of the space charge region (red curve) and approximation by a single layer (green curve). The corresponding near-surface band bending [valence band E_V (blue), conduction band E_C (green), Fermi energy E_F (red), band gap $1.12\,\mathrm{eV}$] of the p-doped Si(111)-(7×7) due to the Fermi level pinning of the 7×7 states at the surface ($0.65\,\mathrm{eV}$ above E_V) is shown in the inset.

depicted before in the Figs. 4.3 and 4.9, where both the conductivities of the space charge layer as well as the surface are fit parameters.

From the fit (red line) shown in Fig. 4.10(a) it is visible that with the calculated parameters of the space charge region the data can be described very well. A value of $\sigma_{2\mathrm{D}} = (3.8 \pm 0.3) \times 10^{-6}\,\mathrm{S}/\square$ is obtained for the Si(111)-(7×7), which is very close to the values on the n-type samples measured before, but slightly smaller. It is visible that the major contribution is resulting from the pure 2D surface conductance (dashed blue line), while the contribution originating from the bulk (green arrow) is only very marginal. A STM measurement of the surface in Figs. 4.11(a) and 4.11(c) reveals that the substrate

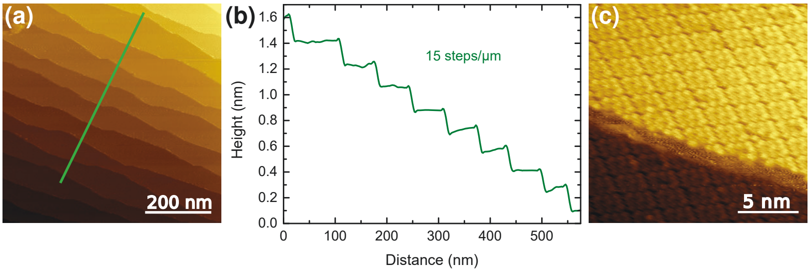

Figure 4.11.: STM images of the p-type Si(111)-(7×7) sample measured in Fig. 4.10. (a) Steps of the Si(111) substrate underneath the 7×7 structure ($U = -1.3\,\mathrm{V}$, $I = 610\,\mathrm{pA}$). (b) Height profile as indicated in (a), which reveals the average atomic step density as $\sim 15\,\mathrm{steps}/\mu\mathrm{m}$. (c) 7×7 structure present on the terraces ($U = 1.4\,\mathrm{V}$, $I = 770\,\mathrm{pA}$).

below the 7×7 reconstruction exhibits on average a step density of $\sim 15\,\mathrm{steps}/\mu\mathrm{m}$, as indicated by the profile in Fig. 4.11(b), which is approximately $7\,\%$ higher than for the n-type substrates before. So, as the measured surface conductivity is a composition of the conductivities of the steps and the step-free terraces, as discussed in section 4.3 before, also a slightly reduced value is expected in the present case. In order to verify this, a simple calculation can be performed by using the relations given in the Eqs. (4.19) and (4.20). With the conductivities for a single step and the step-free terrace obtained before ($\sigma_{\mathrm{surf}} = (9 \pm 2) \times 10^{-6}\,\mathrm{S}/\square$, $\sigma_{\mathrm{step}} = (29 \pm 9)\,\mathrm{S/m}$), in combination with the step density of the p-doped substrate ($\varrho_{\mathrm{step}} = 15\,\mu\mathrm{m}^{-1}$), the expected value for the surface conductivity can be calculated as

$$\sigma_{2\mathrm{D}}^{\mathrm{theo}} = \sqrt{\sigma^{\parallel}\sigma^{\perp}} \overset{(4.19)}{\underset{}{\overset{(4.20)}{=}}} \sqrt{\frac{\sigma_{\mathrm{surf}}}{\frac{1}{\sigma_{\mathrm{surf}}} + \frac{\varrho_{\mathrm{step}}}{\sigma_{\mathrm{step}}}}} = 3.78 \times 10^{-6}\,\mathrm{S}/\square. \tag{4.21}$$

This value is identical to the conductivity actually measured in Fig. 4.10(a), which proves that the slightly reduced surface conductivity is indeed originating from an increased number of substrate steps.

4.4.2. Increased step density of Si(111)

While the effect of the steps observed before in Fig. 4.10 was rather small, a stronger increase in the step density can lead to a more significant reduction of the surface conductivity, as the atomic steps contribute by $80\,\%$ to the total resistance. This is observable in Fig. 4.12(a), which shows a similar measurement of the Si(111)-(7×7) as in Fig. 4.9, but now for an n-type Si(111) substrate (bulk resistivity $5\,\Omega\,\mathrm{cm}$) with a larger miscut angle of $0.5°$. As visible from STM measurements shown in Figs. 4.12(b) and 4.12(c), underneath the closed 7×7 reconstruction the substrate exhibits an average atomic step density of $\sim 29.5\,\mathrm{steps}/\mu\mathrm{m}$.[3] Accordingly, the surface conductivity obtained in Fig. 4.12(a) is

---

[3] Steps with double (multiple) height of one bilayer are considered as two (or more) atomic steps.

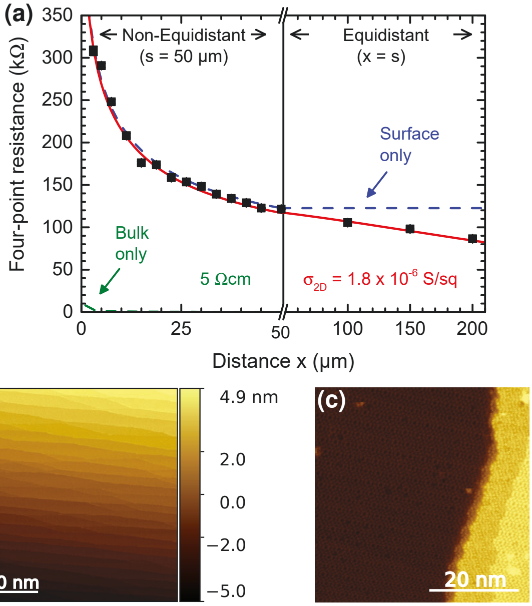

Figure 4.12.: (a) Measured four-point resistance of an n-doped Si(111)-(7×7) sample (bulk resistivity $5\,\Omega\,\mathrm{cm}$) as function of the probe distances s (equidistant configuration) and x (non-equidistant configuration) with $s = 50\,\mu\mathrm{m}$ (similar to Fig. 4.9). A fit by the 3-layer model (red line) results in $\sigma_{2\mathrm{D}} = (1.8 \pm 0.1) \times 10^{-6}\,\mathrm{S}/\square$ (SCL: $5\,\mu\mathrm{m}$, $7 \times 10^{-5}\,\mathrm{S/m}$) with major contribution from the 2D surface (blue line) for small distances, while the bulk (arrow to green line) contributes for larger distances. (b),(c) STM images of the Si(111)-(7×7) surface measured in (a) [(b) $U = -1.2\,\mathrm{V}$, $I = 75\,\mathrm{pA}$, (c) $U = -1.4\,\mathrm{V}$, $I = 100\,\mathrm{pA}$]. The substrate step density is increased to $29.5\,\mathrm{steps}/\mu\mathrm{m}$ [visible in (b)]. On the terraces a closed 7×7-reconstruction is present [visible in (c)].

with $\sigma_{2\mathrm{D}} = (1.8 \pm 0.1) \times 10^{-6}\,\mathrm{S}/\square$ by a factor of ~ 3 reduced compared to the values measured in Fig. 4.9 before. This is very close to the expected value ($2.5 \times 10^{-6}\,\mathrm{S}/\square$) resulting from Eq. (4.21).

A more direct way to reveal the effect of the steps is to use the rotational square method, i.e. to perform angle-dependent four-point measurements with the square tip configuration, as it is depicted in Fig. 4.13. The tip setup is shown in the Figs. 4.13(a) – 4.13(c) and the direction of the substrate step edges with respect to the tip arrangement is visualized by the STM image in Fig. 4.13(a) [not to scale]. In order to prove that all steps are indeed uniformly distributed as stated above, i.e. no step bunching occurs, the complete distance along one side of the square, i.e. $50\,\mu\mathrm{m}$, has been imaged by subsequently recorded STM scans. The composed large-size image containing all of these scans shows equally sized terraces confirming the average density of $29.5\,\mathrm{steps}/\mu\mathrm{m}$ and can be found in Fig. B.1 in the appendix B. From a fit according to Eq. (4.18) to the data in Fig. 4.13(d), the two conductivity components can be obtained as $\sigma^{\parallel} = (7.4 \pm 1.2) \times 10^{-6}\,\mathrm{S}/\square$ and $\sigma^{\perp} =$

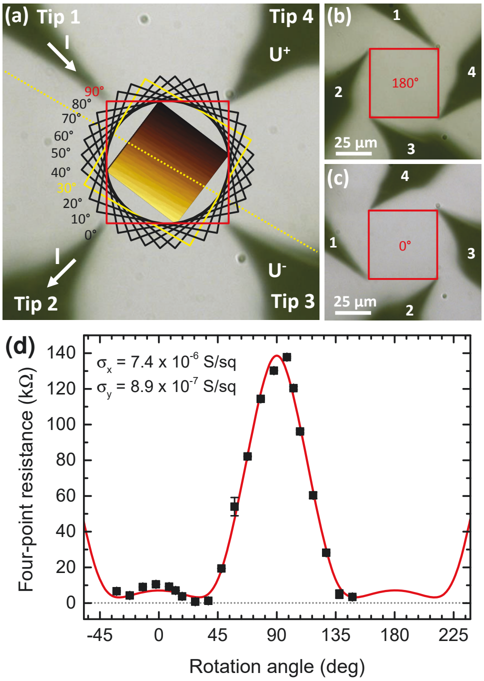

Figure 4.13.: Four-point measurement according to the rotational square method on the Si(111)-(7×7) sample depicted in Fig. 4.12. (a) – (c) Optical microscope images of the four tips positioned at the corners of a square (side length 50 μm). Current and voltage probes are chosen as indicated. A total rotation of 180° is performed with the tips (starting and final points indicated in (b) and (c), respectively) with multiple steps of 10° inside [rotated squares in (a)]. The direction of the step edges with respect to the tip arrangement is visualized by the STM scan (yellow line) in (a) [not to scale]. (d) Measured angle-dependent four point resistance. A fit (red line) according to Eq. (4.18) reveals the two conductivity components $\sigma^{\parallel} = (7.4 \pm 1.2) \times 10^{-6}\,\mathrm{S}/\square$ and $\sigma^{\perp} = (8.9 \pm 0.8) \times 10^{-7}\,\mathrm{S}/\square$. [Note that the angle scale in (d) is shifted with respect to the values indicated in (a). The yellow line in (a) corresponds to the maximum position in (d)].

$(8.9 \pm 0.8) \times 10^{-7}\,\mathrm{S}/\square$. It is directly visible that $\sigma^{\parallel}$ is very close to the value for the step-free terrace obtained before in Fig. 4.7, while $\sigma^{\perp}$ which includes the step contributions, is decreased by a factor of ~ 2 in the present case, as it is expected from Eq. (4.20) for the actual $\sigma^{\parallel}$ and an approximate doubling of the step density compared to Fig. 4.7.

4.4.3. Increased defect density of 7×7 reconstruction

Finally, the influence on the surface conductivity caused by defects in the 7×7 reconstruction should be revealed. As already seen in Figs. 4.1(b) and 4.1(c) in section 4.1.2, there can appear some spots, where the surface is not ideally reconstructed, i.e. holes in the lattice of the 7×7 reconstruction are present, although with a small fraction in the depicted case. For example, such defects can be caused by a too rapid quenching of the Si(111) sample during the preparation of the 7×7 structure, as in this case the time at the transition temperature is not sufficient to achieve a fully reconstructed surface. Nevertheless, for a properly prepared sample, as described in section 4.1.2, in principle the amount of such defects should be negligible small, which can be also proved by STM on the current surface under study. However, if it happens that the density of such surface defects is increased significantly, also an effect on the conductivity of the 7×7 surface may be expected. A simple picture would be that for a very large amount of holes in the reconstruction only very few closed current paths exist, so that the conductivity is substantially reduced. In turn, this means that for conductivity measurements in general also the quality of the surface reconstruction has to be revealed. It has always to be taken into account, besides the step density of the substrate, as discussed before, if it is intended to determine a specific conductivity value characterizing the reconstruction under study.

For the four-point measurements on a defective Si(111)-(7×7), a similar p-doped Si(111) substrate as in Fig. 4.10 is used ($22.5\,\mathrm{k\Omega\,cm}$) with a fresh prepared 7×7 structure, whereby the defects have been introduced accidentally during the preparation process. Subsequently, STM measurements have been performed, as shown in Fig. 4.14. In Fig. 4.14(a), the 7×7 reconstruction is resolved exhibiting a quite large amount of holes in the reconstructed surface and several adsorbates. The fraction of holes compared to the total surface can be estimated to be $11.5\,\%$, while the adsorbates cover $0.8\,\%$ of the surface, both implying that in total only $87.7\,\%$ of the reconstruction is intact. The step density of the substrate, as visible in Fig. 4.14(b), is slightly higher compared to the one in Fig. 4.10 before, and it can be determined on average to $19\,\mathrm{steps}/\mu\mathrm{m}$, as indicated by the height profile in Fig. 4.14(c).

In Fig. 4.15, four-point resistance measurements have been performed on the sample depicted in Fig. 4.14, both by using the linear method [Fig. 4.15(a)] as well as the rotational square method [Fig. 4.15(b)]. A fit according to the 3-layer model applied to the data in Fig. 4.15(a) reveals a surface conductivity of $\sigma_{2\mathrm{D}} = (6.1 \pm 0.4) \times 10^{-7}\,\mathrm{S}/\square$. For the fit,

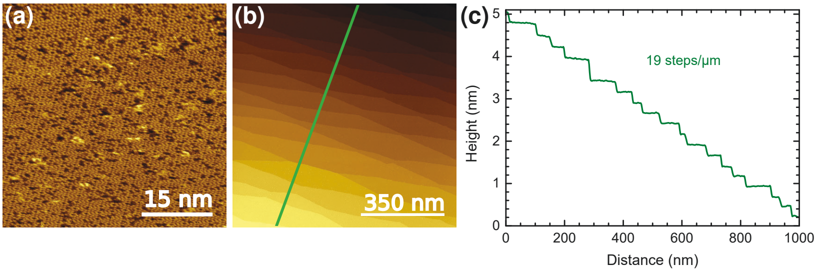

Figure 4.14.: STM images of the defective p-type Si(111)-(7×7) sample measured in Fig. 4.15. (a) Resolved defective 7×7 reconstruction exhibiting $11.5\,\%$ holes and $0.8\,\%$ covered by adsorbates. ($U = -1.2\,\mathrm{V}$, $I = 790\,\mathrm{pA}$). (b) Step edges of the Si(111) substrate ($U = -1.9\,\mathrm{V}$, $I = 120\,\mathrm{pA}$) (c) Height profile as indicated in (b) which reveals an average atomic step density of $19\,\mathrm{steps}/\mu\mathrm{m}$.

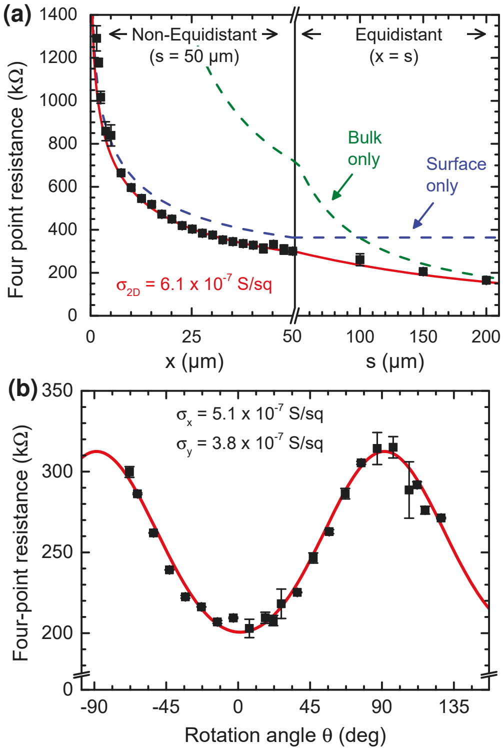

Figure 4.15.: Four-point resistance for the defective p-type Si(111)-(7×7) sample ($22.5\,\mathrm{k\Omega\,cm}$) depicted in Fig. 4.14, measured (a) by the linear distance-dependent method as function of the probe distances s and x, and (b) by the rotational square method as function of rotation angle Θ. (a) A fit according to the 3-layer model (red line) exhibits contributions from both the pure 3D case (green line) and the pure 2D case (blue line), as indicated, and results in a surface conductivity of $\sigma_{\mathrm{2D}} = (6.1 \pm 0.4) \times 10^{-7}\,\mathrm{S}/\square$. For the fit, the space charge region is described by values ($1.2 \times 10^{-3}\,\mathrm{S/m}$, width $22\,\mu\mathrm{m}$) originating from the calculation in Fig. 4.10(b). (b) A fit according to Eq. 4.18 (red line) reveals the two conductivity components as $\sigma^{\parallel} = (5.1 \pm 0.2) \times 10^{-7}\,\mathrm{S}/\square$ and $\sigma^{\perp} = (3.8 \pm 0.1) \times 10^{-7}\,\mathrm{S}/\square$.

the calculation of the space charge region depicted in Fig. 4.10(b) is again used as input ($1.2 \times 10^{-3}\,\mathrm{S/m}$, width $22\,\mu\mathrm{m}$), as in the present case the p-type substrate exhibits the same dopant concentration as before. It is observable that a substantial contribution from the bulk (green line) appears, resulting in a deviation from the pure 2D behavior (blue line) also for small tip distances. This is caused by the reduced value of the surface conductivity which is approximately one order of magnitude smaller, when compared to the results obtained before for samples with a similar step density, as in Figs. 4.4, 4.9 and 4.10. Therefore, the steps can be excluded as a reason for the reduced value, which implies that the surface itself is less conductive, e.g. due to the defects. This can be further proven by the angle-dependent measurement in Fig. 4.15(b) which allows to disentangle the surface from the steps, and reveals from a fit [Eq. (4.18)] the two conductivity components as $\sigma^{\parallel} = (5.1 \pm 0.2) \times 10^{-7}\,\mathrm{S}/\square$ and $\sigma^{\perp} = (3.8 \pm 0.1) \times 10^{-7}\,\mathrm{S}/\square$. It can be seen that the value for $\sigma^{\parallel}$ is at least by a factor of 15 smaller than the results obtained before in Figs. 4.7 and 4.13. As $\sigma^{\parallel}$ describes only the step-free terrace, it is reasonable to conclude that the observed reduction in conductivity is indeed caused by the enhanced amount of defects in the $7{\times}7$ reconstruction. In order to further verify that only the properties of the step-free surface are changed, the step resistance can be recalculated by using additionally $\sigma^{\perp}$ and the step density ϱ_{step}. It results that

$$\sigma_{\mathrm{step}}^{\mathrm{theo}} \overset{(4.20)}{=} \frac{\varrho_{\mathrm{step}}}{\frac{1}{\sigma^{\perp}} - \frac{1}{\sigma^{\parallel}}} = (28.3 \pm 4.4)\,\mathrm{S/m} \tag{4.22}$$

which is identical to the step resistance determined before in section 4.3.

So, it can be concluded that the appearance of defects in the $7{\times}7$ reconstruction implies a substantial reduction of the surface conductivity. In the present case, it has been revealed that for an amount of only approximately $12\,\%$ defects on the surface, the two-dimensional conductivity is reduced by more than one order of magnitude, i.e. down to $\sigma_{\mathrm{Si-7x7}}^{12\,\%\,\mathrm{def.}} = (5.1 \pm 0.2) \times 10^{-7}\,\mathrm{S}/\square$ for the step-free terraces. From a general point of view, it is therefore important to ensure a good quality of the reconstruction under study in order to obtain reliable conductivity values, as a defective surface may lead to an substantially underestimated conductivity.

4.5. Summary

In this chapter, four-point resistance measurements based on a linear distance-dependent tip setup have been combined with an analytically derived 3-layer conductance model, in order to disentangle the surface conductivity on Si(111)-(7×7) surfaces from non-surface contributions which are caused by the conductivity of the bulk and the space charge region. The influence of atomic surface steps has been obtained by measurements using the angle-dependent rotational square setup, which results in a step-free surface conductivity of $\sigma_{\mathrm{surf}}^{\mathrm{Si-7\times7}} = (9 \pm 2) \times 10^{-6}\,\mathrm{S}/\square$ and in a atomic step conductivity of $\sigma_{\mathrm{step}}^{\mathrm{Si-7\times7}} = (29 \pm 9)\,\mathrm{S/m}$ for the Si(111)-(7×7) surface. Furthermore, it has been revealed that the type and concentration of dopants of the Si(111) substrates do not influence the surface conductivity of the $7{\times}7$ reconstruction, as it is expected. However, if the step density on top of the substrate is increased due to a larger miscut angle, the total conductivity of the surface which is a combination between step and terrace conductivity along the current path, is substantially reduced, as the steps contribute by $80\,\%$ to the total resistance. A poor quality of the $7{\times}7$ reconstruction due to an enhanced amount of surface defects, i.e. holes and adsorbates, can instantly reduce the conductivity of the step-free terrace. It has been revealed that for approximately $12\,\%$ defects on the surface, the terrace conductivity of Si(111)-(7×7) is reduced by one order of magnitude. The combined approach presented here for the investigation of Si(111)-(7×7) comprises two quite generic measurement methods, and thus, can be applied easily to various other systems with mixed

2D-3D conduction channels, in order to allow for a determination of the corresponding surface and step conductivities.

The results of this chapter, more specifically mainly from sections 4.1.3, 4.1.4 and 4.3, are largely published in Ref. [103].

5. Analytical N-Layer conductance model

In the previous chapter, it has been demonstrated that measurement data in the presence of multiple conducting channels can be successfully described by a 3-layer model. However, especially for the case of semiconductors this implies that only one layer is available for modelling the space charge region which might not be very precise in general. In fact, it is particularly the space charge region, which significantly governs the current injection between surface and bulk channel, as it will be shown in this chapter. This motivates the extension of the 3-layer model to a more generic model comprising N layers. In the following, such an N-layer model for charge transport close to a surface is derived in analogy to the formalism of the 3-layer model presented before. Moreover, the applicability of the N-layer model is demonstrated by evaluating data from distance-dependent four-point measurements of multiple semiconductors in combination with a calculation of the near-surface band bending, in order to extract values for the surface conductivities.

5.1. The problem of separating conduction channels

As already motivated in the previous chapter, the separation of parallel conduction channels is a relevant task in the field of modern electronic devices. Due to the progressive downscaling the surface-to-volume ratio increases continuously and particularly the surface becomes more and more important as an additional conductance channel for charge transport. In order to assess the influence of this surface channel on the device performance or even functionalize the surface itself, a reliable value for the two-dimensional surface conductivity has to be known. However, the determination from electrical four-point measurements is quite a challenging task, as the main difficulty is to disentangle the 2D conductance at the surface from the conductance through other channels, e.g. the bulk and the space charge layer.

Often indirect measurement methods are used for the separation of the 2D conductance at the surface, but these methods have special requirements on the material and the preparation of the sample under study. For example, one method for separating the surface conductivity is based on the comparison of measurements before and after quenching the surface states by adsorption of atoms or molecules [23, 79, 104–106]. The adsorption species has to be chosen specifically for the material under study and for the quenched system several conditions have to be carefully confirmed. First, all of the surface states have to be quenched and, secondly, the conductivity of the near-surface space charge region has to

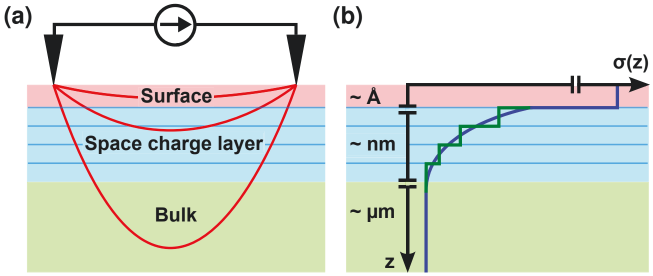

Figure 5.1.: Basic principle of the N-layer model for describing regions of different conductivity along the z-direction by a layered structure with a constant conductivity in each layer. (a) Arrangement of layers for a sample with a surface channel (red), a space charge region (blue) and a bulk (green). An injected current distributes along several current paths (red lines), in dependence of the conductivities of the different regions. (b) Conductivity profile $\sigma(z)$ for the structure in (a). Based on initial calculations of the space charge region, the strong z-dependent conductivity (blue line) can be approximated by a step function (green line), while the values for surface and bulk remains as free parameter to be determined by a fit to measurement data.

remain unchanged under the influence of the adsorbed surface layer. Thirdly, no additional surface conductance has to be induced by the adsorbed layer. If one of these conditions is not fulfilled, the experiments based on the difference method can result in underestimated values for the surface conductivity.

So, it turns out that these indirect methods are not very reliable. Instead of modifying the measurement itself, i.e. perform a special preparation of the sample, it is much more desirable to have a pure evaluation method, which allows to separate the conduction channels inside a sample from standard (distance-dependent) four-point measurements obtained on the surface. For this reason, here a generic multi-layer conductance model (N-layer model) is presented, which is free of any measurement-related requirements. It allows for modelling the measured four-point resistances on samples with regions of different conductivity along their z-axis. For example, such different regions can be attributed to a surface channel, a space charge region caused by a near-surface band bending and a semi-infinite bulk. By using the N-layer model these regions are approximated by a N-layered structure with a fixed conductivity in each layer, as it is schematically shown in Figs. 5.1(a) and 5.1(b). No special sample preparation is necessary and the model can directly be applied to the raw data of standard distance-dependent four-point measurements. Thus, in combination with the knowledge about the conductivity profile in the space charge region [Fig. 5.1(b)] which can be gained easily for semiconductors by a calculation of the near-surface band bending, this permits to directly extract a value for the surface conductivity of the specific sample under study.

In the following section 5.2, several methods are discussed which are based mainly on a 2-layer structure and are intended to model measurements for mixed 2D-3D conduction channels. Moreover, the shortcomings of such 2-layer models are pointed out by emphasizing the significant influence of the space charge region on the current transport, which is visualized by examples for the current distribution and the ratio of surface current. Secondly, in section 5.3 the formalism of the analytical N-layer model is presented. In section 5.4, the application of the N-layer model is demonstrated by means of distance-dependent four-point measurements obtained with a multi-tip STM. For this purpose, several sets of data obtained from the literature for the semiconductors Ge(100)-(2×1) and Si(100)-(2×1) with different types and concentrations of doping are used, as well as direct measurements on p-doped Si(111)-(7×7). From the N-layer model, values for the surface conductivities of these materials are determined.

5.2. Composed 2D-3D conduction channels

A composed 2D-3D conduction channel, for example, arises from a combination of a conductive surface on top of a conducting bulk material. The insufficiency of a description by 2-layer structures is unapparent at first glance, and therefore, will be specifically emphasized in the following.

5.2.1. Methods for approximating parallel channels

For pure 2D or pure 3D charge transport, analytic relations between the four-point resistance and the conductivity exist (cf. chapter 3), e.g. for the equidistant probe setup

$$R_{\text{lin}}^{\text{2D}} = \frac{\ln(2)}{\pi\sigma_{2D}} \qquad \text{and} \qquad R_{\text{lin}}^{\text{3D}} = \frac{1}{2\pi\sigma_{3D}}\, s^{-1}. \tag{5.1}$$

However, if a sample simultaneously consists of both channels, these two equations cannot be applied any more.

For this purpose, often a simple approximation by a parallel-circuit consisting of the four-point resistance of the surface and the bulk, e.g. according to Eq. (5.1) is used, i.e. [62,107]

$$R_{\parallel}(s) = \left(\frac{1}{R_{\text{lin}}^{\text{2D}}} + \frac{1}{R_{\text{lin}}^{\text{3D}}(s)} \right)^{-1}. \tag{5.2}$$

Nevertheless, such an approach is very limited and has several shortcomings. In the parallel-circuit model a complete separation of the surface channel and the bulk is assumed. Apart from the injection points, no transition of the injected current between surface and bulk can occur, e.g. as in most cases also present immediately around the contacts. The splitting of the current only takes place exactly at the injection points and depends on the ratio of the four-point resistances of the two individual layers. However, the two-point resistance, and not the four-point resistance, should determine which amount of current flows through the surface channel and which part through the bulk [27]. Therefore, the exact current path through the sample can depend also on details of the injection, e.g. the contact diameter, which are not included in the parallel-circuit model. The most important point, however, is the fact that in the approximation of the parallel-circuit model the current is injected equally into the surface channel and the bulk, and any influence of a possible near-surface space charge region, which particularly exists in semiconductors, is neglected. But especially this space charge region has a significant influence on the charge transport through the sample, as it will be discussed in detail in the next section 5.2.2. Thus, it can be expected that significant deviations appear, when the parallel-circuit model is compared, for example, to a 3-layer model, as it will be demonstrated also in the next section.

A different approach presented in Ref. [31] uses an approximation for the surface current to solve the current continuity equations for 2D and 3D resulting in a combination of both 2D and 3D conduction channels. This approach removes the artificial separation between surface and bulk and uses a real injection geometry with extended tips, but it takes only into account a two-layer structure consisting of the surface and the bulk, so that the results are very similar to the parallel-circuit model. Any additional conductivity distribution between the surface and the bulk caused by a space charge region is neglected, which is also the major restriction in the parallel-circuit model. For this reason, the model can only be applied, if no near-surface band bending occurs and a sharp transition between surface and bulk exists.

Another approach published in Ref. [108] attempts to describe the deviation from a pure 3D conductance behavior caused by an additional 2D channel with an expansion of distance-dependent terms, and introduces an effective conductivity consisting of the bulk conductivity and a value for the deviation from the pure 3D case. However, although this model may also be able to treat deviations caused by a near-surface space charge region, it is not suitable to determine a value for the surface conductivity, as the deviations from the pure 3D conductance are only indicated by one numerical value, which cannot be easily interpreted as a physical quantity.

In Ref. [61] a computational method is described using no longer an analytical model for the four-point resistance but a finite element calculation for approximating the different conduction channels in the sample. In this case, also the near-surface space charge layer between the surface channel and the 3D bulk can be taken into account. However, as the surface channel has only a depth of several Å, while the space charge layer may be extended up to several μm, very different length scales are involved, so that the finite element calculation of the complete sample geometry can be very sophisticated and computationally time consuming.

5.2.2. Role of the space charge region

The best way to point out the significant role of the space charge region, which is especially important for semiconductors, and the limited applicability of a two-layer model, like the parallel-circuit model, is a comparison of the four-point resistance with the lowest N-layer model including the influence of the space charge region, i.e. the 3-layer model which was discussed in the previous chapter 4. Apart from the surface layer and the bulk region the 3-layer model uses only one additional layer to approximate the space charge region, but despite this quite rough approximation it is able to describe four-point probe resistance measurements much better than the parallel-circuit model and was successfully applied to determine the surface conductivity of the Si(111)-(7×7) surface, as shown before in section 4.1.4.

5.2.2.1. Insufficiency of 2-layer models

In Fig. 5.2(a) the calculated distance-dependent four-point resistance for the Si(111)-(7×7) surface on an n-doped substrate ($700\,\Omega\,\mathrm{cm}$) is shown (orange line) located between the two limiting cases of pure surface conductance (dotted blue line) and pure bulk conductance (dotted red line). The calculation is based on the 3-layer model with parameters obtained in section 4.1.4, and assumes an equidistant linear tip configuration with a tip spacing s. Using the same parameters for surface and bulk conductivity the four-point resistance expected from the parallel-circuit model according to Eq. (5.2) is plotted as solid black line, which exhibits a very strong deviation from the curve based on the 3-layer model. The major reason for this behavior is the absence of the additional space charge layer between surface and bulk in the parallel-circuit model. In the case of the Si(111)-(7×7) surface on an n-doped Si substrate with $\sigma_B = 0.14\,\mathrm{S/m}$ the ratio between the average conductivity of the space charge region σ_{SC} and the bulk can be estimated as $\sigma_{SC}/\sigma_B = 0.002$ (cf. section 4.1.4). For smaller values of this ratio, the deviation of the 3-layer model from the parallel-circuit model increases and the calculated four-point resistance approaches the 2D case (magenta curve). On the other hand, if the ratio becomes larger, the deviation between the two models decreases (green and blue curves). But only if the ratio σ_{SC}/σ_B is close to 1 (red curve), the deviation between both models is so small, that the parallel-circuit model can be used as approximation without a large error. This error is smallest, if the near-surface space charge region vanishes completely, and in this case the parallel-circuit model is a suitable simple approach to approximate the four-point resistance of a two-layer structure consisting of a 2D and a 3D conduction channel.

5.2.2.2. Surface current

The significant influence of the space charge region can also be deduced from the amount of current I_{surf} flowing through the surface compared to the totally injected current I. Based on the 3-layer model, this ratio can be obtained by

$$\frac{I_{\mathrm{surf}}}{I} = \frac{4\sigma_{\mathrm{surf}}}{I} \int_0^\infty dk\, \frac{\sin\left(\frac{3}{2}ks\right)}{k} \Big[a(k)\left(e^{kz_S}-1\right) - b(k)\left(e^{-kz_S}-1\right)\Big], \tag{5.3}$$

whereby a tip distance of $3s$ between the current injecting tips is assumed and the coefficients $a(k)$ and $b(k)$ are given by Eq. (4.8). A derivation of a more general expression for the total amount of current inside the individual layers [Eq. (A.89)], from which Eq. (5.3) can be obtained specifically for the surface, can be found in the appendix A.2.3. In Fig. 5.2(b), the calculated percentage of the surface current based on Eq. (5.3) is shown in dependence of both the conductivity ratios between space charge layer and bulk σ_{SC}/σ_B, as well as surface and bulk $\sigma_S\, z_S^{-1}/\sigma_B$ (thickness of surface layer $z_S \approx 3\,\text{Å}$). A constant

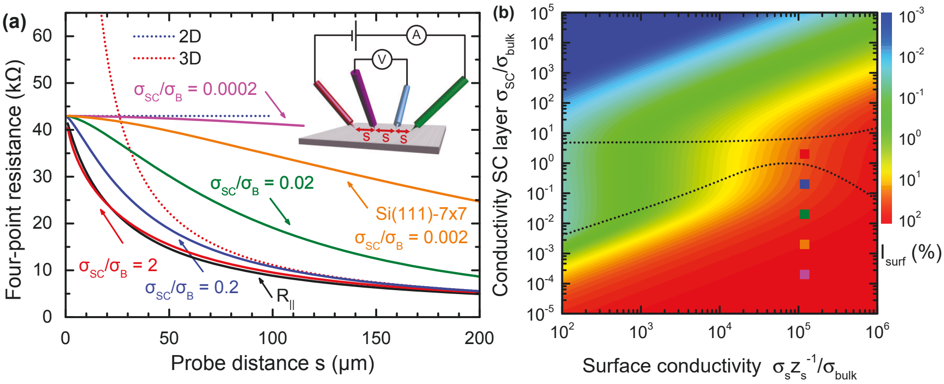

Figure 5.2.: (a) Calculated four-point resistance of the Si(111)-(7 × 7) surface with a bulk conductivity of $\sigma_B = 0.14\,\mathrm{S/m}$ and a surface conductivity of $\sigma_S = 5.14 \times 10^{-6}\,\mathrm{S}/\square$ as a function of the equidistant probe distance s and with the ratio σ_{SC}/σ_B between the conductivities of the space charge layer and the bulk as additional parameter (colored curves). The orange curve located between the two limiting cases of pure 2D and pure 3D conductance (dotted blue and red curves) is based on measurements (cf. section 4.1.4), while the magenta, green, blue and red curves correspond to variations of the ratio σ_{SC}/σ_B over several orders of magnitude. The black curve results from the description by the parallel-circuit model without considering an additional space charge layer between surface and bulk. In the inset, the equidistant linear tip arrangement with the outer current-injecting tips and the inner voltage-measuring tips is shown. (b) Calculated percentage of surface current I_{surf} as function of the ratios $\sigma_S\, z_S^{-1}/\sigma_B$ between the surface conductivity and the bulk ($z_S = 3\,\text{Å}$), and σ_{SC}/σ_B between the conductivity of the space charge layer and the bulk. The colored points correspond to the position of the curves in (a). Inside the region marked by the two dotted lines the parallel-circuit model can be applied for describing the four-point resistance on the surface with an error of less than $10\,\%$.

value of $s = 50\,\mu\mathrm{m}$ for an equidistant four-probe setup is assumed, i.e. the current tips are spaced by $3s = 150\,\mu\mathrm{m}$. The calculation is again based on parameters obtained in section 4.1.4 from the measurement of the Si(111)-(7 × 7) surface.

For a vanishing space charge layer, i.e. $\sigma_{SC}/\sigma_B \approx 1$, the amount of surface current approximately only depends on the ratio $\sigma_S\, z_S^{-1}/\sigma_B$ and increases with an increasing ratio. However, if the influence of the space charge layer becomes larger, i.e. if the ratio σ_{SC}/σ_B deviates from 1, the contour lines in the plot get distorted, so that for large ratios the amount of surface current is reduced and for small ratios enhanced. The reason for this behavior is that the conductivity of the space charge layer controls the current injection into the bulk below. If the near-surface band bending leads to a depletion zone or an inversion zone so that the average conductivity in the space charge region is significantly reduced compared to the bulk, then this region behaves as a blocking region preventing the injected current to flow through the bulk, even if it has a very high conductivity. This results in an enhanced surface domination of charge transport, which cannot be considered in the parallel-circuit model. A direct visualization of the depth-dependent current density inside the sample (cf. Fig. 5.3) makes this fact even more obvious, as it is discussed in the following section 5.2.2.3.

Thus, the parallel-circuit model has only a very limited applicability within a certain range of conductivity parameters, where the space charge region does not play a significant role for the current transport. In Fig. 5.2(b) the dotted lines indicate the region, inside which the parallel-circuit model can be applied to four-point resistance measurements with an error of less than $10\,\%$. Inside this region, the contour lines of the color plot are approximately perpendicular to the x-axis indicating that the surface current is nearly independent of the ratio σ_{SC}/σ_B, which is an essential requirement for the application of the parallel-circuit model. For comparison, the five colored points indicate the positions of the resistance curves from Fig. 5.2(a). Only the red curve, which is very close to the parallel-circuit model, is located inside the dotted region, while the orange curve representing a measurement of the Si(111)-(7 × 7) surface on an n-doped substrate is clearly outside the region.

5.2.2.3. Depth-dependent current density

A more direct way to visualize the significance of the space charge region on the current transport is to plot the depth-dependent current distribution inside the sample. In Fig. 5.3, such a simulated depth-dependent current density according to the 3-layer model is depicted. The absolute value of the in-line component j_x of the current density vector $\boldsymbol{j}(x,y,z)$ is plotted in the xz-plane, i.e. at $y=0$, as function of depth z into the sample and lateral distance x along the tip positioning line. The simulation is based the formalism of the 3-layer model, from which an expression for the current density in x-direction can be derived, as it is shown in the appendix A.2.3. Specifically, for current injecting tips spaced by $3s$, it results from Eq. (A.76) for $|j_x(x,0,z)|$ that

$$\left|j_x(x,0,z)\right| = \sigma(z)\left|\int_0^\infty dk\,\Phi(k,z)k\left(J_1\left(k\left[x+\frac{3}{2}s\right]\right)-J_1\left(k\left[x-\frac{3}{2}s\right]\right)\right)\right| \tag{5.4}$$

with

$$\Phi(k,z)=\begin{cases}a(k)e^{kz}+b(k)e^{-kz}\\ c(k)e^{kz}+d(k)e^{-kz}\\ f(k)e^{-kz}\end{cases}\quad\text{and}\quad \sigma(z)=\begin{cases}\sigma_1 & \text{for } 0\le z\le z_1\\ \sigma_2 & \text{for } z_1\le z\le z_2\\ \sigma_3 & \text{for } z_2\le z\le\infty,\end{cases} \tag{5.5}$$

whereby the coefficients $a(k),\ldots,f(k)$ are defined by Eq. (4.8). The calculation in Fig. 5.3 is based on the same parameters as used before in Fig. 5.2(b), e.g. as $3s = 150\,\mu\mathrm{m}$.

For the first case in Fig. 5.3(a), a very low conducting space charge layer with $\sigma_{SC} \ll \sigma_B$ (thickness $z_{SC} = 2.5\,\mu\mathrm{m}$) is used for the calculation, and the result shows that the majority of the current flows through the surface layer (thickness $z_S = 3\,\text{Å}$), whereas only a very small amount of current is injected through the space charge layer into the bulk. The current density inside the bulk material is one order of magnitude lower than in the case of a vanishing near-surface band bending, where the space charge layer coincides with the bulk ($\sigma_{SC} \approx \sigma_B$), which is depicted in Fig. 5.3(b).

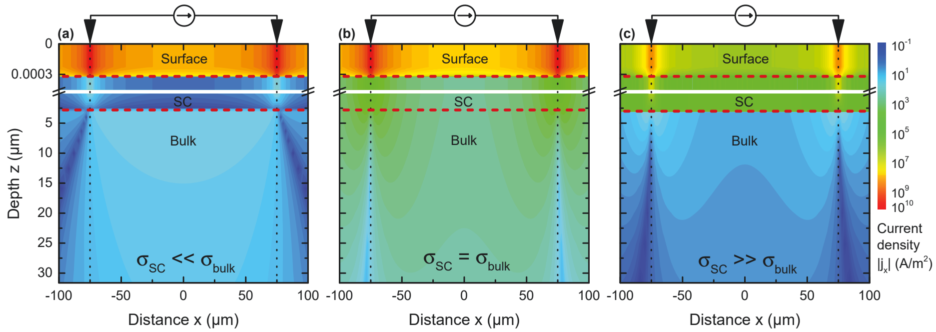

Figure 5.3.: Color plots of the absolute value of the in-line component $|j_x(x, 0, z)|$ of the current density vector $\boldsymbol{j}(\boldsymbol{x})$ in the xz-plane ($y = 0$) as a function of depth z into the sample and lateral distance x along the tip positioning line. The current density is calculated from the 3-layer model for a distance $3s = 150\,\mu\mathrm{m}$ of the current-injecting tips, and for a sample with a bulk conductivity $\sigma_B = 0.14\,\mathrm{S/m}$, a surface conductivity $\sigma_S = 5.14 \times 10^{-6}\,\mathrm{S}/\square$ and an average thickness $z_2 = 2.5\,\mu\mathrm{m}$ of the intermediate space charge layer. The average conductivity of the intermediate space charge layer is varied in the three cases (a) – (c) showing the significant influence of the space charge region on the vertical current distribution in the sample. According to the 3-layer model the red dashed lines indicate the interfaces between the surface, the space charge layer and the bulk. The black dotted vertical lines mark the position of the current-injecting tips on the surface. (a) In the case of a very low conducting space charge layer with $\sigma_{SC} \ll \sigma_B$ ($\sigma_{SC} = 2.5 \times 10^{-4}\,\mathrm{S/m}$) the majority of the current flows through the surface even if the bulk is highly conductive, as the space charge region acts as a blockade for the injection into the bulk and an enhanced 2D transport can be observed. (b) If $\sigma_{SC} = \sigma_B$, there is effectively no space charge region and the current flow through the bulk takes place according to the bulk conductivity. In this case the four-point resistance on the surface can be approximated by the parallel-circuit model. (c) If the space charge layer is highly conductive with $\sigma_{SC} \gg \sigma_B$ ($\sigma_{SC} = 2.5 \times 10^2\,\mathrm{S/m}$), the current flows not only through the surface, but also equally through the space charge layer, while the current in the bulk is again reduced.

On the other hand, if an accumulation zone is formed near the surface with a high conductivity compared to the bulk, this region can act as an additional conductance channel totally surpassing the current flow through the bulk and also reducing the current through the surface states. In this case shown in Fig. 5.3(c), where $\sigma_{SC} \gg \sigma_B$, the current flow through the bulk is again reduced by an order of magnitude, while not only transport through the surface states but also through the space charge region is now preferred equally. As the space charge layer has a finite thickness, the current transport may seem to be purely 2-dimensional for larger probe spacings and the usage of the parallel-circuit model for the four-point resistance on such a system would result in a largely overestimated value for the surface conductivity.

So, it can be concluded that the space charge region is a very important factor for both current injection and current transport inside a sample. Thus, a 2-layer model is in general not sufficient to describe the current transport through the individual conductance channels. Although it results that the 3-layer model is obviously better suitable to describe measurement data over a much broader range of conductivity parameters than the parallel-circuit model, there is still a basic restriction, namely the very rough description of the space charge region by only a single layer. For this reason, it is useful to refine the 3-layer model by introducing more layers, as it will be discussed in the next section.

5.3. Conductance model for *N* layers

Besides surface and bulk channel, the 3-layer model can offer only one remaining layer with a fixed conductivity and thickness in order to describe the space charge region. However, especially for semiconductors which can have a very strong band bending near the surface, this can be a major drawback, as the conductivity profile of the space charge region can exhibit a very strong dependence on the z-position. At latest for the case, when an inversion layer is formed in the near-surface region, the rough approximation by a single layer is not sufficient any more. The near-surface band bending and, thus, the specific conductivity profile in the space charge region can be calculated for semiconductors quite easily based on material parameters, as it will be discussed later on, but a conductance model is needed which can use this information as input. Therefore, in order to allow an approximation of such a conductivity profile by multiple layers, an N-layer model for charge transport is introduced which exhibits a thin surface layer, $N-2$ layers for the near-surface space charge region, and a semi-infinite bulk. In Fig. 5.1, it is visualized schematically, while Fig. 5.4 in the next section shows a more mathematical overview. Such a multi-layer model was first proposed by Schumann and Gardner [99, 109, 110] and primarily applied to the method of spreading resistance measurements [98, 100, 111], but also extended to four-point measurements [101] for determining individual sheet conductivities. However, as far as it is known, it has not yet been used for obtaining the conductivity of surface states of semiconductors in combination with a calculated conductivity profile of the space charge region as input.

A detailed description and mathematical derivation of the N-layer model is shown in the following section 5.3.1. In section 5.3.2 the N-layer model is compared to the 3-layer model in general and the applicability of both models is discussed.

5.3.1. Formalism

The formalism for the N-layer model is very similar to the 3-layer model presented before in section 4.2. Thus, in the following only the principal differences will be highlighted and discussed.

The N-layer model uses a structure as shown in Fig. 5.4 in order to describe the sample properties. It consists of a thin surface layer, multiple intermediate layers and a semi-infinite bulk, all of them characterized by their respective conductivities σ_0, σ_n and σ_{N-1}, and positions of the interfaces z_0 and z_n ($\mathrm{n} = 1, \ldots, N-2$). At the surface a current I is injected by a cylindrical tip with radius r_t. Due to calculation requirements, the surface

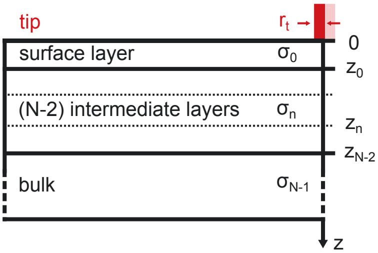

Figure 5.4.: The N-layer model consists of a layered sample structure with N layers described by the conductivities σ_n and the positions of the interfaces z_n ($n = 0, \dots, N-2$), respectively. The first layer 0 and the last layer $N-1$ represent the surface layer and the semi-infinite bulk, respectively. The other layers in between are used to approximate the z-dependent conductivity profile of the space charge region. (It should be noted that all indices are shifted by -1 compared to the 3-layer model.) The current I is injected by a cylindrical tip of radius r_t at the origin on the surface layer.

layer cannot be two-dimensional, so that again a finite thickness of one atomic layer (3 Å) is assumed. In the same way as shown in section 4.2, in order to determine the potential Φ one starts with the Laplace equation

$$\Delta\Phi(\rho, \varphi, z) = 0 \tag{5.6}$$

in cylindrical coordinates. By again considering the angle-independent polar symmetry for one tip, the solution is basically identical to Eq. (4.3), but with the different notation for N individual layers, the set of N equations reads in the present case as

$$\Phi_0(\rho, z) = \int_0^\infty \left[a_0(k)\, e^{kz} + a_1(k)\, e^{-kz}\right] J_0(k\rho)\, dk \tag{5.7a}$$

$$\Phi_n(\rho, z) = \int_0^\infty \left[a_{2n}(k)\, e^{kz} + a_{2n+1}(k)\, e^{-kz}\right] J_0(k\rho)\, dk, \quad n = 1, \dots, N-1 \tag{5.7b}$$

$$\Phi_{N-1}(\rho, z) = \int_0^\infty a_{2N-2}(k)\, e^{-kz}\, J_0(k\rho)\, dk \tag{5.7c}$$

with the $2N-1$ independent coefficients $a_0(k), \dots, a_{2N-2}(k)$ and the *Bessel* function J_0. It should be noted that in comparison to Eq. (4.3) for the 3-layer model all indices are shifted, i.e. starting for the surface layer with *0* and not with *1*. The corresponding $2N-1$ boundary conditions are

$$\sigma_0 \frac{\partial}{\partial z}\Phi_0(\rho, 0) = -j_0\, H(r_t - \rho)\,, \tag{5.8a}$$

$$\sigma_{n-1}\frac{\partial}{\partial z}\Phi_{n-1}(\rho, z_{n-1}) = \sigma_n \frac{\partial}{\partial z}\Phi_n(\rho, z_{n-1})\,, \tag{5.8b}$$

$$\Phi_{n-1}(\rho, z_{n-1}) = \Phi_n(\rho, z_{n-1})\,, \tag{5.8c}$$

$$\sigma_{N-2}\frac{\partial}{\partial z}\Phi_{N-2}(\rho, z_{N-2}) = \sigma_{N-1}\frac{\partial}{\partial z}\Phi_{N-1}(\rho, z_{N-2})\,, \tag{5.8d}$$

$$\Phi_{N-2}(\rho, z_{N-2}) = \Phi_{N-1}(\rho, z_{N-2})\,, \tag{5.8e}$$

which result again from the condition of current injection [Eq. (5.8a)] and continuity of both potential [Eqs. (5.8c), (5.8e)] and current density [Eqs. (5.8b), (5.8d)]. Also, the injected current density is again given by $j_0 = \frac{I}{\pi\, r_t^2}$ (uniform flux condition) for a tip with radius $r_t \approx 25\,\mathrm{nm}$.

In basically the same way, as shown explicitly in section 4.2 for the 3-layer model, a matrix equation determining the coefficients $a_0(k), \ldots, a_{2N-2}(k)$ can be derived from Eqs. (5.8a) – (5.8e), resulting in

$$\begin{pmatrix}
1 & -1 & 0 & 0 & \cdots & \cdots & \cdots & \cdots & 0 \\
 & \mathbf{A}^{0,1} & & 0 & 0 & \cdots & \cdots & \cdots & 0 \\
 & & & 0 & 0 & \cdots & \cdots & \cdots & 0 \\
0 & 0 & & \mathbf{A}^{1,2} & & 0 & 0 & \cdots & \cdots & 0 \\
0 & 0 & & & & 0 & 0 & \cdots & \cdots & 0 \\
\vdots & \vdots & 0 & 0 & \ddots & & 0 & 0 & \cdots & \vdots \\
0 & 0 & 0 & 0 & & & 0 & 0 & \cdots & 0 \\
0 & 0 & \cdots & 0 & 0 & \mathbf{A}^{n-1,n} & & 0 & 0 & 0 \\
0 & 0 & \cdots & 0 & 0 & & & 0 & 0 & 0 \\
0 & 0 & \cdots & \cdots & 0 & 0 & \ddots & & & 0 \\
\vdots & \vdots & \cdots & \cdots & 0 & 0 & & & & 0 \\
0 & 0 & \cdots & \cdots & \cdots & 0 & 0 & & \mathbf{B} & \\
0 & 0 & \cdots & \cdots & \cdots & 0 & 0 & & &
\end{pmatrix}
\cdot
\begin{pmatrix}
a_0(k) \\ a_1(k) \\ a_2(k) \\ a_3(k) \\ a_4(k) \\ \vdots \\ a_{2n-2}(k) \\ a_{2n-1}(k) \\ a_{2n}(k) \\ a_{2n+1}(k) \\ \vdots \\ a_{2N-3}(k) \\ a_{2N-2}(k)
\end{pmatrix}
=
\begin{pmatrix}
I(k,\sigma_0) \\ 0 \\ 0 \\ 0 \\ 0 \\ \vdots \\ 0 \\ 0 \\ 0 \\ 0 \\ \vdots \\ 0 \\ 0
\end{pmatrix} \tag{5.9}$$

with the submatrices

$$\mathbf{A}^{n-1,n} = \begin{pmatrix} \frac{\sigma_{n-1}}{\sigma_n} & -\frac{\sigma_{n-1}}{\sigma_n}\, e^{-2kz_{n-1}} & -1 & e^{-2kz_{n-1}} \\ 1 & e^{-2kz_{n-1}} & -1 & -e^{-2kz_{n-1}} \end{pmatrix} \tag{5.10}$$

and

$$\mathbf{B} = \begin{pmatrix} \frac{\sigma_{N-2}}{\sigma_{N-1}} & -\frac{\sigma_{N-2}}{\sigma_{N-1}}\, e^{-2kz_{N-2}} & e^{-2kz_{N-2}} \\ 1 & e^{-2kz_{N-2}} & -e^{-2kz_{N-2}} \end{pmatrix}, \tag{5.11}$$

and the expression

$$I(k,\sigma_0) = -\frac{j_0}{\sigma_0} \int_0^{r_t} \rho\, J_0(k\rho)\,\mathrm{d}\rho\,. \tag{5.12}$$

Eq. (5.9) can be solved by means of numerical matrix inversion of the $(2N-1) \times (2N-1)$ matrix.

For the potential at the surface, the same considerations apply, as shown before in Eq. (4.10) and Eqs. (4.12) – (4.15) in section 4.2, except that the sum of the coefficients $a(k) + b(k)$ for the 3-layer model has to be replaced by $a_0(k) + a_1(k)$ in the N-layer case. Thus, in analogy to Eq. (4.16), the four-point resistance for a linear equidistant probe setup with spacing s can be expressed in the present case as

$$R_{\mathrm{lin}}^{\mathrm{N-lay}}(s) = \frac{2}{I} \int_0^{\infty} \Big[a_0(k) + a_1(k) \Big] \Big[J_0(ks) - J_0(2ks) \Big] \, dk \,. \tag{5.13}$$

In Eq. (5.13), the numerical matrix inversion for obtaining the coefficients $a_0(k)$ and $a_1(k)$ has to be performed for each single value of k, in order to allow the evaluation of the integral over the Bessel functions. Thus, the calculation can be very time consuming for a large number of layers, especially when the result is fitted to four-point measurement data.

Moreover, the conductivities σ_n and interface positions z_n of all N layers are far too many free parameters for being determined by a single fit. Therefore, the depth-dependent conductivity profile $\sigma_{\mathrm{SCL}}(z)$ of the space charge region has to be calculated before, based on the solution of Poisson's equation using basic material parameters like the Fermi level pinning of the surface states, the band-gap, the effective masses, the mobilities and the bulk doping concentration and type [88]. A more detailed overview about near-surface band bending will be given in the next chapter 6, and particularly, in section 6.4.1 the determination of the z-dependent charge carrier concentrations for the case of a semi-infinite bulk material will be discussed. Based on these results the conductivity profile can be calculated by [88]

$$\sigma_{\mathrm{SCL}}(z) = e\big[\mu_n n(z) + \mu_p p(z)\big] \tag{5.14}$$

with the charger carrier densities $n(z)$ for electrons and $p(z)$ for holes, and the corresponding mobilities μ_n and μ_p, respectively. The approximation of such a conductivity profile $\sigma_{\mathrm{SCL}}(z)$ by a step-like function of $(N-2)$ steps, which is obtained by the condition of a vanishing integrated deviation for each step[1] [cf. insets of Fig. 5.5(a) and 5.5(b)], then determines the values for the parameters $\sigma_1, \ldots, \sigma_{N-2}$ and $z_1, \ldots, z_{N-2}$ as input for the N-layer model.

The thickness of the surface layer z_0 determines the vertical extension of the surface states and can be approximated by the thickness of one atomic layer. However, it turns out that a variation in the range from $1\,\text{Å}$ to $1\,\mathrm{nm}$ does not significantly change the obtained value for the surface conductivity and results only in a small deviation below $1\,\%$. The value for the bulk conductivity σ_{N-1} can be determined by macroscopic resistivity measurements and should be in agreement with the nominal doping concentration. Finally, only one free parameter remains to be determined by a fit to measurement data, which is the surface conductivity σ_0.

The error on σ_0 is obtained from the fitting error in the framework of the N-layer model. As input for the fit, errors for the tip positions, the measured four-point resistance, the calculated conductivity profile for the space charge region and the bulk conductivity are used. As the calculation of the band bending uses several approximations, it is reasonable to assume a larger error on the obtained conductivity profile. However, it shows that even

---

[1] Each step is chosen such that the integrated differences between the step-like function and the conductivity profile (for this specific step) vanish.

a relative error of $50\,\%$ leads only to an error of approximately $5\,\%$ to $15\,\%$ in the surface conductivity. The exact value depends both on the shape of the conductivity profile and on the absolute values for the surface and bulk conductivity. For example, if the current transport is mostly surface or bulk dominated, a large error for the calculated conductivity profile does not have much influence on the obtained surface conductivity value. On the other hand, if the space charge region forms an inversion layer, the exact shape of the conductivity profile is more important, as it controls the current injection into the bulk. Nevertheless, for the conductivity profiles shown in Figs. 5.6 – 5.9, the relative error is assumed to be below $50\,\%$, so that the resulting errors on the surface conductivity fit well in the denoted error limits of the values.

5.3.2. Comparison of 3-layer model and *N*-layer model

If the N-layer model is directly compared to the 3-layer model, the obvious main difference is the more detailed description of the space charge region in the framework of the N-layer model. However, in order to apply the N-layer model, it is necessary to know the exact z-dependence of the conductivity in the space charge layer, as otherwise there are far too many fit parameters, i.e. two for each layer. The z-dependent conductivity profile can be obtained by a calculation using basic material parameters, which are well known for semiconductors. However, if other material systems are studied, these material parameters might not be known exactly and the calculation of the conductivity profile might be difficult or not possible. Also if the preparation method of the sample influences the near-surface doping concentration, the calculated conductivity profile might be not very accurate. In these cases, the N-layer model cannot be used, but a description of the measured four-point resistances by the 3-layer model is still possible, as here the average conductivity and the average width of the space charge region are only two single fit parameters, which can be obtained by a fit to the resistance data. Certainly, the description of the space charge region is now much more approximated, but nevertheless it is possible to obtain an approximate value for the surface conductivity for the studied material from the 3-layer model. A further point concerning the applicability of the 3-layer and N-layer model is that the difference between the two models also depends on the shape of the space charge region conductivity profile and the values of the surface and bulk conductivity. If the transport is mostly surface or bulk dominated, then the 3-layer model might be precise enough. But, if the space charge region contributes significantly to current transport in lateral direction, then the description by the 3-layer model might not be sufficient any more. Also if the space charge region consists of an inversion layer, the approximation by a single step function cannot be very precise and the N-layer model has to be used instead.

In order to demonstrate and visualize the possible differences between the 3-layer and N-layer model with different number of layers N for two cases of sample parameters, a simulation of the distance-dependent four-point resistance is shown in Fig. 5.5. In Fig. 5.5(a) the calculated four-point resistance is plotted as function of the equidistant probe spacing based both on the 3-layer model and the N-layer model with $N = 40$ for different values of the surface conductivity. In the inset the step-like approximations of the space charge

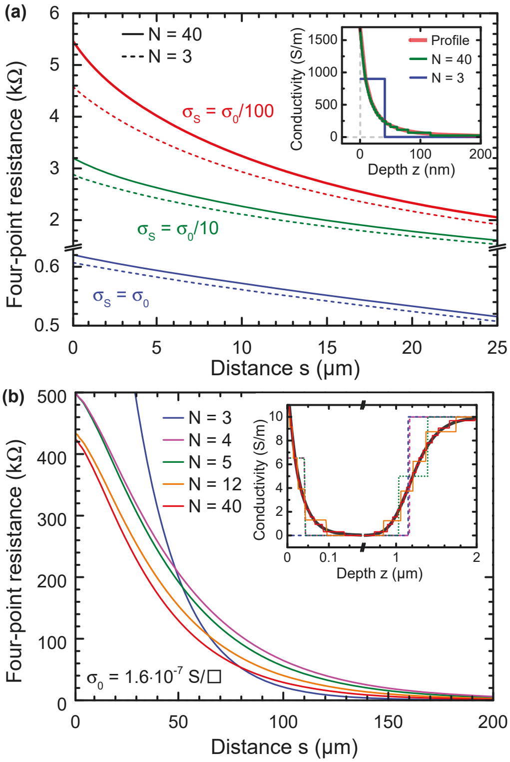

Figure 5.5.: (a) Calculated four-point resistance for different values of the surface conductivity (colored curves) as function of the equidistant probe distance s based on the 3-layer model (dashed lines) and the N-layer model (solid lines) with $N = 40$. The calculation parameters for the bulk conductivity and the space charge layer profile are based on the n-type, almost intrinsic Ge sample ($45\,\Omega\,\mathrm{cm}$) shown in Fig. 5.7. The blue curves correspond to the four-point resistance in the equidistant setup using the measured value of $\sigma_0 = 3.4 \times 10^{-4}\,\mathrm{S}/\square$ according to Fig. 5.7(a), while the green and red curves show the expected four-point resistance for a reduced surface conductivity value by a factor of 10 and 100, respectively. In the inset, the conductivity profile of the space charge layer (red curve) and both the approximations by the 3-layer model (blue) and the N-layer model (green) are shown. (b) Calculated four-point resistance based on different multi-layer models with different number of layers N (colored curves) as function of the equidistant probe spacing s. For the calculation an n-doped sample with a bulk resistivity of $10\,\Omega\,\mathrm{cm}$ and a surface conductivity of $1.6 \times 10^{-7}\,\mathrm{S}/\square$ is assumed. The resulting calculated space charge conductivity profile exhibiting a strong inversion zone is shown in the inset (black curve). The step-like approximations for the different values of N are indicated by the dashed and solid colored curves.

layer for $N = 3$ and $N = 40$ are depicted exhibiting an equal area below the curves. The calculation is based on the values of the n-type, almost intrinsic Ge sample shown in Fig. 5.7 and only the surface conductivity is varied by a factor up to 100 for the different colored curves. The blue curve corresponds to the measurement data in Fig. 5.7 (only the four-point resistance for an equidistant probe setup is now plotted) and the difference between the description by the 3-layer and N-layer model is quite small. The error in the obtained surface conductivity is below $3\,\%$ and so fits well in the denoted error limits given in Fig. 5.7. The reason for the small difference is the high surface conductivity of the Ge samples compared to the near-surface conductivity of the inversion layer. So, the transport is mostly surface dominated and the space charge region does not contribute significantly to the current transport in lateral direction. This enables the rough description of the increasing near-surface conductivity by only a single value, as shown in the inset in Fig. 5.5(a), without producing a large error. However, if the surface conductivity is reduced by a factor of 10 or 100, the contribution of the space charge region to the lateral current transport increases and the near-surface conductivity has to be taken into account more precisely. This is visualized by the green and red curves showing an increasing deviation between 3-layer and N-layer model for decreasing surface conductivity. For the green curve the error on the surface conductivity would be approximately $13\,\%$, while in the case of the red curve it would be already approximately $20\,\%$. This shows that the 3-layer model can be suitable in some cases, but in general the N-layer model is more precise and takes into account more information about the sample. So, if the N-layer model is usable, i.e. if the material parameters are known, it should be preferred.

Fig. 5.5(b) shows a calculation based on the N-layer model for different number of layers N. Again the four-point resistance is plotted as function of the equidistant probe spacing s. In order to demonstrate the difference compared to the 3-layer model, a strong inversion layer (inset) and a small surface conductivity of $\sigma_S = 1.6 \times 10^{-7}\,\mathrm{S}/\square$ were chosen. In this case, the 3-layer model cannot describe the conductivity profile properly, and the expected four-point resistance (blue curve) deviates strongly from the calculated resistance based on the N-layer model with $N = 40$ (red curve), which describes the conductivity profile very precisely. Compared to $N = 40$, the usage of only the 3-layer model would result in this case in a large relative error of 2.2 for the obtained surface conductivity. If more than 3 layers are used, the error decreases rapidly. In the case of $N = 4$ and $N = 5$ layers the error for the surface conductivity would be approximately $20\,\%$ compared to the detailed description by the $N = 40$ layer model. If the number of layers is increased up to $N = 12$, the error reduces to only $2\,\%$. This shows that a further increase of the layer number would not increase significantly the precision of the obtained surface conductivity values, and that already a quite small number of layers (10 to 20 layers) is suitable to obtain values with a small error, which reduces the time consumption for the calculations. Certainly, the form and the extent of the space charge region has a significant influence of the required number of layers, so that it should be chosen specifically for the sample system under study.

In the following section, the application of the N-layer model is demonstrated.

5.4. Application of the *N*-layer model

The advantage of the N-layer model is that it can be used for evaluation of all distance-dependent four-probe resistance measurements without the need of any special sample preparation before the measurement, e.g. in order to quench the surface states [79, 104–106], or special measurement conditions, e.g. varying the temperature [83, 112, 113]. For this reason, the N-layer model is applied first to some already published data of the semiconductor surfaces Ge(100) and Si(100), which were described previously by either pure 2D or pure 3D conductance, but not by a mixed transport channel. In combination with the N-layer model, it is now possible to take into account simultaneously the current transport through the 2D surface and through the 3D bulk, both influenced by the presence of the near-surface space charge layer. So, in the end, the surface conductivities of the materials can be determined from these standard four-point measurements only by a reevaluation of the data. Additionally, the N-layer model is also applied to measurements of the Si(111)-(7×7) structure on p-doped Si(111), which were already discussed in the sections 4.4.1.2 and 4.4.3, but should now be evaluated more precisely by using the N-layer model.

5.4.1. Germanium(100)-(2×1) surface

Distance-dependent four-point transport measurements on the Ge(100) surface were published by Wojtaszek *et al.* [28]. They used a room-temperature, ultra-high vacuum multi-tip STM and carried out four-point resistance measurements on Ge(100) substrates with different bulk doping concentration and type. A symmetric linear probe configuration was used, where the outer current-injecting tips have a distance D and the inner voltage-measuring tips are separated by the distance s. The complete setup is symmetric with respect to the centre plane of the tip positioning line. In Fig. 5.6(a), the experimental data for a p-type Ga-doped sample with a nominal bulk resistivity of $(0.1 - 0.5)\,\Omega\,\mathrm{cm}$ are shown [28]. The measured four-point resistance is plotted as a function of the spacing s between the voltage-measuring tips and with the distance D between the current-injecting tips as additional parameter. In the framework of the publication [28], these data were described by a pure 3D conductance channel. However, it was mentioned that there were some systematic deviations from the 3D model, which increasingly appear, if the voltage-measuring tips approach the positions of the current-injecting tips, i.e. $s/D \geq 0.7$, but the origin of these deviations could not be explained quantitatively. In fact, for the symmetric linear tip configuration, it is particularly the region with a ratio s/D close to 1, where the setup is most sensitive to surface transport and a possible surface conductance channel would have the most influence on the measured four-point resistance. So, it is reasonable to assume that the observed deviations are caused by an additional 2D conductance channel through the surface states of the Ge(100)-(2×1) surface, which cannot be considered by the pure 3D model.

In order to describe this additional 2D transport channel more quantitatively, the existing data are evaluated with the N-layer model. First, the near-surface band bending of the p-type Ge(100) sample is calculated by solving Poisson's equation and using a Fermi level pinning at the surface of $\sim 0.11\,\mathrm{eV}$ above the valence band [114–116]. For the calculation of the conductivity, the z-dependent mobility is approximated by the constant bulk value, as the variation in the mobility is much less than the variation in the exponentially dependent charge carrier density. Also a constant bulk doping concentration is assumed and variations

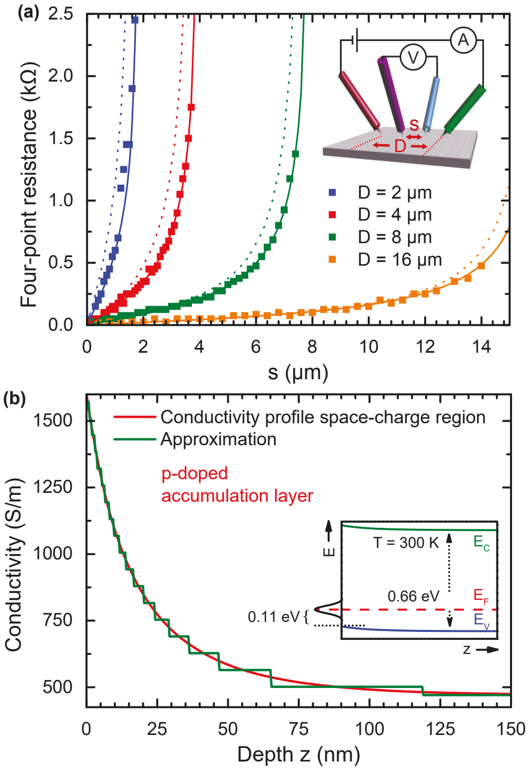

Figure 5.6.: (a) Four-point resistance of a p-doped Ge(100) sample [nominal bulk resistivity $(0.1-0.5)\,\Omega\,\mathrm{cm}$] as function of probe distance s between the inner voltage-measuring tips [28]. Different colored data points correspond to different distances D in the symmetric linear tip configuration shown in the inset. The solid lines represent one single fit to all data points using the N-layer model for charge transport, which results in $\sigma_S = (2.9 \pm 0.6) \times 10^{-4}\,\mathrm{S}/\square$ and $\rho_B = (0.22 \pm 0.01)\,\Omega\,\mathrm{cm}$. The dotted lines indicate the expected four-point resistances for a vanishing surface conductance channel, i.e. $\sigma_S = 0$, taking into account only the space charge region and the bulk. (b) The calculated conductivity profile of the space charge layer as function of the depth z into the sample starting from the surface. This profile is approximated with $N = 20$ layers and used as input for the N-layer model. The band diagram in the inset shows the surface pinning of the Fermi level E_F (red) located $0.11\,\mathrm{eV}$ above the valence band edge and the resulting near-surface band bending of the conduction band E_C (green) and the valence band E_V (blue).

in the static charge density, e.g. caused by ion diffusion, are not taken into account, as this process is usually not known. However, if the nature of ion diffusion is known, the modified z-dependent bulk dopant distribution can be included in Poisson's equation for the calculation of the band bending. Fig. 5.6(b) shows the resulting calculated depth-dependent conductivity profile of the space charge region consisting of a near-surface accumulation layer. This conductivity profile is approximated by a step function of $(N-2)$ steps ($N =$

20) determining the values for σ_n and z_n to be used as input for the N-layer model (further details details in section 5.3). For the symmetric linear tip setup the four-point resistance according to the N-layer model is based on Eq. (4.15) and can be expressed as function of s and D by the equation

$$R^{\mathrm{N-lay}}_{\mathrm{lin,sym}}(s, D) = \frac{2}{I} \int_0^\infty \Big[a_0(k) + a_1(k)\Big] \left[J_0\left(k\,\frac{D-s}{2}\right) - J_0\left(k\,\frac{D+s}{2}\right)\right] \mathrm{d}k \quad (5.15)$$

which is fitted to the measurement data resulting in the colored solid curves shown in Fig. 5.6(a). All four curves for the different values for the distance D correspond to only a single fit with the surface conductivity σ_S and the bulk conductivity σ_B confined close to the range of the nominal values as free parameters. As the conductivity profile of the space charge region also depends on the bulk conductivity, an iterative fitting process is applied, which includes the calculation of the space charge region and the fit to the data in each iteration. For values of $\sigma_S = (2.9 \pm 0.6) \times 10^{-4}\,\mathrm{S}/\square$ and $\rho_B = \sigma_B^{-1} = (0.22 \pm 0.01)\,\Omega\,\mathrm{cm}$ the iterative process converges and the best fit is obtained describing the data very precisely throughout the complete measurement range without any systematic deviations. A further advantage is the resulting single value for each of the parameters σ_S and σ_B, which is sufficient to describe precisely all four resistance curves for the different distances D. In the case of a pure 3D model, as it is used for the fitting process in Ref. [28], it is not possible to model all four data sets with only one value for the bulk conductivity σ_B. The 3D fit has to be applied separately to each curve resulting in different values for σ_B spreading by a relative deviation of $\sim 25\,\%$. However, the measured bulk conductivity should not change during the variation of the tip configuration by the distance D on the same substrate.

This reveals that, even if the transport in the sample is mostly 3D dominated due to the highly conductive bulk and the weak accumulation zone near the surface, a description of the data by a pure 3D model is not sufficient and an additional 2D channel has to be taken into account.

For validating the results for the additional surface conductance channel and ensuring that the observed amount of two-dimensional conductance is not merely caused by the near-surface accumulation layer, the dotted colored curves in Fig. 5.6(a) correspond to the expected four-point resistance for a vanishing surface channel. In these curves, only the bulk conductivity and the conductivity profile of the space charge region according to Fig. 5.6(b) are taken into account, while the value for the surface conductivity σ_S is set to zero. The clearly visible deviation of the dotted curves from the measurement data verifies that an additional 2D surface conductance channel is necessary for describing the measured four-point resistance, and, therefore, proves the existence of conducting surface states.

Fig. 5.7(a) shows similar distance-dependent four-point resistance measurements on an n-type doped, almost intrinsic Ge(100) sample with a nominal bulk resistivity of $\sim 45\,\Omega\,\mathrm{cm}$ [28]. As the measurement data show an enhanced two-dimensional character of conductance, a pure 2D model was used in Ref. [28], which was justified by the presence of a near-surface inversion layer totally preventing the current to be injected into the bulk and acting as a 2D channel, which confines the current close to the surface. However, any possible presence of an additional 2D surface channel caused by surface states was neglected.

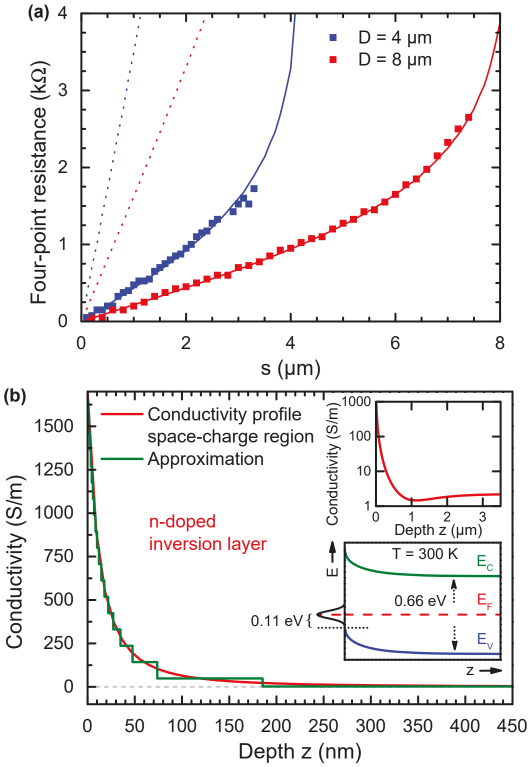

Figure 5.7.: (a) Four-point resistance of an n-type doped, almost intrinsic Ge(100) sample (nominal bulk resistivity $\sim 45\,\Omega\,\mathrm{cm}$) as function of probe distance s between the inner voltage-measuring tips [28]. Different colored data points correspond to different distances D in the symmetric linear tip configuration [inset in Fig. 5.6(a)]. The solid lines represent a single fit to all data points using the N-layer model for charge transport ($N = 20$), which results in $\sigma_S = (3.4 \pm 0.2) \times 10^{-4}\,\mathrm{S}/\square$ and $\rho_B = (45 \pm 22)\,\Omega\,\mathrm{cm}$. The dotted lines correspond to the expected four-point resistances without any surface channel ($\sigma_S = 0$) taking into account only the bulk and the space charge region. (b) Calculated conductivity profile of the space charge region as function of the depth z from the surface (red line). The approximated profile (green line) is used as input for the N-layer model. In the upper inset, the complete range of the conductivity profile of the space charge region exhibiting a shape of an inversion layer is shown. The lower inset depicts the surface pinning of the Fermi level E_F (red) and the induced near-surface band bending of the conduction band E_C (green) and the valence band E_V (blue).

In this case, a further disentanglement between the conductivity of the near-surface p-type part of the inversion layer and the surface conductivity would be required.

So, it is tried again to describe the measurement data with the N-layer model. The calculated conductivity profile of the space charge region shows the expected inversion layer depicted in Fig. 5.7(b). For the calculation, the transition region between p-type and n-type of conduction has not been taken into account and only the absolute value of the conductivity is considered, but, as the majority of the current flows through the near-surface p-type part of the inversion layer and through the surface channel, this approximation should be suitable in the present case. The conductivity profile is described by a step function (green line) and used in combination with the N-layer model for a fit to the data according to Eq. (5.15). In Fig. 5.7(a), the two solid curves result from a single fit with the parameters $\sigma_S = (3.4 \pm 0.2) \times 10^{-4}\,\mathrm{S}/\square$ and $\rho_B = \sigma_B^{-1} = (45 \pm 22)\,\Omega\,\mathrm{cm}$, and describe the data very precisely. For verification, the dotted lines shown in Fig. 5.7(a) again represent the expected four-point resistance without any additional surface channel ($\sigma_S = 0$). The very strong deviation from the measurement data indicates clearly that the observed transport behavior cannot only be caused by the enhanced conductivity close to the surface due to the inversion layer, but that there has to be an additional surface conductance channel also on the n-type sample.

If the results for the p-type and n-type Ge(100) samples are compared, the values for the obtained surface conductivity coincide within the error limits. This is expected, as the surface states should not be influenced by the doping type of the substrate. Thus, this is another confirmation that really the conductivity of the surface states was determined. By combining the results of the p- and n-type sample, a more precise value for the surface conductivity of the Ge(100)-(2×1) surface of $\sigma_{\mathrm{S,Ge(100)}} = (3.1 \pm 0.6) \times 10^{-4}\,\mathrm{S}/\square$ can be obtained.

5.4.2. Silicon(100)-(2×1) surface

Distance-dependent four-point resistance measurements on p-type and n-type doped Si(100) substrates were carried out by Polley *et al.* [27]. For the measurements, a room temperature, ultra-high vacuum multi-tip STM was used with a linear equidistant tip configuration with spacing s between adjacent tips. The current was injected by the outer tips and the potential drop between the inner tips was measured. In Fig. 5.8(a), the measured four-point resistance is shown as a function of the tip distance s for an n-type (blue points) and a p-type (red points) Si(100) substrate both with a nominal bulk resistivity of $(1 - 10)\,\Omega\,\mathrm{cm}$. Although the bulk doping concentrations of p- and n-type sample are similar, the observed transport behavior is completely different. In the p-type case, a 3D conduction channel is more dominant, while in the n-type case the majority of current flows through a 2D transport channel. Again, this was explained by the presence of an inversion layer in the n-type sample preventing the current to flow through the bulk. So, the measured data were described in Ref. [27] by a pure 3D conductance model for the p-type substrate and by a pure 2D model in the n-type case. However, this approach cannot consider any possible mixed 2D-3D conductance channels through the space charge region and the bulk in both samples, and, especially, neglects the two-dimensional surface state, which should be present on the Si(100)-(2×1) surface [117].

For refining the description of the measured data on the Si(100) substrates and for determining a value for the conductivity of the Si(100)-(2×1) surface state, the N-layer model is used. Figs. 5.8(b) and 5.8(c) show the corresponding conductivity profiles of the space

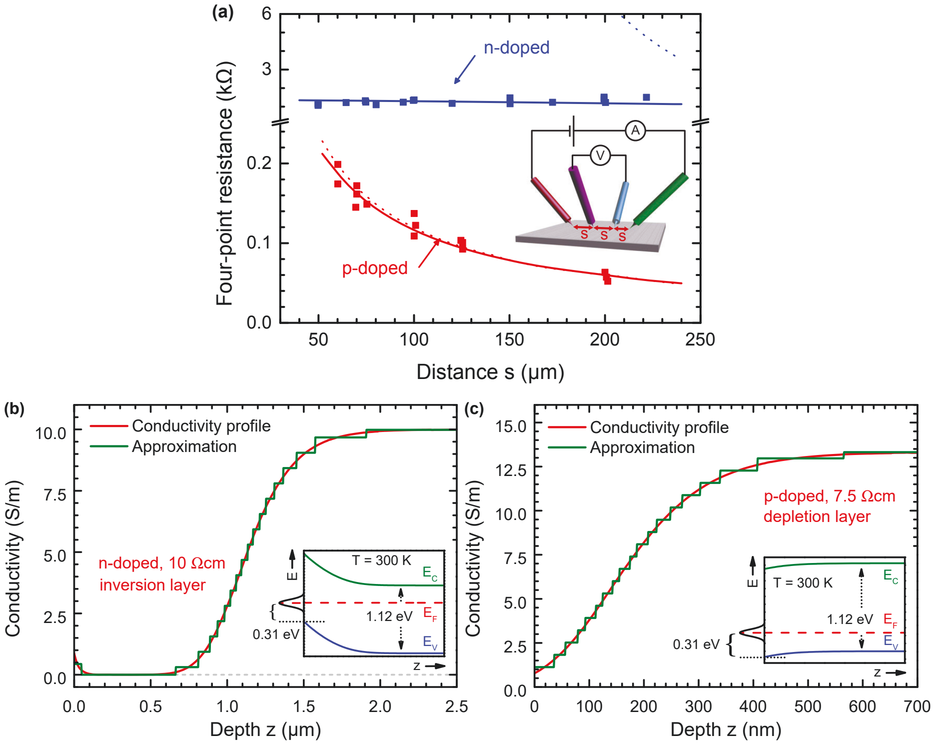

Figure 5.8.: (a) Four point resistance of a p-doped (red) and n-doped (blue) Si(100)-(2×1) sample [nominal bulk resistivity $(1-10)\,\Omega\,\mathrm{cm}$] as function of the equidistant probe distance s reproduced from Ref. [27]. Fits to the data based on the N-layer model are depicted by the solid lines resulting in $\sigma_S = (1.9 \pm 1.4) \times 10^{-4}\,\mathrm{S}/\Box$ and $\rho_B = (7.5 \pm 0.9)\,\Omega\,\mathrm{cm}$ (p-doped), and in $\sigma_S = (1.6 \pm 0.4) \times 10^{-4}\,\mathrm{S}/\Box$ and $\rho_B = (10.0 \pm 7.5)\,\Omega\,\mathrm{cm}$ (n-doped). The dotted lines correspond to the case of a vanishing surface channel ($\sigma_S = 0$). The inset shows the equidistant tip configuration. (b),(c) Calculated conductivity profiles of the space charge region for the p- and n-doped samples (red curves). The approximation by $N = 20$ layers (green curves) is used for the N-layer model. In the insets, the near-surface band bending of the conduction band E_C (green) and the valence band E_V (blue) caused by the surface pinning of the Fermi level E_F (red) due to the surface states located $\approx 0.31\,eV$ above the valence band edge is shown.

charge region for the p-type and n-type Si(100) substrates, respectively. For the calculation, a Fermi level pinning of the surface states of $\sim 0.31\,\mathrm{eV}$ above the valence band is used [83, 117, 118]. In the p-type case, a depletion zone is formed close to the surface, while in the n-type case an inversion layer separates the bulk from the near-surface region. Again, the pn-transition is not considered for the inversion layer, as the n-type bulk does not contribute significantly to current transport. The approximation of the conductivity profiles (green curves) is used as input for fitting the respective measurement data in Fig. 5.8(a) according to Eq. (5.13). The results are depicted as solid curves in Fig. 5.8(a).

For the p-type sample the fit parameters are $\sigma_S = (1.9 \pm 1.4) \times 10^{-4}\,\mathrm{S}/\Box$ for the surface conductivity and $\rho_B = (7.5 \pm 0.9)\,\Omega\,\mathrm{cm}$ for the bulk resistivity, which is confined to the range of the nominal value. In the n-type case, the values are $\sigma_S = (1.6 \pm 0.4) \times 10^{-4}\,\mathrm{S}/\Box$ and $\rho_B = (10.0 \pm 7.5)\,\Omega\,\mathrm{cm}$. The dotted colored curves in Fig. 5.8 correspond again to the case of a vanishing surface conductivity, and show a large deviation for the n-doped sample, while in the p-doped case the deviation is quite small, as the current transport is mostly bulk dominated. So, the four-point resistance measurement for the p-type sample in the chosen tip distance range is not very surface sensitive, and the determined value for the surface conductivity has quite a large error, even if the curve fits quite well to the data. The fitted curve for the n-type substrate shows some larger deviations due to a larger spread and a slight increasing behavior of the data, which might be caused by tip positioning errors or influence of the sample edges. Also averaging of measurement results from several samples rather than using single samples can lead to the visible behavior of the data. However, the obtained value for the surface conductivity is more precise, as the transport behavior in the n-type sample is now more dominated by the near-surface region. So, as both values are still consistent within the error limits, the value resulting from the n-type sample can describe the conductivity of the Si(100)-(2×1) surface state more precisely as $\sigma_{\mathrm{S,Si(100)}} = (1.6 \pm 0.4) \times 10^{-4}\,\mathrm{S}/\Box$.

5.4.3. Silicon(111)-(7×7) surface

Finally, the N-layer model is applied to data measured on the Si(111)-(7×7) surface (p-type substrate, $22.5\,\mathrm{k}\Omega\,\mathrm{cm}$) which have been evaluated before by using the 3-layer model, as depicted in the Figs. 4.10(a) and 4.15(a) in the sections 4.4.1.2 and 4.4.3, respectively. These measurements should now be reevaluated in order to examine, if a description by the more precise N-layer model will result in a modified value of the determined surface conductivity. In Fig. 5.9(a) and 5.9(b), the distance-dependent four-point measurements in the linear setup, corresponding to Fig. 4.10(a) and 4.15(a), respectively, are depicted with a fit (red line) originating from the N-layer model. This time, for modelling the space charge region, a much more precise approximation of the strongly depth-dependent conductivity profile which is caused by the near-surface inversion zone, is achieved by using 28 layers in total, as it is shown by the green step function in Fig. 5.9(c). It is visible that in both cases the fits describe the data as well as before with the 3-layer model and also no substantial deviations for the surface conductivities appear. While for Fig. 5.9(a) the fitted value $\sigma_{\mathrm{2D}} = (3.8 \pm 0.3) \times 10^{-6}\,\mathrm{S}/\Box$ is exactly identical with the one obtained before, the second conductivity value $\sigma_{\mathrm{2D}} = (6.4 \pm 0.3) \times 10^{-7}\,\mathrm{S}/\Box$ in Fig. 5.9(b) differs slightly compared to the 3-layer model. However, the observed deviation is quite marginal and still within the error tolerances. So, it can be concluded that for the present cases the exact profile of the space charge region does not substantially influence the actual current transport in the sample, so that even a very rough approximation of the existing inversion zone by only one layer with fixed conductivity, as performed for the 3-layer model, is sufficient in order to obtain a precise result for the surface conductivity. From a general point of view, this shows that in some cases also a modelling by the more simple and

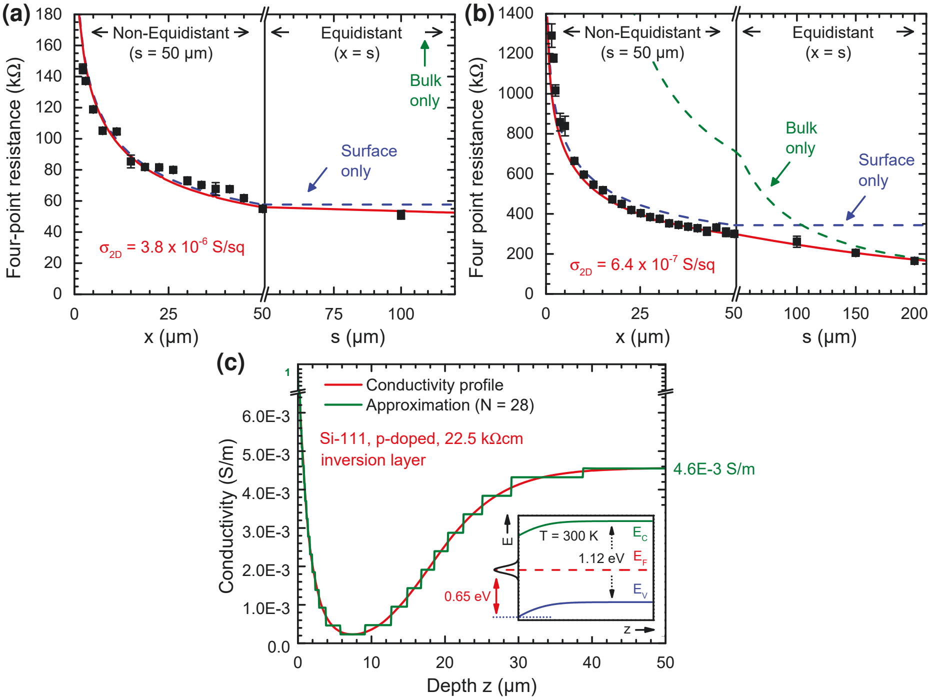

Figure 5.9.: Distance-dependent linear four-point measurements on p-type Si(111)-(7×7) samples ($22.5\,\mathrm{k\Omega\,cm}$) which have been described before by the 3-layer model, are reevaluated by using the N-layer model. A more precise approximation of the conductivity profile in the space charge region by 28 layers is used (c). (a) Measurement data shown before in Fig. 4.10(a) in section 4.4.1.2. A fit by the N-layer model (red line) results in the same value $\sigma_{\mathrm{2D}} = (3.8 \pm 0.3) \times 10^{-6}\,\mathrm{S}/\square$ as before. (b) Measurement data shown before in Fig. 4.15(a) in section 4.4.3. A fit by the N-layer model (red line) results in a slightly different value of $\sigma_{\mathrm{2D}} = (6.4 \pm 0.3) \times 10^{-7}\,\mathrm{S}/\square$ compared to before. (c) Calculation similar to Fig. 4.10(b), but now with an approximation by 28 layers (stepped green curve).

easier applicable 3-layer model is as effective as by the more complicate N-layer model. However, this depends on several parameters, i.e. the absolute conductivity values and ratios between the involved conduction channels in the sample, so that it has to be verified individually for every sample under study.

5.5. Summary

In this chapter, an analytically derived N-layer model for current transport through multiple layers of different conductivity has been presented with the aim to interpret distance-dependent four-point resistance measurements on semiconductor surfaces more precisely. Such a model especially allows for a better approximation of the space charge region, based

Surface reconstruction	Surface conductivity σ_S
Si(100)-(2×1)	$(1.6 \pm 0.4) \times 10^{-4}\,\mathrm{S}/\square$ [Sec. 5.4.2]
Ge(100)-(2×1)	$(3.1 \pm 0.6) \times 10^{-4}\,\mathrm{S}/\square$ [Sec. 5.4.1]
Si(111)-(7×7)	$(8.6 \pm 1.9) \times 10^{-6}\,\mathrm{S}/\square$ [Sec. 4.1.4]
Bi/Si(111)-($\sqrt{3} \times \sqrt{3}$)R30°	$(1.4 \pm 0.1) \times 10^{-4}\,\mathrm{S}/\square$ [Sec. 4.1.3]
Ag/Si(111)-($\sqrt{3} \times \sqrt{3}$)R30°	$(3.1 \pm 0.4) \times 10^{-3}\,\mathrm{S}/\square$ [120]

Table 5.1.: Surface conductivities of different reconstructed and passivated surfaces of silicon and germanium.

on calculated data of the near-surface band bending. As motivation, the important role of the space charge region for the current distribution in a sample has been emphasized and the insufficiency of 2-layer conductance models neglecting this region completely has been discussed, e.g. by the fact that already the lowest case of an N-layer model (i.e. $N = 3$) in general allows for a much better description of four-point resistance data than the often used parallel-circuit model. The formalism for the N-layer model and a discussion about a reasonable number of layers has been performed. Moreover, the application of the N-layer model has been demonstrated, both by the example of already published data from the semiconductor surfaces Ge(100)-(2×1) and Si(100)(2×1) [28], as well as by using data from the Si(111)-(7×7) surface, in the latter case with the aim to refine the evaluation obtained already before with the 3-layer model. From all considered measurement data, the conductivities of the surface states of the corresponding materials haven been determined, as summarized in Tab. 5.1. For comparison, some additional surface conductivities of other reconstructed and passivated Si(111) surfaces are also listed. In total, the presented evaluation method for four-probe resistance measurements by using an N-layer conductance model is quite generic and, thus, can be easily applied to data from various materials in order to determine the corresponding surface conductivities from standard distance-dependent transport measurements.

Most of the results from this chapter, except for section 5.4.3, are published in Ref. [119]. Additionally, the N-layer-model depicted in section 5.3 is conceptually described in the publication in Ref. [44].

6. Parasitic conduction channels in topological insulator thin films

Up to now, only systems with a single 2D conduction channel have been considered, whose conductivity should be extracted from measurements supported by theory, i.e. bulk semiconductors with 2D surface states and an (extended 3D) space charge region in between. However, if a system features more than one 2D channel in parallel, it is much more complicated to disentangle them. In the present chapter, this problem is addressed for the example of thin film systems with topological insulator (TI) materials. Thin films of topological insulators usually exhibit multiple parallel conduction channels for the transport of electrical current. Beside the topologically protected surface states (TSS), parallel channels may exist, namely the interior of the not-ideally insulating TI film, the interface layer to the substrate, and the substrate itself. It is an important issue to minimize the influence of such parasitic parallel channels, in order to be able to take advantage from the auspicious TSS properties for the current transport.

While interface and substrate channel can be characterized experimentally before film growth, as shown later on, particularly the conductivity of the interior (bulk) of the thin TI film is difficult to access by measurements. Hence, for this part, a theoretical approach is presented here which consists in a calculation of the the near-surface band bending in the TI film, and thus the mobile charge carrier density, based on parameters obtained from surface-sensitive experimental methods, i.e. (gate-dependent) four-point resistance measurements and angle-resolved photoelectron spectroscopy (ARPES). While in most cases such calculations are prevented by the usually unknown concentration of unintentional dopants inside the TI material, specifically for the thin-film limit it turns out that the band bending is largely independent of the dopant concentration in the film. Thus, a well-founded estimate of the total mobile charge carrier density and the conductivity of the interior of the thin TI film proves possible. Hence, in combination with the conductivities of the other parasitic channels, this finally gives rise to the possibility to disentangle the important TSS channel from measurements, e.g. by means of a multi-layer conductance model.

6.1. Parallel conduction channels in thin film systems

Topological insulators are candidates for future electronic devices and might be used for low-power spintronics or quantum computing, due to the special properties of their topologically protected surface states (TSS), such as spin-momentum locking and prohibited di-

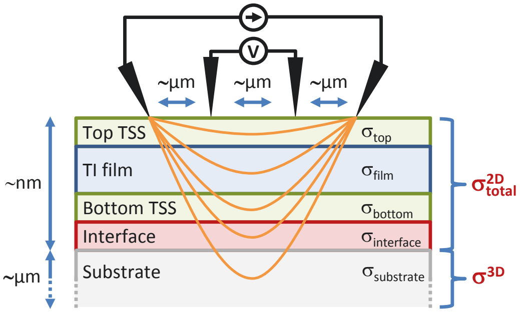

Figure 6.1.: Multiple parallel conduction channels in a topological insulator thin film. The current transport can occur through the top and bottom TSS channels, but also through the interior of the TI film, through the interface layer between film and substrate as well as through the substrate itself. Position-dependent four-probe measurements on the surface can only differentiate between the total 2D conductivity, i.e. the sum of all parallel channels in the thin film, and the 3D substrate conductivity. Note that different from the schematic the film thickness ($\sim$ nm) is much smaller than the usual distance between the tips ($\sim \mu$m).

rect backscattering [121, 122]. In recent years, the compound materials Bi_2Se_3, Bi_2Te_3 and Sb_2Te_3, which belong to the class of van-der-Waals bonded chalcogenides, have emerged as promising TI for applications at room temperature, essentially because of their pronounced band gap [121, 123]. However, for taking advantage of the topological properties of the TI in any transport device, the electrical current has to be transmitted predominantly through the TSS. But for TI bulk crystals the parallel bulk conductance plays a significant role. In fact, the transport through this parasitic channel may even surpass the current transport through the TSS, as has been observed recently [30, 124]. While the influence of the bulk can be suppressed if TI materials are grown as thin films on sufficiently low-conducting substrates, also in this case multiple parallel conduction channels that participate in the total current transport may be present. This is visualized in Fig. 6.1. Beside the TSS channels, the current can also flow through the interior of the not-ideally insulating TI film, through the potentially highly conductive interface layer between the TI film and the substrate, and through the substrate itself. Thus, it is an important task to design future devices based on thin TI films in a manner that minimizes the fraction of the current through the parasitic parallel transport channels.

Clearly, to achieve this goal the conductivities of the parasitic channels in actual MBE-grown thin TI films have to be determined first. At first glance, obvious experiments to this end are distance-dependent four-probe measurements on the surface to disentangle two-dimensional (2D) from three-dimensional (3D) conductance channels, as depicted before in chapters 4 and 5. However, the thickness of the grown TI films (typically 10 nm) poses a challenge here. Specifically, the small vertical length scale makes it impossible to separate the bulk conductance of the TI film as a 3D conductance from the 2D conductance of the TSS, since for this purpose the probes would have to be spaced closer than one quarter of the film thickness. But this is not possible, because this spacing would approach the tip radius [44, 60, 78]. For relevant MBE-grown TI films, position-dependent four-probe measurements are thus only suitable to separate the total 2D conductivity $\sigma^{2\mathrm{D}}_{\mathrm{total}}$ of the thin TI film, which comprises contributions from the top and bottom TSS, the interior of the thin film and the interface channels (Fig. 6.1), from the 3D substrate conductivity. However, since the conductivity of the substrate channel can easily be minimized by choosing an appropriately low-doped substrate as template for the grown TI thin film, separating out its conductivity is not the main issue.

It is thus evident that a different approach has to be taken to decompose what in practical distance-dependent four-tip measurements appears to be an undifferentiated 2D conductivity, into the intrinsic TSS on the one hand and the parasitic thin-film and interface contributions on the other. In the following, this problem is addressed with a two-pronged strategy, dealing separately with the interface and the thin-film channels. First, in the following section 6.2, a method for measuring the conductivity of the interface channel is presented. Then, in section 6.3, an approach for determining the conductivity of the interior of a thin TI film is discussed, which uses input from both surface-sensitive measurement methods and calculations of the near-surface band bending in the thin film, as shown in detail in section 6.4.

6.2. Interface channel

The interface channel arises exactly at the boundary between a thin TI film and its underlying substrate. At the interface the symmetry of the substrate is broken and a reconstruction can establish on the topmost atomic layer of the substrate (i.e. interface reconstruction), similar as it is also the case for a boundary to vacuum (i.e. surface reconstruction). However, in general the properties of such an interface reconstruction can differ from a surface reconstruction (boundary to vacuum) due to the interaction with the thin TI film on top of the substrate. As such a sandwiched geometry is generic for deposited thin films on bulk substrates, also the interface channel is always present for such thin film systems. In dependence of the actual reconstruction established at the interface, such an interface channel can possibly exhibit a relative large two-dimensional conductivity when compared to the TSS channel, and therefore might contribute significantly in current transport. In order to be able to design a device based on a thin TI film in such a way that an appropriate interface with a low conductivity is chosen, in a first step the influences of different interface reconstruction have to be determined, which is discussed in the following.

The most common method for growing thin TI films is van-der-Waals epitaxy, and here it can be observed that the interaction between the TI film and the substrate is very small. A common substrate used for van-der-Waals epitaxy is Si(111). Here, an initial passivation of the surface dangling bonds at the beginning of the growth process results in a weak van-der-Waals coupling of the TI film to the underlying substrate [126–128]. At the same time, due to this initial passivation an interface reconstruction of the Si(111) surface arises, which can potentially have an appreciable two-dimensional conductivity, thus providing an additional parasitic channel for current transport beneath the thin TI film [35, 120, 129].

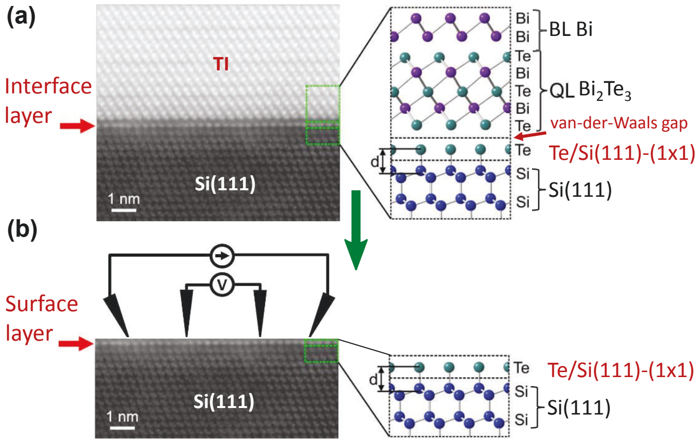

Figure 6.2.: Principle of measurement for determining the interface conductivity between a thin TI film and the underlying substrate. For visualization, a scanning transmission electron microscopy (STEM) image of the material Bi_1Te_1 and the corresponding crystal structure is used, as reproduced from Ref. [125]. (a) For a thin TI film (i.e. Bi_1Te_1 in the shown example) on top of a Si(111) substrate a van-der-Waals gap appears exactly at the interface layer (visible in STEM image and marked in crystal structure). So, the film is spatially slightly separated from the (interface) reconstruction of the substrate. (b) Due to the weak interaction between thin TI film and (Si) substrate, the interface reconstruction, i.e. Te/Si(111)-(1 × 1) in the shown example, can be assumed to be equal to the corresponding surface reconstruction without the TI film on top [as indicated by the transition from (a) to (b)]. Then, the surface is directly accessible and its conductivity can be easily measured by means of four-point probe measurements.

Scanning transmission electron microscopy has revealed that thin TI films often exhibit a sharp interface to a Si(111) substrate [125, 128]. In combination with the predominantly weak van-der-Waals interaction between TI and substrate, it results that the electronic properties of the TI film and the passivated substrate are largely decoupled. Because of this decoupling, it is reasonable to assume that also the properties of the interface reconstruction in the composed TI/substrate system are largely equal to the properties of a surface reconstruction obtained on the substrate without the TI film on top. This suggests that the interface conductivity can in fact be measured as the surface conductivity of the relevant surface reconstruction on the pure substrate. Evidently, it is then sufficient to prepare the pertinent passivation layer on the Si(111) surface and measure its conductivity in order to access the conductivity of the corresponding interface layer. Such measurements of a suitably passivated Si(111) surface can then be routinely performed with a distance-dependent four-probe experiment as seen before (cf. chapter 4). In Fig. 6.2, this measurement procedure is visualized by means of an example using measurement data for the material Bi_1Te_1 [125].

In the following sections, surface conductivity measurements for several surface reconstructions on Si(111) are discussed that are most relevant for the growth of $(Bi_{1-x}Sb_x)_2Te_3$.

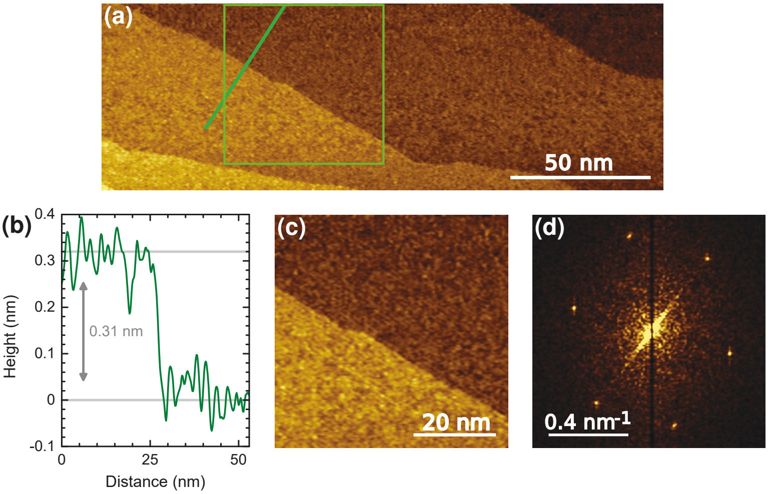

Figure 6.3.: (a) STM image of the Te/Si(111)-(7×7) surface revealing covered terraces with a roughness of $\sigma_{\mathrm{RMS}} = 65\,\mathrm{pm}$ and the monoatomic steps of the underlying Si(111) substrate ($U = 700\,\mathrm{mV}$, $I = 130\,\mathrm{pA}$). (b) Height profile across the step [along green line in (a)]. (c) Enlarged region of the STM image from (a) [indicated by green square in (a)]. Traces of the characteristic corner holes of the (7 × 7)-reconstruction are slightly visible. (d) Fourier transform of (c). The distinct spots show clearly the periodicity of the (7 × 7)-reconstruction.

They reveal that the surface conductivity strongly depends on the type of surface reconstruction (Tab. 6.1). One may therefore expect that this pronounced variation translates to the interface conductivity, meaning that the pertinent surface reconstruction needs to be taken into account when disentangling the parasitic conduction channels from the TSS.

6.2.1. Te/Si(111)-(7×7)

For Te-based van-der-Waals epitaxy, a plausible interface reconstruction is the Te/Si(111)-(7×7) reconstruction, which has been reported as a template for the growth of TI films on Si(111) [130]. It can be prepared by depositing Te on top of a reconstructed Si(111)-(7×7) surface. In a first step, the (7×7)-reconstruction of the Si(111) substrate (p-doped, bulk resistivity $22.5\,\mathrm{k\Omega\,cm}$) is established by heating the substrate to $1200\,^{\circ}\mathrm{C}$ and then slowly decreasing its temperature. Next, the Si(111)-(7×7) surface is passivated by the deposition of one monolayer (ML) Te at a substrate temperature of $300\,^{\circ}\mathrm{C}$, employing a flux of 1 ML/min from a Knudsen cell. STM images of the surface reveal that the terraces are covered by Te with a roughness of $\sigma_{\mathrm{RMS}} = 65\,\mathrm{pm}$, and that the monoatomic steps of the underlying Si(111) substrate with a height of $0.31\,\mathrm{nm}$ are still clearly visible, as shown in the Figs. 6.3(a) and 6.3(b). On the terraces the characteristic corner holes of the Si(111)-(7×7) reconstruction can still be identified [Fig. 6.3(c)], indicating that at least some elements of the (7×7) Si reconstruction are still present below the Te layer. More clearly the corresponding periodicity can be seen as distinct spots in the Fourier transform of the STM image, as shown in Fig. 6.3(d).

To determine the surface conductivity of the Te/Si(111)-(7×7) reconstruction, distance-dependent four-probe measurements with a multi-tip STM at room temperature have been performed. The tip configuration was chosen to be linear but not equidistant (cf. inset of Fig. 6.4). In this non-equidistant arrangement, the distance x between one outer current-injecting tip and the adjacent inner voltage-measuring tip is varied, while the other tips remain constantly spaced by $s = 50\,\mu\mathrm{m}$. Under these experimental circumstances, the four-point resistance for a two-dimensional sheet depends on the distances s and x, as specified before in chapter 3 by Eq. (3.48).

In Fig. 6.4 the measured four-point resistance of the Te/Si(111)-(7×7) surface is plotted as function of the spacing x. The solid red line corresponds to a fit according to Eq. (3.48). The fit corresponds well to the data and results in a surface conductivity of $\sigma^{\mathrm{Te}}_{7\times7} = (8.3 \pm 0.5) \times 10^{-6}\,\mathrm{S}/\square$, which is slightly larger than the surface conductivity of the bare Si(111)-(7×7) surface, measured as $\sigma^{\mathrm{Si}}_{7\times7} = (5.1 \pm 0.7) \times 10^{-6}\,\mathrm{S}/\square$ in section 4.1.4. Any contribution from the Si substrate can be excluded, as the 3D bulk channel would result in a much larger four-point resistance than actually measured (indicated by green arrow). In combination with the results from STM the surface conductivity measurements suggest that the Si(111)-(7×7) reconstruction is still partly intact underneath the deposited Te, while its conductivity is moderately increased by doping from Te. But if $\sigma^{\mathrm{Te}}_{7\times7}$ is compared to typical TSS conductivities of $\sigma_{\mathrm{TSS}} \approx 4$ to $8 \times 10^{-4}\,\mathrm{S}/\square$ [29,34], only $1\,\%$ to $2\,\%$ of the total current would flow through the interface channel, indicating that it does not play a significant role in the overall current transport.

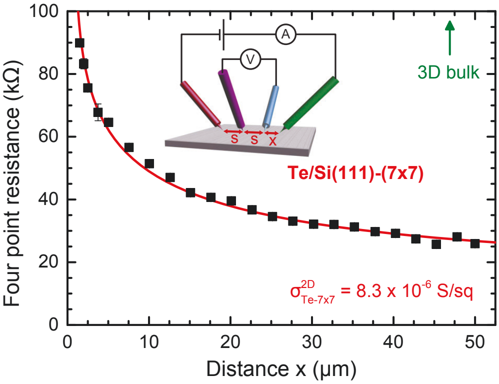

Figure 6.4.: Measured four-point resistance of the Te/Si(111)-(7×7) surface reconstruction as function of the non-equidistant probe spacing x. The red line corresponds to a fit to the data using a pure 2D model according to Eq. (3.48) and results in a surface conductivity of $\sigma^{\mathrm{Te}}_{7\times7} = (8.3 \pm 0.5) \times 10^{-6}\,\mathrm{S}/\square$. The 3D bulk channel of the Si substrate exhibits a much larger four-point resistance than actually measured (indicated by green arrow). In the inset, the linear non-equidistant probe configuration is visualized.

6.2.2. Te/Si(111)-(1×1)

A further plausible interface termination for Te-based van-der-Waals epitaxy is the Te/Si(111)-(1×1) surface. In fact, this reconstruction forms the most common template and, for example, has been used for the growth of Bi_2Te_3 [126] and $BiSbTe_3$ [131].

6.2.2.1. Preparation

In order to determine the surface conductivity by means of four-point probe measurements, the (1×1)-reconstruction is established on a Si(111) substrate (p-doped, bulk resistivity $22.5\,\mathrm{k\Omega\,cm}$) and subsequently terminated with tellurium. First, the substrate is cleaned by a $1\,\%$ HF dip in order to remove any oxide on the surface, and, afterwards, immediately introduced into the UHV chamber (within $10\,\mathrm{min}$). By heating the substrate to $700\,°\mathrm{C}$ the hydrogen is desorbed from the surface and a clean Si(111)-(1×1) structure remains. Then, the substrate is passivated by the deposition of Te with a flux of $1\,\mathrm{ML/min}$ at different substrate temperatures. It turns out that the substrate temperature during deposition significantly influences the quality of the Te-terminated reconstruction, as it will be seen in the following. The deposition has been performed at (a) room temperature for $1\,\mathrm{min}$, (b) $315\,°\mathrm{C}$ for $10\,\mathrm{min}$, and (c) $350\,°\mathrm{C}$ for $10\,\mathrm{min}$. At room temperature the Te only adsorbs on the substrate, so that exactly 1 ML has been deposited. At the elevated temperatures there is a balance between adsorption and desorption of Te on the substrate, so that despite the longer deposition time in total also only 1 ML results on the substrate [132]. Subsequently after finishing the deposition, the substrate is quenched to room temperature.

6.2.2.2. Different deposition temperatures

All of the three samples have been investigated as prepared *in situ* by STM and subsequent distance-dependent four-point measurements. The results are shown in Fig. 6.5. In Fig. 6.5(a), a STM image of the (1×1)-reconstruction terminated with Te deposited at room temperature is depicted. The visible topography suggests due to the large amount of single patches on the surface that no closed Te termination on the Si(111) has been established. The corresponding height distribution [Fig. 6.5(b)] is asymmetric (green curve) and exhibits a width of $\sigma_{\mathrm{RMS}} = 280\,\mathrm{pm}$. It can be fitted by a superposition of multiple Gaussian peaks (red curve), as indicated in Fig. 6.5(b) by the dotted lines for the individual contributions. The maxima of the three Gaussian parts are shifted with respect to each other by $310\,\mathrm{pm}$ (magenta and blue curve) and $220\,\mathrm{pm}$ (blue and yellow curve), and all exhibit different widths as indicated in the plot. The first value seems to correspond to the step height of Si(111), thus the magenta distribution might be explained by the presence of pits in the substrate arising from the HF preparation procedure [133, 134], but since it is not similarly present for other deposition temperatures [cf. Figs. 6.5(d) and 6.5(f)], it is more reasonable to assume that the magenta part is attributed to holes in the Te surface termination, implying that the second part (blue) describes the Te termination itself. The third part (yellow) can then be explained by adsorbates on top of the surface termination, e.g. excess material

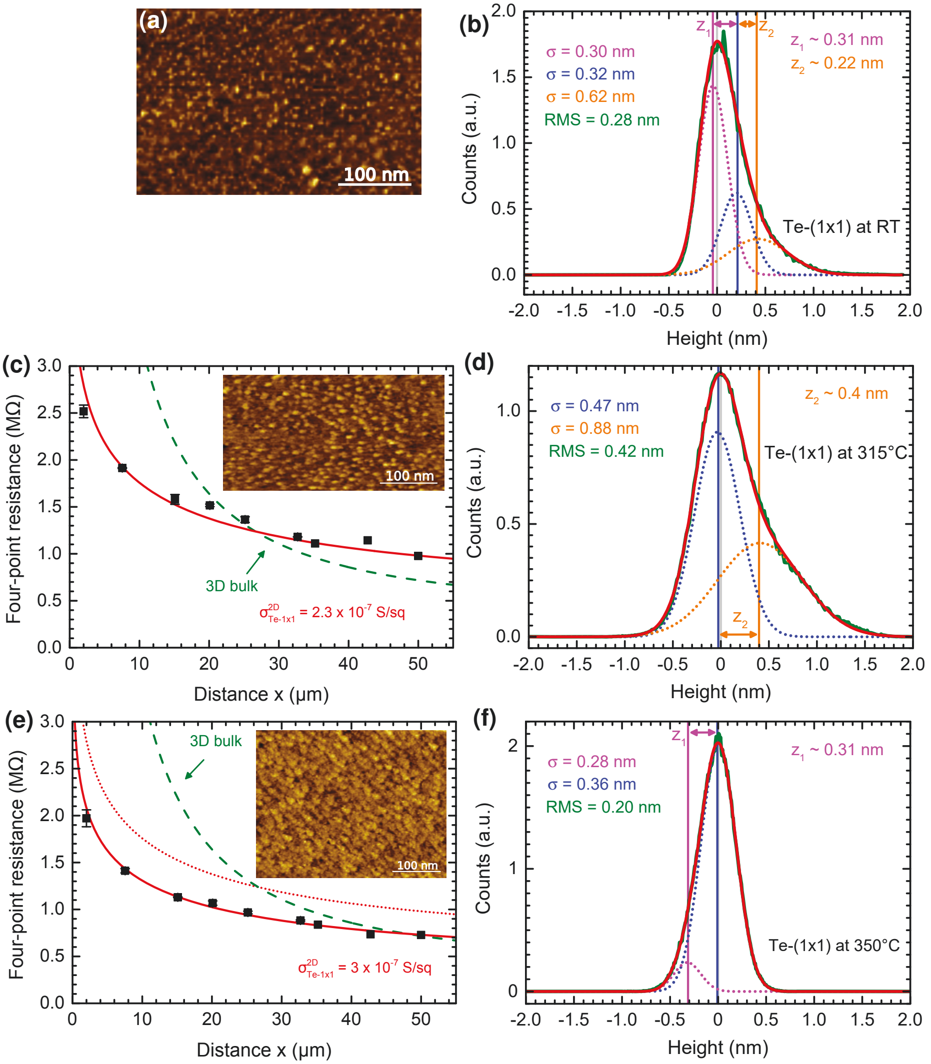

Figure 6.5.: STM and distance-dependent four-point probe measurements of the Te/Si(111)-(1×1) surface reconstruction for Te deposited at different substrate temperatures, i.e. (a) – (b) at room temperature, (c) – (d) at 315 °C, (e) – (f) at 350 °C. In (a) and in the insets of (c),(e) the STM topography is shown with (a) $U = -3.5\,\mathrm{V}$, $I = 15\,\mathrm{pA}$, (c) $U = -1.4\,\mathrm{V}$, $I = 20\,\mathrm{pA}$, and (e) $U = -1\,\mathrm{V}$, $I = 25\,\mathrm{pA}$. In (b),(d),(f) the corresponding height distribution of the STM topography is depicted (green line). A multiple Gaussian peak fit reveals contributions by either holes (dashed magenta line), the Te reconstruction itself (dashed blue line) and adsorbates (dashed yellow line). All parts have different center positions and widths as indicated. In (c),(e) the four-point resistance is plotted as function of the non-equidistant spacing x (tip configuration shown in inset of Fig. 6.4). The data are fitted (red line) by a pure 2D model [Eq. (3.48)] resulting in (c) $\sigma^{\mathrm{Te}^*}_{1\times1} = (2.3 \pm 0.1) \times 10^{-7}\,\mathrm{S}/\square$ and (e) $\sigma^{\mathrm{Te}}_{1\times1} = (3.0 \pm 0.2) \times 10^{-7}\,\mathrm{S}/\square$. For comparison, the curve of (c) is indicated in (e) as dotted red line. A contribution from the 3D substrate (dashed green line) can be excluded.

originating from the Te deposition, which show a twice as broad distribution than the other two parts and are also much less present than the holes. So, from the height distribution it can be concluded that the Te/Si-(1×1) termination is not closed, as the majority of the surface consists out of holes and only a small fraction of it is covered by the Te termination itself. This is also in perfect accordance with the attempt of performing a four-point measurement. Here, it turns out that it is not possible to inject any current into the surface. Even with the tips in hard contact for applied voltages up to $10\,\mathrm{V}$ only a current of less than $10\,\mathrm{nA}$ has been achieved. So, there seems to be no surface conductivity as the termination is simply not connected.

In Figs. 6.5(c) and 6.5(d), the results for the deposition at a temperature of $315\,^{\circ}\mathrm{C}$ are depicted. The STM image [inset in Fig. 6.5(c)] still shows a patched structure but not as separated as before in Fig. 6.5(a). The height distribution in Fig. 6.5(d) again shows an asymmetric curve with now an increased width of $\sigma_{\mathrm{RMS}} = 420\,\mathrm{pm}$. A multiple Gaussian peak fit (red line) reveals that it is composed out of two parts shifted by $\sim 400\,\mathrm{pm}$ with respect to each other. The width of the two parts are different and by comparing to the results of Fig. 6.5(b) it can be assumed that the yellow curve is attributed to adsorbates, while the blue curve is the Te termination itself. It seems that no holes are present, but it should be noted that a small fraction might not be resolved and, thus, could lead to the observed broadening of both parts compared to Fig. 6.5(b). Moreover, the broader and more shifted adsorbate distribution (yellow) also suggests that the fraction of adsorbates is substantially enhanced now. For the distance-dependent four-point measurements, a non-equidistant tip configuration is chosen, as it was used before in section 6.2.1 and is depicted in the inset in Fig. 6.4. The results are depicted in Fig. 6.5(c), where the four-point resistance is plotted as function of the non-equidistant spacing x. From a fit (solid red line) according to Eq. (3.48) a pure two-dimensional conductivity of $\sigma_{1\times1}^{\mathrm{Te}^*} = (2.3 \pm 0.1)\times10^{-7}\,\mathrm{S}/\square$ is obtained. A 3D contribution resulting from the Si substrate would result in a four-point resistance along the dashed green curve and therefore can be excluded.

A third deposition at a temperature of $350\,^{\circ}\mathrm{C}$ has been performed, in order to attempt, if the quality of the Te/Si-(1×1) surface termination can be further improved and a higher surface conductivity can be achieved. The STM image in Fig. 6.5(e) shows a uniformly covered surface, which indicates by comparing to Fig. 6.5(c) that now a much more continuous Te-termination at the surface has been achieved. Also the corresponding height distribution in Fig. 6.5(f) is now nearly perfectly symmetric and with a width of $\sigma_{\mathrm{RMS}} = 200\,\mathrm{pm}$ much narrower than before. There is still a slight imbalance, and when fitted again by multiple Gaussian peaks (red line), apart from the major contribution by the Te termination (blue curve) located at the center, a second small contribution arises (magenta curve), which is shifted by a value of $-310\,\mathrm{pm}$. Again, this magenta part can be attributed to holes in the surface termination, but due to the very small amount they are negligible in the present case. Also it appears that no adsorbates are present indicating that the growth temperature has been chosen optimally in order to enable all the adsorbates to contribute to the (1×1)-termination and to cause any excess material to desorb from the surface. So, a substrate temperature of $350\,^{\circ}\mathrm{C}$ is the best choice for establishing the Te/Si(111)-(1×1) reconstruction. The four-point measurement depicted in Fig. 6.5(e) reveals that the surface exhibits a two-dimensional conductivity of $\sigma^{\mathrm{Te}}_{1\times1} = (3.0 \pm 0.2) \times 10^{-7}\,\mathrm{S}/\square$, as it can be again deduced by a fit (red line) according to Eq. (3.48). The conductivity value is only slightly enhanced compared to the value obtained in Fig. 6.5(c) [for comparison indicated by dotted red line in Fig. 6.5(e)], even if the quality of the reconstruction seems to be improved substantially. Again, a contribution of the 3D substrate to the measured conductivity can be excluded, as the expected four-point resistance (dashed green curve) differs significantly from the actual measurement.

In total, it can be concluded that the Te/Si(111)-(1×1) reconstruction exhibits a surface conductivity of $\sigma^{\mathrm{Te}}_{1\times1} = (3.0 \pm 0.2) \times 10^{-7}\,\mathrm{S}/\square$, which is substantially lower than the conductivity of the Te/Si(111)-(7×7) surface. If this value is compared to typical TSS conductivities of $\sigma_{\mathrm{TSS}} \approx 4 \text{ to } 8 \times 10^{-4}\,\mathrm{S}/\square$, it turns out to be much smaller, such that the interface channel would contribute less than $1\,\%$ to the total current transport in the TI/substrate system. Evidently, this contribution is negligible.

6.2.3. Bi- and Se-based terminations

For Bi-based van-der-Waals epitaxy of TI films, a common growth template is the Bi/Si(111)-($\sqrt{3}\times\sqrt{3}$) surface reconstruction with one monolayer Bi coverage (also named β-phase), which remains stable under Te flux [29, 130, 135–137]. The conductivity of this surface reconstruction is $\sigma^{\mathrm{Bi}}_{\sqrt{3}\times\sqrt{3}} = (1.4\pm0.1)\times10^{-4}\,\mathrm{S}/\square$, as it has been shown previously in section 4.1.3. This value is in the range of typical TSS conductivities, such that in this case a substantial fraction ($20\,\%$ to $35\,\%$) of the total current through the TI/substrate system would be transmitted by the interface channel. Because of this high parasitic conductance a Bi-terminated interface of the Si(111) substrate exhibiting the Bi/Si(111)-($\sqrt{3}\times\sqrt{3}$) reconstruction is not favorable for designing TI devices.

Similar results as for the Te/Si(111) interface terminations can also be expected for Se-based van-der-Waals epitaxy on Si(111) [132, 138, 139]. However, exact values for the surface conductivities of the respective (1×1) and (7×7) reconstructions have not yet been reported in the literature. Furthermore, in the case of initial Se termination, depending on the preparation parameters additional amorphous interface layers up to several nm in thickness can occur [135, 140]. Such extended interface regions can also have a significant effect on the total interface conductivity, which then involves a superposition of the conductivities of the Se/Si(111) substrate surface reconstruction and the additional amorphous layer(s).

Thus, it can be concluded here that the interface conductivity between a thin TI film and the substrate can have a significant influence on the overall current transport. It strongly depends both on the material system and the preparation parameters. Identified values for several common reconstructed interfaces are summarized in Tab. 6.1. For the example of TI films grown by Te-based van-der-Waals epitaxy, such as $\mathrm{Bi_2Te_3}$, $\mathrm{Sb_2Te_3}$ and corresponding ternary and quaternary compounds, the Te/Si(111)-(1×1) interface reconstruction is the best choice, since it exhibits a very low parasitic conductivity that hardly influences the current transport through the TSS channel. It is finally noted that potentially high interface

Surface reconstruction	Surface conductivity σ_S
Te/Si(111)-(7×7)	$(8.3 \pm 0.5) \times 10^{-6}\,\mathrm{S}/\square$ [Sec. 6.2.1]
Te/Si(111)-(1×1)	$(3.0 \pm 0.2) \times 10^{-7}\,\mathrm{S}/\square$ [Sec. 6.2.2]
Bi/Si(111)-($\sqrt{3} \times \sqrt{3}$) 1 ML	$(1.4 \pm 0.1) \times 10^{-4}\,\mathrm{S}/\square$ [Sec. 6.2.3]

Table 6.1.: Surface conductivities of different passivated and reconstructed surfaces of Si(111) used as a substrate for van-der-Waals epitaxy of thin TI films.

conductivities are a general problem not only for TI films but also for other van-der-Waals thin films. They must therefore be determined individually for each material system at hand.

6.3. Thin-film channel

The interior of the TI film is more difficult to separate out experimentally, simply because it is sandwiched between the top and bottom TSS channels. Therefore, a resort to a calculation of its conductivity from experimentally accessible parameters is used. Generically, the TI film conductivity is determined by the charge carrier concentration and the charge carrier mobility. Within this chapter, the charge carrier mobility is regarded as a given material parameter of the TI, and the focus is mainly on the determination of the charge carrier concentration, which in a thin film is principally determined by the dopant concentration and the band bending.

Because the concentration of (unintentional) dopants stemming from the growth process is not known, the charge carrier concentration and conductivity of the film cannot be calculated directly. However, it will be shown here that in the thin-film limit a variation of the dopant concentration does not influence the mobile charge carrier concentration in a significant way. This is in stark contrast to the situation of a half-infinite bulk crystal, where the doping through dopants in the material would lead to a strong shift of the band edges with respect to the Fermi energy inside the bulk, and therefore also to a strong effect on the mobile charge carrier concentration. In a thin film, the shift of the bands with respect to the Fermi energy and the near-surface band bending are much smaller. The reason is the long screening length compared to the film thickness [141–143]. The problem at hand therefore boils down to a calculation of the band bending in the thin film, from which the total charge carrier concentration in the film can be determined by integration, irrespective of the (unknown) dopant concentration.

In order to determine the band bending, two distinct levels of approximation are used. In the symmetric approximation, it is assumed that the TI has identical properties at its surface to the vacuum and its interface to the substrate. In this case, the position of the surface Fermi level relative to the Dirac point, which can be measured at the top TSS by angle-resolved photoemission (ARPES), is enough to calculate the band bending. In contrast, in the asymmetric approximation the surface Fermi level and the Fermi level in the thin film at the interface to the substrate are allowed to differ from each other. In this case, ARPES alone is not enough to determine the band bending in the film. However, if supplemented by gate-dependent four-probe transport measurements on the surface of the TI, the combined experimental information is sufficient to determine the band bending, the carrier concentration and thus the film conductivity. Based on this result, it is finally possible to disentangle the conductivity of the TSS channels [131].

6.4. Band bending in topological insulators

In principle, the bulk of a TI should be insulating, if the Fermi energy is located in the bulk band gap with only the Dirac cone of the TSS crossing it. But unintentional doping during the growth process may cause a considerable bulk conductivity [30, 124]. This in turn may result in an unwanted, substantial current flowing through the interior of the TI film rather than through the TSS. Fortunately, it is principally possible to influence the bulk conductivity of the TI by growing the material as a thin film with a large surface-to-volume ratio, realized for instance by film thicknesses in the range 10 to $100\,\mathrm{nm}$ [126]. In any thin film, there is an influence of the surface and interface states on the film's bulk conductivity, because charge may be transferred between the surface states and the interior of the film, resulting in near-surface and near-interface band bendings and corresponding space charge regions, and a concomitant reduction or increase of the concentration of mobile charge carriers in the film.

For trivial, non-topological surface and interface states with their often large density of states, the pinning of the Fermi level at the surface and interface states usually plays a decisive role for the band bending [88]. In contrast, there exists no Fermi level pinning by topological surface states, because the density of states in their Dirac cones is comparatively small. As a consequence, the filling levels of the TSS (i.e. the Dirac cone) on the energy axis are expected to *change* with each charge that is transferred between TSS and film interior. This warrants the re-examination of the common phenomenon of band bending in thin films for the special situation of a TI material.

In this chapter, the TI thin film is modelled as a narrow-bandgap semiconductor without Fermi level pinning. The near-surface band bending induced by the top and bottom TSS is calculated in a semi-classical approach, which includes both classical electrostatics and quantization effects that arise from the vertical confinement of electrons in the thin film with thicknesses in the range of several nanometers. Specifically, in the first step Poisson's equation, which relates the band curvature to the space charge density, is solved under appropriate boundary conditions. The resultant band bending potential is used in Schrödinger's equation to calculate the quantized eigenenergies which give rise to multiple subbands inside the conduction and valence bands. Since these subbands result in a modification of the effective density of states of valence and conduction bands, Poisson's equation must be solved a second time. Note that an exact solution would require a fully self-consistent solution of Poisson's and Schrödinger's equations. Here, this selfconsistency cycle is truncated after one and a half iterations, deriving the final band bending and mobile charge carrier concentrations from the second solution of Poisson's equation. Initially, this scheme is applied to the simple case of a semi-infinite bulk crystal with a single surface to vacuum. This serves as a reference for the thin film calculations which involve two boundaries, i.e. a surface to vacuum as well as an interface to the film substrate. Here, symmetric boundary conditions are assumed first, i.e. equal charge carrier densities in the top and bottom TSS. Finally, the more general case of asymmetric boundary conditions in a thin film is presented. Further details of the calculations are described below in the sections 6.4.2 and 6.4.3.

Throughout this chapter, the following notation is used: The chemical potential (Fermi energy E_F) is constant across the TI film. The z-dependent position of the valence band edge is denoted as $E_V(z)$. Relative to the valence band edge, the Fermi levels at the top surface, in the bulk of the TI, and at the bottom interface to the substrate are designated as $E_F^{\text{top}} \equiv E_F - E_V^{\text{top}}$, $E_F^{\text{bulk}} \equiv E_F - E_V^{\text{bulk}}$, and $E_F^{\text{bottom}} \equiv E_F - E_V^{\text{bottom}}$, respectively.

6.4.1. Near-surface band bending in a semi-infinite bulk crystal

In this section, the band bending and its determining parameters are discussed for the case of a semi-infinite bulk crystal with one topological surface state at the surface (top TSS).

6.4.1.1. Formalism

Poisson's equation which is expressed by

$$\frac{d^2}{dz^2}\Phi(z) = -\frac{\rho(z)}{\epsilon_0\epsilon_r} \tag{6.1}$$

relates the space charge density $\rho(z)$, measured in units of charge per area, to the spatial curvature of the bands in the space charge region. In writing down this equation, the assumption is used that parallel to the surface no spatial dependence of the bands occurs, i.e. $\Phi(x, y, z) = \Phi(z)$. The potential $\Phi(z)$ is given by

$$q\Phi(z) = E_F - E_{\text{intrinsic}}(z) \tag{6.2}$$

with q being the elementary charge and $E_{\text{intrinsic}}(z)$ the intrinsic level, while the band bending is defined as

$$V(z) \equiv \Phi(z) - \Phi_b, \tag{6.3}$$

where Φ_b is the potential in the bulk, i.e. $\Phi_b \equiv \Phi(z \to \infty)$. In the calculations of band bending, specific material parameters of the TI are used as input, i.e. in particular the band gap and the effective masses of electrons and holes. Moreover, a parabolic approximation for the bulk band edges is used in order to calculate the effective densities of states N_C^{eff} and N_V^{eff} in the valence and conduction bands that determine the mobile charge carrier densities in the (bulk) TI. Further details on this can be found in section 6.5.1. Finally, the non-degeneracy of the TI is assumed, such that the Fermi distribution can be approximated by the Boltzmann distribution.

By introducing the dimensionless potentials

$$u(z) = \frac{q}{k_B T}\Phi(z) \qquad \text{and} \qquad v(z) = \frac{q}{k_B T}V(z), \tag{6.4}$$

where T is the temperature and k_B the Boltzmann constant, Poisson's equation (6.1) becomes [88, 144]

$$\frac{d^2 v}{dz^2} = -\frac{q^2}{\epsilon_0 \epsilon_r k_B T}\left(n_b - p_b + p_b e^{-v} - n_b e^{v}\right). \tag{6.5}$$

The quantities n_b and p_b denote the electron and hole densities in the bulk, respectively, which are proportional to e^{u_b}. The first two terms on the right correspond to the static charge caused by the dopant atoms in the material and the last two terms on the right specify how the mobile charge carrier densities in the space charge region are modified by the band bending $v(z)$. Eq. (6.5) can be expressed as

$$\frac{d^2 v}{dz^2} = \frac{1}{L^2}\left(\frac{\sinh(u_b + v)}{\cosh(u_b)} - \tanh(u_b)\right), \tag{6.6}$$

with the effective *Debye* length

$$L = \sqrt{\frac{\epsilon_0 \epsilon_r k_B T}{q^2 (n_b + p_b)}}. \tag{6.7}$$

By multiplying both sides of Eq. (6.6) with $2\frac{dv}{dz}$ and using $2\frac{dv}{dz}\frac{d^2v}{dz^2} = \frac{d}{dz}(\frac{dv}{dz}\frac{dv}{dz})$, it can be integrated to yield, after taking the square root,

$$\frac{dv}{dz} = \operatorname{sgn}(-v)\frac{\sqrt{2}}{L}\sqrt{\frac{\cosh(u_b + v)}{\cosh(u_b)} - v\,\tanh(u_b) + c}. \tag{6.8}$$

The integration constant c must be determined from the boundary conditions. For a semi-infinite bulk crystal the boundary conditions are

$$\left.\frac{dv}{dz}\right|_{z\to\infty} = 0 \qquad \text{and} \qquad v(0) = v_{\text{top}} = \frac{1}{k_B T}\left[E_F^{\text{top}} - E_F^{\text{bulk}}\right]. \tag{6.9}$$

Inserting these boundary conditions into Eq. (6.8) and expressing the hyperbolic functions by exponentials leads to the solution [88, 144]

$$z(v) = \operatorname{sgn}(-v)\frac{L}{\sqrt{2}}\int_{v_{\text{top}}}^{v(z)}\sqrt{\frac{e^{u_b} + e^{-u_b}}{e^{u_b}(e^{v'} - v' - 1) + e^{-u_b}(e^{-v'} + v' - 1)}}\,dv'. \tag{6.10}$$

More details on the derivation of Eqs. (6.5) – (6.10) are listed in the appendix A.3. Eq. (6.10) can be integrated numerically and inverted to determine the band bending $v(z)$. Since the latter is influenced decisively by the boundary condition, i.e, the surface position of the Fermi level relative to the band edges (E_F^{top}), in the next section it will be turned to a discussion of the factors which determine this parameter.

6.4.1.2. Topological surface states

The Fermi energy at the surface of a conventional semiconductor is often pinned at a fixed position E_F^{top} relative to the band edges. This is a consequence of a high density of states of the semiconductor surface states. In contrast, the surface density of states of the intrinsic TSS in TIs is relatively low, which is the outcome of the specific linear dispersion of the TSS, i.e. the Dirac cone $E(k) = \hbar v_F k$ [145]. As a result, there is no pinning of E_F^{top} by the intrinsic TSS at the surface of a TI.

The charge carrier density of Dirac electrons in the TSS, generated by charge transfer from the film, can be written as a function of energy E up to which the cone is filled as [131]

$$n_{\mathrm{TSS}}(E) = \frac{1}{4\pi\hbar^2 v_F^2}\left(E^2 - E_0^2\right) . \tag{6.11}$$

Here, E_0 represents an initial filling level that may be caused by surface doping due to surface defects or adsorbates (see below). In the absence of surface defects, $E_0 = 0$. The filling level of the Dirac cone in a TI, i.e. the surface Fermi energy E_F^{top}, can be determined by surface-sensitive ARPES measurements and then used as a known parameter in the band bending calculations. Since there is no pinning, E_F^{top} is subject to several external factors, in particular the bulk dopant concentration, the density of adsorbates on the surface, and the presence of a gate voltage. The influence of these parameters will be discussed in more detail below.

6.4.1.3. Non-topological, trivial defect states

The charge neutrality level (CNL) of a surface state is the position of the Fermi level at which the surface is uncharged. In the case of a TI the CNL of the intrinsic TSS coincides

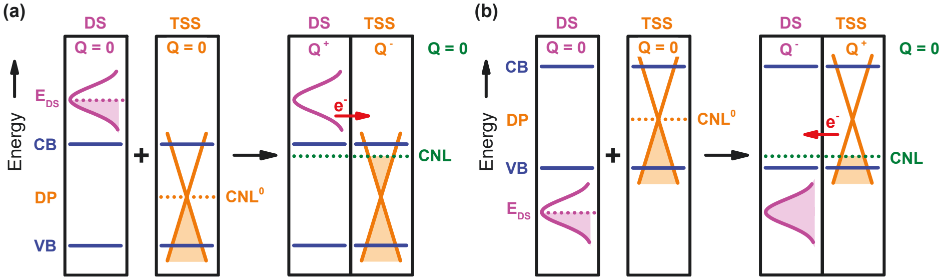

Figure 6.6.: Principle of the formation of the CNL level of the TI surface for the presence of additional charged trivial defect states (DS). Both the DS (magenta) located around E_{DS} and the TSS (Dirac cone, orange) would be filled up to their individual charge neutrality levels (dotted lines), if they were artificially separated from each other [left parts of (a) and (b)]. However, if the DS and TSS are combined (right parts), a charge transfer occurs, resulting in a common aligned CNL (green line). This final CNL is influenced by the position of the DS (E_{DS}) either above (a) or below (b) the Dirac point (DP).

with the Dirac point. However, the presence of additional trivial defect states (DS) at the surface of the TI, for example surface vacancies or additional adsorbates, may have a strong influence on the CNL of the TSS. Specifically, the surface doping caused by such trivial defects may modify the filling level of the TSS in order to fulfill charge neutrality of the surface. Therefore, the CNL of the combined TSS/DS system (considered as isolated from the bulk) is generally not located at the Dirac point. A schematic that illustrates the shift of the surface CNL from the intrinsic value of the TSS, i.e. the Dirac point, to a new value that is determined by surface charge neutrality between the DS and the TSS is displayed in Fig. 6.6. The density of states of the trivial DS (magenta) is centered around E_{DS}. For the position of E_{DS} two different cases are considered in Figs. 6.6(a) and 6.6(b). Initially (before electrical connection with the TSS), the DS is neutral and filled up to its charge neutrality level E_{DS} (dotted magenta line). The isolated Dirac cone of the TSS (orange) is also neutral and filled up to the Dirac point which represents the initial charge neutrality level CNL^0 of the TI surface (dotted orange line). If the trivial DS and the TSS are connected, a charge transfer occurs, yielding a common value for the CNL of the TI surface (dotted green line). For a DS above the Dirac point, as shown in Fig. 6.6(a), electrons flow into the TSS, increasing the filling level of the Dirac cone and reducing the filling level of the DS. As a result, the DS becomes positively charged and the TSS negatively charged, but in total the neutrality condition is maintained. Similarly, for a DS positioned below the Dirac point, Fig. 6.6(b), charge transfer occurs in the reverse direction. Electrons from the TSS flow into the DS, which results in a negative DS and a positive TSS with a common CNL below the Dirac point. In the examples in Fig. 6.6, the DS is either completely filled or completely depleted by the charge transfer to or from the TSS, respectively. However, depending on the properties of the DS, i.e. its position E_{DS} and width, it is also conceivable that the DS remains partially filled after charge transfer.

In conclusion, the CNL of the TI surface and thus the filling level of the TSS is influenced by the presence of any additional trivial DS. Both a change of the filling level of the DS and a shift of E_{DS} provoke a corresponding shift of the surface CNL. This overall surface CNL becomes relevant when the charge exchange between the surface and the bulk of the TI is enabled and influences the resultant near-surface band bending.

6.4.1.4. Charge transfer between TSS and bulk

Generally speaking, band bending is governed by the condition of charge neutrality: the total charge (per unit area) in surface states and the total mobile charge per unit area in the space charge layer must be equal and of opposite sign. This charge neutrality involves charge transfer between the surface and the space charge layer. To understand this charge transfer conceptually, a situation is considered in which surface and bulk are initially disconnected [146]. In this situation, the filling level of the TI surface (comprising TSS and DS) corresponds to its charge neutrality level (CNL) at which the separated TI surface itself is neutral (only in the absence of any DS, this CNL coincides with the Dirac point). In the separated bulk, neutrality implies the absence of any band bending below the surface, thus the charge neutrality level corresponds to the bulk Fermi level. If surface and bulk are connected to each other, the separate CNL of bulk and surface will in general not be aligned to each other. As a consequence, charge will flow from the component with the higher CNL to the component with the lower one. In the process, surface and space charge layer will become charged and the bands in the near-surface region will bend, but overall charge neutrality is conserved. The CNL of the TI surface (TSS plus DS) can thus be described as the initial filling level up to which the (neutral) TI surface is filled before equilibration with the bulk. As such, it is not a quantity that can be measured.

6.4.1.5. Relevant parameters for overall band bending

For an extended bulk crystal, the surface CNL, the surface Fermi energy E_F^{top}, and the bulk Fermi energy E_F^{bulk} (which represents the bulk dopant concentration) all influence the charge that finally resides in the TSS and space charge layer, and thus the band bending. The three parameters are interdependent: if two of them are given, the third one is fixed by the charge neutrality condition. It is clear that the surface CNL, and thus also the initial filling level of the TSS, is a conceptual quantity that describes a neutral TI surface (comprising both TSS and DS) which is isolated from the bulk of the TI crystal; it is therefore not measurable. However, the surface Fermi energy E_F^{top} and thus the final filling level of the Dirac cone can be directly observed by ARPES measurements. In contrast, the exact value for the bulk Fermi energy E_F^{bulk} is not known, as the exact density of dopants in the bulk TI material is often unspecified, so that E_F^{bulk} has to remain as a free parameter in the calculations.

6.4.1.6. Example calculations

In order to explore the interplay of the three key parameters and their impact on the band bending in a semi-infinite bulk TI crystal, Fig. 6.7 outlines band diagrams for three different bulk dopant concentrations, i.e. nondegenerate p-doped [Fig. 6.7(a)], intrinsic [Fig. 6.7(b)] and nondegenerate n-doped [Fig. 6.7(c)]. For the calculated diagrams, a specific value for either E_F^{top} (blue) or the surface CNL (gray) is used – the respective other parameter results from the condition of charge neutrality. For all three blue diagrams in Figs. 6.7(a) – 6.7(c), the value of E_F^{top} is fixed to the midgap position. Such a situation was experimentally realized in the quaternary BiSbTeSe system [147], for example.

For the p-doped TI in Fig. 6.7(a), a downward band bending with a negatively charged space charge region is obtained. The TSS is positively charged, as indicated by the calculated CNL above E_F. The filling level of the Dirac cone has thus been reduced and electrons have flown into the space charge region (highlighted blue area). In case of an even stronger downward band bending, as obtained for example by a degenerately doped bulk, a non-topological two-dimensional electron gas (2DEG) with quantized states is expected near the surface. This has been observed experimentally [148–150]. In this limit, the description by Poisson's equation has to be replaced by the Schrödinger-Poisson approach even for an extended bulk crystal.

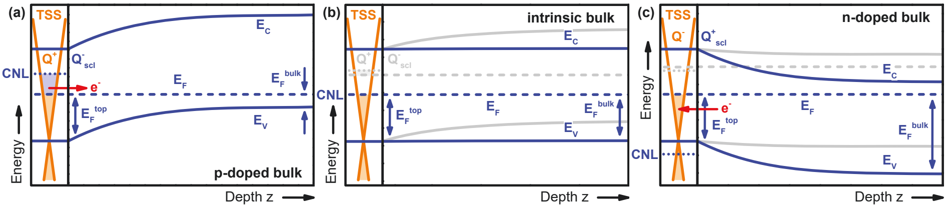

Figure 6.7.: Principle of band bending in extended TI bulk crystals for three different bulk dopant concentrations, i.e. (a) p-doped ($E_F^{\text{bulk}} = 35\,\text{meV}$, $p_{\text{bulk}} = 4 \times 10^{17}\,\text{cm}^{-3}$), (b) intrinsic ($E_F^{\text{bulk}} = 130\,\text{meV}$, $n_{\text{bulk}} = p_{\text{bulk}} = 1 \times 10^{16}\,\text{cm}^{-3}$), and (c) n-doped ($E_F^{\text{bulk}} = 225\,\text{meV}$, $n_{\text{bulk}} = 4 \times 10^{17}\,\text{cm}^{-3}$), in combination with fixed values for either the surface Fermi energy E_F^{top} (blue) or the charge neutrality level CNL (gray) of the TI surface (TSS plus DS). On the left of each panel, the partially filled (highlighted orange area) Dirac cone of the TSS is shown, and on the right the calculated conduction and valence bands are plotted as function of depth z into the crystal. The Fermi energy E_F (dashed line, constant) and both the surface Fermi energy E_F^{top} and the bulk Fermi energy E_F^{bulk} (blue arrows) are indicated. For the blue diagrams E_F^{top} is fixed to a midgap value of $130\,\text{meV}$, resulting in different band bendings and CNL positions (dotted lines) from (a) to (c). In contrast, the gray diagrams (b,c) exhibit a fixed CNL at $230\,\text{meV}$ [same as in (a)], so that in this case E_F^{top} varies from (a) to (c) and the shape of band bending differs from the blue-colored case. Further calculation parameters m^*, v_{Fermi}, T, E_{Dirac} and E_{gap} are listed in Tab. 6.2.

In Fig. 6.7(b), the bulk Fermi energy E_F^{bulk} is in the midgap position, representing the intrinsic character of the bulk of the TI. In conjunction with the assumed midgap position of E_F^{top} this results in flat bands. In this case, the calculated CNL is equal to E_F, indicating that no charge transfer has occurred. Note that the CNL in Fig. 6.7(b) is different from the one in obtained in Fig. 6.7(a), because its value must depend on E_F^{bulk} if a constant midgap position of E_F^{top} is assumed.

For the n-doped TI in Fig. 6.7(c), an upward band bending is obtained, if a midgap position of E_F^{top} is assumed (blue lines). The calculated CNL is now far below the E_F, indicating a charge transfer of electrons from the bulk into the Dirac cone.

If on the other hand the CNL is assumed to be constant (instead of E_F^{top} as discussed above), the resulting band bendings for the same three bulk dopant concentrations as considered before turn out to be completely different. This is demonstrated by the gray band diagrams in Figs. 6.7(b) – 6.7(c). Physically, a constant value for the CNL corresponds to a fixed surface configuration with a specific density of surface defects or adsorbates. Specifically, in Fig. 6.7(b) the flat bands for the midgap position of E_F^{bulk} give way to a downward band bending, because now E_F^{top}, being dependent on both E_F^{bulk} and CNL, is not positioned midgap any more. Similarly, in Fig. 6.7(c) the same position of the CNL as for the gray bands in Fig. 6.7(b) yields a much weaker upward band bending, with a different position of E_F^{top}(dashed gray line).

Two conclusions can be drawn from the above examples: (1) Comparing blue versus gray bands in each panel, Figs. 6.7(b) and 6.7(c), it can be observed that a variation of the CNL due to surface defect states directly influences E_F^{top}, if the bulk dopant concentration remains constant. Therefore, if the surface defect concentration is increased over time, a shifting E_F^{top} is expected. This effect of surface degradation due to long-time storage of TIs in vacuum or exposure to air has indeed been observed experimentally by ARPES measurements [148, 151, 152]. (2) Comparing the blue bands in Fig. 6.7(a) and gray bands in Figs. 6.7(b) and 6.7(c) among each other (fixed CNL) shows that the bulk dopant concentration, which varies from Figs. 6.7(a) to 6.7(c), has a strong influence on E_F^{top} and therefore also on the band bending. Thus, for an extended semi-infinite bulk crystal both the surface Fermi energy E_F^{top} and the bulk dopant concentration, represented by E_F^{bulk}, must be known to perform an exact calculation of the near-surface band bending (Note that this makes the knowledge of difficult-to-determine CNL superfluous, because the latter is at any rate determined by E_F^{top} and E_F^{bulk}). Remarkably, this is in contrast to the situation for thin TI films, for which the band bending can be calculated reasonably well *without* the knowledge of E_F^{bulk}, as it will be shown in the next section.

6.4.2. Symmetric band bending in a thin film

In this section, a symmetric approach for the calculation of the band bending in thin films with two topological states at the boundaries is presented.

6.4.2.1. Top and bottom topological surface states

In the case of a thin TI film, there exist two TSS, one each at the top and bottom surfaces of the film (note that the bottom surface of the film corresponds to its interface to the substrate). The bottom TSS is not directly accessible by surface sensitive methods and therefore difficult to investigate. Thus, if no further information is available, it is a reasonable first approximation to assume that the properties, in particular the filling levels, of the bottom TSS are identical to the top TSS. This symmetric approximation, in which only information about the top TSS is needed and in which the boundary conditions on the top and bottom surfaces are the same, is considered in the present section.

For a thin film of thickness d with two surfaces and $E_F^{\text{top}} = E_F^{\text{bottom}}$, the problem is symmetric with respect to $z_0 = d/2$, and the appropriate boundary conditions are

$$\left.\frac{dv}{dz}\right|_{z_0=\frac{d}{2}} = 0 \qquad \text{and} \qquad v(0) = v(d) = v_{\text{top}} = \frac{1}{k_B T}\left[E_F^{\text{top}} - E_F^{\text{bulk}}\right]. \tag{6.12}$$

The solution of Eq. (6.8) for these boundary conditions, which evidently must lead to a symmetric band bending, can be expressed in the interval of $0 \leq z \leq \frac{d}{2}$ by

$$z(v) = A \int\limits_{v_{\text{top}}}^{v(z)} \sqrt{\frac{e^{u_b} + e^{-u_b}}{e^{u_b}\left(e^{v'} - e^{v\left(\frac{d}{2}\right)} - v' + v\left(\frac{d}{2}\right)\right) + e^{-u_b}\left(e^{-v'} - e^{-v\left(\frac{d}{2}\right)} + v' - v\left(\frac{d}{2}\right)\right)}}\, dv' \tag{6.13}$$

with the prefactor $A = \operatorname{sgn}(-v)\frac{L}{\sqrt{2}}$. More details about the derivation can be found in appendix A.3.3. Eq. (6.13) has to be calculated iteratively, because the potential $v\left(\frac{d}{2}\right)$ is not known *a priori*. In the first iteration step, $v\left(\frac{d}{2}\right)$ is determined by numerical inversion, i.e. the upper limit of the integral is set to $v(z) = v\left(\frac{d}{2}\right)$ and $z(v) = \frac{d}{2}$ is inserted. Afterwards, the equation can be solved for the remaining values $v(z)$ in the interval $0 \leq z < \frac{d}{2}$. The case of symmetric band bending in a thin film has been considered before in the framework of the Schottky approximation [153, 154]. However, the latter approximation is only valid for depletion layers with a strong band bending $|eV_{\text{top}}| \gg k_BT$, whence all free charge carriers are transferred from the interior of the film into the TSS, resulting in a completely depleted and insulating material in the film. But since both direction and quantity of the charge transfer are influenced by several parameters, as illustrated in section 6.4.1 in detail, depletion layers with small band bending as well as accumulation layers are conceivable, for which a description within the Schottky approximation is insufficient.

6.4.2.2. Quantization

Due to finite thickness of the film, the quantization arising from the confinement of electrons in the direction perpendicular to the film must be taken into account. As stated above, this requires the solution of coupled Poisson's and Schrödinger's equations. For weak band bending, which turns out to be the relevant situation for the thin TI films studied here (see below), the potential can be approximated as a square potential with infinite barriers when solving the Schrödinger equation. Further details of the calculation can be found in section 6.5. It turns out that the calculated mobile charge carrier density in the thin TI film, which is discussed in the following, is reduced by a factor of 2 to 2.5 compared to the purely classical approach in which only Poisson's equation is solved.

6.4.2.3. Influence of the film thickness

In addition to the three parameters which jointly determine the band bending of a semi-infinite bulk TI crystal (see above), a fourth parameter becomes relevant in the thin-film limit — the film thickness d. It influences the amount of charge which can be transferred between the surface and the TI film. As the film thickness decreases, the total charge that can be transferred into the space charge region becomes increasingly limited, with the result of a less pronounced band bending, because charge neutrality imposes the same limit on the surface charges (TSS/DS) on both surfaces. Again, all four parameters E_F^{top}, E_F^{bulk}, CNL and d are interdependent, such that one parameter is given by the other three.

In order to illustrate the effect of limited charge transfer by means of an example, in Fig. 6.8 the calculated band bending at room temperature is displayed for the TI material BiSbTe_3 (considered in more detail in section 6.4.2.6) as function of depth z for three different bulk dopant concentrations, i.e. n-doped [Fig. 6.8(a)], intrinsic [Fig. 6.8(b)] and p-doped [Fig. 6.8(c)]. The red band diagrams belong to a 10 nm thin film, while the blue bands represent the corresponding extended bulk crystal with the same bulk dopant concentration and position of the surface Fermi energy E_F^{top}. For the calculation, the band gap is set to 260 meV and a fixed $E_F^{\text{top}} = 240\,\text{meV}$ has been chosen. Moreover, the Dirac point coincides with the edge of the valence band and the effective mass is set to $m^* = 0.15\,m_e$,

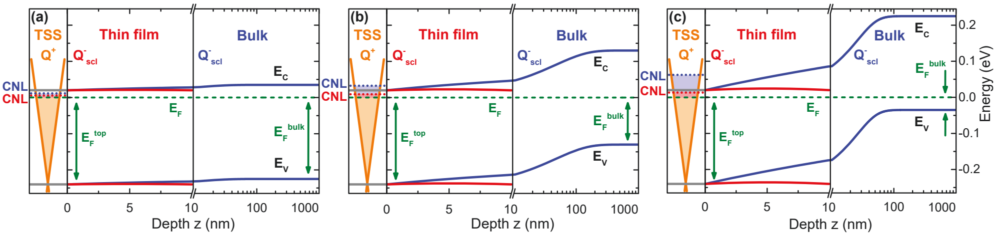

Figure 6.8.: Calculated band diagrams using the symmetric approximation for a $10\,\mathrm{nm}$ BiSbTe$_3$ thin film for three different dopant concentrations, i.e. (a) n-doped ($E_F^{\mathrm{bulk}} = 225\,\mathrm{meV}$, $n_{\mathrm{bulk}} = 4 \times 10^{17}\,\mathrm{cm}^{-3}$), (b) intrinsic ($E_F^{\mathrm{bulk}} = 130\,\mathrm{meV}$, $n_{\mathrm{bulk}} = p_{\mathrm{bulk}} = 1 \times 10^{16}\,\mathrm{cm}^{-3}$), and (c) p-doped ($E_F^{\mathrm{bulk}} = 35\,\mathrm{meV}$, $p_{\mathrm{bulk}} = 4 \times 10^{17}\,\mathrm{cm}^{-3}$). For all diagrams, the surface Fermi energy E_F^{top} is set to 20 meV below the conduction band edge resulting from ARPES measurements [131]. Further parameters of the calculation are listed in Tab. 6.2. In the central parts of the panels (a) – (c), the conduction and valence bands of the thin film are shown as function of depth z from the surface (red lines), while in the left parts of (a) – (c) the partially filled Dirac cone (orange) of the top TSS is depicted. The blue lines show the band bending in a corresponding extended bulk crystal exhibiting the same dopant concentration as the thin film. The Fermi energy (dashed green line) and both E_F^{bulk} and E_F^{top} (arrows) are indicated. In contrast to the bulk case, the band positions in the thin film are not influenced significantly by the dopant concentration. The CNLs (colored dotted lines) are different for the thin film (red) and the bulk (blue), but in both cases positioned above E_F^{top}, giving rise to a downward band bending due to a transfer of negative charges from the TSS to the film or bulk.

in agreement with ARPES measurements [131]. All parameters of the calculation are summarized in Tab. 6.2.

In Fig. 6.8, it can be observed that for the bulk crystal (blue curves) the dopant concentration, represented in the calculations by the value of the bulk Fermi energy E_F^{bulk}, strongly influences the actual E_F^{bulk}, and results in a strong increase of the near-surface band bending in Fig. 6.8(b) (intrinsic material) and 6.8(c) (p-doped material), since E_F^{top} is fixed close to the conduction band by construction. In contrast, in the thin-film limit (red curves) the bending of the bands remains weak and largely independent of the dopant concentration, even for different dopant types (Fig. 6.8(a) n-doped vs. Fig. 6.8(c) p-doped). Thus, in the thin film the valence band position relative to the Fermi level can differ strongly from its value in a bulk crystal with the same dopant concentration [Fig. 6.8(c)]. This at first glance surprising behavior of the film can be rationalized by the behavior of the CNL of the TSS, which turns out to be very different for the thin film (red dotted lines in Fig. 6.8) and the bulk (blue dotted lines): On the one hand, charge transfer from the TSS into the TI (only this direction occurs in Fig. 6.8) is strongly suppressed for the thin film – the red (thin film) CNL appears always close to E_F at the surface, while the blue (bulk) CNL is consistently located above the red one, for Fig. 6.8(c) actually substantially above the red. On the other hand, even the comparatively little charge that is transferred from the TSS into the thin film is sufficient to change the whole film from intrinsic to n-type [Fig. 6.8(b)] or indeed from p-type to n-type [Fig. 6.8(c)]. At this point, it has to be distinguished between the dopant

Parameter	Value
m^*	$0.15\,m_e$
v_{Fermi}	$5.6 \times 10^{-5}\,\text{ms}^{-1}$
T	$300\,\text{K}$
E_{Dirac}	$0\,\text{eV}$ (at valence band)
E_{gap}	$0.26\,\text{eV}$
E_F^{top} ($V_{\text{gate}} = 0\,\text{V}$)	$0.24\,\text{eV}$
$n_{\text{TSS}}^{\text{top}}$ ($V_{\text{gate}} = 0\,\text{V}$)	$4 \times 10^{12}\,\text{cm}^{-2}$

Table 6.2.: Different fixed parameters used as input for the band banding calculations for the TI system BiSbTe$_3$ as reported in Ref. [131].

and doping concentrations in the TI material. The former describes the concentration of defects in the material, determined by the growth conditions, while the latter specifies the concentration of mobile charge carriers in the material. In an extended crystal the concentration of dopants directly controls the concentration of mobile carriers, i.e. the doping, but for a thin TI film with an additional source of charges, the TSS, this is not true. For example, in Fig. 6.8(b) the dopant concentration in the film corresponds to an intrinsic bulk TI material, but the additionally transferred charges from the TSS are sufficient to nearly fully n-dope the film [Fig. 6.8(b)], or even completely saturate all acceptors in the p-type film material of Fig. 6.8(c) and still result in essentially the same n-doping as in Fig. 6.8(b). As there is a small increase in charge transfer from Figs. 6.8(a) to 6.8(c), also the band bending increases slightly, but it is still very weak compared to the bulk case (blue).

In conclusion, Fig. 6.8 illustrates a significant difference compared to the case of the semi-infinite bulk crystal in the section 6.4.1: For a 10 nm thin film the band bending across the complete film is largely independent of the dopant concentration in the film; in fact, the bands remain nearly flat at the surface position E_F^{top} for widely varying bulk dopant levels. Thus, the position of the Fermi energy inside the film deviates strongly from the bulk Fermi energy E_F^{bulk} of a corresponding semi-infinite bulk crystal with the same dopant concentration. Notably, this allows the approximation of the total mobile charge carrier concentration in the thin film from information gained from surface-sensitive measurements, even if the dopant concentration inside the film material remains unknown.

6.4.2.4. Screening

The weak band bending in the thin TI film is linked to the long screening length L compared to the small film thickness d. This is immediately obvious from Eq. (6.6), which shows that the curvature of the band bending potential v is inversely proportional to the square of L. A small curvature of course also limits the value of v that can be reached over the thickness $d \ll L$ of the film. If the film thickness d approaches the screening length L, the total charge transfer between TSS and film becomes larger, resulting in an increasingly stronger band bending. For $d > 2L$, the space charge region in the film becomes the same as in an extended bulk crystal.

According to Eq. (6.7), the screening length L also depends on the carrier densities $n_b + p_b$. The larger $n_b + p_b$, the shorter is L. Therefore, the near independence of the band bending on the bulk dopant concentration in the thin film is only found for not too high dopant levels in the TI material. Furthermore, a long screening length can also be caused by a large dielectric constant, which is characteristic for many TI materials. For example, for BiSbTe$_3$ a value of $\epsilon_r \approx 100$ is reported [141–143].

6.4.2.5. Degenerate doping

In Fig. 6.8, only non-degenerate doping levels in the TI have been considered, all of which apparently lead to a downward band bending. Of course, it is in principle also possible that the dopant concentration is sufficiently high for the TI material to be degenerately n-doped, with E_F^{bulk} above the conduction band edge. According to the calculations, electrons from the film then flow into the TSS. But because of the limited number of available charge carriers, the Fermi energy in the film drops below the conduction band and in the end nearly coincides with E_F^{top}, resulting in a weak upward band bending. Thus, again the finite film thickness $d \ll L$ leads to an effective suppression of band bending in the film in the case of a slight degenerate doping.

Only for very strong degenerate doping the screening length can become so small that a stronger band bending is obtained in the thin TI film, leading to a pronounced dependency of the charge carrier density in the film on the film dopant concentration. However, the case of such a strong degenerately doped TI film, where the Fermi energy is located deep inside the bulk bands, is undesirable, as in this case the interior of the film will become the dominant parasitic conduction channel due to the high DOS of the bulk states. State of the art growth of ternary or even quaternary materials avoids this undesirable case of degenerate doping. Furthermore, it is clear that for degenerately doped materials the Boltzmann approximation is not valid any more. Instead, all calculations must employ the Fermi-Dirac distribution. Indeed, such calculations are possible, but the equations are more complex.

Thus, all calculations presented in this chapter are performed for the more relevant case of non-degenerate doping. It has to be noted that already a surface Fermi level E_F^{top} only 20 meV below the conduction band edge, which is assumed in Fig. 6.8, stretches the validity of the Boltzmann approximation. In this case, the deviation between the Fermi-Dirac and Boltzmann distributions is up to $50\,\%$, but as the value of the Boltzmann distribution is larger compared to the Fermi-Dirac distribution, i.e. $f_{\text{FD}}(E - E_F) < f_{\text{B}}(E - E_F)$, the band bending, when calculated with the Boltzmann distribution, will only be overestimated. The true band bending will be even smaller.

6.4.2.6. The example of BiSbTe$_3$

Within this chapter, the focus is on the specific TI material (Bi$_{1-x}$Sb$_x$)$_2$Te$_3$ with $x = 0.5$, i.e. BiSbTe$_3$, which was studied extensively in Ref. [131, 155]. Fig. 6.8 used above to illustrate generic properties of band bending in thin TI films, was already calculated for this case. The assumption of a fixed E_F^{top} in Figs. 6.8(a) to 6.8(c) corresponds to the situation in which a definite value of E_F^{top} is measured by ARPES on an MBE-grown BiSbTe$_3$ film; the different values of the surface CNL in Figs. 6.8(a) to 6.8(c) would then indicate different surface concentrations of adsorbates and/or surface defects. From this perspective, each band diagram in Fig. 6.8 corresponds to a distinct initial state which after charge transfer between the surface and the film interior results in the final state observed by a particular ARPES measurement (i.e. in the present case E_F^{top} = 240 meV [131]). The aim is to identify the most likely initial state and therefore also the corresponding band bending scenario.

In BiSbTe$_3$, the surface Fermi energy E_F^{top} is observed to be very close to the conduction band edge, as measured by ARPES [131, 155]. As demonstrated in Fig. 6.8, this results in *weak* downward band bending for p-, intrinsic and n-type dopant concentrations. On the other hand, if the film material is strongly or even degenerately n-doped, a result can also be a weak upward bending (see section above). Generally, such a situation with upward band bending, obtained for a E_F^{top} positioned further away from the conduction band edge, has been discussed recently within the Schottky approximation [153, 154]. However, a high dopant concentration in the bulk would be in contradiction with the aim to grow films of ternary TI material systems with a minimal conductivity of the interior of the film gap [126]. For this reason, the case of upward band bending is excluded for the material BiSbTe$_3$ discussed here.

Furthermore, as long as E_F^{top} in BiSbTe$_3$ is positioned below the conduction band edge, as observed in ARPES [131, 155], a *strong* downward band bending which would produce a non-topological 2DEG near the surface can also be excluded. A 2DEG has been observed in recent studies [148–150], but in all these cases E_F^{top} is positioned deep inside the conduction band, while the Fermi energy inside the film material is still inside the band gap.

The doping character of a thin TI film can be strongly influenced by the stoichiometric composition [151, 156, 157]. In some experiments on (Bi$_{1-x}$Sb$_x$)$_2$Te$_3$ and (Bi$_{1-x}$Sb$_x$)$_2$Se$_3$ with stoichiometric parameters $x \neq 0.5$, the surface Fermi energy E_F^{top} is found closer to mid-gap [158, 159]. If such a situation occurs, for appropriate film thicknesses and screening lengths the thin film could possibly become fully depleted, as almost all negative mobile charge carriers flow into the TSS. This would result in a midgap position of the Fermi energy inside the film, and, in these circumstances, the film material would be completely insulating. However, this state of affairs can be excluded for the case of BiSbTe$_3$, since E_F^{top} is located very close to the conduction band edge, as measured by ARPES [131, 155]. Therefore, it can be concluded that for BiSbTe$_3$ from the experiment in Ref. [131] the band bending must be *weakly* downward.

6.4.2.7. Mobile charge carrier density

Within the Boltzmann approximation, the mobile charge carrier density can be calculated from the potential $v(z)$ by $n_e(z) = n_b \exp[v(z)]$ and $p_h(z) = p_b \exp[-v(z)]$ for electrons and holes, respectively. Integrating the sum of $n_e(z)$ and $p_h(z)$ over the thickness d of the thin film results in the total mobile charge carrier density

$$n_{\text{film}}\left(E_F^{\text{top}}, E_F^{\text{bulk}}\right) = \int_0^d n_i \left[e^{\left[u_b\left(E_F^{\text{bulk}}\right)+v\left(z,E_F^{\text{top}},E_F^{\text{bulk}}\right)\right]} + e^{-\left[u_b\left(E_F^{\text{bulk}}\right)+v\left(z,E_F^{\text{top}},E_F^{\text{bulk}}\right)\right]}\right] dz \tag{6.14}$$

inside the film material, with n_i denoting the intrinsic charge carrier concentration. In general, n_{film} is both dependent on the dopant concentration in the film, which is represented in the equation by the bulk Fermi energy E_F^{bulk} of a corresponding bulk crystal with same dopant density, and on the surface Fermi energy E_F^{top}.

In Fig. 6.9, the total mobile charge carrier density as function of the dopant level expressed by the bulk Fermi energy E_F^{bulk} is plotted for a thin film of BiSbTe$_3$ with $d = 10\,\text{nm}$ [131]. The surface Fermi energy E_F^{top} is an additional free parameter. As long as E_F^{top} is well within the band gap of BiSbTe$_3$, the charge carrier concentration in the thin film is nearly independent of E_F^{bulk}, i.e. $n_{\text{film}}(E_F^{\text{top}}, E_F^{\text{bulk}}) \approx n_{\text{film}}(E_F^{\text{top}})$. Only in the vicinity of the band edges, where also the Boltzmann approximation becomes less accurate, a deviation from

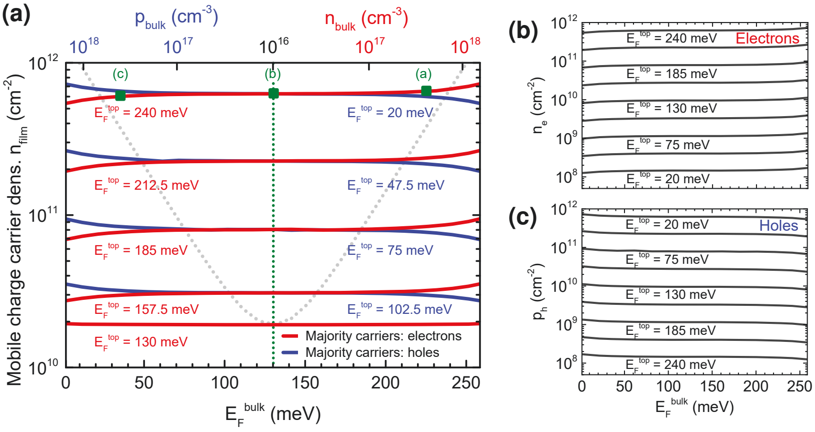

Figure 6.9.: (a) Integrated total mobile charge carrier density n_{film} based on the symmetric approximation for a thin TI film as function of the dopant concentration represented by the bulk Fermi energy E_F^{bulk}. The surface Fermi energy E_F^{top} is an additional parameter. For E_F^{bulk} inside the band-gap, the calculated film carrier density is approximately constant and, thus, independent of the dopant concentration. The type of majority carriers in the thin film [either electrons (red) or holes (blue)] is indicated. On the upper horizontal axis, the associated 3D majority charge carrier densities of a bulk crystal, i.e. p_{bulk} on the left and n_{bulk} on the right, are shown. The green squares correspond to the values of E_F^{bulk} and E_F^{top} used in the band diagrams in Figs. 6.8(a) – 6.8(c), while the dotted green line corresponds to a vertical cut plotted in Fig. 6.15 along the red dotted diagonal. For comparison, the dotted gray line shows the strong exponential dependence of the total charge carrier density expected inside an extended bulk crystal (values converted to 2D units by integrating over a width of $10\,\text{nm}$ inside the bulk). (b),(c) Individual contributions of electrons (b) and holes (c).

the constant charge carrier concentration is observed. Note that the mobile charge carrier concentration is of course influenced by the surface Fermi energy E_F^{top}.

As a quantitative example, for $E_F^{\mathrm{top}} = 240\,\mathrm{meV}$, as found in Ref. [131], the calculated charge carrier concentration in the BiSbTe$_3$ film is $\sim 6 \times 10^{11}\,\mathrm{cm}^{-2}$, which is close to the charge carrier density inside the Dirac cone of the top TSS of $4 \times 10^{12}\,\mathrm{cm}^{-2}$, indicating that there may be a contribution by the interior of the film to the overall charge transport in the TI system. Fortunately, in this example it turns out that the mobility of the bulk material at room temperature is very low ($< 2\,\mathrm{cm}^2/\mathrm{Vs}$) compared to the TSS channels [131, 156–158, 160], with the result that the conductivity of the film interior is negligible. However, this could be completely different for other material systems, especially at low temperatures, where the mobility may be larger by factors of 10 to 50. Thus, each case has to be considered individually.

Thus, it can be concluded that by measuring the surface Fermi energy E_F^{top}, the charge carrier concentration inside the TI thin film can be determined, even if the dopant concentration (E_F^{bulk}) is unknown. If also the mobility of the TI material is known, the conductivity of the parasitic conduction channel that is constituted by the film interior in the TI system can directly be calculated. It should be stressed again that this is in strong contrast to the behavior of an extended bulk crystal, where the charge carrier density shows a strong dependence on the dopant concentration, which is indicated by the dotted gray curve in Fig. 6.9.

6.4.2.8. General interplay of parameters

In conclusion of this part, some further examples of near-surface band bending in thin TI films should be shown. This examples are selected in such a way that the influence of the individual parameters on the specific shape of the bands is visualized, so that the general mechanism of band bending is revealed more clearly. As already discussed in detail in sections 6.4.1.5 and 6.4.2.3, the charge transfer between the TSS and the TI bulk (and thus the band bending) is determined by four interdependent parameters: the charge neutrality level (CNL) of the combined TSS/DS system, the surface Fermi energy E_F^{top}, the bulk Fermi energy E_F^{bulk} (given by the bulk dopant concentration), and the film thickness d. If three of them are given, the fourth parameter is fixed by the condition of charge neutrality.

In order to demonstrate the interplay of these four parameters and their effect on the band bending, several cases with different initial conditions are considered and plotted as band diagrams in Fig. 6.10 and Fig. 6.11. Each band diagram is again calculated for both a $10\,\mathrm{nm}$ thin film (red) and the equivalent bulk crystal (blue) of the TI material BiSbTe$_3$, which was also considered throughout before. However, the difference to Fig. 6.8 is that now the parameters of the calculation are not solely based on measurements, but chosen with the aim to exemplify as clearly as possible their strong influence on the shape of band bending. In each set of band diagrams, i.e. Figs. 6.10(a) – 6.10(c), Figs. 6.11(a) – 6.11(c) and Figs. 6.11(d) – 6.11(f), the dopant concentration, represented by E_F^{bulk}, is varied from n- to p-type.

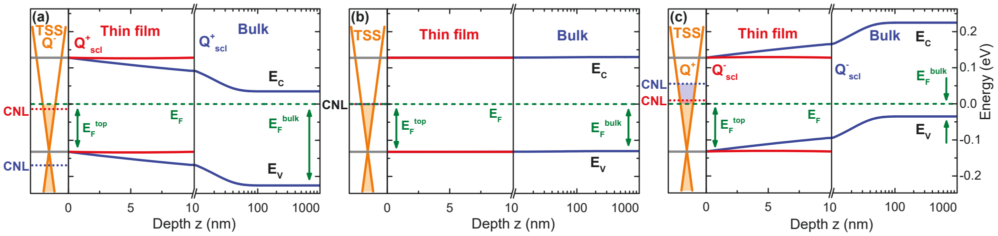

Figure 6.10.: Calculated band bending for a $10\,\mathrm{nm}$ thin film (red) and equivalent bulk crystal (blue) of the TI BiSbTe$_3$ as presented in Fig. 6.8, but now for a fixed mid-gap position of the surface Fermi energy $E_F^{\mathrm{top}} = 130\,\mathrm{meV}$. From (a) to (c) the dopant concentration is varied, which is represented by different values for the bulk Fermi energy E_F^{bulk}: (a) $225\,\mathrm{meV}$, (b) $130\,\mathrm{meV}$, and (c) $35\,\mathrm{meV}$. Because the parameter E_F^{top} differs from the case displayed in Fig. 6.8, the resulting band bendings and CNLs are also different.

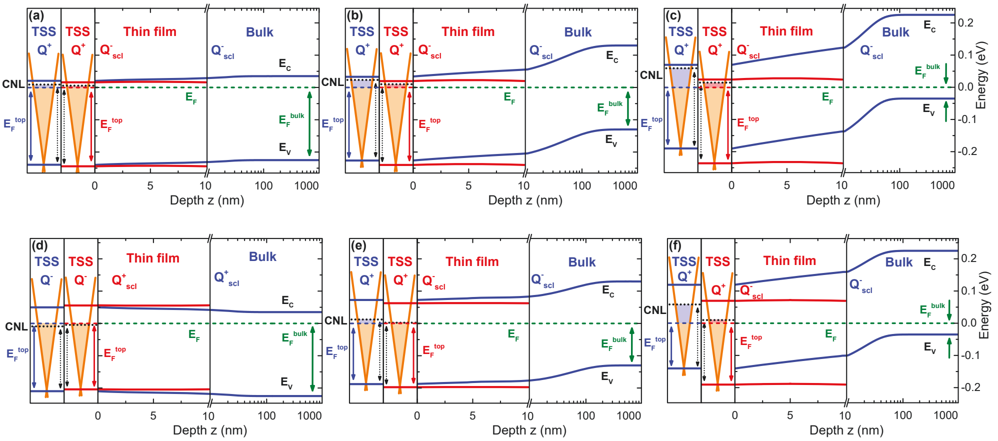

Figure 6.11.: Calculated band bending for a $10\,\mathrm{nm}$ thin film (red) and equivalent bulk crystal (blue) of the TI BiSbTe$_3$ as presented in Fig. 6.8, but now for a fixed value of the charge neutrality level (black dotted line), i.e. for a fixed surface defect density, with $\mathrm{CNL} = 250\,\mathrm{meV}$ for (a) to (c) and $\mathrm{CNL} = 200\,\mathrm{meV}$ for (d) to (f). From (a) to (c) and (d) to (f) the dopant concentration is varied, as represented by the bulk Fermi energy E_F^{bulk}: (a),(d) 225 meV, (b),(e) 130 meV, and (c),(f) 35 meV. In contrast to the data shown in Fig. 6.8, the parameter CNL is constant among the top (bottom) panels, such that the calculated values for E_F^{top} come out different for both thin film and extended bulk crystal on the one hand, and for different dopant concentrations on the other hand. Due to the alignment of the Fermi energy E_F (green dashed line) throughout all plots and the different values of E_F^{top}, the Dirac cones for the thin film and the extended bulk are vertically displaced with respect to each other and plotted separately on the left of each panel.

In Fig. 6.10, the surface Fermi energy is set to a constant mid-gap position of $E_F^{\mathrm{top}} = 130\,\mathrm{meV}$. This results in distinct CNL values for the thin film and the bulk crystal, and also for the three different dopant concentrations. While for the extended bulk crystal the change of CNL and band bending with dopant concentration is significant, it is rather small for the thin film: For all dopant concentrations in Fig. 6.10, the Fermi level in the thin film remains very close to mid-gap, because mobile charges flow almost completely into the TSS. The interior of the film is thus intrinsically doped (fully depleted), irrespective of the dopant concentration in the film material. If moreover the TI material is intrinsic (i.e. E_F^{bulk} in mid-gap position), the CNL is independent of the film thickness d and therefore coincides for the thin film and the bulk cases [Fig. 6.10(b)], resulting in flat bands in both cases.

In Fig. 6.11, the charge neutrality level (black dotted line) is kept constant and fixed at $250\,\mathrm{meV}$ for Figs. 6.11(a) – 6.11(c) and at $200\,\mathrm{meV}$ for Figs. 6.11(d) – 6.11(f). Because all band diagrams in Fig. 6.11 are aligned to a common Fermi level (green), the CNL and the Dirac cones for the thin film and for the extended bulk appear vertically displaced, but the position of the CNL with respect to the conduction band is the same in both cases (black dotted arrows). A fixed CNL corresponds to the same specific concentration of surface defects in all cases. As a result, the calculated values for E_F^{top} are now different for both thin film and extended bulk crystal on the one hand, and for different dopant concentrations on the other hand. Also the shape of band bending varies between all cases [even upward band bending is observed in Fig. 6.11(d)].

The calculations in Fig. 6.11 show that the CNL (resulting from a certain concentration of surface defects) directly influences the position of the surface Fermi energy E_F^{top}, and correspondingly the overall band bending. As E_F^{top} is accessible by ARPES, this effect is directly visible in measurements. For example, a variation of E_F^{top} with time due to an increasing surface contamination has been experimentally observed [148, 150–152]. Concomitantly, the filling level of the TSS changes, and thus the concentration of charge carriers inside. This in turn may lead to different properties of the TSS, e.g. a different conductivity. For this reason, it is difficult to characterize the TI properly after exhibiting it to ambient conditions, as it is for example necessary for the lithographic fabrication of electrical contacts for subsequent conductivity measurements. Only as long as ultra-high vacuum conditions are maintained, a change of the TSS properties due to adsorbates on the surface (and corresponding change of CNL) can be excluded. This highlights the great advantage of *in situ* transport measurements by means of multi-probe STM.

6.4.3. Asymmetric band bending in a thin film

So far, the band bending has been treated by a symmetric approach assuming equal surface Fermi energies E_F^{top} and E_F^{bottom}. However, in general, different environments and thus different surface defect densities will result in distinct surface Fermi energies E_F^{top} and E_F^{bottom} at the top and the bottom of the TI film. Therefore, the boundary conditions at the top and bottom surfaces are not identical, yielding an asymmetric band bending. In this situation, the calculation of the band bending is more complex than in the symmetric limit. An outline is given in the following section, while in section 6.4.3.2 the practical usage is demonstrated based on information from gate-dependent measurements.

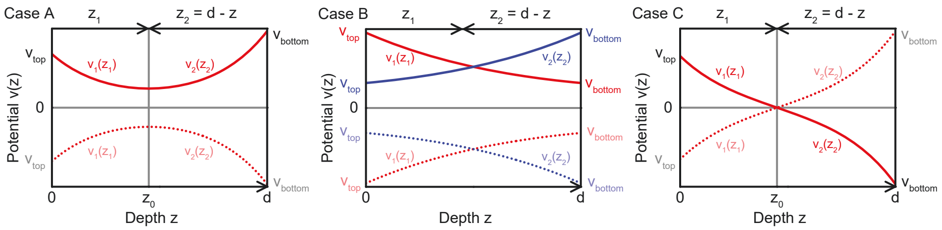

Figure 6.12.: Three different cases A - C for the asymmetric potential $v(z)$ of a $10\,\mathrm{nm}$ thin film with different surface potentials v_{top} and v_{bottom} on the top and bottom surface of the TI film, respectively, plotted as function of depth z from the top surface. The coordinates z_1 and z_2 are indicated. In order to visualize that the shape of potential depends strongly on the boundary conditions, several distinct potential curves are plotted: solid and dotted lines in each panel exhibit boundary conditions with inverted signs. For case B, the blue curves display the potentials obtained by interchanging the values of v_{top} and v_{bottom}.

6.4.3.1. Formalism

In the following, the equations for the calculation of the asymmetric band bending which are based on the solution of Poisson's equation given before in Eq. (6.8), are presented in detail.

Concerning the shape of the potential, three different cases, labelled A to C, can be distinguished. They are shown schematically in Fig. 6.12 and fulfill the conditions

$$\text{(A)} \qquad \left.\frac{dv}{dz}\right|_{z=z_0} = 0 \qquad \text{for} \quad 0 \le z_0 \le d, \tag{6.15}$$

$$\text{(B)} \qquad \left.\frac{dv}{dz}\right|_{z=z_0} \neq 0 \qquad \text{for} \quad 0 \le z_0 \le d, \tag{6.16}$$

$$\text{(C)} \qquad v(z = z_0) = 0 \qquad \text{for} \quad 0 \le z_0 \le d. \tag{6.17}$$

For cases A and B the signs of the surface potentials v_{top} and v_{bottom} are equal, while for case C the signs are opposite. To simplify the calculation of the band bending for cases A and C, the function $v(z)$ is split into two branches, namely $v_1(z_1)$ with $z_1 \equiv z$ for $0 \le z \le z_0$ and $v_2(z_2)$ with $z_2 \equiv d - z$ for $z_0 \le z \le d$ (or equivalently $d - z_0 \ge z_2 \ge 0$). Note that the origin of z_2 is located at the bottom surface of the thin film and that z_2 increases towards the top surface, whereas z_1 (and z) have their origin at the top surface and increase towards the bottom one. The transition between v_1 and v_2 at z_0 must be continuous and differentiable, leading to the following matching conditions between the branches:

$$\text{(A)} \quad v_1(z_0) = v_2(d - z_0) =: v_0 \qquad \text{and} \qquad \left.\frac{dv_1}{dz_1}\right|_{z_1=z_0} = -\left.\frac{dv_2}{dz_2}\right|_{z_2=d-z_0} = 0, \tag{6.18}$$

$$\text{(C)} \quad v_1(z_0) = v_2(d - z_0) = 0 \qquad \text{and} \qquad \left.\frac{dv_1}{dz_1}\right|_{z_1=z_0} = -\left.\frac{dv_2}{dz_2}\right|_{z_2=d-z_0}. \tag{6.19}$$

Two additional boundary conditions are determined by the initial values of the potential at the surfaces of the film., i.e. for cases A and C it is

$$\text{(A), (C)} \qquad v_1(0) = v_{\text{top}} \qquad \text{and} \qquad v_2(0) = v_{\text{bottom}}. \tag{6.20}$$

For case B only one function, either $v_1(z_1)$ or $v_2(z_2)$, needs to be calculated, and thus the two boundary conditions are either

$$\text{(B)} \qquad \begin{aligned} & v_1(0) = v_{\text{top}} && \text{and} \qquad v_1(d) = v_{\text{bottom}}, \\ \text{or} \quad & v_2(0) = v_{\text{bottom}} && \text{and} \qquad v_2(d) = v_{\text{top}}, \end{aligned} \tag{6.21}$$

respectively. Thus, in the end, for each branch two boundary conditions are available, as it is necessary.

In detail, the band bending $v_i(z_i)$ for cases A to C is obtained by inserting the appropriate boundary conditions from Eqs. (6.18) – (6.21) into Eq. (6.8). Hereby, the index $i = 1, 2$ denotes the two branches $v_1(z_1)$ and $v_2(z_2)$ of the potential $v(z)$, and $v_{\text{top,bottom}}$ represents the corresponding surface potential, i.e. for $i = 1$ the first index ($_{\text{top}}$) and for $i = 2$ the second index ($_{\text{bottom}}$) has to be used. Below, the results are discussed individually for each case. Additional information about the derivation of the solutions can be found in the appendix A.3.4.

Case A

In the left panel of Fig. 6.12, the band bending corresponding to case A is shown. The surface potentials v_{top} and v_{bottom} are either both positive (red solid line) or both negative (red dotted line) and exhibit only a small difference. If z_0 is chosen at the extremum (minimum or maximum) of $v(z)$, the two branches $v_1(z_1)$ and $v_2(z_2)$ can be calculated in analogy to Eq. (6.13) for the intervals $0 \leq z_1 \leq z_0$ and $0 \leq z_2 \leq d - z_0$ by

$$z_i(v_i) = A_i \int\limits_{\substack{v_{\text{top,}} \\ \text{bottom}}}^{v_i(z_i)} \underbrace{\sqrt{\frac{e^{u_b} + e^{-u_b}}{e^{u_b}\left(e^{v'} - e^{v_0} - v' + v_0\right) + e^{-u_b}\left(e^{-v'} - e^{-v_0} + v' - v_0\right)}}}_{=:\, F_A(u_b, v', v_0)} \, dv' \tag{6.22}$$

with the prefactor $A_i = \text{sgn}(-v_i)\frac{L}{\sqrt{2}}$, respectively. An additional auxiliary condition is

$$\text{sgn}(-v_{\text{top}})\frac{L}{\sqrt{2}}\left[\int_{v_{\text{top}}}^{v_0} F_A(u_b, v', v_0)\, dv' + \int_{v_{\text{bottom}}}^{v_0} F_A(u_b, v', v_0)\, dv'\right] - d = 0 \tag{6.23}$$

which results from the first matching condition of case A [Eq. (6.18)] and determines the constant v_0.

Case B

In case B (center panel of Fig. 6.12) there is no local extremum in the potential $v(z)$ because the difference between the boundary values v_{top} and v_{bottom} is larger than in case A, resulting in a more pronounced slope of the band potential. The calculation of the gate-dependent band bending in section 6.4.3.2 assumes case B. Again, both v_{top} and v_{bottom} have the same sign, either positive (solid lines) or negative (dotted lines). Although not imperative, also two branches of $v(z)$ are defined in the present case: Specifically, z_0 is placed at the surface which has the smaller surface potential, i.e. $z_0 \equiv 0$ if $|v_{\text{top}}| < |v_{\text{bottom}}|$ and $z_0 \equiv d$ if $|v_{\text{bottom}}| < |v_{\text{top}}|$. In the former case $v(z)$ is given by $v_2(z_2)$, in the latter by $v_1(z_1)$. If the values of v_{top} and v_{bottom} are interchanged, $v_1(z_1)$ has to be replaced by $v_2(z_2)$ or vice versa. Both potential functions can be calculated by

$$z_i(v_i) = \operatorname{sgn}(-v_i)\frac{L}{\sqrt{2}}\int_{v_{\text{top,bottom}}}^{v_i(z_i)} \underbrace{\sqrt{\frac{e^{u_b}+e^{-u_b}}{e^{u_b}\left(e^{v'}-v'+c\right)+e^{-u_b}\left(e^{-v'}+v'+c\right)}}}_{=:\,F_B(u_b,v',c)}\,dv' \tag{6.24}$$

based on the conditions

$$\big(z_i = z_1 \ \wedge\ 0 \le z_1 \le d\big) \ \Leftrightarrow\ |v_{\text{top}}| > |v_{\text{bottom}}|, \tag{6.25a}$$

$$\big(z_i = z_2 \ \wedge\ 0 \le z_2 \le d\big) \ \Leftrightarrow\ |v_{\text{top}}| < |v_{\text{bottom}}|. \tag{6.25b}$$

The auxiliary condition which determines the constant c, reads as

$$\operatorname{sgn}\big(|v_{\text{top}}| - |v_{\text{bottom}}|\big)\operatorname{sgn}(-v_{\text{top}})\frac{L}{\sqrt{2}}\int_{v_{\text{top}}}^{v_{\text{bottom}}} F_B(u_b,v',c)\,dv' - d = 0\,. \tag{6.26}$$

Case C

Case C is visualized in the right panel of Fig. 6.12. As v_{top} and v_{bottom} have opposite signs, there must appear a root at a finite z between 0 and d. This z is identified with the z_0 that separates the potential into two branches v_1 and v_2. In the thin TI film, this root corresponds to a change of the type of band bending, from a depletion to an accumulation zone or vice versa. Both branches can be calculated by applying Eq. (6.24) separately for $0 \le z_1 \le z_0$ and for $0 \le z_2 \le d - z_0$, with the modified auxiliary condition

$$\operatorname{sgn}(-v_{\text{top}})\frac{L}{\sqrt{2}}\int_{v_{\text{top}}}^{v_{\text{bottom}}} F_B(u_b,v',c)\,dv' - d = 0 \tag{6.27}$$

that determines the constant c.

Transition between the cases A - C

Starting from the symmetric case of band bending with $v_{\text{top}} = v_{\text{bottom}}$, case A has to be applied if there is only a slight imbalance between v_{top} and v_{bottom} that breaks the symmetry between the top and bottom surfaces of the film. The transition to case B occurs once the local minimum (maximum) of the potential function $v(z)$ reaches one of the surfaces of the film ($z_0 = 0$ or $z_0 = d$) because the difference between $|v_{\text{top}}|$ and $|v_{\text{bottom}}|$ becomes sufficiently large. Within the coordinates of the two branches $v_{1,2}(z_{1,2})$ (see above) the potential minimum (maximum) is then located at $z_{1,2} = d$. So, the condition for the transition point is

$$\left.\frac{dv_{1,2}}{dz_{1,2}}\right|_{z_{1,2}=d} = 0. \tag{6.28}$$

This condition is fulfilled for a potential value $v_{1,2}(d)$ which can be expressed relative to the surface potential $v_{\text{top,bottom}}$ by introducing a threshold Δ as $v_{1,2}(d) = v_{\text{top,bottom}} - \Delta$. This threshold then determines the maximum difference between v_{top} and v_{bottom} up to which no transition between case A and B occurs. In analogy to Eq. (6.13), the threshold Δ follows as

$$A_i \int\limits_{\substack{v_{\text{top},}\\ \text{bottom}}}^{\substack{v_{\text{top},} - \Delta\\ \text{bottom}}} \sqrt{\frac{e^{u_b} + e^{-u_b}}{\begin{gathered} e^{u_b}\left(e^{v'} - e^{v_{\text{top,bottom}} - \Delta} - v' + v_{\text{top,bottom}} - \Delta\right) \\ + e^{-u_b}\left(e^{-v'} - e^{-v_{\text{top,bottom}} + \Delta} + v' - v_{\text{top,bottom}} + \Delta\right)\end{gathered}}}\, dv' = d \tag{6.29}$$

with the prefactor $A_i = \operatorname{sgn}(-v_i)\frac{L}{\sqrt{2}}$. When the absolute value of the difference between v_{top} and v_{bottom} is smaller than Δ, i.e. $\big||v_{\text{top}}| - |v_{\text{bottom}}|\big| \leq \Delta$, case A is used. When the difference is larger than Δ, i.e. $\big||v_{\text{top}}| - |v_{\text{bottom}}|\big| > \Delta$, case B has to be applied. If the signs of v_{top} and v_{bottom} become different, the transition to case C occurs.

6.4.3.2. Information from gate-dependent measurements

To calculate the band bending in a thin film with asymmetric boundary conditions, both E_F^{top} and E_F^{bottom} have to be known. While E_F^{top} can be measured by ARPES (see above), E_F^{bottom} must be extracted from gate-dependent four-point transport measurements. The procedure is described in detail in Ref. [131]. To this end, a bottom gate electrode is integrated into the substrate of the TI film and the four-point resistance of the film is measured with a multi-tip STM as function of the applied gate voltage. Due to quantum capacitance effects that arise because the DOS in the TSS is small, the induced electric field of the gating electrode does not only have a strong influence on the filling level of the bottom TSS, but also on that of the top TSS. Thus, it can be concluded that E_F^{bottom} can be determined via gate-dependent measurements, if E_F^{top} is known.

For the quantization effects, the potential in the film is approximated by a triangular well of length d with infinite barriers on both sides. Its slope is determined by the difference between the top and bottom surface Fermi levels E_F^{top} and E_F^{bottom}. This approximation is applicable if the band bending in the film is weak, otherwise the potential would exhibit a curvature. Further details of the calculations are discussed in the section 6.5.

In Fig. 6.13, the asymmetric band bending in a BiSbTe$_3$ film with $d = 10\,\text{nm}$ is shown for three different gate voltages, i.e. +30 V, 0 V, and −30 V. All three band diagrams are

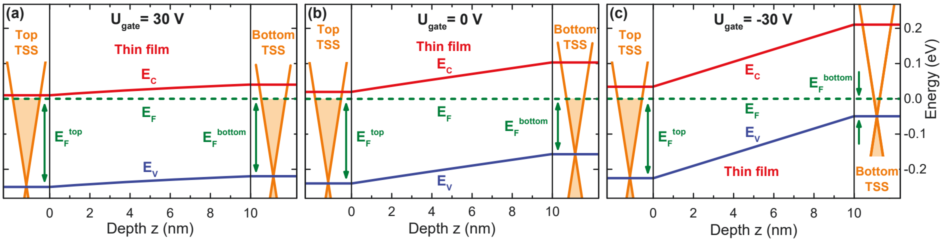

Figure 6.13.: Gate-dependent band bending for a 10 nm thin BiSbTe$_3$ film with intrinsic dopant concentration ($E_F^{\text{bulk}} = 130\,\text{meV}$, $n_{\text{bulk}} = p_{\text{bulk}} = 1 \times 10^{16}\,\text{cm}^{-3}$) as function of the depth z into the film for different gate voltages, i.e. 30 V (a), 0 V (b) and -30 V (c). The calculation is based on asymmetric boundary conditions with the same parameters as used in Fig. 6.8 and additional information from gate-dependent transport measurements [131]. In the central part of each diagram, the bands inside the thin film are depicted, while on the left and right side of the panels the top and bottom TSS are shown, respectively. The Fermi energy E_F (green dashed line) and both E_F^{top} and E_F^{bottom} (green arrows) are indicated. Due to different surface Fermi energies E_F^{top} at $z = 0$ and E_F^{bottom} at $z = 10\,\text{nm}$ [(a) 250 meV, 220 meV; (b) 240 meV, 155 meV; (c) 225 meV, 50 meV] the resulting band bending in the thin film is asymmetric. The bottom gate voltage influences both surface Fermi levels in a different way, as described in detail in Ref. [131], and leads to an increase in the strength of band bending from (a) to (c). Hence, the mobile charge carrier density inside the thin film is significantly influenced by the gate voltage.

calculated for an intrinsic film dopant concentration (i.e. $E_F^{\text{bulk}} = 130\,\text{meV}$). Similar to the symmetric case, the band bending turns out to be approximately the same for different dopant concentrations (not shown). However, Fig. 6.13 clearly shows that the varying gate voltage causes different concentrations of induced charge carriers in the top and bottom TSS [131], and thus results in different filling levels of the Dirac cones and different surface Fermi energies E_F^{top} and E_F^{bottom}. Specifically, the band bending increases if the gate voltage becomes more negative [Figs. 6.13(a) – 6.13(c)], as the charge carrier concentration in the bottom TSS is stronger influenced by the gating than in the top TSS. As a consequence, also the charge carrier density in the thin film varies strongly with gate voltage. This dependency of the total mobile charge carrier density on the gate voltage is plotted for the case of a BiSbTe$_3$ film with $d = 10\,\text{nm}$ in Fig. 6.14(a). The inset depicts the measurement setup used in Ref. [131]. However, if the dopant concentration in the thin film is changed at a fixed gate voltage, the integrated charge carrier density remains nearly constant. This is illustrated in Fig. 6.14(b), where the strongly z-dependent carrier density resulting from Fig. 6.13 is integrated over the film [Eq. (6.14)] and plotted as function of the film dopant concentration, represented by the bulk Fermi energy of a corresponding extended crystal, and the applied gate voltage as additional parameter. It can be observed that nearly the same behavior results as in the symmetric approximation (Fig. 6.9), i.e. the total mobile charge carrier density n_{film} in the thin film is nearly independent of E_F^{bulk}. It does, however, strongly depend on the applied gate voltage.

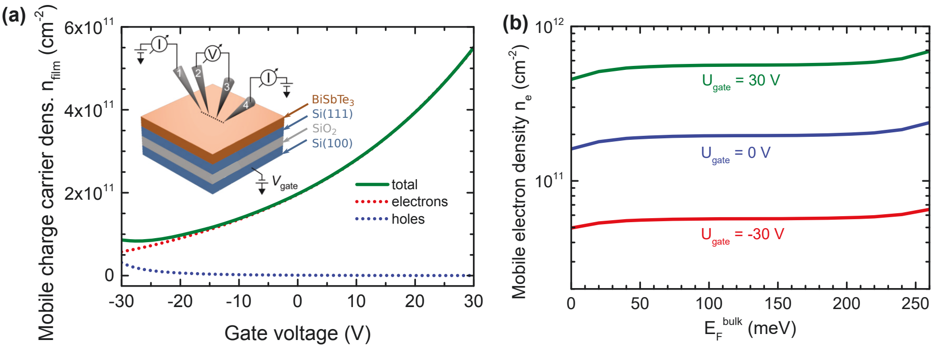

Figure 6.14.: (a) Calculated total mobile charge carrier density n_{film} inside a $10\,\text{nm}$ thin BiSbTe$_3$ film as function of the applied gate voltage (solid green line). The calculation is based on asymmetric boundary conditions for a thin film with intrinsic dopant concentration $n_{\text{bulk}} = p_{\text{bulk}} = 1 \times 10^{16}\,\text{cm}^{-3}$ ($E_F^{\text{bulk}} = 130\,\text{meV}$) and on parameters from Ref. [131]. The individual contributions by electrons (red) and holes (blue) are depicted by the dotted lines. In the inset, the transport measurement setup and the sample configuration from Ref. [131] is shown. (b) Integrated total mobile charge carrier density inside the $10\,\text{nm}$ BiSbTe$_3$ film as function of dopant concentration (represented by E_F^{bulk} of a corresponding extended crystal) and gate voltage as additional parameter.

6.4.3.3. Comparison between asymmetric and symmetric boundary conditions

Finally, the results for asymmetric boundary conditions are compared to those obtained in the symmetric case. It is to be expected that for a given parameter set E_F^{top} and E_F^{bottom} the mobile charge carrier density n_{film} will differ from one that is calculated in the symmetric approximation. This becomes apparent in Fig. 6.15, where the total mobile charge carrier density of a BiSbTe$_3$ film with $d = 10\,\text{nm}$ is plotted (based on parameters from Ref. [131]) as function of the top and bottom surface Fermi levels. The diagonal dotted red line corresponds to symmetric boundary conditions with $E_F^{\text{top}} = E_F^{\text{bottom}}$. The plot reveals that for a specific measured E_F^{top} and unknown E_F^{bottom}, i.e. along a vertical cut through the diagram, n_{film} can vary by up to one order of magnitude. It should be noted that the contour lines in Fig. 6.15 are symmetric, because both electrons and holes contribute to the total mobile charge carrier density. The blue points correspond to the charge carrier densities obtained for the gate-dependent band diagrams in Figs. 6.13(a) – 6.13(c), while the dotted connection line between the blue points expresses the general gate-dependency of n_{film} shown in Fig. 6.14(a), providing the corresponding E_F^{top} and E_F^{bottom}. For example, for $E_F^{\text{top}} = 240\,\text{meV}$ and $E_F^{\text{bottom}} = 156\,\text{meV}$, as determined in Ref. [131] for a vanishing gate voltage, the calculated charge carrier density in the film is $\sim 2 \times 10^{11}\,\text{cm}^{-2}$, which is only one third of the value calculated in the symmetric approximation.

Thus, it can be concluded that the charge carrier density in the thin TI film can be calculated more precisely with asymmetric boundary conditions. Because the gate-dependent measurements not only provide the band bending but also the charge carrier mobility in the film, the conductivity of the interior of the TI film can finally be determined [131].

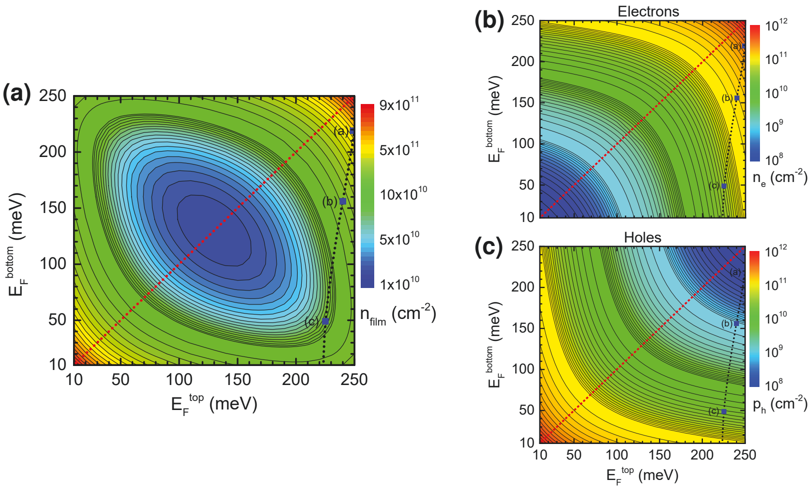

Figure 6.15.: (a) Color plot of the mobile charge carrier density n_{film} as function of the top and bottom surface Fermi energy E_F^{top} and E_F^{bottom}, respectively, for the specific case considered in Ref. [131]. The charge carrier density is calculated for a thin film with intrinsic dopant concentration. The diagonal dotted red line indicates the symmetric case with $E_F^{\text{top}} = E_F^{\text{bottom}}$ and corresponds to a cut at the position of the dotted green line in Fig. 6.9. The marked blue points correspond to the charge carrier concentrations resulting from the band diagrams depicted in Figs. 6.13(a) – 6.13(c), while the dotted black line in between shows the general gate-dependent behavior. (b),(c) Same plots as in (a), but showing the individual contributions of electrons (b) and holes (c).

6.5. Schrödinger-Poisson approach for band bending in thin films

In this section, first the concept of the effective density of states in the classical Poisson approach is discussed. Moreover, the modifications of the classical calculation of the band bending, specifically concerning the effective density of states, which are necessitated by the Schrödinger-Poisson approach, are presented.

6.5.1. Classical Poisson approach

6.5.1.1. Concept of effective density of states

The charge carrier density in the conduction band (electrons) is given by

$$n_e(z) = \int_{E_C(z)}^{\infty} n_C^{\text{dos}}\left(E - E_C(z)\right) \frac{1}{e^{\frac{E-E_F}{k_B T}}+1}\, dE \tag{6.30}$$

with the Fermi energy E_F, the conduction band edge $E_C(z)$ and the density of states $n_{C,\text{2D}}^{\text{dos}}(E) = \frac{m_e^*}{\pi\hbar^2}$ and $n_{C,\text{3D}}^{\text{dos}}(E) = \frac{(2m_e^*)^{3/2}}{2\pi^2\hbar^3}\sqrt{E}$ for the 2D and 3D cases, respectively, assuming parabolic bands. For non-degenerate semiconductors with the Fermi energy positioned well in between the band edges the Boltzmann approximation for the Fermi-Dirac distribution can be used. Eq. (6.30) can then be approximated as [88]

$$n_e(z) = N_C^{\text{eff}}\, e^{-\frac{(E_C(z)-E_F)}{k_BT}} \tag{6.31}$$

with the effective density of states $N_{C,\text{2D}}^{\text{eff}} = \frac{m_e^* k_BT}{\pi\hbar^2}$ and $N_{C,\text{3D}}^{\text{eff}} = 2\left(\frac{2m_e^*\pi k_BT}{h^2}\right)^{3/2}$ for the 2D and 3D cases, respectively. Conceptually, the effective density of states N^{eff} corresponds to a theoretical density of states that would be present, if all empty states of the conduction band were concentrated at the lower conduction band edge at E_C. The charge carrier density in the valence band (holes) can be described in the same way by using the effective hole mass m_h^* and the valence band edge $E_V(z)$ in Eq. (6.31), resulting in

$$p_h(z) = N_V^{\text{eff}}\, e^{\frac{E_V(z)-E_F}{k_BT}} \tag{6.32}$$

with $N_{V,\text{2D}}^{\text{eff}} = \frac{m_h^* k_BT}{\pi\hbar^2}$ and $N_{V,\text{3D}}^{\text{eff}} = 2\left(\frac{2m_h^*\pi k_BT}{h^2}\right)^{3/2}$ for the 2D and 3D cases, respectively.

6.5.1.2. Effective density of states in the Poisson approach

For the calculation of the near-surface band bending $E_C(z)$ and $E_V(z)$ within the classical approach, the Poisson equation specified before in Eq. (6.5) for the dimensionless potential $v(z)$ has to be solved. In this equation, the first two terms on the right side correspond to the static charge density $\rho_{\text{static}} = q[N_D^+ - N_A^-]$ caused by the homogeneous concentration of charged donors N_D^+ and acceptors N_A^- in the material, which can be expressed by the mobile bulk charge carrier densities n_b and p_b by using the condition of charge neutrality

$$n_b + N_A^- = p_b + N_D^+ \tag{6.33}$$

as $\rho_{\text{static}} = q[n_b - p_b]$. The last two terms on the right side of Eq. (6.5) correspond to the position-dependent mobile charge density $\rho_{\text{mobile}}(z) = q[p(z) - n(z)]$ of electrons and holes, which can be expressed by the Eqs. (6.45) and (6.48) (see below). Thus, with $\rho(z) = \rho_{\text{static}} + \rho_{\text{mobile}}(z)$ and the dimensionless potential $v(z)$, the Poisson equation in its present form directly follows from Eq. (6.1). With the definition given in Eqs. (6.2) – (6.4), i.e. based on

$$q\Phi(z) = k_BTu(z) = E_F - E_i(z), \tag{6.34}$$

the potential $v(z)$ can be written as

$$v(z) = \frac{q}{k_BT}\Big[\Phi(z) - \Phi_b\Big] = \frac{1}{k_BT}\Big[E_i^b - E_i(z)\Big], \tag{6.35}$$

where the indices i and b denote the intrinsic level and the bulk limit (for $z \to \infty$), respectively. The intrinsic level E_i^b in the bulk material depends on the effective densities of states as

$$E_i^b\left(N_C^{\text{eff}}, N_V^{\text{eff}}\right) = \frac{E_C^b + E_V^b}{2} + \frac{k_BT}{2}\ln\left(\frac{N_V^{\text{eff}}}{N_C^{\text{eff}}}\right). \tag{6.36}$$

Eq. (6.36) is also valid for all other values of z, such that

$$E_i(z) = \frac{E_C(z) + E_V(z)}{2} + \frac{k_B T}{2} \ln\left(\frac{N_V^{\text{eff}}}{N_C^{\text{eff}}}\right). \tag{6.37}$$

If the Eqs. (6.36) and (6.37) are inserted into Eq. (6.35) and additionally the relation between the band edges $E_{\text{gap}} = E_C(z) - E_V(z) = E_C^b - E_V^b$ is used, the potential $v(z)$ can be expressed as

$$v(z) = \frac{1}{k_B T}\Big[E_V^b - E_V(z)\Big]. \tag{6.38}$$

Thus, from a solution $v(z)$ of the Poisson equation [Eq. (6.5)] the final shape of band bending $E_V(z)$ with respect to the bulk valence band edge E_V^b can be calculated as

$$E_V(z) = E_V^b - k_B T v(z). \tag{6.39}$$

Eq. (6.39) does not directly depend on the effective densities of states. However, in order to obtain the potential $v(z)$ by solving Poisson's equation [Eq. (6.5)], the knowledge of the effective densities of states N_C^{eff} and N_V^{eff} is required, because the charge carrier densities inside the bulk n_b and p_b depend on them, which will be shown in the following.

By using Eq. (6.31) and additionally inserting the relation for the intrinsic charge carrier density which immediately follows from $n_i^2 = n_e(z)\, p_h(z)$, i.e.

$$n_i\left(N_C^{\text{eff}}, N_V^{\text{eff}}\right) = \sqrt{N_C^{\text{eff}} N_V^{\text{eff}}}\, e^{-\frac{E_{\text{gap}}}{2k_B T}} \tag{6.40}$$

with the band gap $E_{\text{gap}} = E_C(z) - E_V(z)$, the mobile electron charge carrier density $n_e(z)$ can be rewritten as

$$\begin{aligned} n_e(z) &\overset{(6.31)}{=} N_C^{\text{eff}}\, e^{-\frac{(E_C(z)-E_F)}{k_B T}} = \sqrt{N_C^{\text{eff}} N_V^{\text{eff}}}\, e^{\frac{-E_C(z)+E_V(z)}{2k_B T}} \sqrt{\frac{N_C^{\text{eff}}}{N_V^{\text{eff}}}}\, e^{\frac{-E_C(z)-E_V(z)}{2k_B T}}\, e^{\frac{E_F}{k_B T}} \\ &\overset{(6.40)}{=} n_i\left(N_C^{\text{eff}}, N_V^{\text{eff}}\right) e^{\frac{E_F}{k_B T}} \sqrt{\frac{N_C^{\text{eff}}}{N_V^{\text{eff}}}}\, e^{\frac{-E_V(z)-E_C(z)}{2k_B T}}. \end{aligned} \tag{6.41}$$

From Eq. (6.37) it follows that

$$e^{-\frac{E_i(z)}{k_B T}} = e^{\frac{-E_C(z)-E_V(z)}{2k_B T} - \frac{1}{2}\ln\left(\frac{N_V^{\text{eff}}}{N_C^{\text{eff}}}\right)} = e^{\frac{-E_C(z)-E_V(z)}{2k_B T}} \left(e^{\ln\left(\frac{N_V^{\text{eff}}}{N_C^{\text{eff}}}\right)}\right)^{-\frac{1}{2}} = e^{\frac{-E_C(z)-E_V(z)}{2k_B T}} \sqrt{\frac{N_C^{\text{eff}}}{N_V^{\text{eff}}}}, \tag{6.42}$$

and by inserting Eq. (6.42) into Eq. (6.41), the equation

$$n_e(z) \overset{(6.42)}{=} n_i\left(N_C^{\text{eff}}, N_V^{\text{eff}}\right) e^{\frac{E_F - E_i(z)}{k_B T}} \overset{(6.34)}{=} n_i\left(N_C^{\text{eff}}, N_V^{\text{eff}}\right) e^{u(z)} \tag{6.43}$$

is obtained. Then, the electron charge carrier density inside the bulk n_b can be expressed as

$$n_b = n_i\left(N_C^{\mathrm{eff}}, N_V^{\mathrm{eff}}\right)\, e^{\frac{E_F - E_i^b\left(N_C^{\mathrm{eff}}, N_V^{\mathrm{eff}}\right)}{k_B T}} \overset{(6.34)}{=} n_i\left(N_C^{\mathrm{eff}}, N_V^{\mathrm{eff}}\right)\, e^{u_b\left(N_C^{\mathrm{eff}}, N_V^{\mathrm{eff}}\right)}\,. \tag{6.44}$$

If the exponential term in Eq. (6.43) is expanded by u_b and the definition for the potential $v(z)$ in Eq. (6.35) is used, the electron charge carrier density can be rearranged as

$$n_e(z) \overset{(6.35)}{=} n_i\left(N_C^{\mathrm{eff}}, N_V^{\mathrm{eff}}\right)\, e^{u_b\left(N_C^{\mathrm{eff}}, N_V^{\mathrm{eff}}\right)+v(z)} \overset{(6.44)}{=} n_b\left(N_C^{\mathrm{eff}}, N_V^{\mathrm{eff}}\right)\, e^{v(z)}. \tag{6.45}$$

Following similar considerations as shown in Eqs. (6.41) – (6.45), but starting with Eq. (6.32), the hole charge carrier density results in

$$p_h(z) = n_i\left(N_C^{\mathrm{eff}}, N_V^{\mathrm{eff}}\right)\, e^{-\frac{E_F - E_i(z)}{k_B T}} \overset{(6.34)}{=} n_i\left(N_C^{\mathrm{eff}}, N_V^{\mathrm{eff}}\right)\, e^{-u(z)}\,, \tag{6.46}$$

inside the bulk it is given by

$$p_b = n_i\left(N_C^{\mathrm{eff}}, N_V^{\mathrm{eff}}\right)\, e^{-\frac{E_F - E_i^b\left(N_C^{\mathrm{eff}}, N_V^{\mathrm{eff}}\right)}{k_B T}} \overset{(6.34)}{=} n_i\left(N_C^{\mathrm{eff}}, N_V^{\mathrm{eff}}\right)\, e^{-u_b\left(N_C^{\mathrm{eff}}, N_V^{\mathrm{eff}}\right)} \tag{6.47}$$

and by introducing the potential $v(z)$ it can be expressed as

$$p_h(z) \overset{(6.35)}{=} n_i\left(N_C^{\mathrm{eff}}, N_V^{\mathrm{eff}}\right)\, e^{-u_b\left(N_C^{\mathrm{eff}}, N_V^{\mathrm{eff}}\right)-v(z)} \overset{(6.47)}{=} p_b\left(N_C^{\mathrm{eff}}, N_V^{\mathrm{eff}}\right)\, e^{-v(z)}\,. \tag{6.48}$$

Thus, the effective densities of states N_C^{eff} and N_V^{eff} can have a crucial influence on the shape of band bending. They are necessary for the calculation of the bulk charge carrier densities n_b and p_b [Eqs. (6.44) and (6.47)], which in turn are needed for the solution $v(z)$ of the Poisson equation [Eq. (6.5)] and for the determination of the charge carrier densities $n_e(z)$ and $p_h(z)$ inside the space charge region [Eqs. (6.45) and (6.48)]. For an extended 3D crystal or a pure 2D sheet, in conjunction with the assumption of parabolic bands, the effective densities of states that were presented above can be used. However, for a system in which charge carriers are confined in one direction to within a length of the order of the wave length of the electrons, quantization effects have to be taken into account. This is outlined in the following section. The above considerations for semiconductors can be transferred straightforwardly to topological insulators, employing the arguments presented in section 6.4.

6.5.2. Quantum mechanical modifications

In order to take quantization effects on the occupation of the valence and conduction bands into account, which arise from an electron confinement on the length scale of the wave function, e.g. in thin films with thicknesses in the range of a few nm, a quantum mechanical approach must be used and the Schrödinger equation has to be solved in addition to the Poisson equation. For thin TI films a model system is used which is extended in the x- and

y-directions, but confined in the z-dimension. The quantized band states resulting from the solution of the Schrödinger equation can then be expressed by modified effective densities of states and used as input for the band bending calculation.

Specifically, the solution proceeds in three steps: In the first step, Poisson's equation is solved for a classical 3D system with a finite width in the z-direction, assuming a parabolic shape of the bands (as shown in detail in section 6.4). In the next step, the resulting band bending potential $v(z)$ is used in the Schrödinger equation to calculate quantization levels. To this end, the top and bottom surfaces of the thin film are treated as potential barriers which are very high compared to the potential inside the film. This is justified by the large work function of the TI in comparison to its band gap [161–163]. Moreover, it turns out that the band bending in all considered cases has a rather weak curvature, such that the problem can be framed in terms of generic potential wells. In other words, the exact solutions of the Schrödinger equation for the given $v(z)$ are approximated very well by the solutions for potential wells of either square or triangular shapes. Their quantized eigenenergies result in a modification of the densities of states within the conduction and valence bands. In particular, the bands are not continuous any more, but instead multiple discrete two-dimensional subbands arise for each of both bands due to the confinement in one dimension. The correspondingly modified effective densities of states of this quasi-two-dimensional system are used in the final calculation step, in which Poisson's equation is solved once again to determine the band bending $v(z)$ in the thin film.

6.5.2.1. Square well

Symmetric boundary conditions for the calculation of the band bending in thin films, which are presented in section 6.4.2, result in a potential without a slope and only with very weak curvature. This potential can be approximated by a square well with infinite barriers on both sides, resulting in a confinement in the z-direction, while the x- and y- directions are assumed to be infinitely extended. The solution of the Schrödinger equation for such a square well results in the eigenenergies [164]

$$E_j(k_x, k_y) = \epsilon_j + \frac{\hbar^2}{2m^*}\left(k_x^2 + k_y^2\right) \qquad \text{with } \epsilon_j = \frac{\hbar^2}{2m^*}\left(\frac{j\pi}{d}\right)^2 \tag{6.49}$$

with the integer number $j = 1, 2, \ldots$ and the film thickness d. The electron charge carrier density in the conduction band then results from the sum over all subbands j as

$$n_{e,\text{square}} = \sum_{j\geq 1} n_j^{\text{2D}} \overset{(6.31)}{=} \sum_{j\geq 1} \frac{m_e^* k_B T}{\pi\hbar^2} e^{-\frac{\left(E_C+\epsilon_j-E_F\right)}{k_B T}} = \underbrace{\left[\frac{m_e^* k_B T}{\pi\hbar^2} \sum_{j\geq 1} e^{-\frac{\epsilon_j}{k_B T}}\right]}_{N^{\text{eff}}_{\text{C,square}}} e^{-\frac{(E_C-E_F)}{k_B T}}, \tag{6.50}$$

where the two-dimensional charge carrier density n_j^{2D} of the subband j is given by Eq. (6.30) with the integration starting from $E_C + \epsilon_j$. According to Eq. (6.31) it can be expressed by using the Boltzmann approximation. From a comparison of Eq. (6.50) with

Eq. (6.31) the modified effective density of states $N_{C,\text{square}}^{\text{eff}}$ can be extracted as

$$N_{C,\text{square}}^{\text{eff}} = \frac{m_e^* k_B T}{\pi \hbar^2} \sum_{j \geq 1} e^{-\frac{\epsilon_j}{k_B T}} \overset{(6.49)}{=} \frac{m_e^* k_B T}{\pi \hbar^2} \sum_{j \geq 1} e^{-\frac{\hbar^2 \pi^2 j^2}{2 m_e^* k_B T d^2}} . \tag{6.51}$$

The modified effective density of states $N_{V,\text{square}}^{\text{eff}}$ of the valence band is given by the same expression, albeit replacing the effective mass m_e^* with m_h^*. Note that $N_{C,\text{square}}^{\text{eff}}$ and $N_{V,\text{square}}^{\text{eff}}$ only depend on the width of the square well, i.e. the thickness d of the thin TI film. In particular, the solutions are independent of the value of the surface Fermi energy E_F^{top}, since the potential barriers (work function) at the top and bottom surfaces of the film are high compared to the potential in the film. Because of the relatively high work function (e.g. $\approx 5\,\text{eV}$ for Bi_2Te_3 [161, 162]), any corrections resulting from the principally more accurate solution of a square well with finite barrier height remain rather small, such that the approximation of the barriers as being infinitely high is well justified in this case.

6.5.2.2. Triangular well

If the band bending in thin films is calculated with asymmetric boundary conditions (section 6.4.3), the square well potential is not a suitable approximation any more. While the band bending potential still shows a very weak curvature, it now exhibits a constant slope that is determined by the difference between the top and bottom surface Fermi energies E_F^{top} and E_F^{bottom} (cf. Fig. 6.13 in section 6.4.3). Hence, a triangular well of thickness d with infinitely high barriers at either surface of the thin film provides a better description of the band bending potential. The potential in a triangular well can be expressed as

$$V_{\text{triangle}}(z) = qFz \tag{6.52}$$

where the slope F is determined by the difference between the top and bottom surface Fermi energies

$$F\left(E_F^{\text{top}}, E_F^{\text{bottom}}\right) = \frac{E_F^{\text{top}} - E_F^{\text{bottom}}}{q\,d} . \tag{6.53}$$

With this potential the Schrödinger equation reads

$$\left[-\frac{\hbar^2}{2m^*}\frac{\mathrm{d}^2}{\mathrm{d}z^2} + qFz\right]\Psi(z) = E\Psi(z) \tag{6.54}$$

which after the variable substitution

$$\xi(z) = \underbrace{\left(\frac{2m^* qF}{\hbar^2}\right)^{\frac{1}{3}}}_{:=\xi_0} \left(z - \frac{E}{qF}\right) \tag{6.55}$$

becomes

$$\frac{\mathrm{d}^2}{\mathrm{d}\xi^2}\Psi(\xi) = \xi\Psi(\xi). \tag{6.56}$$

A solution of Eq. (6.56) is given by [164]

$$\Psi(\xi) = A_i(\xi) + CB_i(\xi) \tag{6.57}$$

where $A_i(\xi)$ and $B_i(\xi)$ are the Airy functions and C is a constant. By inserting the boundary conditions $\Psi(\xi(z = 0)) = 0$ at the top surface and $\Psi(\xi(z = d)) = 0$ at the bottom surfaces of the thin film, the equation system

$$\begin{aligned} &A_i(\xi(0)) + CB_i(\xi(0)) = 0 \\ &A_i(\xi(d)) + CB_i(\xi(d)) = 0 \end{aligned} \tag{6.58}$$

is obtained. Eliminating the constant C and resubstitution finally results in

$$A_i\left(\xi_0\left(d - \frac{E}{qF}\right)\right) - \frac{A_i\left(-\xi_0\frac{E}{qF}\right)}{B_i\left(-\xi_0\frac{E}{qF}\right)}\, B_i\left(\xi_o\left(d - \frac{E}{qF}\right)\right) = 0. \tag{6.59}$$

Eq. (6.59) has to be solved numerically to determine the quantized eigenenergies E_j that satisfy the equation. If these eigenenergies are calculated for a specific potential slope F, they can be inserted for ϵ_j in Eq. (6.51) to determine the modified effective densities of states $N^{\text{eff}}_{C,\text{triangle}}$ and $N^{\text{eff}}_{V,\text{triangle}}$ for the conduction and valence bands, respectively. These effective densities of states can then be used as input for the final step of the band bending calculation. However, it has to be noted that they now depend not only on the width d of the triangular well (the film thickness), but also on the slope F of the potential, which in turn depends on the difference between the top and bottom surface Fermi energies. Thus, $N^{\text{eff}}_{C,\text{triangle}}$ and $N^{\text{eff}}_{V,\text{triangle}}$ have to be calculated for each pair E_F^{top}, E_F^{bottom} separately.

Within the above approximation of the Schrödinger-Poisson approach, only the eigenenergies resulting from the solution of the Schrödinger equation are used, while the simultaneously determined wave functions $\Psi(z)$ are not considered. However, in principle the probability density $|\Psi(z)|^2$ resulting from the electron and hole wave functions must be inserted as an additional factor in front of the corresponding mobile charge carrier densities in the differential equation [Eq. (6.5)] before solving the Poisson equation in the final step. Evidently, this complicates the solution due to the additional z-dependence. Since the effect of the $|\Psi(z)|^2$-induced modification of the mobile charge carrier densities on the band bending is expected to be small, the wave functions are neglected and a uniform distribution of the mobile carriers in each subband across the thin film is assumed, as discussed above. This may lead to a slight overestimation of the band bending in the immediate vicinity of the surfaces, where the effect of the probability density on the mobile charge carrier distribution is strongest, because (1) the weak curvature in conjunction with the large barrier height implies that the subband wave functions tend to vanish towards the film surfaces, and (2) at room temperature nearly only the first subband is occupied ($\approx 95\,\%$) such that the probability density of the mobile carriers in the center of the thin film is at maximum and decreases towards the surfaces (e.g. as for the case of a square well the wave function of the lowest energetic state is the first mode of sine).

If not the integrated mobile charge carrier density is of interest, but the position-dependent distribution of the mobile charge carriers $n_{\text{film}}(z) = n_e(z) + p_h(z)$ in the thin film, one may use the following approximation for obtaining a more exact solution by additionally including the probability density of the corresponding wave functions: In Eq. (6.14) in section 6.4.2.7, the probability densities $|\Psi(z)|^2$ could be used as prefactor to the corresponding charge carrier densities $n_e(z)$ and $p_h(z)$. With this approximation, the probability density has no effect on the band bending potential $v(z)$ itself, but simply modifies the distribution of the mobile charge carriers in the film. Evidently, this approach is only useful if the z-dependence of the carrier density $n_{\text{film}}(z)$ in the thin film is of interest. If only the total mobile charge carrier density of the film is important, as it results from the integration of Eq. (6.14), the additional factor $|\Psi(z)|^2$ makes no difference.

6.6. Summary

In this chapter, it was shown that thin TI films usually exhibit parallel conduction channels through the interface layer and the interior of the film. These parasitic channels participate in the overall current transport and therefore can potentially reduce the fraction of the total current that flows through the TSS channel significantly. As a consequence, the desired benefit from the unique properties of the TI, for instance spin-momentum locking, would be partially lost. However, if the parasitic transport channels are understood in detail, the possibility arises to tune them towards a negligible influence compared to the auspicious TSS channel.

In order to determine the interface conductivity of thin TI films grown by van-der-Waals epitaxy, only the initial substrate termination has to be prepared and, afterwards, the interface conductivity can directly be measured by surface-sensitive four-probe transport measurements performed with a multi-tip STM.

The conductivity of the film interior can be determined by a combination of surface-sensitive experimental methods, such as ARPES and gate-dependent four-probe transport measurements, and band bending calculations in the thin-film limit. In the latter the TI film is treated similar to semiconductors, but without the assumption of Fermi level pinning, because the DOS of the TSS is typically small. In the symmetric approximation, where the measured value of the top surface Fermi level from ARPES is also applied to the non-accessible bottom surface, the total mobile charge carrier density in the film material can be calculated. This calculation is possible even if the concentration of dopants that are unintentionally incorporated during film growth is unknown, because in the thin-film limit the carrier density is nearly independent of the film dopant concentration for the desirable case of moderate film doping, i.e. a non-degenerate doping. The band bending calculations can be refined by employing asymmetric boundary conditions, if gate-dependent four-probe measurements on the top surface are used as additional input besides ARPES. Then, the conductivity of the interior of the thin film can be calculated unambiguously and the role of this channel for current transport in the TI system can be evaluated.

It is finally stressed that the methods presented in this chapter are rather general and can be applied to very different classes of TI materials. The information gained in this way can be important for designing future electronic devices based on TI materials in such a way that the majority of current is exclusively transported by the TSS, and thus most benefit can be gained from the topological properties of the material in question.

The results described in this chapter are largely published in Ref. [165], except for the data presented in section 6.2.2 which are included in Ref. [125] to a small extent. Additionally, results from section 6.4.3.2 are used in the publication in Ref. [131].

7. The weak topological insulator $Bi_{14}Rh_3I_9$

Besides two-dimensional surface channels, as treated throughout before, also one-dimensional conducting channels can exist at surfaces. In this case, the main difficulty which arises for characterizing their transport properties, is to disentangle them from a surrounding 2D surface channel. In this chapter, this problem is addressed by the example of a weak topological insulator. For this purpose, the first experimentally realized weak topological insulator $Bi_{14}Rh_3I_9$ is investigated by means of a multi-tip STM. The class of weak topological insulators can be understood in first order by a reduction of the dimensionality, as it is formed by a stack of 2D topological insulators. In contrast to strong 3D topological insulators, as discussed in detail in the previous chapter, a weak 3D TI does not exhibit two-dimensional surface states, but one-dimensional edge states on the top surface. These one-dimensional channels appearing at all step edges are predicted to form ballistically conducting lines on the surface making weak topological insulators a very interesting candidate for future electronic devices. In the following, these edge states on the top surface are probed by scanning tunneling spectroscopy and scanning tunneling potentiometry. Furthermore, the overall conductivity of the surface is measured by means of distance-dependent four-point measurements.

7.1. Weak topological insulators

Similar to strong topological insulators, also weak topological insulators exhibit topologically protected states, giving rise to the well-known properties of topological materials, i.e. spin-momentum locking and prohibited direct backscattering. However, there are some differences between strong and weak TIs concerning the dimensionality and position of the topological states. In principle, the term *weak* is slightly misleading, as it was initially introduced to express the expected instability of the topological surface states caused by disorder, which might introduce a gap in the surface states [166, 167]. However, recent works have elaborated that disorder can even stabilize the surface state resulting in a robust topological state also in weak TIs [168–171].

Strong three-dimensional TIs exhibit topologically protected two-dimensional surface states inside the band-gap on all surfaces. Inside the bulk material these states are not present, which results in an insulating bulk, if the Fermi energy is positioned inside the band-gap. Due to the states present on the surfaces, these surfaces are often termed as *bright surfaces*.

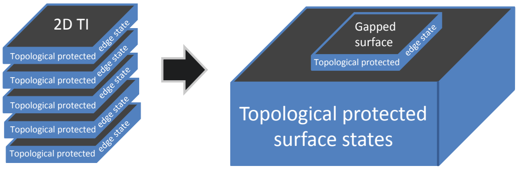

Figure 7.1.: Principle of the formation of a weak 3D topological insulator. A stack of multiple non-interacting 2D topological insulators with one-dimensional edge states can be used to construct a weak 3D topological insulator. The weak 3D TI exhibits bright surfaces along the stacking direction and dark surfaces without topological states perpendicular to the stacking. Every islands on the dark surface exhibits a 1D topological edge state. The drawing is reproduced from Ref. [175].

In contrast, a weak TI does not have surface states on all surfaces. This can be easily understood by the structure of a weak TI, which is visualized in Fig. 7.1. A simple way to construct a weak 3D TI is the stacking of multiple 2D TI sheets on top of each other with suppressed interlayer interaction [166, 172]. The 2D TI sheets only exhibit one-dimensional topological edge states at the surroundings of the sheets but no states on the surface itself (*dark surface*) due to the reduced dimensionality. The resulting stack, i.e. the weak 3D TI, then shows bright surfaces on all sides along the stacking direction due to the combined 1D edge states of the single layers, but the surfaces perpendicular to the stacking, i.e. the topmost and the bottommost surface, remain dark without any topological surface states. This implies then that also single-layer islands on the dark surfaces are surrounded by one-dimensional topological edge states at the step edges. Due to the special topological properties the backscattering in these 1D channels is predicted to be prohibited, so that an ideal conductance in the ballistic transport regime is expected with a conductivity of e^2/h, as long as time-reversal symmetry is not broken [171, 173]. As the 1D edge states appear at every boundary of the dark surface, it is also possible to scratch a 1D channel into the surface [174]. This gives rise to the possibility to artificially produce a network of ballistically conducting lines on a weak topological insulator making it an interesting candidate for future electronic devices.

7.2. $Bi_{14}Rh_3I_9$ crystal

$Bi_{14}Rh_3I_9$ was the first synthesized weak topological insulator material [176, 177]. In the following, its structure and surface topography probed by STM are discussed.

7.2.1. Crystal structure

The compound $Bi_{14}Rh_3I_9$ consists of two different ionic layers, which are alternately stacked, as it is visualized in Fig. 7.2(a). These two layers are the 2D topological insulator $[(Bi_4Rh)_3I]^{2+}$ and the trivial insulator $[Bi_2I_8]^{2-}$. The 2D TI exhibits a graphene-like honeycomb lattice formed by the heavy elements Bi, Rh and I, which are arranged in

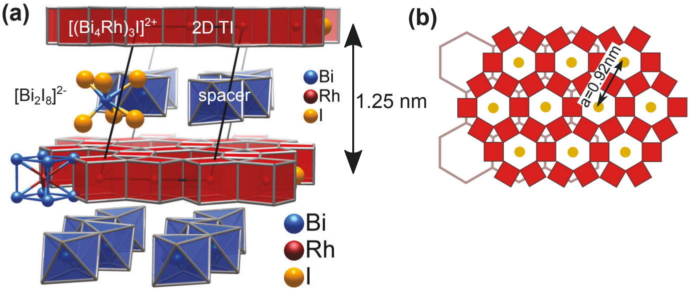

Figure 7.2.: (a) Crystal structure of $Bi_{14}Rh_3I_9$ consisting of an alternately stacking of the 2D topological insulator $[(Bi_4Rh)_3I]^{2+}$ and the insulating spacer $[Bi_2I_8]^{2-}$. (b) Top view of the honeycomb lattice structure of the 2D TI. (a) and (b) are reproduced from Ref. [175].

hexagonal rings of rhodium-centered bismuth cubes with the iodine atoms in the center [Fig. 7.2(b)]. In contrast to graphene the spin-orbit interaction in $Bi_{14}Rh_3I_9$ is much larger due to the heavy elements, which in combination with the graphene-like structure gives rise to topological effects [178]. The trivial insulating layers act as a spacer preventing an interlayer coupling between the 2D TI layers. The spacing between two consecutive 2D TI layers is equal to $1.25\,\mathrm{nm}$ [175].

7.2.2. Sample preparation

The $Bi_{14}Rh_3I_9$ crystals were synthesized by *Dr. Bertold Rasche* from the *Department of Chemistry* at the *TU Dresden* as described in Ref. [177]. Afterwards the crystals were transported to the *Research Center Jülich* under ambient conditions. All crystals were rather small in size up to approximately $1 \times 1 \times 0.2\,\mathrm{mm}^3$. For the STM measurements, one crystal is glued with a carbon-based glue (*DuPont* 7105), which is expected not to

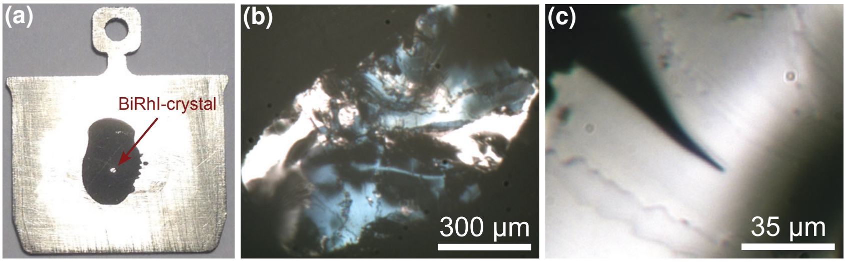

Figure 7.3.: (a) $Bi_{14}Rh_3I_9$ crystal glued with a carbon-based glue onto a *Omicron* sample holder. (b) Optical microscope image of the cleaved crystal inside the UHV (c) Enlarged image of a light-reflecting region of the crystal surface with a STM tip in front of it.

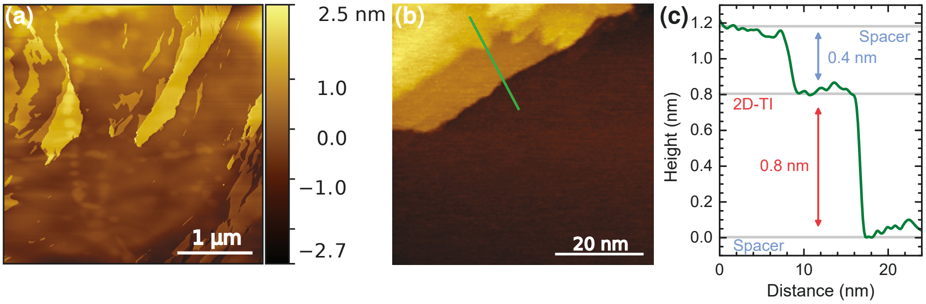

Figure 7.4.: (a) Large-area STM image of the $Bi_{14}Rh_3I_9$ surface ($U = 500\,\mathrm{mV}$, $I = 110\,\mathrm{pA}$). (b) Enlarged STM image of a double step edge on the $Bi_{14}Rh_3I_9$ surface ($U = -15\,\mathrm{mV}$, $I = 90\,\mathrm{pA}$). (c) Height profile along the green line marked in (b). Two different step heights of $0.8\,\mathrm{nm}$ and $0.4\,\mathrm{nm}$ are visible belonging to the 2D TI and the spacer layer, respectively.

react with the $Bi_{14}Rh_3I_9$ compound, onto a standard *Omicron* sample holder, as shown in Fig. 7.3(a). Afterwards the sample holder with the $Bi_{14}Rh_3I_9$ crystal was baked at a temperature of $120\,°\mathrm{C}$ for curing the glue.

In order to obtain a clean surface of the $Bi_{14}Rh_3I_9$ for the STM measurements, the crystal was cleaved inside the UHV chamber. This is possible due to the weak coupling of the layers in the $Bi_{14}Rh_3I_9$ structure. For this purpose, a piece of copper tape with a small metal wire at the upper end (not shown here) was pushed onto the crystal surface before it was transferred into the UHV. Inside the UHV chamber, the metal wire could be grabbed with the pincers at the manipulator and the copper tape was pulled from the crystal surface at a pressure of $1 \times 10^{-10}\,\mathrm{mbar}$. As a few layers of the crystal remain at the copper tape, the $Bi_{14}Rh_3I_9$ surface was cleaved and a clean surface for STM investigations was established.

In Fig. 7.3(b), an image of the cleaved $Bi_{14}Rh_3I_9$ crystal is shown, which is obtained by the optical microscope mounted at the multi-tip STM with lowest magnification. It is visible that the surface is not perfectly flat, as the light is not reflected homogeneously, which was always the case for the Si substrates measured before. This makes it much more difficult to identify and control the tips in front of the crystal surface. The only possibility is to zoom into the strongly light-reflecting regions, where the tips can be clearly seen [Fig. 7.3(c)]. However, as these reflecting regions are not very large, one has to be careful to bring all four tips together without a collision between them or with the crystal surface.

7.2.3. Surface topography probed by STM

Large-area STM scans of the $Bi_{14}Rh_3I_9$ surface, as shown in Fig. 7.4(a), reveal that there is no flat surface on the micrometer scale, but multiple islands which are partly connected and exhibit step edges with different heights. It turns out that basically two distinct step heights are present which can be identified with steps from the two different layers of the crystal, i.e. the 2D TI and the spacer [175]. Enlarged STM scans of step edges, as depicted exemplarily in Fig. 7.4(b) with the corresponding height profile in Fig. 7.4(c), reveal that the apparent heights[1] of neighbouring layers are $0.8\,\mathrm{nm}$ and $0.4\,\mathrm{nm}$ which can be attributed to the step heights of a 2D TI layer and a spacer layer, respectively [175]. Thus, the apparent step height of two combined adjacent layers, which is equal to the apparent spacing between two consecutive layers of the same type, i.e. between two 2D TI layers or two spacer layers, is with $1.2\,\mathrm{nm}$ in accordance with the crystal structure ($1.25\,\mathrm{nm}$) shown before in Fig. 7.2. In the following, such a composed layer of 2D TI and spacer is denoted as *double layer* (DL), irrespective of the stacking order, and the step present at the collective edge of this two adjacent layers is referred to as *double step*. In the same way, in order to commonly denote either 2D TI or spacer, the term *single layer* is used, while on the other side two consecutive double layers are termed as a *quadruple layer* (QL).

Without resolving the atomic structure of the surface it is not directly possible from the STM image to conclude, which layer is the topmost layer, i.e. the 2D TI or the spacer. However, by measuring the different step heights at step edges, which are composed out of the basic layer heights, it is possible to identify the layers. Moreover, an identification of the spacer layer is also possible by the thermovoltage obtained from potentiometry measurements (cf. Fig. 7.18), as it will be discussed in more detail later on in section 7.5.2.2. Since one disadvantage of the first method, i.e evaluating the step topography, is that in order to properly assign all of the layers at least one single spacer layer has to be found in the STM image which seems to be rarely the case for the studied crystals, particularly the potentiometry is a better alternative for identifying the layers. From both methods it turns out that for the studied crystals the dominant topmost layer is the 2D TI layer and that the majority of step edges are extended over either a single or multiples of double layers, thus exhibiting a height of multiples of $1.2\,\mathrm{nm}$. This implies that basically only steps between 2D TI layers are present, while there are only a very few regions on the surface, where the spacer layer appears. Such a result seems to be in contrast to the findings from Ref. [175], where the spacer was the predominant layer on top, but such differences might be explained by some variations in the preparation or cleaving process of the crystals, or in the crystal growth itself. Nevertheless, here this statement can be well founded by the STM data, as shown in the following sections.

7.3. Probing the edge state by scanning tunneling spectroscopy

An appropriate method for measuring the edge state of $\mathrm{Bi_{14}Rh_3I_9}$ at step edges is scanning tunneling spectroscopy. This method combines the excellent spatial resolution of the STM tip with an additional energy resolution, and thus is suitable to reveal not only the lateral position of the edge states on the surface, but also their distribution in energy with respect to the Fermi level, as it will be shown in this section.

---

[1] In STM, an apparent step height results from a combination of geometric and electronic effects.

7.3.1. Measurement principle

In principle, a conventional STM in constant-current mode does not directly measure the topography of a sample surface, but it more specifically images a contour of constant local density of states (LDOS) while scanning over the surface, as beside the distance between tip and sample also the LDOS of the surface influences the tunneling current in dependence of the applied bias voltage [179, 180]. This can be used for directly probing the LDOS of the surface. In first order approximation, the derivative of the tunneling current dI/dV is directly proportional to the LDOS of the sample surface at the tip position and at the corresponding energy of the applied bias voltage [181]. So, by ramping the bias voltage and simultaneously measuring dI/dV by means of a lock-in amplifier, the LDOS can be measured locally on the sample surface as function of energy. For this point spectroscopy mode, the tip has to be stabilized prior to measurement at one point of the surface and the STM feedback loop has to be switched off for avoiding a tip crash at the zero crossing of the bias voltage. Another measurement mode is the acquisition of dI/dV-maps. Here, the bias voltage is not ramped, but the dI/dV signal is recorded simultaneously during scanning. This enables to directly image the spatial distribution of the LDOS at the corresponding energy of the applied bias voltage. In contrast, the point spectroscopy mode gives direct access to the energetic dependence of the LDOS at one specific point of the surface. For obtaining both, i.e spatial and energetic resolution, in one measurement, either point spectroscopy measurements at each pixel of the STM image have to performed during scanning, which is very time consuming, or multiple dI/dV-maps at different bias voltages have to be recorded. The latter is more suitable for determining local changes of the LODS at distinct energies, which is desired for measuring the edge state of $Bi_{14}Rh_3I_9$. With the software of the multi-tip STM it is possible to record up to 10 dI/dV-maps at different bias voltages line-by-line, i.e. the same line is measured consecutively after each time changing the bias voltage. When all different values for the voltage are passed, the next line is scanned. This method reduces the drift effects between the dI/dV images significantly and allows for a better comparison of the spatial distribution of the LDOS for different energies. All of the dI/dV-maps presented below in the sections 7.3.2 and 7.3.3 are recorded by this method. As all spectroscopic measurements are acquired at room temperature, the possible energy resolution is significantly reduced compared to low-temperature measurements. It can be approximated by

$$\Delta E \approx \sqrt{(3.3\,k_BT)^2 + (2.5\,eV_{\mathrm{mod}})^2} \tag{7.1}$$

with the temperature T and RMS value of the modulation voltage V_{mod} [182]. For room temperature ($T = 300\,\mathrm{K}$) and a modulation voltage of $V_{\mathrm{mod,RMS}} = 8.8\,\mathrm{mV}$ a energy resolution of $\Delta E \approx 88\,\mathrm{meV}$ is obtained.

7.3.2. Step edges

Low-temperature point spectroscopy measurements at $6\,\mathrm{K}$ on $Bi_{14}Rh_3I_9$ have already been performed in Ref. [174] as shown in Fig. 7.5. It was found that the LDOS in the vicinity

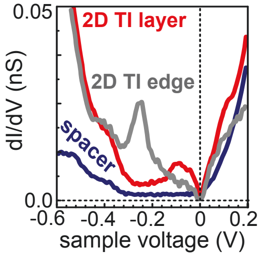

Figure 7.5.: Low-temperature (6 K) spectroscopic dI/dV measurement of the surface of $Bi_{14}Rh_3I_9$ at different positions, as indicated. The plot is reproduced from Ref. [175].

of step edges of the 2D TI layer shows a significant increase in intensity (gray curve) compared to the LDOS of the 2D TI layer terraces (red curve). Furthermore, the peak in the LDOS at the step edges is located inside the band gap of the 2D TI ranging from $-0.15\,\mathrm{eV}$ to $-0.35\,\mathrm{eV}$. As in the case of $Bi_{14}Rh_3I_9$ the energy dispersion of the topological state is different from most strong 3D TIs, as it results from tight-binding calculations [175], such a peak inside the band gap of the 2D TI is expected for the presence of the topological edge state. In contrast, for the topological state of strong 3D TIs forming a Dirac cone at the surface with a vanishing LDOS at the Dirac point, the dI/dV curve would show a minimum at the Dirac point while increasing towards the boundaries of the bulk band gap. The spacer layer (blue curve) exhibits only a pronounced band gap with an approximately vanishing LDOS inside corresponding to its nature of a trivial insulator. As the band gap of the 2D TI and the position of the edge state is not located at the Fermi energy, the 1D edge channels are not directly accessible for electric transport measurement, which is discussed below in section 7.4 in more detail.

In Fig. 7.6 the edge state is spatially resolved by several dI/dV maps acquired with the multi-tip STM. A double step edge is chosen with the 2D TI as the topmost layer, i.e. a step over a 2D TI layer and the adjacent spacer layer, as it is shown by the STM image in Fig. 7.6(a) and the corresponding height profile in Fig. 7.6(b). The Figs. 7.6(c) – 7.6(i) depict the dI/dV images recorded at different bias voltages as labeled in the corresponding image. It is visible that in between a bias voltage of $-15\,\mathrm{mV}$ and $-250\,\mathrm{mV}$ a pronounced intensity arises exclusively at the position of the double step edge, while this intensity vanishes for bias voltages of $-400\,\mathrm{mV}$ and lower values, as well as for voltages of $250\,\mathrm{mV}$ and higher. There is a slight shift of the energies compared to the measurement presented in Fig. 7.5, but a reason for this can be the cleaving procedure of the crystal during sample preparation, which can influence the properties of the surface, as it is discussed in more detail below in section 7.4. Also due to the lower energy resolution at room temperature the peak in the LDOS for the edge state appears much broader. But in total, the measured intensity of the edge state is located inside the band gap of the 2D TI, the intensity of the edge state is continuous along the step edge and the measured width of the state is smaller than approximately $2\,\mathrm{nm}$, which is all in accordance with previous measurements [174].

Due to the distinct values of bias voltage used in the measurement in Fig. 7.6, the voltage

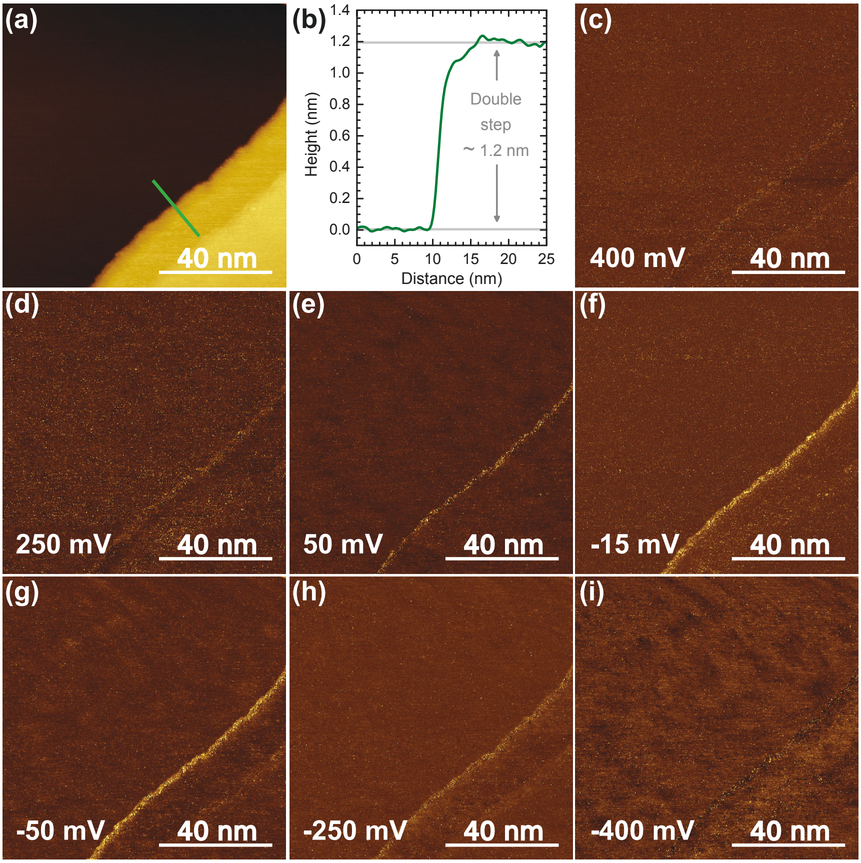

Figure 7.6.: Spectroscopic dI/dV measurement of a double step edge [STM image in (a), height profile in (b)] on $Bi_{14}Rh_3I_9$ for different bias voltages [(c) – (i)]. The step is formed by two consecutive single-layer steps of the 2D TI and the spacer with the 2D TI layer as topmost layer on the terraces. A slightly appearing parallel step edge in (a) is caused by double-tip effects. Measurement parameters are: $U = 400\,\mathrm{mV}$ (a), $I_{\mathrm{stab}} = 300\,\mathrm{pA}$, $V_{\mathrm{mod,RMS}} = 9\,\mathrm{mV}$, $f_{\mathrm{mod}} = 980\,\mathrm{Hz}$.

range of the peak intensity of the edge state cannot be determined precisely. In order to improve that a second measurement was performed, as shown in Fig. 7.7, with a more narrow range of bias voltages. Here, a surface structure with step edges of different height was chosen, i.e. one double step edge and a trench in the surface with a depth of $2.4\,\mathrm{nm}$ ranging over four layers, both with the 2D TI as topmost layer at the terraces. In Fig. 7.7(a) the STM image of the structure is shown and in Fig. 7.7(b) the corresponding height profile is depicted. The Figs. 7.7(c) – 7.7(l) show the measured dI/dV maps for bias voltages from $100\,\mathrm{mV}$ to $-250\,\mathrm{mV}$. Here, it is clearly visible that the intensity of the edge state appears at approximately $+15\,\mathrm{mV}$ and vanishes at $-250\,\mathrm{mV}$ with the maximum located around $-150\,\mathrm{mV}$. So, the maximum is shifted by approximately $100\,\mathrm{mV}$ compared to Ref. [174],

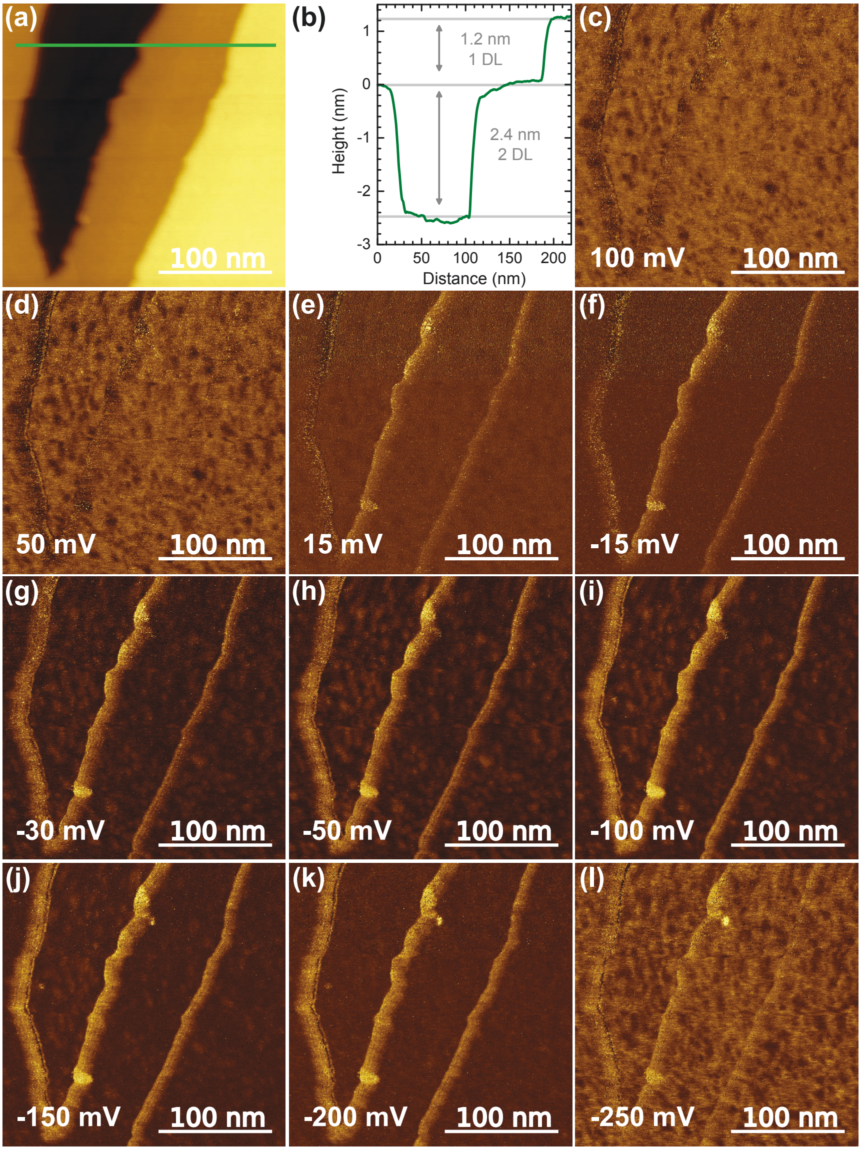

Figure 7.7.: Spectroscopic dI/dV measurement of a double and quadruple steps [STM image in (a), height profile in (b)] on the $Bi_{14}Rh_3I_9$ surface for different bias voltages [(c) – (l)]. The topmost layer on the terraces is the 2D TI. Measurement parameters are: $U = 100\,\mathrm{mV}$ (a), $I_{\mathrm{stab}} = 90\,\mathrm{pA}$, $V_{\mathrm{mod,RMS}} = 18\,\mathrm{mV}$, $f_{\mathrm{mod}} = 980\,\mathrm{Hz}$.

which can be caused by a different surface morphology, as discussed later in section 7.4. The intensity of the edge state at the quadruple step appears slightly stronger than that at

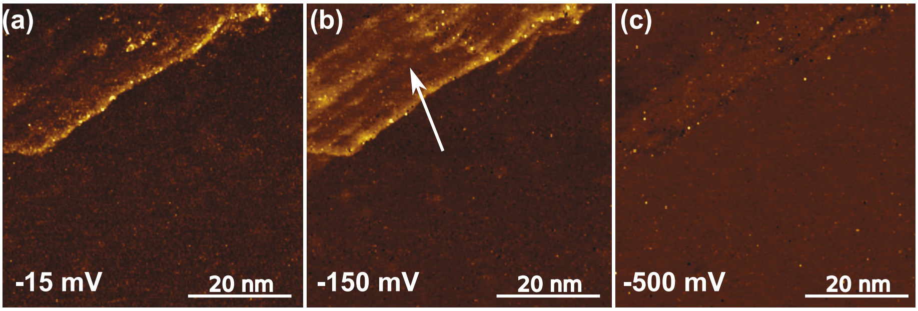

Figure 7.8.: Spectroscopic dI/dV measurement of a single-layer step of the spacer and the 2DTI on the $Bi_{14}Rh_3I_9$ surface for different bias voltages [(a) – (c)]. The white arrow indicates the position of the spacer step edge. Topography and height profile are shown in Figs. 7.4(b) and 7.4(c). Measurement parameters are: $I_{\mathrm{stab}} = 90\,\mathrm{pA}$, $V_{\mathrm{mod,RMS}} = 9\,\mathrm{mV}$, $f_{\mathrm{mod}} = 980\,\mathrm{Hz}$.

the double step [cf. Figs. 7.7(i) – 7.7(k)], which is expected due to twice edge channels at this position and the corresponding pronounced LDOS. Compared to the measurement in Fig. 7.6, the width of the edge state seems to be much broader now, but this is most probably a measurement artefact and caused only by a very blunt tip, as it is also visible from the reduced sharpness of the topography in Fig. 7.7(a). Nevertheless, a positive side effect is that the spatial broadening of the edge state intensity due to the blunt tip makes it more visible in the dI/dV maps. A subsequent dI/dV-measurement on a smaller area of the same step structure can be found in Fig. B.2 in the appendix B together with another measurement on a different double step edge (Fig. B.3), both yielding similar results as discussed before.

The topological edge state should only appear at the step edges of the 2D TI layers, while it should not be present at the edges of the insulating spacer layer. For proving this, a dI/dV measurements is performed at two adjacent single-layer steps, as it is shown in Fig. 7.8. The corresponding topography of the steps was already shown in Fig. 7.4(b) together with the height profile [Fig. 7.4(c)], which identify them unambiguously as steps in the 2D TI and the spacer layer, respectively. The dI/dV maps in Figs. 7.8(a) – 7.8(c) show that for an energy around $-150\,\mathrm{meV}$, where the LDOS of the edge state located at the step edge of the 2D TI shows its maximum intensity, there is a vanishing intensity at the position of the spacer layer step edge, which is indicated by the white arrow in Fig. 7.8(b). As the single-layer step of the spacer is only present at the position marked by the arrow, i.e. below the green line of the height profile indicated in Fig. 7.4(b), the vanishing LDOS can only be observed at this position. On the left and the right side of the arrow, the step edge changes to a double step, so that here the edge state of the 2D TI appears again. Also for other energy values no pronounced intensity of the LDOS at the spacer edge appears [Figs. 7.8(a) and 7.8(c)] indicating that no additional edge state is present. A further prove for the disappearance of the edge state at the spacer layer can be obtained from thermovoltage measurements [cf. Fig. 7.18(b)], as it will be discussed in section 7.5.2.2.

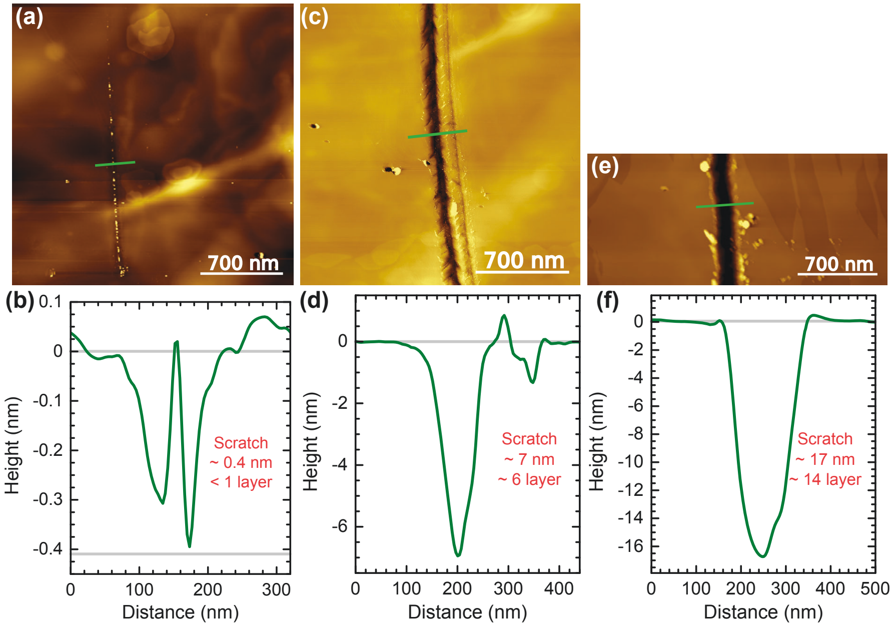

Figure 7.9.: STM images of scratches with different depth [(a),(c),(e)] into the $Bi_{14}Rh_3I_9$ surface performed with a tungsten STM tip and the corresponding height profiles [(b),(d),(f)]. Measurement parameters are: $U = -500\,\mathrm{mV}$, $I = 90\,\mathrm{pA}$.

7.3.3. Artificial scratches induced by tip contact

A unique property of a weak TI is, that the edge states appear at every step edge of the 2D TI sheet on the dark surface. This makes it possible to artificially create such edge channels by simply scratching a trench into the surface [174]. If the depth of such a trench is extended at least over one 2D TI layer, an topological edge channel is obtained at the position of the scratch. So, in principle, a complete network of such one-dimensional ballistically conducting lines on the surface can be fabricated which makes 3D weak topological insulator to an interesting material for future electronic devices.

7.3.3.1. Scratching into the surface

For scratching structures into surfaces, one can benefit from the usage of a multi-tip. With such an instrument, the scratch can be fabricated with one tip, and the subsequent imaging of the scratched surface can be done by using another tip. If only a STM with one tip is available, the subsequent STM scan after the scratch can be very challenging, but it may work. However, any additional spectroscopic measurement with the same tip used for the scratch is nearly impossible.

Here, a multi-tip STM is used, where first two tips are brought together in the same region of the sample surface. Then, the tip, which is intended to be used for scratching, is approached into tunneling contact and afterwards into hard contact with the surface, as described before in section 2.3.2. Afterwards, the tip is pushed even more downwards for several nanometers, which can be precisely controlled by the z-piezo, and then moved slowly across the sample surface by using the lateral movement of the piezo-scanner in the full range of up to $3.6\,\mu\mathrm{m}$. In this way, a scratch into the topmost 2D TI layer of the $\mathrm{Bi_{14}Rh_3I_9}$ crystal is obtained, as it is shown in Fig. 7.9 for different indentation depths of the tip. The subsequent imaging of the scratch is done by the second tip by moving it to the position of the scratch, which can be controlled by the optical microscope, and performing a large-area scan in order to find the scratch on the surface.

As the STM tips are arranged in an angle of $45\,^\circ$ with respect to the surface, and therefore act like a spring, they can bend away from the surface when being pushed towards it. So, the movement necessary for the scratching tip in z-direction is always much higher than the obtained indentation depth of the tip into the sample [44]. For this reason, the depth of the scratches depicted in Fig. 7.9 are always much smaller than the z-movement of the tip into the surface with respect to the position of initial hard contact. For Fig. 7.9(a) the movement in z-direction was approximately $10\,\mathrm{nm}$, but the maximum depth of the scratch is only $\sim\!0.4\,\mathrm{nm}$, as it can be deduced from the corresponding height profile in Fig. 7.9(b). In this case, not even the topmost layer is completely scratched and additionally a lot of residues of the tip are visible along the scratch. By increasing the setpoint of the tip indentation up to $100\,\mathrm{nm}$, a much deeper scratch is obtained as shown in Figs. 7.9(c) and 7.9(d). Now, the depth is $\sim\!7\,\mathrm{nm}$, so that it is extended approximately over 6 double layers, i.e. 6 consecutive 2D TI layers. Besides the main scratch a second smaller scratch with depth of $1\,\mathrm{nm}$ can be observed resulting from a special microstructure of the tip. When the tip is further pushed into the surface by increasing the z-setpoint up to $300\,\mathrm{nm}$, the obtained tip indentation also increases resulting now in a scratch with a depth of $\sim\!17\,\mathrm{nm}$ and a corresponding extension over 14 2D-TI layers, as it is depicted in the Figs. 7.9(e) and 7.9(f). With increasing indentation depth also the width of the scratches slightly increases from $80\,\mathrm{nm}$ [Figs. 7.9(a) and 7.9(c)] to $130\,\mathrm{nm}$ [Fig. 7.9(e)]. However, the width also depends on the sharpness of the used tip.

7.3.3.2. dI/dV-spectroscopy of scratches

In order to prove that the topological edge states of the $\mathrm{Bi_{14}Rh_3I_9}$ are also present at artificial scratches on the surface, a dI/dV measurement is performed at a small area of the scratch depicted in Fig. 7.9(c). The results of the measurement are plotted in Fig. 7.10. The considered part of the scratch shown in Fig. 7.10(a) also exhibits the $7.5\,\mathrm{nm}$ deep trench in the center and the additional smaller trench next to it with a depth of $1.2\,\mathrm{nm}$ corresponding to exactly one double layer, as it can be deduced from the height profile in Fig. 7.10(b). The bias voltage-dependent spectroscopic images in Figs. 7.10(c) – 7.10(l) show unambiguously a pronounced intensity of the LDOS at the position of the trenches within a range from $-15\,\mathrm{mV}$ to $-250\,\mathrm{mV}$ with a maximum at $-150\,\mathrm{mV}$, as it was exactly the case for the appearance of the topological state at step edges shown in section 7.3.2

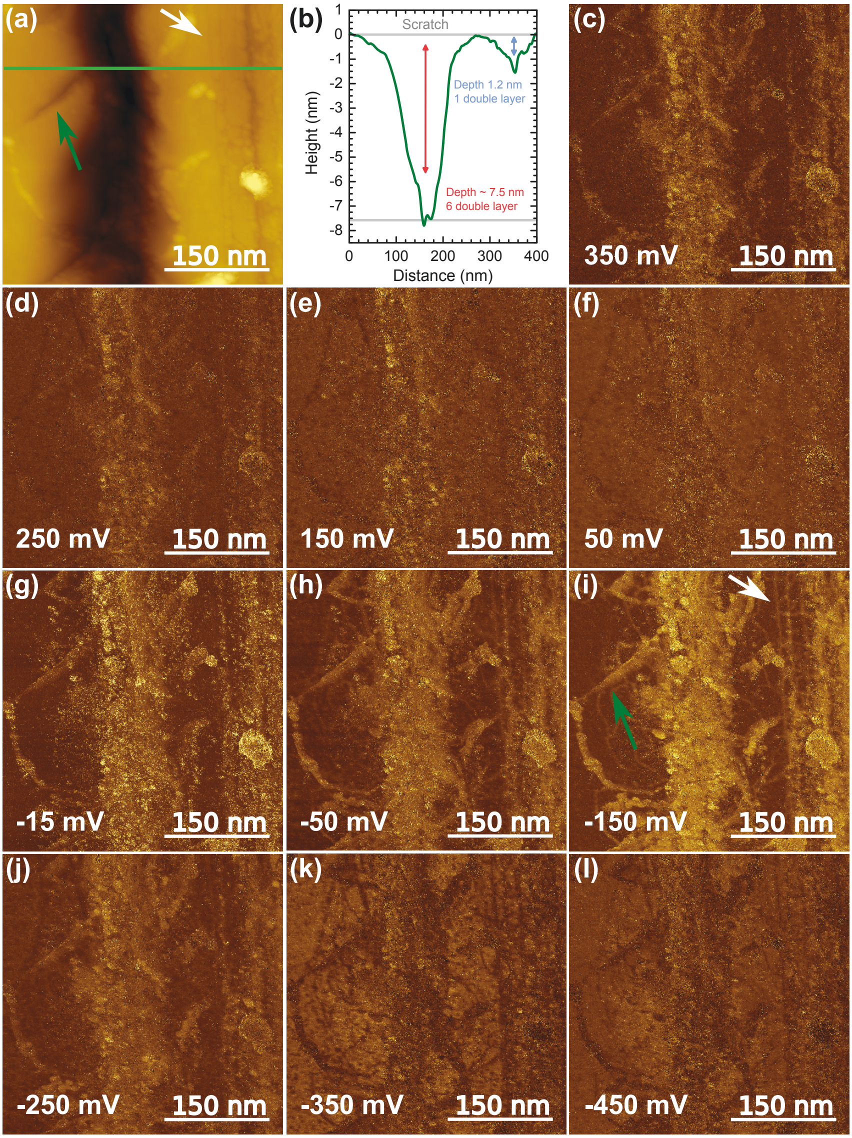

Figure 7.10.: Spectroscopic measurements of an artificially created scratch into the $Bi_{14}Rh_3I_9$ surface shown in (a) with the height profile in (b). (c) – (l) dI/dV maps at different bias voltages. The pairs of colored arrows in (a) and (i) correlate features in the topography to the intensity in the LDOS as discussed in the text. Measurement parameters are: $U = 350\,\mathrm{mV}$ (a), $I_{\mathrm{stab}} = 300\,\mathrm{pA}$, $V_{\mathrm{mod,RMS}} = 7\,\mathrm{mV}$, $f_{\mathrm{mod}} = 980\,\mathrm{Hz}$.

before. Beside the deep main trench in the center, which shows a spatially broad intensity of the edge state over the complete width of the trench [Fig. 7.10(i)], also all smaller rifts in the topmost layers next to the main trench exhibit a pronounced LDOS and, therefore, an edge state, e.g. as it is marked by the pair of green arrows in the Figs. 7.10(a) and 7.10(i). Very small near-surface scratches with a depth of only a few Å, which are visible on the right side in parallel to the deep trench, show a reduced intensity of the LDOS, as they are extended at maximum only over one 2D TI layer, but their edge states seem to be spatially very well-defined. These states form nearly an ideal narrow line along the trench with a width of only a few nm, which is similar to the shape of the edge states at step edges, as it is visible at the position of the pair of white arrows [Figs. 7.10(a) and 7.10(i)]. A second measurement at another scratch in the $\mathrm{Bi}_{14}\mathrm{Rh}_3\mathrm{I}_9$ surface yielding similar results can be found in Fig. B.4 in the appendix B.

7.4. Four-point probe measurements

In principle, in order to attempt to measure the conductivity of the 1D edge channels on the dark surface of the $\mathrm{Bi}_{14}\mathrm{Rh}_3\mathrm{I}_9$, local charge transport measurements can be performed with the multi-tip STM. However, in the present case it turned out that the band gap of the 2D TI and the edge states located inside are not positioned at the Fermi energy, as shown before in section 7.3.2. So, unfortunately the edge states are not directly accessible by electrical transport measurements without any possibility of gating or chemical doping. Nevertheless, the possible appearance of further conductance channels for charge transport in the $\mathrm{Bi}_{14}\mathrm{Rh}_3\mathrm{I}_9$ can be revealed by distance-dependent four-point probe measurements on the surface, as it is discussed in the following.

7.4.1. Linear tip configuration

In order to separate a possible overall surface conductance of the topmost layer in $\mathrm{Bi}_{14}\mathrm{Rh}_3\mathrm{I}_9$, which in the present case turned out to be predominantly the 2D TI layer, as discussed before, from any bulk contributions, the non-equidistant linear tip configuration with tip distances on the $\mu\mathrm{m}$-scale can be used, as it is visualized in Fig. 7.11(c). The results of the corresponding four-point measurements are depicted in Fig. 7.11(a), where the obtained four-point resistance is plotted as function of the non-equidistant spacing x between the outer current injecting tip and the adjacent inner voltage measuring tip [Fig. 7.11(c)], while the equidistant spacing $s = 20\,\mu\mathrm{m}$ between the other tips is kept constant. For each tip position, the four-point resistance is extracted from the slope of an $I(V)$-curve, while the injected current is up to $500\,\mu\mathrm{A}$.

The measured data cannot be described properly by either a pure 2D or a pure 3D transport model, as it is indicated by the corresponding fits of the blue and green dotted lines [cf. Eqs. (3.48) and (3.50)], respectively, which indicates that both conductance channels in parallel are present. Therefore, a multi-layer model for charge transport consisting of a 2D surface channel and a 3D bulk channel is used, which is outlined in Fig. 7.11(b). Such a

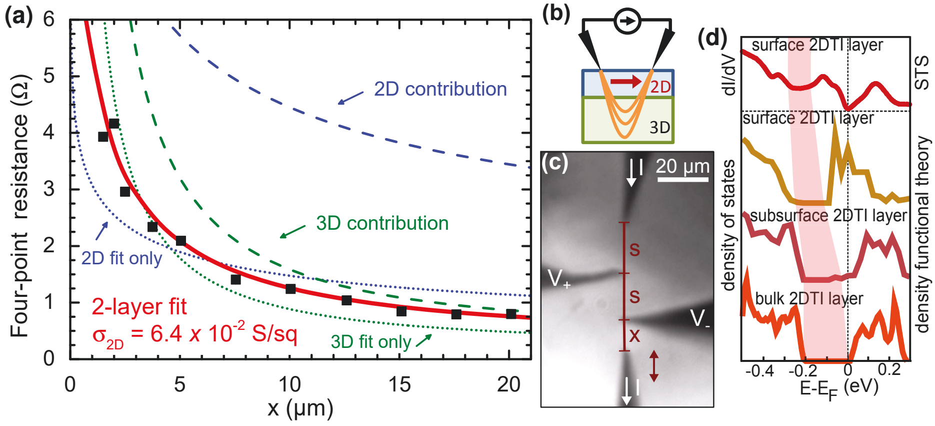

Figure 7.11.: (a) Measured four-point resistance using the non-equidistant linear tip configuration as function of the spacing x between one current injecting tip and the adjacent voltage measuring tip [as shown in (c)]. The spacing between the other tips is set to $s = 20\,\mu\mathrm{m}$. Both fits according to a pure 2D (blue) and a pure 3D (green) transport model are depicted by the dotted lines, while a fit using a two-layered model [as shown in (b)] is indicated by the solid red line, resulting in $\sigma_{2\mathrm{D}} = (6.4 \pm 0.5) \times 10^{-2}\,\mathrm{S}/\Box$ and $\sigma_{3\mathrm{D}} = (9.2 \pm 0.8) \times 10^{3}\,\mathrm{S/m}$. These two individual contributions of 2D and 3D transport resulting from the two-layer model are plotted separately as dashed blue and green curves, respectively. (b) Sketch of the applied two-layer model consisting of a 2D surface channel and 3D bulk channel in parallel. (c) Optical microscope image of the tips on the surface arranged in the non-equidistant linear configuration with the distances s and x. (d) STS measurement data (upper curve) as obtained in Ref. [183] and DFT calculations (lower curves) for the LDOS of the 2D TI layer in dependency of its position inside the crystal. The band gap region is marked by the highlighted red area. This plot is reproduced from Ref. [183].

two-layered model can be described in the same way as the 3-layer model presented before in section 4.2 by Eq. (4.17), when the conductivities of the space charge layer and the bulk are set to the same value.[2] This proceeding is applicable in the present case, as it turns out that the space charge region does not have much influence on the current transport, so that an intermediate layer is not needed. The application of such a 2-layer model results in the best fit to the experimental data, as shown by the solid red line in Fig. 7.11(a), yielding conductivities for the 2D and 3D contributions of $\sigma_{2\mathrm{D}} = (6.4 \pm 0.5) \times 10^{-2}\,\mathrm{S}/\Box$ and $\sigma_{3\mathrm{D}} = (9.2 \pm 0.8) \times 10^{3}\,\mathrm{S/m}$, respectively. For the calculations, the thickness of the surface layer is set to $8\,\text{Å}$, in accordance with the thickness of one 2D TI layer, and the depth of the bulk is assumed to be infinitely. The individual 2D and 3D contributions are visualized by the dashed blue (2D) and green (3D) lines in Fig. 7.11(a). If both conductivity values for the 2D surface and the 3D bulk are compared directly, it turns out that a finite sheet of $\sim 7\,\mu\mathrm{m}$ thickness with a bulk conductivity of $9.2 \times 10^{3}\,\mathrm{S/m}$ would exhibit the same conductivity as the surface layer with $6.4 \times 10^{-2}\,\mathrm{S}/\Box$. Thus, it can be deduced that

---

[2] In order to obtain the coefficients $a(k)$ and $b(k)$, the conductivities of the surface σ_1 and the intermediate-layer σ_2 have to be equalized in Eq. (4.11).

the conductivity of the topmost layer is enhanced by a factor of $\frac{7\,\mu\mathrm{m}}{1.2\,\mathrm{nm}} \sim 5800$ compared to one of the layers below, whereby as interlayer spacing $1.2\,\mathrm{nm}$ is assumed, since the insulating spacer does not contribute to transport.

The transport measurements reveal that besides a bulk channel also a sizeable contribution of the 2D surface conductance to current transport exists. In principle, one would expect that for a weak topological insulator the surface conductivity of the dark surface vanishes and also the bulk material is largely insulating, giving rise to transport only through the one-dimensional edge states on the surface. However, this is only true, if the Fermi energy is located inside the band gap of the material, both inside the bulk and at the surface. Moreover, the Fermi energy has to coincide with the energetic position of the topological edge states at the surface. Unfortunately, for the $\mathrm{Bi}_{14}\mathrm{Rh}_3\mathrm{I}_9$ this is not the case, as it was already visible from the spectroscopic measurements shown in section 7.3.2 revealing that particularly at the surface the Fermi energy is not located inside the band gap. A more detailed insight can be obtained by DFT calculations performed for a thin film consisting of two 2D TI layers and two spacer layers, which are alternatingly stacked [183]. In Fig. 7.11(d), the calculated density of states of the 2D TI layer is plotted as function of energy for different positions in the crystal, i.e. for increasing distance from the surface (lower three curves). It is visible that at the surface the topmost 2D TI layer is strongly n-doped (yellow curve), so that the band gap (highlighted red area) is shifted substantially away from the Fermi energy, which is in accordance with measurements of the LDOS at the surface (top curve). Immediately at the position of the Fermi energy an increased density of states is present, which in turn leads to a high conductivity of the surface layer, as it also results from the four-point measurements. It should be noted that the large LDOS at the Fermi energy is not visible in the low-temperature measurements due to a pronounced Coulomb gap [183]. For the subsurface 2D TI layer the band gap starts to shift towards the Fermi energy (magenta curve) and already for the third 2D TI layer (orange curve) the bulk position is reached with the Fermi energy located directly at the conduction band edge. In this case, the density of states directly at the Fermi energy vanishes, but as the transport measurements are performed at room temperature, the thermal broadening of the Fermi edge leads to an excitation of charge carriers into the conduction band and still results in a certain conductivity of the bulk material, as measured in Fig. 7.11(a). If the density of states at the Fermi energy is compared between bulk and surface [Fig. 7.11(d)], it is directly visible that inside the bulk it is much more suppressed, which supports the measurement results that the surface of the $\mathrm{Bi}_{14}\mathrm{Rh}_3\mathrm{I}_9$ crystal is significantly more conductive than the bulk material.

A possible reason for the shift of the band gap of the surface 2D TI layer compared to the bulk position is the charge transfer between neighbouring layers. Due to the ionic stacking of the $\mathrm{Bi}_{14}\mathrm{Rh}_3\mathrm{I}_9$ crystal each individual layer is charged, and it turns out that the twofold positive charge of the 2D TI layer $[(\mathrm{Bi}_4\mathrm{Rh})_3\mathrm{I}]^{2+}$ results from a transfer of one electron per unit cell to each of the two surrounding spacer layers $[\mathrm{Bi}_2\mathrm{I}_8]^{2-}$ [183]. This case occurs in the equilibrium inside the bulk and results in a Fermi energy located at the upper edge of the band gap. However, at the surface the symmetry of the crystal is broken, as one of the spacer layers is missing. So, charge transfer can occur only to the spacer layer below and one negative charge per unit cell remains at the topmost 2D TI layer. This results in a strong

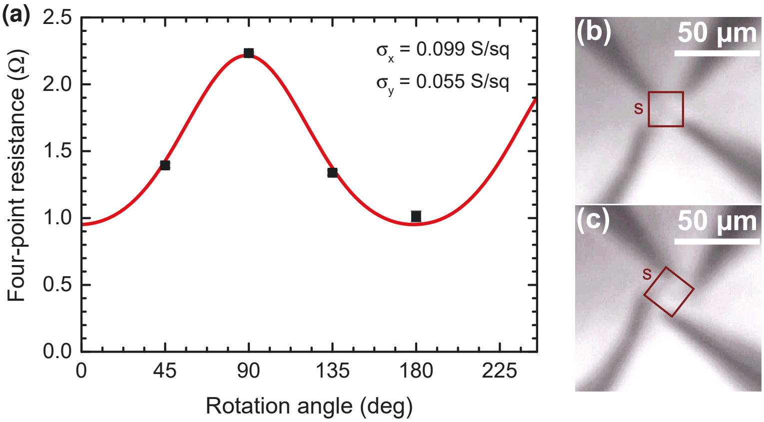

Figure 7.12.: (a) Measured four-point resistance using the rotational square method as function of the rotation angle and corresponding fit to the data (solid red line). The distance between the tips positioned at the edges of the square is $s = 20\,\mu\mathrm{m}$. (b),(c) Optical microscope images of the four tips arranged in the square configuration for two distinct rotation angles.

n-doping of the surface and the Fermi energy is correspondingly shifted into the conduction band. The extent of this shift can be influenced by the ratio between 2D TI layer and spacer layer covering the surface. A decreasing fraction of the spacer layer directly leads to an increased n-doping and a pronounced shift of the Fermi energy. So, the initial cleaving procedure of the crystal can influence the surface properties significantly. Moreover, such an excessive n-doping of the surface is perfectly in accordance with the findings that the majority of the surface is covered by the 2D TI layer and not by the spacer.

7.4.2. Square tip configuration

In order to investigate the anisotropy of the surface conductance of the $\mathrm{Bi_{14}Rh_3I_9}$ crystal additional four-point measurements are performed using the rotational square method. In Fig. 7.12(a), the measured four-point resistance is plotted as function of the rotation angle for a tip distance at the edges of the square of $s = 20\,\mu\mathrm{m}$. The corresponding tip configuration is visualized by the optical images for two distinct rotation angles shown in the Figs. 7.12(b) and 7.12(c). A fit according to Eq. (3.83) describes the data very well (solid red line), and results in the two components of the surface conductivity $\sigma_x = (9.9 \pm 0.6) \times 10^{-2}\,\mathrm{S}/\Box$ and $\sigma_y = (5.5 \pm 0.2) \times 10^{-2}\,\mathrm{S}/\Box$. So, the resulting anisotropy is $\sigma_x/\sigma_y \approx 2$. The geometric mean $\sqrt{\sigma_x \sigma_y} = (7.4 \pm 0.3) \times 10^{-2}\,\mathrm{S}/\Box$ is in accordance with the measured conductivity in the linear tip configuration shown in the previous section. The minor deviation between both values can be explained by the additional contribution of the bulk conduction channel, which is not taken into account in Eq. (3.83). However, as the surface channel dominates in the present case, the deviation is only very small and, therefore, negligible.

In principle, one would expect on average an anisotropy for the surface conductance of a weak TI exhibiting on one hand a slightly conducting dark surface, e.g. as it may arise from a surface Fermi energy not located around the center of the band gap, and on the other hand ballistically conducting edge channels aligned along a preferential direction, e.g. as it results from a favoured direction of the step edges on the surface. Such a slightly preferred step orientation can be observed in Fig. 7.4(a) for the $\mathrm{Bi_{14}Rh_3I_9}$ surface. However, in the present case the topological edge channels do not substantially participate in current transport, as discussed before. Moreover, the 2D TI surface layer is so highly conductive with $\sigma_{\mathrm{2D}} = 6.4 \times 10^{-2}\,\mathrm{S}/\square$ that it totally surpasses the conductance of a single 1D ballistic channel with $G_{\mathrm{1D,ball}} = \frac{e^2}{h} \approx 4 \times 10^{-5}\,\mathrm{S}$ by three orders of magnitude. Even if the total number of step edges inside the square of $20 \times 20\,\mu\mathrm{m}^2$ is considered, it would require more than 10^3 ballistic channels in parallel for at least equalizing both conductivities. However, for an edge-state-induced anisotropy a higher conductivity along the direction of the edge channels compared to the surrounding dark surface is necessary. Both reasons, i.e. the edge states not located at the Fermi energy and the highly conductive dark surface, imply a pronounced current flow through the surface layer rather than through the edge channels, thus any contribution of the topological states to the measured anisotropy has to be excluded.

So, the observed anisotropy in the surface conductivity is most probably caused only by an additional resistance arising from step edges located perpendicular to the current path, e.g. as it was similarly observed for the Si(111)-(7×7) surface in section 4.3. However, in the case of $\mathrm{Bi_{14}Rh_3I_9}$ two different kinds of step edges are present on the surface, i.e. edges at the spacer and at the 2D TI layer. Even if basically only steps at collective edges of both layers were considered, which in fact seem to be favoured, it would be very difficult to determine a reliable value for the step density, since neither these steps are uniformly distributed nor only double steps appear, but mostly steps with a multiple height of them. Thus, it is not useful to conclude for the single step resistivity without the knowledge of the specific step distribution inside the measured quadratic area on the surface.

7.5. Probing the edge state by scanning tunneling potentiometry

A further powerful tool of a multi-tip STM is scanning tunneling potentiometry. With this method the current-induced local potential on the surface of a sample can be mapped and thus, based on the potential distribution the influence of small nano-scaled structures, e.g. as defects and step edges, on the lateral current transport can be revealed. In the following, scanning tunneling potentiometry is used to investigate the surface of the $\mathrm{Bi_{14}Rh_3I_9}$.

7.5.1. Measurement principle

The possibility to perform scanning tunneling potentiometry measurements with the multi-tip setup was implemented recently [120]. The acquisition of the potential signal is done in parallel to a standard STM scan. For each pixel of the scanned area the tip is first stabilized according to the constant-current mode. Then, the feedback is switched off and the applied tip bias voltage is swept in order to search for a vanishing tunneling current. At this point, where no tunneling current appears, the Fermi levels of tip and sample are aligned and the applied bias voltage is exactly equal to the local surface potential. Afterwards, the feedback is switched on again and the tip moves to the next pixel, where the complete procedure is repeated.

In principle, so far this can be done also with a single-tip STM. However, the great advantage of the multi-tip STM is that besides the scanning tip two further tips can be used to inject a lateral current across the scanned area. Usually, such a transport field is applied while performing scanning tunneling potentiometry, as the influence on the lateral transport wants to be studied. So, any local deviations of the potential from the overall slope of the transport field give insight into the perturbations of local structures onto the overall lateral current flow. However, also potentiometry without applying a transport field exists, as discussed later. With two STM tips the current can be applied in various directions and in direct vicinity to the scanned sample area. This would be not possible with fixed contacts on the sample, as needed for a single-tip STM. Additionally, the fourth tip of a multi-tip STM is very useful as reference by probing the sample potential stationary at a fixed position, in order to reveal any potential fluctuations caused by a variation of the injected current. Such potential fluctuations also affect the potential image and have to be subtracted from the measured signal.

7.5.2. Potentiometry at step edges

In order to probe the edge channels the scanning tunneling potentiometry measurements are performed at the step edges of the 2D TI layer on the $Bi_{14}Rh_3I_9$ surface. Fig. 7.13 shows

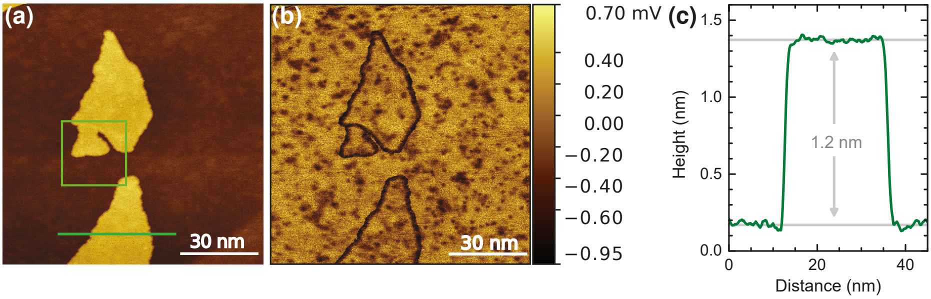

Figure 7.13.: Scanning potentiometry measurement of double-stepped islands on the $Bi_{14}Rh_3I_9$ surface. The topmost layer of the islands and the terrace is the 2D TI layer. (a) Topography image ($U = -100\,\mathrm{mV}$, $I = 240\,\mathrm{pA}$). The green square marks the section which is measured in Fig. 7.17. (b) Potential map of the same area as in (a). A transport current of $I_{\mathrm{transp}} \approx 600\,\mu\mathrm{A}$ is applied along the vertical direction (current direction pointing upwards) by two tips spaced by a distance of $7.5\,\mu\mathrm{m}$. (c) Height profile of the islands along the green line in (a).

the results of such a measurement for the topography [Fig. 7.13(a)] and the corresponding potential landscape [Fig. 7.13(b)]. The imaged area of the surface exhibits islands with an double step edge at the borderlines, i.e. a combined step of a spacer and a 2D TI layer, as it can be seen in the corresponding height profile shown in Fig. 7.13(c). The topmost layer on both the island and the surrounding terrace is the 2D TI layer. This cannot directly be deduced from the image in Fig. 7.13(b), but it is visible in Fig. 7.16(a) showing a larger overview of the same surface region (section of Fig. 7.13 is indicated by the green square), in which a single step of the spacer layer can be measured [Fig. 7.16(c)], so that the arrangement of the layers can be identified.

7.5.2.1. Transport field

For the potentiometry measurement, a transport field is applied along the vertical direction of the potential map shown in Fig. 7.13(b). A current of $I_{\mathrm{transp}} \approx 600\,\mu\mathrm{A}$ is injected by applying a voltage of $U_{\mathrm{transp}} = 250\,\mathrm{mV}$ with two tips spaced by a distance of $7.5\,\mu\mathrm{m}$, while the scanned area is approximately in the center between the two tips. During measurement the injected current is not perfectly constant, but varies slightly along the vertical (slow) scanning direction around its nominal value of $600\,\mu\mathrm{A}$ by approximately $\pm 20\,\mu\mathrm{A}$. This is visible in Fig. 7.14(a), which shows a record of the current through one of the injecting tips during the potentiometry scan. A reason for this current fluctuation is that the contacts between tip and sample are not perfectly stable, as the tip might drift either away from or towards the sample surface with time. In turn, this changes slightly the contact resistance at the injecting tips, and, as the applied transport voltage remains constant, also the injected current is changed. As the thermal drift of the tips is rather slow, the change in current occurs predominantly along the vertical scanning direction and not along a single line of the potentiometry scan. Nevertheless, even if the current fluctuation appears to be rather small, it has a serious impact on the measured potential landscape in the potentiometry scan. A time-dependent injection current leads to a change of the voltage drop across the sample with time. Additionally, a changed ratio between the voltage drop across the sample and the voltage drop at the injection points (contact resistance) causes a lateral shift of

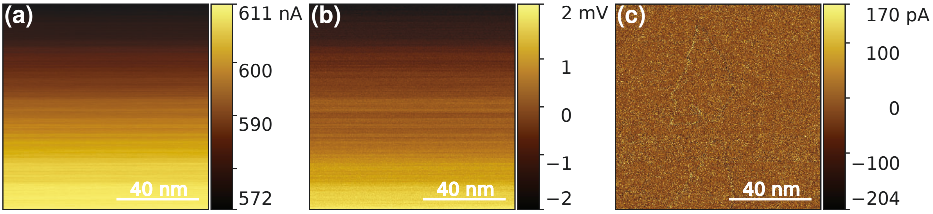

Figure 7.14.: Additional measurement signals for the potentiometry measurement shown in Fig. 7.13. (a) Injected current recorded during the potentiometry scan. (b) Reference potential recorded during the potentiometry scan. The potential is acquired with the fourth STM tip at a fixed position in hard contact with the surface. (c) Position-dependent tunneling current during the acquisition of the potentiometry signal.

the potential distribution inside the sample, i.e. the zero point shifts with time. Both effects are time-dependent, but in a potentiometry scan acquired at a fixed position on the sample, they appear to be position-dependent along the vertical direction and, as they cannot be distinguished from the real local potential fluctuations, they result in a (line by line) distortion of the measured potential landscape. For this reason, it is often useful to rotate the scanning direction by 90° with respect to the transport field, in order to decouple it from the potential fluctuations along the slow scanning direction. However, this was not done for the measurements presented in this section. In order to disentangle such undesired fluctuation effects reliably from the transport field, the usage of an additional reference is possible, which clearly identifies the time-dependent contributions. For this reason, the fourth STM tip is used as a stationary voltage probe at a fixed position in hard contact with the sample. Such a record of the stationary potential fluctuations for the potentiometry scan from Fig. 7.13(b) is shown in Fig. 7.14(b), which exhibits a rather large time-dependent[3] change in potential of approximately $4\,\mathrm{mV}$ along the vertical direction. This reference signal can then be subtracted from the measured potential, which in the present case has been already done for the potential map shown in Fig. 7.13(b). In Fig. 7.14(c), the tunneling current during potentiometry measurement is depicted. As expected, it does not show any significant structures and is almost always close to zero, which excludes any additional artefacts in Fig. 7.13(b) due to a non-vanishing tunneling current during potential acquisition.

As for the potentiometry the scanned area is located in the center in between the current injecting tips, and the distance towards the tips is rather large compared to the size of the scan, the current density can be assumed to be homogeneous in the measured area. So, in the potentiometry data in Fig. 7.13(b) this should result in a linear slope of the potential along the vertical direction. However, as the surface conductivity of the topmost 2D TI layer is extremely large, as discussed in the previous section 7.4, the potential drop at the surface on the length scale of the scanned area is so small that it is not visible in the potential map. This can be directly understood by looking at a calculation of the expected potential drop as function of the scan size, as it is plotted in Fig. 7.15. For the calculation, a four-point probe setup is used with a linear symmetric tip configuration, where the outer current injecting tips are spaced by $D = 7.5\,\mu\mathrm{m}$ and arranged symmetrically with respect to the inner voltage measuring tips, as shown in the inset in Fig. 7.15(a). Such a tip arrangement is equivalent to the potentiometry setup, if the scanned region is assumed to be positioned in between the two inner tips, i.e. the voltage measuring tips would be placed on the top and bottom scan line in the corresponding potentiometry image, respectively. So, in this case the spacing s between the inner two tips directly equals the edge length of the scanned area in the potentiometry setup. In the inset in Fig. 7.15(a), this scanned area, as it would be present for the corresponding potentiometry setup, is indicated by the yellow square between the inner tips. The calculated voltage drop at the surface is based on a two-layer model in analogy to Eq. (5.15) and incorporates the results of the previous four-point measurements for surface and bulk conductivity, as discussed in section 7.4. Moreover, a lateral current of $600\,\mu\mathrm{A}$ is assumed, as it was similarly applied for the potentiometry.

---

[3] Since the tip is fixed (not scanning), the apparent position-dependent image is only a record of the time-dependent signal at the tip position.

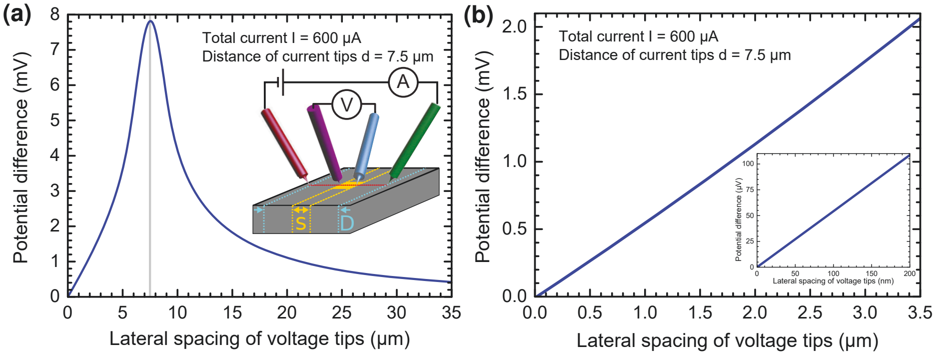

Figure 7.15.: Calculated voltage drop as function of the spacing s between the voltage measuring tips arranged in a linear symmetric tip configuration [shown in the inset of (a)]. The calculation is based on a two-layer model in analogy to Eq. (5.15) and on the conductivity parameters for the $Bi_{14}Rh_3I_9$ crystal ($\sigma_{2D} = (6.4 \pm 0.5) \times 10^{-2}\,\mathrm{S}/\square$ and $\sigma_{3D} = (9.2 \pm 0.8) \times 10^{3}\,\mathrm{S/m}$), as obtained in section 7.4. Furthermore, the parameters of the potentiometry measurement depicted in Fig. 7.13 are used, i.e. a transport current of $I_{\mathrm{transp}} \approx 600\,\mu\mathrm{A}$ and a spacing of the current injecting tips of $D = 7.5\,\mu\mathrm{m}$. In order to achieve a direct comparison with the potentiometry setup, the spacing s is assumed to be equal to the lateral scan size of a corresponding potentiometry measurement [corresponding scan area indicated as yellow square in the inset of (a)]. (a) Overview of the non-linear function for the potential drop, which exhibits a maximum at $s = D$ (gray line). (b) Magnification of the linear regime of the function for values of s, which are in the range of scan sizes used for potentiometry measurements. Inset: Further magnification to the nanometer regime.

In Fig. 7.15(a), an overview of the voltage drop as function of the spacing s between the inner tips, i.e. the vertical scan size, is plotted, which exhibits the expected non-linear dependency for the symmetric configuration. The maximum of the curve (vertical gray line) is at the value $s = D = 7.5\,\mu\mathrm{m}$, where the positions of the voltage measuring tips and current injecting tips coincide, i.e. both have the same spacing. Certainly, a comparison with a corresponding potentiometry setup is not very useful for this specific case, as such a tip arrangement is not realistic and the involved distances are way too large. However, the simulation can give some insight into the lateral distribution of the transport field used for the potentiometry, as at the position $s = D$ the value of the simulated curve in Fig. 7.15(a) directly corresponds to the voltage drop caused by the applied transport field between the current injecting tips. As the maximum of the simulated curve with $\sim 8\,\mathrm{mV}$ is much lower than the transport voltage of $\sim 250\,\mathrm{mV}$, the majority of the applied voltage drops directly at the contact resistances between the tips and the surface. In the present case, both contact resistances sum up to a value of $R_{\mathrm{contact}} \sim 242\,\mathrm{mV}/600\,\mu\mathrm{A} \sim 403\,\Omega$, while the resistance of the $Bi_{14}Rh_3I_9$ crystal itself is only $R \sim 8\,\mathrm{mV}/600\,\mu\mathrm{A} \sim 13\,\Omega$. This leads to a contribution of $\sim 97\,\%$ for the contact resistance with respect to the total resistance. It should be noted here that such a determination of the contact resistance is only possible, because the conductivity of the $Bi_{14}Rh_3I_9$ crystal is already known before due to a prior four-point measurement.

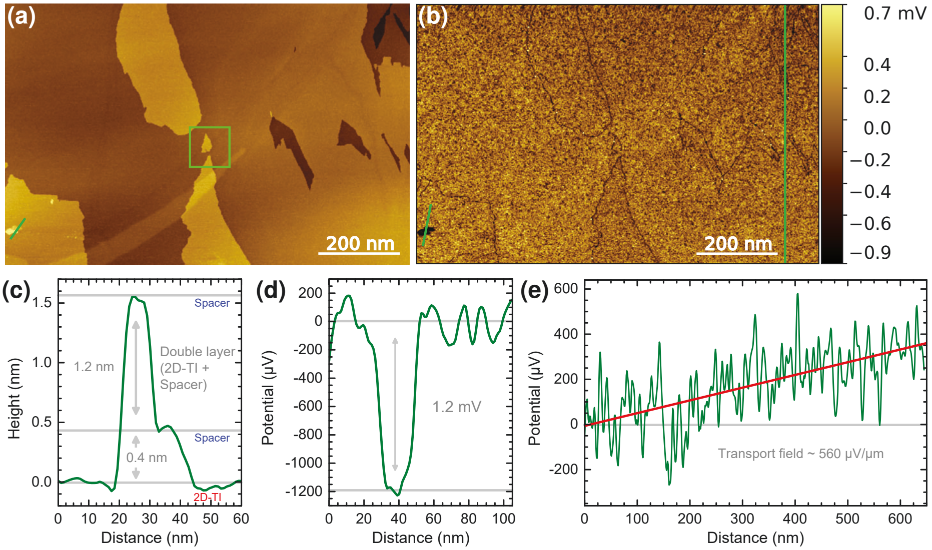

Figure 7.16.: Large-size potentiometry measurement of the same surface region as in Fig. 7.13 [position of the image in Fig. 7.13(a) is indicated by the green square in (a)]. (a) Topography image ($U = -150\,\mathrm{mV}$, $I = 240\,\mathrm{pA}$). (b) Potential map of the same area as in (a). A transport field is applied along the vertical direction (pointing upwards) with $I_{\mathrm{transp}} = 600\,\mu\mathrm{A}$ and a tip spacing of $7.5\,\mu\mathrm{m}$. (c) Height profile along the green line indicated in (a). From the profile a single spacer layer can be identified indicating that the sample area in Fig. 7.13 (green square) only exhibits the 2D TI layer as topmost layers. (d) Potential profile across the step edges between 2D TI layer and spacer layer [left green line in (b)]. (e) Potential profile along the vertical direction [right green line in (b)] indicating the overall voltage drop due to the transport field. From a linear fit (red line) a value of $560\,\mu\mathrm{V}/\mu\mathrm{m}$ can be extracted.

In order to focus more on the potential drop across a single potentiometry scan, Fig. 7.15(b) depicts a magnification of the linear regime appearing for smaller tip distances s, which are now on the length scale of the scanned regions for the potentiometry. In the inset of Fig. 7.15(b), a further magnification down to the nanoscale regime is shown, which is similar to the scan size used in Fig. 7.13(b). Here, it is visible that for a vertical scan size of $100\,\mathrm{nm}$, as it is the case in Fig. 7.13(b), only a potential drop of about $46\,\mu\mathrm{V}$ is expected. Such a small slope of $\sim 460\,\mu\mathrm{V}/\mu\mathrm{m}$ is not visible in the small-sized potential map in Fig. 7.13(b), as it is exceeded by the appearance of much stronger features at the step edges and on the terraces, which will be discussed in the following paragraph. Nevertheless, if the size of the potentiometry scan is increased, also a larger total voltage drop across the imaged area due to the transport field is expected, which then can be identified even against the background of larger local features. This is the case in Fig. 7.16, where such a large-area potentiometry measurement is shown, which corresponds to an overview scan of the same $Bi_{14}Rh_3I_9$ region as before with the section depicted in Fig. 7.13(a) located at the position of the green square in Fig. 7.16(a). For the potential map depicted in Fig. 7.16(b) a similar transport field is applied as before ($I_{\mathrm{transp}} = 600\,\mu\mathrm{A}$, tip spacing $7.5\,\mu\mathrm{m}$). In the potential map itself, no voltage drop from the transport field is clearly visible, but from the profile line along the vertical direction, as shown in Fig. 7.16(e), the potential slope can be unambiguously identified. From a linear fit to the profile line a value of $560\,\mu\mathrm{V}/\mu\mathrm{m}$ can be extracted, which is very close to the expected value discussed before. Indeed, the voltage drop of the transport field can now be identified, but apart from that the large-size potential map in Fig. 7.16(b) is not very useful, as at the same time any local potential structures cannot be resolved precisely. However, especially such local changes induced by the transport field, e.g. along the edge channels, are of special interest. This local potential structure can only be resolved in smaller-sized measurements, as in Fig. 7.13, but since here not even the overall transport field is visible, it is impossible to measure any local changes caused by the transport current. So it can be concluded that any influence of a transport field on the local potential at the edge channels of the $\mathrm{Bi}_{14}\mathrm{Rh}_3\mathrm{I}_9$ crystal cannot be revealed, as the surface conductivity of the present crystals is simply too large. (It should be noted that even if the detection would be possible, no potential changes are expected for the present crystals, as here the edge channels are not located at E_F and so do not participate in current transport, as already discussed before).

7.5.2.2. Thermovoltage

In fact, it turned out that the transport field seems to have no significant influence on the potential landscape of the $\mathrm{Bi}_{14}\mathrm{Rh}_3\mathrm{I}_9$ surface. When the potentiometry is performed without any transport field, the potential map shows exactly the same structure as before with a transport field. For example, this is visible in Fig. 7.17, where an enlarged section of the surface region shown before in Fig. 7.13 [indicated by the green square in Fig. 7.13(a)] is measured. If the potential map in Fig. 7.17(b) is compared to the one in Fig. 7.13(b), apart from the enlargement nearly no difference can be identified. In both images a strong contrast in the potential signal appears exactly at the position of the step edges of the 2D TI

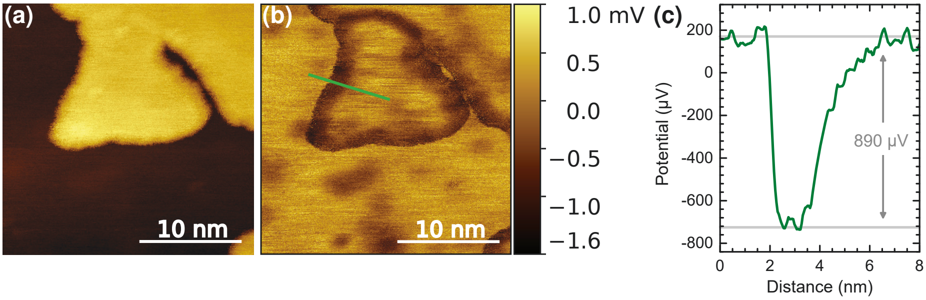

Figure 7.17.: Enlarged potentiometry scan of a section of the region depicted in Fig. 7.13 [marked with a green square in Fig. 7.13(a)]. (a) Topography image ($U = -100\,\mathrm{mV}$, $I = 240\,\mathrm{pA}$). (b) Potential map of the same area as in (a). No transport field is applied. (c) Potential profile across the step edge [along the green line in (b)].

layer islands, where the edge channel is supposed to be located. However, it can be clearly excluded that this contrast is caused by real current transport inside the sample due to the missing transport field in Fig. 7.17(b). In the vicinity of the step edge, there is a confined drop of the local potential, while the potential on both the 2D TI island and the surrounding 2D TI terrace is equal. A profile line across the step, as shown in Fig. 7.17(c), reveals that the strength of the potential drop is about $900\,\mu\mathrm{V}$ and the spatial extent is $\sim 1\,\mathrm{nm}$ to $2\,\mathrm{nm}$, which equals nearly exactly the expected width of the edge channel. Furthermore, from the profile in Fig. 7.17(c) and the map in Fig. 7.17(b) it is visible that the potential drop at the step edges is not symmetric. It appears that there is always a sharp potential drop on the outer surroundings of the islands, while on the inner side of the edge channel, i.e. the side pointing towards the center of the islands, the potential rather slowly increases again up to the same value as on the surrounding terrace. In addition to the sharp potential drop at the step edges, there are further patches on both the terrace and the islands, which exhibit a more blurry and apparent arbitrary variation or the surface potential. However, the strength of these variations is on the same scale as for the step edges.

The measured local potential structure seems to be a static feature of the $\mathrm{Bi_{14}Rh_3I_9}$ surface, as it is identically present for both with and without a transport field. A reason for such a feature is the appearance of thermovoltage, which arises due to a slight temperature difference between tip and sample. Such a temperature mismatch can occur easily during STM measurement, as, e.g. already some incident light is sufficient to heat either tip or sample, and the thermal coupling in the vacuum across the tunneling barrier is only very weak. Different temperatures lead to different Fermi distributions in tip and sample, and, as a result, a thermocurrent arises without any applied bias voltage. In order to compensate this thermocurrent a specific voltage V_{th} has to be applied at the tunneling contact. During a potentiometry measurement without an applied transport field, it is exactly this thermovoltage V_{th}, which is measured by the condition of a vanishing tunneling current. By using the Tersoff-Hamann approach for the tunneling current, the first (leading) term of the thermovoltage V_{th} can be expressed as [120, 184, 185]

$$V_{\mathrm{th}}(x,y) = \frac{\pi^2 k_B^2}{6e}\left(T_{\mathrm{t}}^2 - T_{\mathrm{s}}^2\right)\left(\frac{1}{\rho_{\mathrm{s}}(x,y,E)} \cdot \frac{\partial \rho_{\mathrm{s}}(x,y,E)}{\partial E}\right)\Bigg|_{E=E_F}, \tag{7.2}$$

where T_t and T_s are the temperatures of the tip and sample, respectively, and $\rho_s(x,y,E)$ is the (position-dependent) local density of states (LDOS) of the sample. The temperatures are rather fixed parameters for a specific potentiometry measurement, but due to the spatial dependence of the LDOS also a lateral variation of the thermovoltage V_{th} can be obtained. The LDOS term within the parentheses in Eq. (7.2) can be rewritten in a shorter way resulting in

$$V_{\mathrm{th}}(x,y) \propto \left(T_{\mathrm{t}}^2 - T_{\mathrm{s}}^2\right) \frac{\mathrm{d}\ln\left[\rho_{\mathrm{s}}(x,y,E)\right]}{\mathrm{d}E}\Bigg|_{E=E_F}. \tag{7.3}$$

From Eq. (7.3), it is directly visible that not the absolute value of the LDOS is crucial for the thermovoltage, but only the derivative of the logarithmic value, i.e. the local slope of the LDOS. So, it can be concluded that with a measurement of the thermovoltage V_{th} the

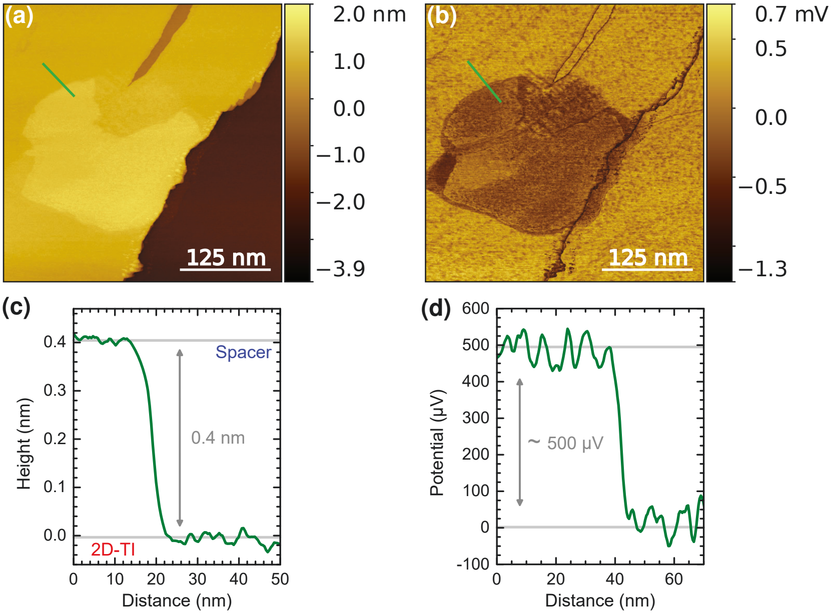

Figure 7.18.: Potentiometry measurement at a step edge of a spacer layer on top of a 2D TI layer. (a) Topography image ($U = -500\,\mathrm{mV}$, $I = 210\,\mathrm{pA}$) (b) Potential map of the same area as in (a). No transport field is applied. A contrast between the regions of the 2D TI layer and the spacer layer is visible. (c) Height profile across the step edge of the spacer layer [along the green line indicated in (a)]. (d) Potential profile across the step edge of the spacer layer [along the green line line indicated in (b)].

spatial variations of the slope of the LDOS at the Fermi energy E_F can be mapped on the sample surface.

From the potential maps in Figs. 7.13(b) and 7.17(b) it therefore results that at the position of the step edges around the 2D TI islands a significant change of the LDOS occurs. Exactly such a behavior would be expected for an edge state, but, however, it does not prove any topological properties, as in principle such a voltage drop can also be caused by trivial states being present only at the step edges. Moreover, also across the terraces a certain variation of the LDOS is present without a correlation to any topographic feature.

In both measurements (cf. Figs. 7.13 and 7.17) the 2D TI layer is the topmost layer everywhere in the depicted sample area, so that no potential difference between islands and surrounding terraces is visible, as the LDOS is equal for both. However, this can be different, if not only double-layer steps are present, but also single-layer steps between 2D TI and spacer layer, as it is the case in the measurement in Fig. 7.18. Here, a certain area of the sample is covered by the spacer as topmost layer, as it is visible from the STM image in Fig. 7.18(a) and the height profile in Fig. 7.18(c). In the corresponding potential map in Fig. 7.18(b) a strong contrast appears between the spacer and the surrounding 2D TI layer. The potential drop occurs now on the complete spacer island, and has a strength of $\sim 500\,\mu\mathrm{V}$, as it can be deduced from the profile line in Fig. 7.18(d). Thus, in the present case the position of the spacer layer can be identified also from the potential map.

This potentiometry-based approach in order to distinguish between spacer and 2D TI as topmost layer can even be applied, if no single-layer step edge appears in the mapped sample area, i.e. the surface is completely covered by either the spacer or the 2D TI layer. Thus, for this purpose potentiometry is more advantageous compared to measuring the step heights directly, since the latter requires at least one single step edge of the spacer, while the contrast in thermovoltage is an inherent feature of the spacer surface itself. However, since potentiometry only allows to determine potential differences, but not absolute values, another reference is necessary in this case. Such a reference can be obtained by using the potential variation caused by the edge state of a 2D TI layer, as measured before. In Fig. 7.18(b) the voltage drop occurring at the position of an edge state with respect to the 2D TI surface [measured for the double step at the top of Fig. 7.18(b)] is with $\sim 900\,\mu\mathrm{V}$ in accordance to the prior results from Fig. 7.17(b). Thus, it immediately follows that the difference in potential between spacer surface and edge states of the 2D TI layer at a double step edge would be only $\sim 400\,\mu\mathrm{V}$, if the spacer forms the topmost layer. With this information it is possible to unambiguously distinguish both types of layers from a potentiometry measurement, thus allowing to identify the regions of the $\mathrm{Bi}_{14}\mathrm{Rh}_3\mathrm{I}_9$ covered by a spacer or a 2D TI as topmost layer, e.g. in Fig. 7.13. As already discussed before, from multiple large-size scans it turns out that the majority of the surface is covered by the 2D TI layer, while the spacer layer appears only in very few regions.

It should be explicitly noted here that in Figs. 7.18(b) and 7.18(d) no additional voltage drop exactly at the edge of the spacer layer island occurs. So, it can be excluded that the edge state causing the voltage drop of $\sim 900\,\mu\mathrm{V}$, as visible in Figs. 7.13(b) and 7.17(b), is present around the spacer islands. This gives a further prove that the edge state observed before appears only at the step edges of the 2D TI layer and not at the one of the spacer layer, which is in accordance with the topological edge state.

In Fig. 7.16(b), also a potential drop at a spacer layer is visible (lower left edge of the image), but from the profile line in Fig. 7.16(d) it seems to have a larger value above $1\,\mathrm{mV}$. A reason is that in this case not only a single spacer layer is present, but in close vicinity to it also a double-layer step (2D TI and spacer layer) exists. However, at the edge of a 2D TI layer a much larger voltage drop appears. Due to the limited spatial resolution of the large-size scan in Fig. 7.16(b) it is assumable that both contributions cannot be separated, and therefore the visible potential drop mainly originates from the step edge and not from the spacer. Further on, its strength is basically in accordance to the value of $\sim 900\,\mu\mathrm{V}$ resulting from the edge state, when the enhanced uncertainty is considered ($\pm 200\,\mu\mathrm{V}$), as visible on the terraces in Fig. 7.16(d). Thus, the measurement in Fig. 7.18 should be more precise.

From the strength of the potential drops obtained before, two estimates are possible: (a) the temperature difference between tip and sample can be calculated, and (b) the ratio between the LDOS slope of the edge channel and the plain 2D TI layers at the Fermi energy can be approximated.

First, the temperature difference between tip and sample during measurement should be estimated. In order to do this, the measured potential drop between spacer and 2D TI layer, i.e. $\Delta V^{\mathrm{th}}_{\mathrm{2DTI}\leftrightarrow\mathrm{spacer}}$, obtained in Fig. 7.18(b) is used. By taking into account Eqs. (7.2) and (7.3), it follows that

$$\begin{aligned}\Delta V^{\mathrm{th}}_{\mathrm{2DTI}\leftrightarrow\mathrm{spacer}} &= V^{\mathrm{th}}_{\mathrm{2DTI}} - V^{\mathrm{th}}_{\mathrm{spacer}} &(7.4)\\ &= \frac{\pi^2 k_B^2}{6e}\left(T_{\mathrm{t}}^2 - T_{\mathrm{s}}^2\right)\left[\underbrace{\left.\frac{\mathrm{d}\ln\left[\rho_{\mathrm{2DTI}}(E)\right]}{\mathrm{d}E}\right|_{E_F}}_{\sim 30\,\mathrm{eV}^{-1}} - \underbrace{\left.\frac{\mathrm{d}\ln\left[\rho_{\mathrm{spacer}}(E)\right]}{\mathrm{d}E}\right|_{E_F}}_{\sim 0}\right]. &(7.5)\end{aligned}$$

In Eq. (7.5), the slope of the logarithmic LDOS at E_F for the 2DTI layer is approximated by a value obtained from a DFT calculation [183], while the corresponding value for the spacer layer is taken from a dI/dV-measurement [174], as shown before in Fig. 7.5, and additionally verified by the calculation in Ref. [183]. By inserting the measured value of $\Delta V^{\mathrm{th}}_{\mathrm{2DTI}\leftrightarrow\mathrm{spacer}} \sim 500\,\mu\mathrm{V}$ into Eq. (7.5), a temperature difference between tip and sample of $\Delta T \sim 2\,\mathrm{K}$ can be obtained ($T_t = 300\,\mathrm{K}$ is assumed). A possible explanation for such a relative large temperature mismatch might be that prior to any four-tip STM measurements always a source of light is needed, which illuminates the sample in order to see the actual positions of the tips in the optical microscope. Even if the measurement itself is done without any light, a possibly enhanced temperature of the sample caused by the illumination before can persist also during potentiometry measurement, and would lead to the observed thermovoltage.

In a second step, an estimation of the ratio between the LDOS slope of the edge channels and the 2D TI layer is given by using the potential drop measured at the step edges in Fig. 7.17(b), i.e. $\Delta V^{\mathrm{th}}_{\mathrm{edge}\leftrightarrow\mathrm{2DTI}}$. It follows that

$$\begin{aligned}&\Delta V^{\mathrm{th}}_{\mathrm{edge}\leftrightarrow\mathrm{2DTI}} = V^{\mathrm{th}}_{\mathrm{edge}} - V^{\mathrm{th}}_{\mathrm{2DTI}} &(7.6)\\ \Leftrightarrow\quad &V^{\mathrm{th}}_{\mathrm{edge}} = \underbrace{\Delta V^{\mathrm{th}}_{\mathrm{edge}\leftrightarrow\mathrm{2DTI}}}_{\sim 900\,\mu\mathrm{V}} + \underbrace{V^{\mathrm{th}}_{\mathrm{2DTI}}}_{\overset{(7.5)}{=}\Delta V^{\mathrm{th}}_{\mathrm{2DTI}\leftrightarrow\mathrm{spacer}} \sim 500\,\mu\mathrm{V}} &(7.7)\\ \Leftrightarrow\quad &V^{\mathrm{th}}_{\mathrm{edge}} \sim 1400\,\mu\mathrm{V}. &(7.8)\end{aligned}$$

For the ratio then results

$$\frac{\left.\frac{\mathrm{d}\ln[\rho_{\mathrm{edge}}(E)]}{\mathrm{d}E}\right|_{E_F}}{\left.\frac{\mathrm{d}\ln[\rho_{\mathrm{2DTI}}(E)]}{\mathrm{d}E}\right|_{E_F}} \overset{(7.3)}{\sim} \frac{V^{\mathrm{th}}_{\mathrm{edge}}}{V^{\mathrm{th}}_{\mathrm{2DTI}}} \sim \frac{1400\,\mu\mathrm{V}}{500\,\mu\mathrm{V}} \sim 2.8 \tag{7.9}$$

and for the slope of the logarithmic LDOS of the edge channel an approximation of $\left.\frac{\mathrm{d}\ln[\rho_{\mathrm{edge}}(E)]}{\mathrm{d}E}\right|_{E_F} \sim 84\,\mathrm{eV}^{-1}$ can be obtained. So, the LDOS slope of the edge state is approximately by a factor 3 larger than the one of the 2D TI layer, which indicates a stronger increase (or decrease) of the LDOS near the Fermi edge, as it is expected for the topological edge state. As the measured thermovoltage only depends on the derivative of the

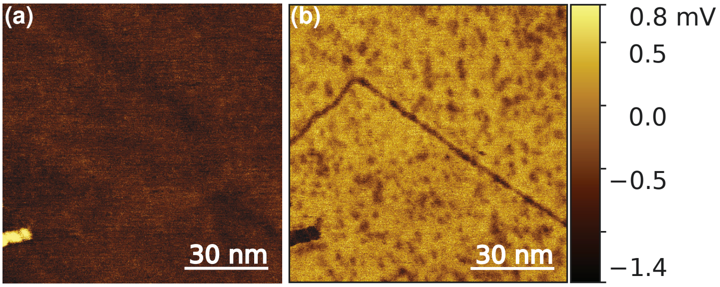

Figure 7.19.: Potentiometry measurement on the 2D TI layer of the $\mathrm{Bi}_{14}\mathrm{Rh}_3\mathrm{I}_9$ surface without any significant step edges. (a) Topography image ($U = -110\,\mathrm{mV}$, $I = 240\,\mathrm{pA}$). (b) Potential map of the same area as in (a). No transport field is applied. A strong contrast along a line across the image is visible, which does not correspond to any topographic structure in (a).

(logarithmic) LDOS, no further information about the exact value of the LDOS of the edge channel is possible. Moreover, since the edge channel is not located immediately at the Fermi energy, all of the previous findings can describe at most only the tail of the edge state extended towards the Fermi edge (cf. Figs. 7.6 and 7.7).

However, some conclusion can be drawn from the thermovoltage measurements shown before. It is visible that the LDOS exactly at the 2D TI step edges differs from the one of the plain 2D TI layers. This proves the existence of an edge state on the $\mathrm{Bi}_{14}\mathrm{Rh}_3\mathrm{I}_9$ surface, which appears exactly at the steps of the 2D TI layer, exhibits a spatial width of $\sim 2\,\mathrm{nm}$ and is not present at the steps of the spacer layer. This result confirms the previous results from the spectroscopic measurements in section 7.3 and indicate that the topological edge state has been measured.

At the end of this section, it should be noted that an edge state has not necessarily to appear only on the surface, but it can also be present inside a subsurface layer of the $\mathrm{Bi}_{14}\mathrm{Rh}_3\mathrm{I}_9$ crystal. For example, this is visible in the thermovoltage measurement depicted in Fig. 7.19. In Fig. 7.19(a) the topography of a plain 2D TI layer is shown, while the corresponding potential map is presented in Fig. 7.19(b). It is visible that in Fig. 7.19(b) a narrow potential drop occurs along a straight line across the surface region, as it was similarly observed before for the edge state at the 2D TI layer step edges [Fig. 7.13(b)]. However, when compared to Fig. 7.19(a), no topographic feature can be identified, which correlates to the measured potential structure. So, it can be concluded that there is obviously no step edge on the surface and that the observed change in the LDOS along the line has to be caused by a structural feature being present below the topmost 2D TI layer, which is not observable in the topographic image. An explanation would be that there is a line defect in the second (or lower) 2D TI layer below the surface, e.g. a dislocation line, which does not cause a change in the topographic height, but exhibits an edge state along the defect line. This locally changed LDOS in the subsurface layer then also contributes to the tunneling process and, therefore, causes a shift of the thermovoltage also on the surface, which can be measured by potentiometry. This proves the thermovoltage measurement to be a versatile tool for detecting changes of the LDOS not only exactly on the sample surface, but also in subsurface layers, similarly as it can be also achieved with spectroscopic dI/dV measurements.

7.6. Summary

Within this chapter the weak topological insulator $\mathrm{Bi_{14}Rh_3I_9}$ has been investigated in order to reveal the one-dimensional topological edge state, which is expected to be present at every step edge on the dark surface of the 2D TI layers inside the stacked material. In spectroscopic dI/dV measurements this edge state can be observed exactly at the step edges of the 2D TI layers, exhibiting a spatial extent of $\sim 2\,\mathrm{nm}$ around the step edge and an energetic maximum of the LDOS located around $\sim -150\,\mathrm{meV}$. This indicates that for the present crystals the edge state is not located exactly at the Fermi energy. Furthermore, the edge state is similarly also present at trenches, which can be artificially scratched into the surface. From distance-dependent four-point measurements in combination with a two-layer model the conductivities of the surface and the subsurface (bulk) channel can be deduced as $\sigma_{\mathrm{2D}} = (6.4 \pm 0.5) \times 10^{-2}\,\mathrm{S}/\square$ and $\sigma_{\mathrm{3D}} = (9.2 \pm 0.8) \times 10^{3}\,\mathrm{S/m}$. It turns out that the surface conductivity of the present crystals is quite large due to surface doping. Scanning potentiometry measurements are performed with and without a transport field. Due to the facts that the edge state cannot contribute to current transport, as not located at E_F, and that the overall surface conductivity is very large, it is not possible to reveal the topological nature of the edge state from the potential distribution during real current transport. However, measuring only the thermovoltage without lateral current transport turns out to be sufficient in order to find spatial variations of the LDOS at the position of step edges. Here, a local potential drop of $\sim 900\,\mu\mathrm{V}$ can be observed exactly at the step edges of the 2D TI layers, while it is not present at the steps of the spacer layer. Thus, it is possible to reveal substantial LDOS changes present only at the edges of the 2D TI layer, as it is expected for the topological edge state and in accordance with the previous spectroscopic measurements.

The main problems in measuring any transport-related properties of the edge channel directly are that the edge state is not located at E_F at that the surrounding dark surface is not insulating, but exhibits an extensive conductivity due to undesired doping. So, for future measurements this two issues have to be resolved by fabricating appropriate $\mathrm{Bi_{14}Rh_3I_9}$ crystals. Then, it would be possible to reveal the topological properties from the potential distribution on the surface during current transport. Exactly along the edge channel a constant potential would be expected with a potential drop only at the beginning and at the end of the one-dimensional channel, as it applies for an ballistic channel, while the surrounding (dark) surface still exhibits the normal diffusive transport, i.e. it shows a potential slope due to the transport field.

Some excerpts of the data presented in sections 7.4.1 and 7.5.2.1 are included in the publication in Ref. [186].

8. Conclusion

Within the framework of this thesis, the relevant issue of disentangling parallel conduction channels inside conductive materials, based on information from electrical transport measurements on the surface, has been researched. In general, such parallel channels can be present, when the conductivity of the material is not completely homogeneous, i.e. when continuous regions in parallel along the current path exist which exhibit an increased or reduced conductivity compared to each other. Specifically, when current transport in lateral direction is considered, as it results from an injection solely at the surface, such regions are mainly formed either by layers in parallel to the surface, ranging from rather thick segments down to single atomic layers, or by spatially-limited paths on the surface itself. As it has been shown throughout this thesis, such specific properties apply to a wide range of various material systems. Besides straightforwardly to handle single 2D or 3D conducting channels, highly conductive two-dimensional surface states on top of bulk semiconductors with a band-bending-induced space charge region in between have been investigated, as well as quasi-2D epitaxially grown thin films of topological insulators with multiple 2D conducting channels inside caused by the interior of the film, the topological surface states on top and bottom side and the interface to the bulk substrate. Furthermore, also one-dimensional edge states appearing on surfaces of weak topological insulators, surrounded by both a conductive surface layer and an underlying bulk crystal, have been covered. All of these systems exhibit both different compositions and very different properties of the parallel channels, e.g. as dimensionality and length-scale. If the properties of one of these conducting channels are of interest, e.g. the conductivity, the difficult task arises, how to disentangle this specific channel from all the other channels in parallel. Such a question is particularly of high importance for the development of future electronic devices, as only the knowledge about the strength of conduction channels allows for improvements in order to keep undesired effects due to parasitic channels, e.g. as high current consumption, as less as possible, or even enables new developments by taking advantage of specific channels, e.g, based on topological states.

Here, in order to approach this problem, the primarily used experimental tool has been a multi-tip STM which allows to perform position-dependent electrical four-probe resistance measurements on surfaces with tip spacings within the micro- or even nanoscale. The fundamentals of such an instrument operating at room temperature and under ultra-high-vacuum conditions have been presented in chapter 2. However, for the majority of cases, not only experimental measurements are sufficient, but also supporting theoretical models are necessary, in order to describe the measured data properly and to extract the relevant information about the materials under study, e.g. as the conductivity of the surface states. For this reason, within this thesis two different types of multi-layer models have been developed and the application of a further calculation-based method using input from surface-sensitive experiments has been shown up.

In order to determine the conductivity of materials exhibiting either a pure 2D or 3D channel, it is sufficient to perform distance-dependent four-probe measurements with a linear tip configuration, as the specific distance-dependency of the four-point resistance is characteristic for the dimensionality of the sample. Moreover, simple analytic expressions exist in order to obtain the conductivity from such measurements, as shown in chapter 3. In a similar manner, by performing angle-dependent measurements, the anisotropy on the surface, e.g. as caused by atomic steps, can be studied. However, if both conduction channels are combined, i.e. as it is the case for surface states present on top of a semiconducting bulk, it starts to get complicated. Here, the expressions for pure 2D and 3D channels cannot be applied any longer, thus, a new model is needed relating the measured resistance data to the properties of the conducting channels. Moreover, it has turned out that a 2-layer model is not sufficient in general, as especially in semiconductors the near-surface space charge region has a significant influence on both the current injection and the lateral transport, and, therefore, has to be taken into account. Thus, first a 3-layer model has been introduced in chapter 4 which is based on basic analytical expressions. This model offers a description of the sample by a surface channel, a channel through the space charge region and a bulk channel, all of them with individual conductivities and thicknesses. Distance-dependent four-probe resistance measurements in combination with such a 3-layer model have successfully allowed to reliably reveal the long-sought conductivity of the Si(111)-(7×7) surface states. Moreover, in order to further disentangle the surface channel into the contributions of step-free terrace and the atomic steps, the rotational square method has been applied. Thus, a combination of both, i.e. distance-dependent measurements supported by a 3-layer model and the angle-dependent setup, has unambiguously allowed to separate the influences of defect density in the surface reconstruction and step density of the Si(111) on the overall conductivity of the surface layer.

In order to refine the quite rough approximation of the space charge region within the 3-layer model by only a single layer of fixed conductivity, in chapter 5 an extended model with N layers has been presented. Such a model allows for a more precise description of the strongly z-dependent conductivity inside the space charge zone, which especially applies when an inversion layer is present. However, due to the very large number of parameters, the N-layer model cannot be only fitted to resistance measurement data, but needs additional information from band bending calculations as input. These calculations are based on basic material parameters which are known for semiconductors, but not necessarily for other materials under study. Thus, the N-layer model can indeed be more precise, but on the other hand the 3-layer model is more flexible in application, as the only prerequisite is a set of distance-dependent four-point resistance data and all relevant information can be obtained from a fit to the data. It has been demonstrated that with an N-layer model it is possible to precisely extract the surface conductivities for Ge(100)-(2×1) and Si(100)-(2×1). Nevertheless, for the case of Si(111)-(7×7), it has turned out that the obtained value for the conductivity of the surface states is basically the same as the one resulting from the 3-layer model before, thus, implying that in this case already a 3-layer model is sufficient.

However, obviously this depends in general on the specific properties of the space charge region.

For epitaxially grown thin films, multiple two-dimensional conducting channels in parallel can exist, as it has been discussed specifically for the case of topological insulator materials in chapter 6. Here, besides the ordinary bulk substrate, the interface layer, the quasi-2D interior of the film and the surface states can participate in current transport. Particularly, for TI materials the surface states split into two parts, i.e. the topological states on top and bottom side of the film. In order to determine the conductivity of the interface channel, it can be investigated prior to film growth by means of distance-dependent four-probe measurements on a corresponding substrate exhibiting the same surface reconstruction as present later on underneath the thin TI film. Due to the weak coupling between TI film and substrate, the properties of the interface layer can be expected to be the same without the film on top. The film itself is more difficult to handle, since due to its quasi-2D nature any distance-dependent measurements cannot help to disentangle the interior of the film from the TSS channels. For this purpose, the film conductivity has been deduced from the mobile charge carrier concentration inside which can be obtained by a calculation of the near-surface band bending with additional information from surface-sensitive measurements, i.e. angle-resolved photoemission spectroscopy and gate-dependent four-point measurements. Specifically, for the thin-film limit, it has turned out that the amount of charge carriers inside the film is nearly independent from the usually unknown dopant concentration and only governed by more easily accessible surface properties. So, this method allows for a reliable estimation of the film conductivity, and thus, by revealing the contribution of the film interior to current transport, helps to determine the TSS conductivity from measurements.

Another type of conducting channels are one-dimensional channels arising from edge states on surfaces, e.g. present on weak topological insulators, as it has been treated in chapter 7 specifically for the material $Bi_{14}Rh_3I_9$. In contrast to all of the conduction channels discussed before, such edge states are localized on the accessible surface, and thus their presence can be easily verified by means of scanning tunneling spectroscopy which has revealed an enhanced density of states in the vicinity of step edges compared to the surroundings. Moreover, these edge states also evolve at artificial scratches which in principle allows to create an arbitrary pattern of ballistically conducting channels on the surface. However, as it holds for all conduction channels, in order to actually contribute to current transport the involved electronic states have to be located at the Fermi edge, but for the case of $Bi_{14}Rh_3I_9$ it has turned out that the edge states are only close to the Fermi energy. Furthermore, due to unintentional surface doping the surrounding dark surface exhibits a extremely large conductivity, as deduced from distance-dependent four-point measurements. Both facts make it very difficult to disentangle the 1D channels from transport measurements, but nevertheless an attempt has been started. Since due to the small lateral extent of the edge channels a contacting by four tips is very difficult, scanning tunneling potentiometry is the method of choice. However, as expected, here no transport-related contrast is visible and the same structure appears in subsequent thermovoltage measurements without a transport field, thus only proving the existence of the edge states but not showing their transport properties. Nevertheless, for a more sophisticated sample, in principle it would be possible to disentangle the edge channels by using the presented methods.

A further project which has been started, concerns a method to reveal spin-polarized transport in topological insulators. Due to the spin-momentum locking in the topological states, a spin-polarized current can be generated simply by inducing a lateral current flow in the TSS channel. By means of a four-point measurement with one spin-polarized tip involved, an additional contribution from a spin-voltage can be measured besides the ohmic part, which allows for conclusions about the spin-polarization of the current in the TSS, as it has been already reported, but only for the case of lithographically-fabricated contacts [187–190]. In order to prepare for such spin-polarized four-point measurements, a setup for an electromagnetic coil has been developed which allows for an *in situ* switching of the spin-polarization of a ferromagnetic STM tip. More details about this coil can be found in the appendix C.3. However, due to limited time, such measurements have not been performed within this thesis, but the project has been continued successfully by *Arthur Leis* [38].

Finally, it should be stressed that all methods and theoretical models presented within this thesis are universally applicable, and thus can be applied basically to many other systems than covered here, in order to extract relevant information about their properties from surface-sensitive measurements. Particularly, the 3- and N-layer models might provide a substantial improvement in understanding and interpreting distance-dependent measurements on surfaces in order to disentangle multiple conduction channels, and thus can lead to a considerable progress in the field of transport measurements based on multi-tip STMs. Also, the demonstrated method for obtaining the conductivity of thin TI films can be very advantageous in general, as it provides information about a region which is non-accessible by direct measurements and thus helps to characterize the TSS channel in order to allow for a fabrication of tailored TI films based on the obtained information.

In total, the presented methods can support the applicability of the multi-tip STM technique, and thus can help that it evolves to an even more powerful tool in the future. Indeed, many further fields of applications are conceivable for this universal technique, e.g. the investigation of magneto-transport down to the nanoscale at low temperatures or the study of time-dependent transport phenomena by developing a multi-tip instrument in analogy to a time-resolved single-tip STM [191]. Particularly for this two cases, some work for the implementation has already been done up to now. Thus, multi-tip STM proves to be an interesting technique with high potential for future research.

Bibliography

[1] Herbert Kroemer, *Nobel lecture: Quasielectric fields and band offsets: teaching electrons new tricks*. Reviews of Modern Physics **73**, 783 (2001). DOI:10.1103/revmodphys.73.783

[2] Herbert Kroemer, *Heterostructure devices: A device physicist looks at interfaces*. Surface Science **132**, 543 (1983). DOI:10.1016/0039-6028(83)90561-7

[3] B. Jayant Baliga, *Fundamentals of Power Semiconductor Devices* (Springer US, 2008). DOI:10.1007/978-0-387-47314-7

[4] Junji Kotani, Masafumi Tajima, Seiya Kasai, and Tamotsu Hashizume, *Mechanism of surface conduction in the vicinity of schottky gates on AlGaN/GaN heterostructures*. Applied Physics Letters **91**, 093501 (2007). DOI:10.1063/1.2775834

[5] Z. H. Liu, G. I. Ng, H. Zhou, S. Arulkumaran, and Y. K. T. Maung, *Reduced surface leakage current and trapping effects in AlGaN/GaN high electron mobility transistors on silicon with SiN/Al_2O_3 passivation*. Applied Physics Letters **98**, 113506 (2011). DOI:10.1063/1.3567927

[6] Brianna S. Eller, Jialing Yang, and Robert J. Nemanich, *Electronic surface and dielectric interface states on GaN and AlGaN*. Journal of Vacuum Science & Technology A: Vacuum, Surfaces, and Films **31**, 050807 (2013). DOI:10.1116/1.4807904

[7] Yury Turkulets and Ilan Shalish, *Surface states in AlGaN/GaN high electron mobility transistors: Quantitative energetic profiles and dynamics of the surface fermi level*. Applied Physics Letters **115**, 023502 (2019). DOI:10.1063/1.5100572

[8] A. Cho, *Trio wins Nobel for effects of topology on exotic matter*. Science **354**, 21 (2016). DOI:10.1126/science.354.6308.21

[9] M. Konig, S. Wiedmann, C. Brune, A. Roth, H. Buhmann, L. W. Molenkamp, X.-L. Qi, and S.-C. Zhang, *Quantum spin hall insulator state in HgTe quantum wells*. Science **318**, 766 (2007). DOI:10.1126/science.1148047

[10] G. Binnig, H. Rohrer, Ch. Gerber, and E. Weibel, *Tunneling through a controllable vacuum gap*. Applied Physics Letters **40**, 178 (1982). DOI:10.1063/1.92999

[11] G. Binnig and H. Rohrer, *Scanning tunneling microscopy*. Surface Science **126**, 236 (1983). DOI:10.1016/0039-6028(83)90716-1

[12] G. Binnig, H. Rohrer, Ch. Gerber, and E. Weibel, *Surface studies by scanning tunneling microscopy*. Physical Review Letters **49**, 57 (1982). DOI:10.1103/physrevlett.49.57

[13] Ichiro Shiraki, Fuhito Tanabe, Rei Hobara, Tadaaki Nagao, and Shuji Hasegawa, *Independently driven four-tip probes for conductivity measurements in ultrahigh vacuum*. Surface Science **493**, 633 (2001). DOI:10.1016/s0039-6028(01)01276-6

[14] Olivier Guise, Hubertus Marbach, John T. Yates, Moon-Chul Jung, Jeremy Levy, and Joachim Ahner, *Development and performance of the nanoworkbench: A four tip STM for conductivity measurements down to submicrometer scales*. Review of Scientific Instruments **76**, 045107 (2005). DOI:10.1063/1.1878213

[15] Rei Hobara, Naoka Nagamura, Shuji Hasegawa, Iwao Matsuda, Yuko Yamamoto, Yutaka Miyatake, and Toshihiko Nagamura, *Variable-temperature independently driven four-tip scanning tunneling microscope*. Review of Scientific Instruments **78**, 053705 (2007). DOI:10.1063/1.2735593

[16] Vasily Cherepanov, Evgeny Zubkov, Hubertus Junker, Stefan Korte, Marcus Blab, Peter Coenen, and Bert Voigtländer, *Ultra compact multitip scanning tunneling microscope with a diameter of 50 mm*. Review of Scientific Instruments **83**, 033707 (2012). DOI:10.1063/1.3694990

[17] Seiji Higuchi, Osamu Kubo, Hiromi Kuramochi, Masakazu Aono, and Tomonobu Nakayama, *A quadruple-scanning-probe force microscope for electrical property measurements of microscopic materials*. Nanotechnology **22**, 285205 (2011). DOI: 10.1088/0957-4484/22/28/285205

[18] Ireneusz Morawski and Bert Voigtländer, *Simultaneously measured signals in scanning probe microscopy with a needle sensor: Frequency shift and tunneling current*. Review of Scientific Instruments **81**, 033703 (2010). DOI:10.1063/1.3321437

[19] Ireneusz Morawski, Richard Spiegelberg, Stefan Korte, and Bert Voigtländer, *Combined frequency modulated atomic force microscopy and scanning tunneling microscopy detection for multi-tip scanning probe microscopy applications*. Review of Scientific Instruments **86**, 123703 (2015). DOI:10.1063/1.4936975

[20] Taizo Kanagawa, Rei Hobara, Iwao Matsuda, Takehiro Tanikawa, Akiko Natori, and Shuji Hasegawa, *Anisotropy in conductance of a quasi-one-dimensional metallic surface state measured by a square micro-four-point probe method*. Physical Review Letters **91**, 036805 (2003). DOI:10.1103/physrevlett.91.036805

[21] Michael K. Yakes, Daniel Gunlycke, Joseph L. Tedesco, Paul M. Campbell, Rachael L. Myers-Ward, Charles R. Eddy, D. Kurt Gaskill, Paul E. Sheehan, and Arnaldo R. Laracuente, *Conductance anisotropy in epitaxial graphene sheets generated by substrate interactions*. Nano Letters **10**, 1559 (2010). DOI:10.1021/nl9035302

[22] Iwao Matsuda, Masashi Ueno, Toru Hirahara, Rei Hobara, Harumo Morikawa, Canhua Liu, and Shuji Hasegawa, *Electrical resistance of a monatomic step on a crystal surface*. Physical Review Letters **93**, 236801 (2004). DOI:10.1103/physrevlett.93.236801

[23] Bruno V. C. Martins, Manuel Smeu, Lucian Livadaru, Hong Guo, and Robert A. Wolkow, *Conductivity of Si(111)-(7×7): The role of a single atomic step*. Physical Review Letters **112**, 246802 (2014). DOI:10.1103/physrevlett.112.246802

[24] Do Kyung Lim, Osamu Kubo, Yoshitaka Shingaya, Tomonobu Nakayama, Young Heon Kim, Jeong Yong Lee, Masakazu Aono, Hangil Lee, Dohyun Lee, and Sehun Kim, *Low resistivity of Pt silicide nanowires measured using double-scanning-probe tunneling microscope*. Applied Physics Letters **92**, 203114 (2008). DOI:10.1063/1.2935329

[25] Alex M. Lord, Thierry G. Maffeis, Olga Kryvchenkova, Richard J. Cobley, Karol Kalna, Despoina M. Kepaptsoglou, Quentin M. Ramasse, Alex S. Walton, Michael B. Ward, Jürgen Köble, and Steve P. Wilks, *Controlling the electrical transport properties of nanocontacts to nanowires*. Nano Letters **15**, 4248 (2015). DOI: 10.1021/nl503743t

[26] Andreas Nägelein, Matthias Steidl, Stefan Korte, Bert Voigtländer, Werner Prost, Peter Kleinschmidt, and Thomas Hannappel, *Investigation of charge carrier depletion in freestanding nanowires by a multi-probe scanning tunneling microscope*. Nano Research **11**, 5924 (2018). DOI:10.1007/s12274-018-2105-x

[27] Craig M. Polley, Warrick R. Clarke, Jill A. Miwa, Michelle Y. Simmons, and Justin W. Wells, *Microscopic four-point-probe resistivity measurements of shallow, high density doping layers in silicon*. Applied Physics Letters **101**, 262105 (2012). DOI:10.1063/1.4773485

[28] Mateusz Wojtaszek, Jakub Lis, Rafal Zuzak, Bartosz Such, and Marek Szymonski, *Inversion layer on the Ge(001) surface from the four-probe conductance measurements*. Applied Physics Letters **105**, 042111 (2014). DOI:10.1063/1.4891858

[29] Sebastian Bauer and Christian A. Bobisch, *Nanoscale electron transport at the surface of a topological insulator*. Nature Communications **7**, 11381 (2016). DOI: 10.1038/ncomms11381

[30] Lucas Barreto, Lisa Kühnemund, Frederik Edler, Christoph Tegenkamp, Jianli Mi, Martin Bremholm, Bo Brummerstedt Iversen, Christian Frydendahl, Marco Bianchi, and Philip Hofmann, *Surface-dominated transport on a bulk topological insulator*. Nano Letters **14**, 3755 (2014). DOI:10.1021/nl501489m

[31] Corentin Durand, X.-G. Zhang, Saban M. Hus, Chuanxu Ma, Michael A. McGuire, Yang Xu, Helin Cao, Ireneusz Miotkowski, Yong P. Chen, and An-Ping Li, *Differentiation of surface and bulk conductivities in topological insulators via four-probe spectroscopy*. Nano Letters **16**, 2213 (2016). DOI:10.1021/acs.nanolett.5b04425

[32] Masaharu Hirose, Eika Tsunemi, Kei Kobayashi, and Hirofumi Yamada, *Influence of grain boundary on electrical properties of organic crystalline grains investigated by dual-probe atomic force microscopy*. Applied Physics Letters **103**, 173109 (2013). DOI:10.1063/1.4826582

[33] Ruisong Ma, Qing Huan, Liangmei Wu, Jiahao Yan, Wei Guo, Yu-Yang Zhang, Shuai Wang, Lihong Bao, Yunqi Liu, Shixuan Du, Sokrates T. Pantelides, and Hong-Jun Gao, *Direct four-probe measurement of grain-boundary resistivity and mobility in millimeter-sized graphene*. Nano Letters **17**, 5291 (2017). DOI:10.1021/acs.nanolett.7b01624

[34] Felix Lüpke, Markus Eschbach, Tristan Heider, Martin Lanius, Peter Schüffelgen, Daniel Rosenbach, Nils von den Driesch, Vasily Cherepanov, Gregor Mussler, Lukasz Plucinski, Detlev Grützmacher, Claus M. Schneider, and Bert Voigtländer, *Electrical resistance of individual defects at a topological insulator surface*. Nature Communications **8**, 15704 (2017). DOI:10.1038/ncomms15704

[35] J. Homoth, M. Wenderoth, T. Druga, L. Winking, R. G. Ulbrich, C. A. Bobisch, B. Weyers, A. Bannani, E. Zubkov, A. M. Bernhart, M. R. Kaspers, and R. Möller, *Electronic transport on the nanoscale: Ballistic transmission and ohm's law*. Nano Letters **9**, 1588 (2009). DOI:10.1021/nl803783g

[36] Jens Baringhaus, Ming Ruan, Frederik Edler, Antonio Tejeda, Muriel Sicot, Amina Taleb-Ibrahimi, An-Ping Li, Zhigang Jiang, Edward H. Conrad, Claire Berger, Christoph Tegenkamp, and Walt A. de Heer, *Exceptional ballistic transport in epitaxial graphene nanoribbons*. Nature **506**, 349 (2014). DOI:10.1038/nature12952

[37] Saban M. Hus, X.-G. Zhang, Giang D. Nguyen, Wonhee Ko, Arthur P. Baddorf, Yong P. Chen, and An-Ping Li, *Detection of the spin-chemical potential in topological insulators using spin-polarized four-probe STM*. Physical Review Letters **119**, 137202 (2017). DOI:10.1103/physrevlett.119.137202

[38] Arthur Leis, Michael Schleenvoigt, Abdur Rehman Jalil, Vasily Cherepanov, Gregor Mussler, Detlev Grützmacher, F. Stefan Tautz, and Bert Voigtländer, *Room temperature in-situ measurement of the spin voltage of a* $BiSbTe_3$ *thin film*. Scientific Reports **10**, 2816 (2020). DOI:10.1038/s41598-020-59679-9

[39] Vasily Cherepanov, Peter Coenen, and Bert Voigtländer, *A nanopositioner for scanning probe microscopy: The KoalaDrive*. Review of Scientific Instruments **83**, 023703 (2012). DOI:10.1063/1.3681444

[40] Tomoya Uetake, Toru Hirahara, Yoichi Ueda, Naoka Nagamura, Rei Hobara, and Shuji Hasegawa, *Anisotropic conductivity of the Si(111) 4×1-In surface: Transport mechanism determined by the temperature dependence*. Physical Review B **86**, 035325 (2012). DOI:10.1103/physrevb.86.035325

[41] Ch. Blömers, T. Grap, M. I. Lepsa, J. Moers, St. Trellenkamp, D. Grützmacher, H. Lüth, and Th. Schäpers, *Hall effect measurements on InAs nanowires*. Applied Physics Letters **101**, 152106 (2012). DOI:10.1063/1.4759124

[42] Corentin Durand, Maxime Berthe, Younes Makoudi, Jean-Philippe Nys, Renaud Leturcq, Philippe Caroff, and Bruno Grandidier, *Persistent enhancement of the carrier density in electron irradiated InAs nanowires*. Nanotechnology **24**, 275706 (2013). DOI:10.1088/0957-4484/24/27/275706

[43] Felix Lüpke, David Cuma, Stefan Korte, Vasily Cherepanov, and Bert Voigtländer, *Four-point probe measurements using current probes with voltage feedback to measure electric potentials*. Journal of Physics: Condensed Matter **30**, 054004 (2018). DOI:10.1088/1361-648x/aaa31e

[44] Bert Voigtländer, Vasily Cherepanov, Stefan Korte, Arthur Leis, David Cuma, Sven Just, and Felix Lüpke, *Multi-tip scanning tunneling microscopy: Experimental techniques and data analysis*. Review of Scientific Instruments **89**, 101101 (2018). DOI: 10.1063/1.5042346

[45] F. Wenner, *A method of measuring earth resistivity*. Bulletin of the Bureau of Standards **12**, 469 (1915). DOI:10.6028/bulletin.282

[46] Sergey Fomel, *Geophysics Today: A Survey of the Field as the Journal Celebrates its 75th Anniversary* (Society of Exploration Geophysicists, 2010). DOI:10.1190/1.9781560802273

[47] John M. Reynolds, *An Introduction to Applied and Environmental Geophysics*, 2nd edition (John Wiley & Sons, New York, 2011). ISBN 978-1-119-95714-0

[48] Robert Gaige Van Nostrand and Kenneth L. Cook, *Interpretation of resistivity data*. US Geological Survey Professional Paper **499** (1966). DOI:10.3133/pp499

[49] L. Valdes, *Resistivity measurements on germanium for transistors*. Proceedings of the IRE **42**, 420 (1954). DOI:10.1109/jrproc.1954.274680

[50] W. Murray Bullis, *Standard measurements of the resistivity of silicon by the four probe method*. Technical Report NBS-9666, NASA-CR-86032, National Bureau of Standards, Washington D.C. (1967)

[51] W. Murray Bullis, *Measurement methods for the semiconductor device industry – A summary of NBS activity*. Technical Report 511, National Bureau of Standards, Washington D.C. (1969), DOI:10.6028/nbs.tn.511

[52] Michael B. Heaney, *Electrical conductivity and resistivity*, in: John G. Webster (ed.), *Electrical Measurement, Signal Processing, and Displays*, chapter 7 (CRC Press, 2003), ISBN 0-8493-1733-9, DOI:10.1201/9780203009406

[53] Eugene W. Chase, *Ohms per square – What!* Technical Report, Electro-Tech Systems, Inc., Philadelphia, PA, ESD Journal (2008), www.esdjournal.com/techpapr/ohms.htm

[54] *The international system of units (SI)*, International Bureau of Weights and Measures, Sèvres (2019), ISBN 978-92-822-2272-0, www.bipm.org/en/publications/si-brochure

[55] Frank Keywell and George Dorosheski, *Measurement of the sheet resistivity of a square wafer with a square four-point probe*. Review of Scientific Instruments **31**, 833 (1960). DOI:10.1063/1.1717065

[56] A Mircea, *Semiconductor sheet resistivity measurements on square samples*. Journal of Scientific Instruments **41**, 679 (1964). DOI:10.1088/0950-7671/41/11/307

[57] Sara Zolfaghar Tehrani, W.L. Lim, and L. Lee, *Correction factors for films resistivity measurement*. Measurement **45**, 219 (2012). DOI:10.1016/j.measurement.2011.11.019

[58] Robert A. Weller, *An algorithm for computing linear four-point probe thickness correction factors*. Review of Scientific Instruments **72**, 3580 (2001). DOI:10.1063/1.1394186

[59] Junsheng Shi and Yicai Sun, *New method of calculating the correction factors for the measurement of sheet resistivity of a square sample with a square four-point probe*. Review of Scientific Instruments **68**, 1814 (1997). DOI:10.1063/1.1147998

[60] I. Miccoli, F. Edler, H. Pfnür, and C. Tegenkamp, *The 100th anniversary of the four-point probe technique: the role of probe geometries in isotropic and anisotropic systems*. Journal of Physics: Condensed Matter **27**, 223201 (2015). DOI:10.1088/0953-8984/27/22/223201

[61] J. W. Wells, J. F. Kallehauge, and Ph. Hofmann, *Surface-sensitive conductance measurements on clean and stepped semiconductor surfaces: Numerical simulations of four point probe measurements*. Surface Science **602**, 1742 (2008). DOI:10.1016/j.susc.2008.02.041

[62] J. W. Wells, K. Handrup, J. F. Kallehauge, L. Gammelgaard, P. Bøggild, M. B. Balslev, J. E. Hansen, P. R. E. Petersen, and Ph. Hofmann, *The conductivity of Bi(111) investigated with nanoscale four point probes*. Journal of Applied Physics **104**, 053717 (2008). DOI:10.1063/1.2969769

[63] V. M. Tatarnikov, *Use of probes for measuring the electrical conductance of anisotropic plates*. Measurement Techniques **13**, 877 (1970). DOI:10.1007/bf01061555

[64] J. D. Wasscher, *Note on four-point resistivity measurements on anisotropic conductors*. Philips Research Reports **16**, 301 (1961)

[65] L. J. van der Pauw, *Determination of resistivity tensor and Hall tensor of anisotropic conductors*. Philips Research Reports **16**, 187 (1961)

[66] H. A. Lorentz, *Het theorema van Poynting over de energie van het electromagnetisch veld en een paar algemene stellingen over de voortplanting van het licht*, volume 4, 176 (Verslagen Koninklijke Akademie van Wetenschappen, Amsterdam, 1896)

[67] S. Ballantine, *Reciprocity in electromagnetic, mechanical, acoustical, and interconnected systems*. Proceedings of the IRE **17**, 927 (1929). DOI:10.1109/jrproc.1929.221771

[68] K. S. S. Kumar, *Electric Circuits and Networks* (Dorling Kindersley, 2008). ISBN 9788131713907

[69] R. Rymaszewski, *Relationship between the correction factor of the four-point probe value and the selection of potential and current electrodes*. Journal of Physics E: Scientific Instruments **2**, 170 (1969). DOI:10.1088/0022-3735/2/2/312

[70] G. F. C. Searle, *On resistances with current and potential terminals*. The Electrician **66**, 999 (1911)

[71] D. C. Worledge, *Reduction of positional errors in a four-point probe resistance measurement*. Applied Physics Letters **84**, 1695 (2004). DOI:10.1063/1.1655697

[72] David S. Perloff, *Four-point probe correction factors for use in measuring large diameter doped semiconductor wafers*. Journal of The Electrochemical Society **123**, 1745 (1976). DOI:10.1149/1.2132683

[73] E. W. Carpenter, *Some notes concerning the Wenner configuration*. Geophysical Prospecting **3**, 388 (1955). DOI:10.1111/j.1365-2478.1955.tb01384.x

[74] D. S. Perloff, J. N. Gan, and F. E. Wahl, *Dose accuracy and doping uniformity of ion implantation equipment*. Solid State Technology **24**, 112 (1981)

[75] L. J. van der Pauw, *A method of measuring specific resistivity and Hall effect of discs of arbitrary shape*. Philips Research Reports **13**, 1 (1958)

[76] L. J. van der Pauw, *A method of measuring the resistivity and Hall coefficient on lamellae of arbitrary shape*. Philips Technical Review **20**, 220 (1958)

[77] Sune Thorsteinsson, Fei Wang, Dirch H. Petersen, Torben Mikael Hansen, Daniel Kjær, Rong Lin, Jang-Yong Kim, Peter F. Nielsen, and Ole Hansen, *Accurate microfour-point probe sheet resistance measurements on small samples*. Review of Scientific Instruments **80**, 053902 (2009). DOI:10.1063/1.3125050

[78] Ph. Hofmann and J. W. Wells, *Surface-sensitive conductance measurements*. Journal of Physics: Condensed Matter **21**, 013003 (2008). DOI:10.1088/0953-8984/21/1/013003

[79] Marie D'angelo, Keiko Takase, Nobuhiro Miyata, Toru Hirahara, Shuji Hasegawa, Akinori Nishide, Manami Ogawa, and Iwao Matsuda, *Conductivity of the Si(111) 7×7 dangling-bond state*. Physical Review B **79**, 035318 (2009). DOI:10.1103/physrevb.79.035318

[80] G. Binnig, H. Rohrer, Ch. Gerber, and E. Weibel, *7 × 7 reconstruction on Si(111) resolved in real space*. Physical Review Letters **50**, 120 (1983). DOI:10.1103/physrevlett.50.120

[81] Bert Voigtländer, *Fundamental processes in Si/Si and Ge/Si epitaxy studied by scanning tunneling microscopy during growth*. Surface Science Reports **43**, 127 (2001). DOI:10.1016/s0167-5729(01)00012-7

[82] Kunio Takayanagi, Yasumasa Tanishiro, Shigeki Takahashi, and Masaetsu Takahashi, *Structure analysis of Si(111)-7×7 reconstructed surface by transmission electron diffraction*. Surface Science **164**, 367 (1985). DOI:10.1016/0039-6028(85)90753-8

[83] Kwonjae Yoo and H. H. Weitering, *Electrical conductance of reconstructed silicon surfaces*. Physical Review B **65**, 115424 (2002). DOI:10.1103/physrevb.65.115424

[84] Manuel Smeu, Hong Guo, Wei Ji, and Robert A. Wolkow, *Electronic properties of si(111)-7×7 and related reconstructions: Density functional theory calculations*. Physical Review B **85**, 120 (2012). DOI:10.1103/physrevb.85.195315

[85] R. J. Hamers, R. M. Tromp, and J. E. Demuth, *Surface electronic structure of si (111)-(7×7) resolved in real space*. Physical Review Letters **56**, 1972 (1986). DOI: 10.1103/physrevlett.56.1972

[86] K. Romanyuk, J. Mysliveček, V. Cherepanov, T. Sekiguchi, S. Yoshida, K. M. Itoh, and B. Voigtländer, *Optimized Ge nanowire arrays on Si by modified surfactant mediated epitaxy*. Physical Review B **75**, 241309 (2007). DOI:10.1103/physrevb.75.241309

[87] Marcus Blab, *Ladungstransportmessungen an Si(111) Oberflächen mit einem Multispitzen-Rastertunnelmikroskop*, Ph.D. thesis, RWTH Aachen University, Forschungszentrum Jülich GmbH, Zentralbibliothek Verlag (2014)

[88] Hans Lüth, *Solid Surfaces, Interfaces and Thin Films*, 6th edition (Springer Verlag, Heidelberg, 2015). DOI:10.1007/978-3-319-10756-1

[89] G. Hollinger and F. J. Himpsel, *Oxygen chemisorption and oxide formation on Si(111) and Si(100) surfaces*. Journal of Vacuum Science & Technology A: Vacuum, Surfaces, and Films **1**, 640 (1983). DOI:10.1116/1.572199

[90] M. Liehr, M. Renier, R. A. Wachnik, and G. S. Scilla, *Dopant redistribution at Si surfaces during vacuum anneal*. Journal of Applied Physics **61**, 4619 (1987). DOI: 10.1063/1.338372

[91] S. S. Iyer, S. L. Delage, and G. J. Scilla, *Origin and reduction of interfacial boron spikes in silicon molecular beam epitaxy*. Applied Physics Letters **52**, 486 (1988). DOI:10.1063/1.99420

[92] H. M. Zhang, Kazuyuki Sakamoto, G. V. Hansson, and R. I. G. Uhrberg, *High-temperature annealing and surface photovoltage shifts on Si(111) 7×7*. Physical Review B **78**, 035318 (2008). DOI:10.1103/physrevb.78.035318

[93] D. J. Robbins, A. J. Pidduck, J. L. Glasper, I. M. Young, and C. Pickering, *The measurement of surface boron on silicon wafers annealed in vacuum and gas ambients*. Thin Solid Films **183**, 299 (1989). DOI:10.1016/0040-6090(89)90454-9

[94] S. Bensalah, J.-P. Lacharme, and C. A. Sébenne, *Effect of vacuum annealings on the electronic properties of clean Si(111) surfaces*. Physical Review B **43**, 14441 (1991). DOI:10.1103/physrevb.43.14441

[95] Frederik Edler, Ilio Miccoli, Herbert Pfnür, and Christoph Tegenkamp, *Space charge layer effects in silicon studied by in situ surface transport*. Journal of Physics: Condensed Matter **31**, 214001 (2019). DOI:10.1088/1361-648x/ab094e

[96] S. Bouzidi, F. Coletti, J. M. Debever, P. A. Thiry, P. Dumas, and Y. J. Chabal, *Inverse-photoemission spectroscopy of the unreconstructed, ideally H-terminated Si(111) surface*. Physical Review B **45**, 1187 (1992). DOI:10.1103/physrevb.45.1187

[97] John David Jackson, *Classical Electrodynamics*, 3rd edition (Wiley, New York, 1999). ISBN 978-0-471-30932-1

[98] M. S. Leong, S. C. Choo, and C. C. Wang, *Spreading resistance calculations for graded structures based on the uniform flux source boundary condition*. Solid-State Electronics **20**, 255 (1977). DOI:10.1016/0038-1101(77)90193-9

[99] P. A. Schumann and E. E. Gardner, *Application of multilayer potential distribution to spreading resistance correction factors*. Journal of The Electrochemical Society **116**, 87 (1969). DOI:10.1149/1.2411781

[100] H. L. Berkowitz, *Errors in resistivities calculated by multilayer analysis of spreading resistances*. Journal of The Electrochemical Society **126**, 1479 (1979). DOI: 10.1149/1.2129311

[101] C.-W. Wang, A. M. Sastry, K. A. Striebel, and K. Zaghib, *Extraction of layerwise conductivities in carbon-enhanced, multilayered $LiFePO_4$ cathodes*. Journal of The Electrochemical Society **152**, A1001 (2005). DOI:10.1149/1.1890766

[102] M. S. Leong, S. C. Choo, and L. S. Tan, *The role of source boundary condition in spreading resistance calculations*. Solid-State Electronics **21**, 933 (1978). DOI: 10.1016/0038-1101(78)90291-5

[103] Sven Just, Marcus Blab, Stefan Korte, Vasily Cherepanov, Helmut Soltner, and Bert Voigtländer, *Surface and step conductivities on Si(111) surfaces*. Physical Review Letters **115**, 066801 (2015). DOI:10.1103/physrevlett.115.066801

[104] Shuji Hasegawa and Shozo Ino, *Surface structures and conductance at epitaxial growths of Ag and Au on the Si(111) surface*. Physical Review Letters **68**, 1192 (1992). DOI:10.1103/physrevlett.68.1192

[105] Yukio Hasegawa, In-Whan Lyo, and Phaedon Avouris, *Measurement of surface state conductance using STM point contacts*. Surface Science **357-358**, 32 (1996). DOI: 10.1016/0039-6028(96)00052-0

[106] C. L. Petersen, F. Grey, and M. Aono, *Oxidation of clean silicon surfaces studied by four-point probe surface conductance measurements*. Surface Science **377-379**, 676 (1997). DOI:10.1016/s0039-6028(96)01470-7

[107] Edward Perkins, Lucas Barreto, Justin Wells, and Philip Hofmann, *Surface-sensitive conductivity measurement using a micro multi-point probe approach*. Review of Scientific Instruments **84**, 033901 (2013). DOI:10.1063/1.4793376

[108] Jakub Lis, Mateusz Wojtaszek, Rafal Zuzak, Bartosz Such, and Marek Szymonski, *Appearance of effective surface conductivity: An experimental and analytic study*. Physical Review B **92**, 035309 (2015). DOI:10.1103/physrevb.92.035309

[109] P. A. Schumann and E. E. Gardner, *Spreading resistance correction factors*. Solid-State Electronics **12**, 371 (1969). DOI:10.1016/0038-1101(69)90092-6

[110] E. E. Gardner and P. A. Schumann, *Measurement of resistivity of silicon epitaxial layers by the three-point probe technique*. Solid-State Electronics **8**, 165 (1965). DOI:10.1016/0038-1101(65)90047-x

[111] T. Clarysse, W. Vandervorst, E. J. H. Collart, and A. J. Murrell, *Electrical characterization of ultrashallow dopant profiles*. Journal of The Electrochemical Society **147**, 3569 (2000). DOI:10.1149/1.1393940

[112] J. W. Wells, J. F. Kallehauge, T. M. Hansen, and Ph. Hofmann, *Disentangling surface, bulk, and space-charge-layer conductivity in Si(111)-(7×7)*. Physical Review Letters **97**, 206803 (2006). DOI:10.1103/physrevlett.97.206803

[113] T. Tanikawa, K. Yoo, I. Matsuda, S. Hasegawa, and Y. Hasegawa, *Nonmetallic transport property of the Si(111) 7×7 surface*. Physical Review B **68**, 113303 (2003). DOI:10.1103/physrevb.68.113303

[114] P. Tsipas and A. Dimoulas, *Modeling of negatively charged states at the Ge surface and interfaces*. Applied Physics Letters **94**, 012114 (2009). DOI:10.1063/1.3068497

[115] A. Dimoulas, P. Tsipas, A. Sotiropoulos, and E. K. Evangelou, *Fermi-level pinning and charge neutrality level in germanium*. Applied Physics Letters **89**, 252110 (2006). DOI:10.1063/1.2410241

[116] Peter Broqvist, Audrius Alkauskas, and Alfredo Pasquarello, *Defect levels of dangling bonds in silicon and germanium through hybrid functionals*. Physical Review B **78**, 075203 (2008). DOI:10.1103/physrevb.78.075203

[117] Per Mårtensson, Antonio Cricenti, and Göran V. Hansson, *Photoemission study of the surface states that pin the fermi level at Si(100) 2×1 surfaces*. Physical Review B **33**, 8855 (1986). DOI:10.1103/physrevb.33.8855

[118] F. J. Himpsel, P. Heimann, T. C. Chiang, and D. E. Eastman, *Geometry-dependent Si(2p) surface core-level excitations for Si(111) and Si(100) surfaces*. Physical Review Letters **45**, 1112 (1980). DOI:10.1103/physrevlett.45.1112

[119] Sven Just, Helmut Soltner, Stefan Korte, Vasily Cherepanov, and Bert Voigtländer, *Surface conductivity of Si(100) and Ge(100) surfaces determined from four-point transport measurements using an analytical n-layer conductance model*. Physical Review B **95**, 075310 (2017). DOI:10.1103/physrevb.95.075310

[120] F. Lüpke, S. Korte, V. Cherepanov, and B. Voigtländer, *Scanning tunneling potentiometry implemented into a multi-tip setup by software*. Review of Scientific Instruments **86**, 123701 (2015). DOI:10.1063/1.4936079

[121] D. Hsieh, Y. Xia, D. Qian, L. Wray, F. Meier, J. H. Dil, J. Osterwalder, L. Patthey, A. V. Fedorov, H. Lin, A. Bansil, D. Grauer, Y. S. Hor, R. J. Cava, and M. Z. Hasan, *Observation of time-reversal-protected single-dirac-cone topological-insulator states in Bi_2Te_3 and Sb_2Te_3*. Physical Review Letters **103**, 146401 (2009). DOI:10.1103/physrevlett.103.146401

[122] Pedram Roushan, Jungpil Seo, Colin V. Parker, Y. S. Hor, D. Hsieh, Dong Qian, Anthony Richardella, M. Z. Hasan, R. J. Cava, and Ali Yazdani, *Topological surface states protected from backscattering by chiral spin texture*. Nature **460**, 1106 (2009). DOI:10.1038/nature08308

[123] Haijun Zhang, Chao-Xing Liu, Xiao-Liang Qi, Xi Dai, Zhong Fang, and Shou-Cheng Zhang, *Topological insulators in Bi_2Se_3, Bi_2Te_3 and Sb_2Te_3 with a single dirac cone on the surface*. Nature Physics **5**, 438 (2009). DOI:10.1038/nphys1270

[124] Zhi Ren, A. A. Taskin, Satoshi Sasaki, Kouji Segawa, and Yoichi Ando, *Large bulk resistivity and surface quantum oscillations in the topological insulator Bi_2Te_2Se*. Physical Review B **82**, 241306(R) (2010). DOI:10.1103/physrevb.82.241306

[125] Felix Lüpke, Sven Just, Gustav Bihlmayer, Martin Lanius, Martina Luysberg, Jiří Doležal, Elmar Neumann, Vasily Cherepanov, Ivan Ošt'ádal, Gregor Mussler, Detlev Grützmacher, and Bert Voigtländer, *Chalcogenide-based van der waals epitaxy: Interface conductivity of tellurium on Si(111)*. Physical Review B **96**, 035301 (2017). DOI:10.1103/physrevb.96.035301

[126] M. Lanius, J. Kampmeier, S. Kölling, G. Mussler, P. M. Koenraad, and D. Grützmacher, *Topography and structure of ultrathin topological insulator Sb_2Te_3 films on Si(111) grown by means of molecular beam epitaxy*. Journal of Crystal Growth **453**, 158 (2016). DOI:10.1016/j.jcrysgro.2016.08.016

[127] Atsushi Koma, *Van der waals epitaxy – A new epitaxial growth method for a highly lattice-mismatched system*. Thin Solid Films **216**, 72 (1992). DOI:10.1016/0040-6090(92)90872-9

[128] Svetlana Borisova, Julian Krumrain, Martina Luysberg, Gregor Mussler, and Detlev Grützmacher, *Mode of growth of ultrathin topological insulator Bi_2Te_3 films on Si(111) substrates*. Crystal Growth & Design **12**, 6098 (2012). DOI:10.1021/cg301236s

[129] Takehiro Tanikawa, Iwao Matsuda, Taizo Kanagawa, and Shuji Hasegawa, *Surface-state electrical conductivity at a metal-insulator transition on silicon*. Physical Review Letters **93**, 016801 (2004). DOI:10.1103/physrevlett.93.016801

[130] Guanhua Zhang, Huajun Qin, Jing Teng, Jiandong Guo, Qinlin Guo, Xi Dai, Zhong Fang, and Kehui Wu, *Quintuple-layer epitaxy of thin films of topological insulator Bi_2Se_3*. Applied Physics Letters **95**, 053114 (2009). DOI:10.1063/1.3200237

[131] Felix Lüpke, Sven Just, Markus Eschbach, Tristan Heider, Ewa Młyńczak, Martin Lanius, Peter Schüffelgen, Daniel Rosenbach, Nils von den Driesch, Vasily Cherepanov, Gregor Mussler, Lukasz Plucinski, Detlev Grützmacher, Claus M. Schneider, F. Stefan Tautz, and Bert Voigtländer, *In situ disentangling surface state transport channels of a topological insulator thin film by gating*. npj Quantum Materials **3**, 46 (2018). DOI:10.1038/s41535-018-0116-1

[132] Namrata Bansal, Yong Seung Kim, Eliav Edrey, Matthew Brahlek, Yoichi Horibe, Keiko Iida, Makoto Tanimura, Guo-Hong Li, Tian Feng, Hang-Dong Lee, Torgny Gustafsson, Eva Andrei, and Seongshik Oh, *Epitaxial growth of topological insulator* Bi_2Se_3 *film on Si(111) with atomically sharp interface*. Thin Solid Films **520**, 224 (2011). DOI:10.1016/j.tsf.2011.07.033

[133] R. Houbertz, U. Memmert, and R. J. Behm, *Morphology of anodically etched Si(111) surfaces: A structural comparison of* NH_4F *versus HF etching*. Journal of Vacuum Science & Technology B: Microelectronics and Nanometer Structures **12**, 3145 (1994). DOI:10.1116/1.587490

[134] G. S. Higashi, R. S. Becker, Y. J. Chabal, and A. J. Becker, *Comparison of Si(111) surfaces prepared using aqueous solutions of* NH_4F *versus HF*. Applied Physics Letters **58**, 1656 (1991). DOI:10.1063/1.105155

[135] H. D. Li, Z. Y. Wang, X. Kan, X. Guo, H. T. He, Z. Wang, J. N. Wang, T. L. Wong, N. Wang, and M. H. Xie, *The van der waals epitaxy of* Bi_2Se_3 *on the vicinal Si(111) surface: an approach for preparing high-quality thin films of a topological insulator*. New Journal of Physics **12**, 103038 (2010). DOI:10.1088/1367-2630/12/10/103038

[136] Yusuke Sakamoto, Toru Hirahara, Hidetoshi Miyazaki, Shin-ichi Kimura, and Shuji Hasegawa, *Spectroscopic evidence of a topological quantum phase transition in ultrathin* Bi_2Se_3 *films*. Physical Review B **81**, 165432 (2010). DOI:10.1103/physrevb.81.165432

[137] Toru Hirahara, Yusuke Sakamoto, Yasuo Takeichi, Hidetoshi Miyazaki, Shin-ichi Kimura, Iwao Matsuda, Akito Kakizaki, and Shuji Hasegawa, *Anomalous transport in an* n*-type topological insulator ultrathin* Bi_2Se_3 *film*. Physical Review B **82**, 155309 (2010). DOI:10.1103/physrevb.82.155309

[138] R. D. Bringans and Marjorie A. Olmstead, *Bonding of Se and ZnSe to the Si(100) surface*. Physical Review B **39**, 12985 (1989). DOI:10.1103/physrevb.39.12985

[139] S. Q. Wu, Yinghui Zhou, Qi-Hui Wu, C. I. Pakes, and Zi-Zhong Zhu, *Adsorption of selenium atoms at the Si(111)-7×7 surface: A combination of scanning tunnelling microscopy and density functional theory studies*. Chemical Physics **382**, 41 (2011). DOI:10.1016/j.chemphys.2011.02.006

[140] Liang He, Faxian Xiu, Yong Wang, Alexei V. Fedorov, Guan Huang, Xufeng Kou, Murong Lang, Ward P. Beyermann, Jin Zou, and Kang L. Wang, *Epitaxial growth of* Bi_2Se_3 *topological insulator thin films on Si(111)*. Journal of Applied Physics **109**, 103702 (2011). DOI:10.1063/1.3585673

[141] Dohun Kim, Sungjae Cho, Nicholas P. Butch, Paul Syers, Kevin Kirshenbaum, Shaffique Adam, Johnpierre Paglione, and Michael S. Fuhrer, *Surface conduction of topological dirac electrons in bulk insulating* Bi_2Se_3. Nature Physics **8**, 459 (2012). DOI:10.1038/nphys2286

[142] Fan Yang, A. A. Taskin, Satoshi Sasaki, Kouji Segawa, Yasuhide Ohno, Kazuhiko Matsumoto, and Yoichi Ando, *Dual-gated topological insulator thin-film device for efficient fermi-level tuning*. ACS Nano **9**, 4050 (2015). DOI:10.1021/acsnano.5b00102

[143] C. E. ViolBarbosa, Chandra Shekhar, Binghai Yan, S. Ouardi, Eiji Ikenaga, G. H. Fecher, and C. Felser, *Direct observation of band bending in the topological insulator* Bi_2Se_3. Physical Review B **88**, 195128 (2013). DOI:10.1103/physrevb.88.195128

[144] A. Many, Y. Goldstein, and N.B. Grover, *Semiconductor Surfaces* (North Holland, Amsterdam, 1965)

[145] K. S. Novoselov, A. K. Geim, S. V. Morozov, D. Jiang, M. I. Katsnelson, I. V. Grigorieva, S. V. Dubonos, and A. A. Firsov, *Two-dimensional gas of massless dirac fermions in graphene*. Nature **438**, 197 (2005). DOI:10.1038/nature04233

[146] Thomas Heinzel, *Mesoscopic Electronics in Solid State Nanostructures*, 3rd edition (Wiley-VCH Verlag, Berlin, 2010). ISBN 978-3-527-40932-7

[147] T. Arakane, T. Sato, S. Souma, K. Kosaka, K. Nakayama, M. Komatsu, T. Takahashi, Zhi Ren, Kouji Segawa, and Yoichi Ando, *Tunable dirac cone in the topological insulator* $Bi_{2-x}Sb_xTe_{3-y}Se_y$. Nature Communications **3**, 636 (2012). DOI:10.1038/ncomms1639

[148] Marco Bianchi, Dandan Guan, Shining Bao, Jianli Mi, Bo Brummerstedt Iversen, Philip D.C. King, and Philip Hofmann, *Coexistence of the topological state and a two-dimensional electron gas on the surface of* Bi_2Se_3. Nature Communications **1**, 128 (2010). DOI:10.1038/ncomms1131

[149] P. D. C. King, R. C. Hatch, M. Bianchi, R. Ovsyannikov, C. Lupulescu, G. Landolt, B. Slomski, J. H. Dil, D. Guan, J. L. Mi, E. D. L. Rienks, J. Fink, A. Lindblad, S. Svensson, S. Bao, G. Balakrishnan, B. B. Iversen, J. Osterwalder, W. Eberhardt, F. Baumberger, and Ph. Hofmann, *Large tunable rashba spin splitting of a two-dimensional electron gas in* Bi_2Se_3. Physical Review Letters **107**, 096802 (2011). DOI:10.1103/physrevlett.107.096802

[150] Hadj M. Benia, Chengtian Lin, Klaus Kern, and Christian R. Ast, *Reactive chemical doping of the* Bi_2Se_3 *topological insulator*. Physical Review Letters **107**, 177602 (2011). DOI:10.1103/physrevlett.107.177602

[151] Desheng Kong, Judy J. Cha, Keji Lai, Hailin Peng, James G. Analytis, Stefan Meister, Yulin Chen, Hai-Jun Zhang, Ian R. Fisher, Zhi-Xun Shen, and Yi Cui, *Rapid surface oxidation as a source of surface degradation factor for* Bi_2Se_3. ACS Nano **5**, 4698 (2011). DOI:10.1021/nn200556h

[152] James G. Analytis, Jiun-Haw Chu, Yulin Chen, Felipe Corredor, Ross D. McDonald, Z. X. Shen, and Ian R. Fisher, *Bulk fermi surface coexistence with dirac surface state in* Bi_2Se_3*: A comparison of photoemission and shubnikov–de haas measurements*. Physical Review B **81**, 205407 (2010). DOI:10.1103/physrevb.81.205407

[153] Matthew Brahlek, Nikesh Koirala, Namrata Bansal, and Seongshik Oh, *Transport properties of topological insulators: Band bending, bulk metal-to-insulator transition, and weak anti-localization*. Solid State Communications **215-216**, 54 (2015). DOI:10.1016/j.ssc.2014.10.021

[154] Matthew Brahlek, Nikesh Koirala, Maryam Salehi, Namrata Bansal, and Seongshik Oh, *Emergence of decoupled surface transport channels in bulk insulating Bi_2Se_3 thin films*. Physical Review Letters **113**, 026801 (2014). DOI:10.1103/physrevlett.113.026801

[155] Jens Kellner, Markus Eschbach, Jörn Kampmeier, Martin Lanius, Ewa Młyńczak, Gregor Mussler, Bernhard Holländer, Lukasz Plucinski, Marcus Liebmann, Detlev Grützmacher, Claus M. Schneider, and Markus Morgenstern, *Tuning the dirac point to the fermi level in the ternary topological insulator $(Bi_{1-x}Sb_x)_2Te_3$*. Applied Physics Letters **107**, 251603 (2015). DOI:10.1063/1.4938394

[156] Liang He, Xufeng Kou, Murong Lang, Eun Sang Choi, Ying Jiang, Tianxiao Nie, Wanjun Jiang, Yabin Fan, Yong Wang, Faxian Xiu, and Kang L. Wang, *Evidence of the two surface states of $(Bi_{0.53}Sb_{0.47})_2Te_3$ films grown by van der waals epitaxy*. Scientific Reports **3**, 3406 (2013). DOI:10.1038/srep03406

[157] C. Weyrich, M. Drögeler, J. Kampmeier, M. Eschbach, G. Mussler, T. Merzenich, T. Stoica, I. E. Batov, J. Schubert, L. Plucinski, B. Beschoten, C. M. Schneider, C. Stampfer, D. Grützmacher, and Th. Schäpers, *Growth, characterization, and transport properties of ternary $(Bi_{1-x}Sb_x)_2Te_3$ topological insulator layers*. Journal of Physics: Condensed Matter **28**, 495501 (2016). DOI:10.1088/0953-8984/28/49/495501

[158] Jinsong Zhang, Cui-Zu Chang, Zuocheng Zhang, Jing Wen, Xiao Feng, Kang Li, Minhao Liu, Ke He, Lili Wang, Xi Chen, Qi-Kun Xue, Xucun Ma, and Yayu Wang, *Band structure engineering in $(Bi_{1-x}Sb_x)_2Te_3$ ternary topological insulators*. Nature Communications **2**, 574 (2011). DOI:10.1038/ncomms1588

[159] Yosuke Satake, Junichi Shiogai, Daichi Takane, Keiko Yamada, Kohei Fujiwara, Seigo Souma, Takafumi Sato, Takashi Takahashi, and Atsushi Tsukazaki, *Fermi-level tuning of the dirac surface state in $(Bi_{1-x}Sb_x)_2Se_3$ thin films*. Journal of Physics: Condensed Matter **30**, 085501 (2018). DOI:10.1088/1361-648x/aaa724

[160] Xiaoyue He, Tong Guan, Xiuxia Wang, Baojie Feng, Peng Cheng, Lan Chen, Yongqing Li, and Kehui Wu, *Highly tunable electron transport in epitaxial topological insulator $(Bi_{1-x}Sb_x)_2Te_3$ thin films*. Applied Physics Letters **101**, 123111 (2012). DOI:10.1063/1.4754108

[161] D. Haneman, *Photoelectric emission and work functions of InSb, GaAs, Bi_2Te_3 and germanium*. Journal of Physics and Chemistry of Solids **11**, 205 (1959). DOI:10.1016/0022-3697(59)90215-x

[162] Byungki Ryu, *Work function of bismuth telluride: First-principles approach*. Journal of the Korean Physical Society **72**, 122 (2018). DOI:10.3938/jkps.72.122

[163] H. Qian, H. Tong, L. J. Zhou, B. H. Yan, H. K. Ji, K. H. Xue, X. M. Cheng, and X. S. Miao, *Low work function of crystalline GeTe/Sb*$_2$*Te*$_3$ *superlattice-like films induced by te dangling bonds*. Journal of Physics D: Applied Physics **49**, 495302 (2016). DOI:10.1088/0022-3727/49/49/495302

[164] John H. Davies, *The Physics of Low-dimensional Semiconductors* (Cambridge University Press, 1997). DOI:10.1017/cbo9780511819070

[165] Sven Just, Felix Lüpke, Vasily Cherepanov, F. Stefan Tautz, and Bert Voigtländer, *Parasitic conduction channels in topological insulator thin films*. Physical Review B **101**, 245413 (2020). DOI:10.1103/physrevb.101.245413

[166] Liang Fu, C. L. Kane, and E. J. Mele, *Topological insulators in three dimensions*. Physical Review Letters **98**, 106803 (2007). DOI:10.1103/physrevlett.98.106803

[167] Liang Fu and C. L. Kane, *Topological insulators with inversion symmetry*. Physical Review B **76**, 045302 (2007). DOI:10.1103/physrevb.76.045302

[168] Zohar Ringel, Yaacov E. Kraus, and Ady Stern, *Strong side of weak topological insulators*. Physical Review B **86**, 045102 (2012). DOI:10.1103/physrevb.86.045102

[169] Roger S. K. Mong, Jens H. Bardarson, and Joel E. Moore, *Quantum transport and two-parameter scaling at the surface of a weak topological insulator*. Physical Review Letters **108**, 076804 (2012). DOI:10.1103/physrevlett.108.076804

[170] Koji Kobayashi, Tomi Ohtsuki, and Ken-Ichiro Imura, *Disordered weak and strong topological insulators*. Physical Review Letters **110**, 236803 (2013). DOI:10.1103/physrevlett.110.236803

[171] Yukinori Yoshimura, Akihiko Matsumoto, Yositake Takane, and Ken-Ichiro Imura, *Perfectly conducting channel on the dark surface of weak topological insulators*. Physical Review B **88**, 045408 (2013). DOI:10.1103/physrevb.88.045408

[172] Hideaki Obuse, Shinsei Ryu, Akira Furusaki, and Christopher Mudry, *Spin-directed network model for the surface states of weak three-dimensional* $\mathbb{Z}_2$ *topological insulators*. Physical Review B **89**, 155315 (2014). DOI:10.1103/physrevb.89.155315

[173] M. König, S. Wiedmann, C. Brune, A. Roth, H. Buhmann, L. W. Molenkamp, X.-L. Qi, and S.-C. Zhang, *Quantum spin hall insulator state in HgTe quantum wells*. Science **318**, 766 (2007). DOI:10.1126/science.1148047

[174] Christian Pauly, Bertold Rasche, Klaus Koepernik, Marcus Liebmann, Marco Pratzer, Manuel Richter, Jens Kellner, Markus Eschbach, Bernhard Kaufmann, Lukasz Plucinski, Claus M. Schneider, Michael Ruck, Jeroen van den Brink, and Markus Morgenstern, *Subnanometre-wide electron channels protected by topology*. Nature Physics **11**, 338 (2015). DOI:10.1038/nphys3264

[175] Christian Pauly, *Strong and weak topology probed by surface science: topological insulator properties of phase change alloys and heavy metal graphene*, Ph.D. thesis, RWTH Aachen University, Aachen (2015)

[176] Bertold Rasche, Anna Isaeva, Michael Ruck, Sergey Borisenko, Volodymyr Zabolotnyy, Bernd Büchner, Klaus Koepernik, Carmine Ortix, Manuel Richter, and Jeroen van den Brink, *Stacked topological insulator built from bismuth-based graphene sheet analogues*. Nature Materials **12**, 422 (2013). DOI:10.1038/nmat3570

[177] Bertold Rasche, Anna Isaeva, Alexander Gerisch, Martin Kaiser, Wouter Van den Broek, Christoph T. Koch, Ute Kaiser, and Michael Ruck, *Crystal growth and real structure effects of the first weak 3d stacked topological insulator* $Bi_{14}Rh_3I_9$. Chemistry of Materials **25**, 2359 (2013). DOI:10.1021/cm4010823

[178] C. L. Kane and E. J. Mele, *Quantum spin hall effect in graphene*. Physical Review Letters **95**, 226801 (2005). DOI:10.1103/physrevlett.95.226801

[179] J. Tersoff and D. R. Hamann, *Theory and application for the scanning tunneling microscope*. Physical Review Letters **50**, 1998 (1983). DOI:10.1103/physrevlett.50.1998

[180] J. Tersoff and D. R. Hamann, *Theory of the scanning tunneling microscope*. Physical Review B **31**, 805 (1985). DOI:10.1103/physrevb.31.805

[181] A. Selloni, P. Carnevali, E. Tosatti, and C. D. Chen, *Voltage-dependent scanning-tunneling microscopy of a crystal surface: Graphite*. Physical Review B **31**, 2602 (1985). DOI:10.1103/physrevb.31.2602

[182] Markus Morgenstern, *Probing the local density of states of dilute electron systems in different dimensions*. Surface Review and Letters **10**, 933 (2003). DOI:10.1142/s0218625x0300575x

[183] Christian Pauly, Bertold Rasche, Klaus Koepernik, Manuel Richter, Sergey Borisenko, Marcus Liebmann, Michael Ruck, Jeroen van den Brink, and Markus Morgenstern, *Electronic structure of the dark surface of the weak topological insulator* $Bi_{14}Rh_3I_9$. ACS Nano **10**, 3995 (2016). DOI:10.1021/acsnano.6b00841

[184] J. A. Støvneng and P. Lipavský, *Thermopower in scanning-tunneling-microscope experiments*. Physical Review B **42**, 9214 (1990). DOI:10.1103/physrevb.42.9214

[185] T. Druga, M. Wenderoth, J. Homoth, M. A. Schneider, and R. G. Ulbrich, *A versatile high resolution scanning tunneling potentiometry implementation*. Review of Scientific Instruments **81**, 083704 (2010). DOI:10.1063/1.3469809

[186] Markus Morgenstern, Christian Pauly, Jens Kellner, Marcus Liebmann, Marco Pratzer, Gustav Bihlmayer, Markus Eschbach, Lukacz Plucinski, Sebastian Otto, Bertold Rasche, Michael Ruck, Manuel Richter, Sven Just, Felix Lüpke, and Bert Voigtländer, *Strong and weak 3d topological insulators probed by surface science methods*. physica status solidi (b) 2000060 (2020). DOI:10.1002/pssb.202000060

[187] Yuichiro Ando, Takahiro Hamasaki, Takayuki Kurokawa, Kouki Ichiba, Fan Yang, Mario Novak, Satoshi Sasaki, Kouji Segawa, Yoichi Ando, and Masashi Shiraishi, *Electrical detection of the spin polarization due to charge flow in the surface state of the topological insulator* $Bi_{1.5}Sb_{0.5}Te_{1.7}Se_{1.3}$. Nano Letters **14**, 6226 (2014). DOI:10.1021/nl502546c

[188] Jianshi Tang, Li-Te Chang, Xufeng Kou, Koichi Murata, Eun Sang Choi, Murong Lang, Yabin Fan, Ying Jiang, Mohammad Montazeri, Wanjun Jiang, Yong Wang, Liang He, and Kang L. Wang, *Electrical detection of spin-polarized surface states conduction in* $(Bi_{0.53}Sb_{0.47})_2Te_3$ *topological insulator*. Nano Letters **14**, 5423 (2014). DOI:10.1021/nl5026198

[189] C. H. Li, O. M. J. van ‘t Erve, J. T. Robinson, Y. Liu, L. Li, and B. T. Jonker, *Electrical detection of charge-current-induced spin polarization due to spin-momentum locking in* Bi_2Se_3. Nature Nanotechnology **9**, 218 (2014). DOI:10.1038/nnano.2014.16

[190] André Dankert, Johannes Geurs, M. Venkata Kamalakar, Sophie Charpentier, and Saroj P. Dash, *Room temperature electrical detection of spin polarized currents in topological insulators*. Nano Letters **15**, 7976 (2015). DOI:10.1021/acs.nanolett.5b03080

[191] Christian Saunus, Jan Raphael Bindel, Marco Pratzer, and Markus Morgenstern, *Versatile scanning tunneling microscopy with 120 ps time resolution*. Applied Physics Letters **102**, 051601 (2013). DOI:10.1063/1.4790180

[192] B. Davies, *Hankel transforms*, in: *Integral Transforms and their Applications*, 237–253 (Springer New York, 1985), DOI:10.1007/978-1-4899-2691-3_15

[193] A. D. Poularikas, *Transforms and Applications Handbook*, Electrical Engineering Handbook, 3rd edition (CRC Press, 2010). ISBN 978-1-4200-6652-4

[194] Gabriel Cramer, *Introduction à l’Analyse des Lignes Courbes Algébriques* (Chez les Freres Cramer & Cl. Philibert, Genève, 1750)

[195] Klaus Weltner, *Mathematik für Physiker und Ingenieure 2* (Springer Verlag Berlin Heidelberg, 2013). DOI:10.1007/978-3-642-25519-9

[196] Lothar Papula, *Mathematik für Ingenieure und Naturwissenschaftler Band 2* (Springer Fachmedien Wiesbaden, 2015). DOI:10.1007/978-3-658-07790-7

[197] Israil S. Gradstein and Jossif M. Ryschik, *Summen-, Produkt- und Integral-Tafeln, Band 2* (Verlag Harri Deutsch, Thun, Frankfurt/Main, 1981). ISBN 3-87144-350-6

Publications

Publications containing results from this thesis

1. S. Just, M. Blab, S. Korte, V. Cherepanov, H. Soltner, and B. Voigtländer, *Surface and Step Conductivities on Si(111) Surfaces*. Physical Review Letters **115**, 066801 (2015). DOI:10.1103/physrevlett.115.066801

2. S. Just, H. Soltner, S. Korte, V. Cherepanov, and B. Voigtländer, *Surface conductivity of Si(100) and Ge(100) surfaces determined from four-point transport measurements using an analytical N-layer conductance model*. Physical Review B **95**, 075310 (2017). DOI:10.1103/physrevb.95.075310

3. S. Just, F. Lüpke, V. Cherepanov, F. S. Tautz, and B. Voigtländer, *Parallel conduction channels in topological insulator thin films*. Physical Review B **101**, 245413 (2020). DOI:10.1103/PhysRevB.101.245413

4. F. Lüpke, S. Just, G. Bihlmayer, M. Lanius, M. Luysberg, J. Doležal, E. Neumann, V. Cherepanov, I. Ošt'ádal, G. Mussler, D. Grützmacher, and B. Voigtländer, *Chalcogenide-based van der Waals epitaxy: Interface conductivity of tellurium on Si(111)*. Physical Review B **96**, 035301 (2017). DOI:10.1103/PhysRevB.96.035301

5. F. Lüpke, S. Just, M. Eschbach, T. Heider, E. Młyńczak, M. Lanius, P. Schüffelgen, D. Rosenbach, N. von den Driesch, V. Cherepanov, G. Mussler, L. Plucinski, D. Grützmacher, C. M. Schneider, F. S. Tautz, and B. Voigtländer, *In situ disentangling surface state transport channels of a topological insulator thin film by gating*. npj Quantum Materials **3**, 46 (2018). DOI:10.1038/s41535-018-0116-1

6. B. Voigtländer, V. Cherepanov, S. Korte, A. Leis, D. Cuma, S. Just, and F. Lüpke, *Multi-tip scanning tunneling microscopy: Experimental techniques and data analysis*. Review of Scientific Instruments **89**, 101101 (2018). DOI:10.1063/1.5042346

7. M. Morgenstern, C. Pauly, J. Kellner, M. Liebmann, M. Pratzer, G. Bihlmayer, M. Eschbach, L. Plucinski, S. Otto, B. Rasche, M. Ruck, M. Richter, S. Just, F. Lüpke, and B. Voigtländer, *Strong and Weak 3D Topological Insulators Probed by Surface Science Methods*. Physica Status Solidi B, 2000060 (2020). DOI:10.1002/pssb.202000060

Further publications

1. S. Just, S. Zimmermann, V. Kataev, B. Büchner, M. Pratzer, and M. Morgenstern, *Preferential antiferromagnetic coupling of vacancies in graphene on* SiO_2*: Electron spin resonance and scanning tunneling spectroscopy*. Physical Review B **90**, 125449 (2014). DOI:10.1103/PhysRevB.90.125449

2. C. Pauly, M. Liebmann, A. Giussani, J. Kellner, S. Just, J. Sánchez-Barriga, E. Rienks, O. Rader, R. Calarco, G. Bihlmayer, and M. Morgenstern, *Evidence for topological band inversion of the phase change material* $Ge_2Sb_2Te_5$. Applied Physics Letters **103**, 243109 (2013). DOI:10.1063/1.4847715

Acknowledgements

The research work for this thesis has been performed in the workgroup of Prof. Dr. Bert Voigtländer of the *Peter Grünberg Institut (PGI-3)* at the *Forschungszentrum Jülich*. In the following, I would like to thank all the people who substantially supported me during this time.

At first, I want to thank especially my supervisor **Prof. Dr. Bert Voigtländer** for his extensive support in performing the experiments, the many fruitful discussions in order to find new methods for data evaluation and further interesting research topics, as well as his assistance and endurance for improving and correcting publications. He always is willingly to provide help when problems occur, both for experiment as well as for theory, and his broad knowledge about surface science has helped me significantly during my thesis.

Special thanks also go to **Prof. Dr. Markus Morgenstern** from the *II. Physikalisches Institut B* at the *RWTH Aachen*, where I accomplished my master thesis before, for continuous support, fruitful discussions and new ideas, for the collaboration concerning the $Bi_{14}Rh_3I_9$ samples, specifically for inviting me to participate in several of the annual institute's conferences at the *Söllerhaus* which allowed me to get some broader overview about other interesting topics under research, and finally for agreeing to be the associate assessor for this thesis.

Then, I want to thank **Prof. Dr. Stefan Tautz** for the opportunity to accomplish this thesis in his institute and for his support with corrections of publications.

Also, I gratefully acknowledge the support from **Dr. Helmut Soltner** from the *Zentralinstitut für Engineering, Elektronik und Analytik (ZEA-1)*, who helped me substantially by his deep knowledge about simulations and the theoretical aspects for the development of new models for data evaluation.

Moreover, I would like to thank **Dr. Felix Lüpke** for the collaborations concerning the connection between experiments and theoretical calculations for the conductivity of topological insulator thin films, and certainly for being always a good office partner.

Thanks go to **Dr. Vasily Cherepanov** for help in repairing the multi-tip STM when necessary and further technical assistance in application, and to **Dr. Stefan Korte** for general support and discussions about multi-tip STMs.

Furthermore, I would like to thank **Dr. Marcus Blab** for the initial introduction into the multi-tip instrument and the assistance with first measurements at the beginning of my thesis, as well as **Arthur Leis** for his support with measurements towards the end and **David Cuma** for providing any help when needed.

Additionally, I want to acknowledge **Dipl.-Ing. Franz-Peter Coenen** and **Helmut Stoll-**

werk for extensive technical assistance concerning the experimental setup and the implementation of modifications.

Many thanks go to all **collaborators** at the **PGI-9**, **RWTH Aachen** and the **TU Dresden** for fabricating and providing samples, and to all the other people at the **PGI-3** for providing a good atmosphere and a great working environment.

Finally, I want to thank my mother **Renate Just** for her continuous support during the complete time of my education.

Appendix A. Mathematical derivations

In this first part of the appendix, several mathematical derivations are presented as supplement in order to provide more fundamentals about the equations and statements shown in the chapters 3 – 6.

A.1. Tip configurations for 2D systems

A.1.1. Linear tip configuration with arbitrary alignment

In order to show in general that for an anisotropic system a linear tip configuration is not suitable for revealing the two conductivity components σ_x and σ_y from four-point measurements, an arbitrarily aligned in-line setup is considered, as depicted in Fig. A.1. The four tips have a symmetrical spacing with a distance L between the outer current injecting tips (A, B) and a distance s between the inner voltage probing tips (C, D). The linear geometry is rotated by an angle θ with respect to one of the principal axes (here the x-axis) of the anisotropic system. Thus, the positions of the four tips can be expressed as

$$\boldsymbol{x}_A = \begin{pmatrix} 0 \\ 0 \end{pmatrix}, \ \boldsymbol{x}_B = L \begin{pmatrix} \cos(\theta) \\ \sin(\theta) \end{pmatrix}, \ \boldsymbol{x}_C = \frac{L-s}{2} \begin{pmatrix} \cos(\theta) \\ \sin(\theta) \end{pmatrix}, \ \boldsymbol{x}_D = \frac{L+s}{2} \begin{pmatrix} \cos(\theta) \\ \sin(\theta) \end{pmatrix}. \quad \text{(A.1)}$$

In order to consider a 2D system, these vectors have to be inserted into Eq. (3.73) and the four-point resistance according to $R_{AB,DC} = \frac{-\Phi_{CD}^{AB}}{I}$ has to be calculated. It follows with

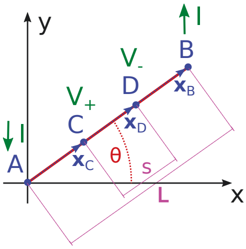

Figure A.1.: Arbitrarily rotated linear tip configuration for an anisotropic system. A symmetric arrangement is chosen with a spacing L between the outer (current injecting) tips at positions A and B, and a spacing s between the inner (voltage measuring) tips located at C and D. The in-line setup is rotated by θ with respect to the principal axes of the anisotropic system.

the prefactor $A := \frac{1}{4\pi\sqrt{\sigma_x\sigma_y}}$ that

$$R_{\text{lin}}^{\text{2D}} = -A\ln\left[\frac{\sigma_y\left(\frac{L+s}{2}\cos(\theta)-L\cos(\theta)\right)^2+\sigma_x\left(\frac{L+s}{2}\sin(\theta)-L\sin(\theta)\right)^2}{\sigma_y\left(\frac{L+s}{2}\cos(\theta)\right)^2+\sigma_x\left(\frac{L+s}{2}\sin(\theta)\right)^2}\right.$$
$$\left.\times\frac{\sigma_y\left(\frac{L-s}{2}\cos(\theta)\right)^2+\sigma_x\left(\frac{L-s}{2}\sin(\theta)\right)^2}{\sigma_y\left(\frac{L-s}{2}\cos(\theta)-L\cos(\theta)\right)^2+\sigma_x\left(\frac{L-s}{2}\sin(\theta)-L\sin(\theta)\right)^2}\right] \tag{A.2}$$

$$= -A\ln\left[\frac{\sigma_y\left(-L+s\right)^2\cos^2(\theta)+\sigma_x\left(-L+s\right)^2\sin^2(\theta)}{\sigma_y\left(L+s\right)^2\cos^2(\theta)+\sigma_x\left(L+s\right)^2\sin^2(\theta)}\right.$$
$$\left.\times\frac{\sigma_y\left(L-s\right)^2\cos^2(\theta)+\sigma_x\left(L-s\right)^2\sin^2(\theta)}{\sigma_y\left(-L-s\right)^2\cos^2(\theta)+\sigma_x\left(-L-s\right)^2\sin^2(\theta)}\right] \tag{A.3}$$

$$\overset{\ln\left[a^2\right]=2\ln[a]}{=} -2A\ln\left[\frac{\sigma_y\left(L-s\right)^2\cos^2(\theta)+\sigma_x\left(L-s\right)^2\sin^2(\theta)}{\sigma_y\left(L+s\right)^2\cos^2(\theta)+\sigma_x\left(L+s\right)^2\sin^2(\theta)}\right] \tag{A.4}$$

$$= -2A\ln\left[\frac{\left(L-s\right)^2\left(\sigma_y\cos^2(\theta)+\sigma_x\sin^2(\theta)\right)}{\left(L+s\right)^2\left(\sigma_y\cos^2(\theta)+\sigma_x\sin^2(\theta)\right)}\right] \tag{A.5}$$

$$\overset{\ln\left[a^2\right]=2\ln[a]}{=} -4A\ln\left[\frac{L-s}{L+s}\right] \tag{A.6}$$

$$\overset{-\ln[a]=\ln\left[\frac{1}{a}\right]}{=} \frac{1}{\pi\sqrt{\sigma_x\sigma_y}}\ln\left[\frac{L+s}{L-s}\right]. \tag{A.7}$$

Specifically, for an equidistant configuration, i.e. $L = 3s$, follows that

$$R_{\text{lin,e}}^{\text{2D,anisotropic}}(\sigma_x,\sigma_y) = \frac{1}{\pi\sqrt{\sigma_x\sigma_y}}\ln\left[\frac{3s+s}{3s-s}\right] = \frac{1}{\pi\sqrt{\sigma_x\sigma_y}}\ln[2]. \tag{A.8}$$

Thus, it turns out that the resulting four-point resistance does not depend on the rotation angle θ of the linear tip setup. As a result, only the geometric mean $\sigma = \sqrt{\sigma_x\sigma_y}$ of the anisotropic conductivity components can be measured, in the same way as it also applies for the isotropic case [cf. Eq. (3.44)] . So, it is proven that for any possible alignment of an in-line tip setup it is not possible to reveal σ_x and σ_y individually from a four-point measurement. For this purpose, a square or a rhombic tip configuration has to be used.

A.1.2. Rhombic tip configuration

In the rhombic tip configuration, both the current and voltage tips are each positioned at the opposite corners of a rhombus which in general can be characterized by its two diagonals $\tilde{s}$ and L, or by the side length s and the interior angle γ. However, here only the special case of a square is considered, so that $\tilde{s} = L = \sqrt{2}s$ and $\gamma = \frac{\pi}{2}$. Such a tip

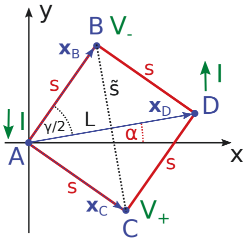

Figure A.2.: Rhombic tip configuration for the special case of a square with side length s, so that $\tilde{s} = L = \sqrt{2}s$ and $\gamma = \frac{\pi}{2}$. The current injecting tips (A, D) as well as the voltage measuring tips (B, C) are positioned at the opposite corners of the square. The current direction, i.e. the diagonal $\overline{AD}$ of the square, is rotated by α with respect to the principal axes of the anisotropic system. The angle α is differently defined compared to the rotation angle θ of the square tip configuration, i.e. $\theta = \alpha + \frac{\pi}{4}$. The labels of the tips are chosen in such a way that the configuration, i.e. (AD, BC), is comparable to the square configuration as depicted in Fig. 3.7.

arrangement is depicted in Fig. A.2 with the current injecting tips at A and D, and the voltage probing tips at B and C. The orientation of the square is characterized by the angle α between the current direction, i.e. the diagonal $\overline{AD}$ of the square, and one of the principal axes of the anisotropically conducting sample system, i.e. the orientations of σ_x and σ_y, respectively. The rotation angle α is differently defined compared to the angle θ of the square configuration [cf. Eq. (3.83)], as in the present case the current direction is along the diagonal of the square, thus it follows that $\theta = \alpha + \frac{\pi}{4}$.

According to the drawing in Fig. A.2, the positions of the four tips can be expressed as

$$\begin{aligned} \boldsymbol{x}_A &= \begin{pmatrix} 0 \\ 0 \end{pmatrix}, \; \boldsymbol{x}_B = \frac{L}{\sqrt{2}} \begin{pmatrix} \cos\left(\alpha + \frac{\pi}{4}\right) \\ \sin\left(\alpha + \frac{\pi}{4}\right) \end{pmatrix}, \; \boldsymbol{x}_C = \frac{L}{\sqrt{2}} \begin{pmatrix} \cos\left(\alpha - \frac{\pi}{4}\right) \\ \sin\left(\alpha - \frac{\pi}{4}\right) \end{pmatrix} \text{ and} \\ \boldsymbol{x}_D &= L \begin{pmatrix} \cos(\alpha) \\ \sin(\alpha) \end{pmatrix}. \end{aligned} \tag{A.9}$$

The terms in the arguments can be simplified by using the trigonometric addition theorems, so that

$$\sin\left(\alpha \pm \frac{\pi}{4}\right) = \sin(\alpha)\cos\left(\frac{\pi}{4}\right) \pm \cos(\alpha)\sin\left(\frac{\pi}{4}\right) = \frac{1}{\sqrt{2}}\Big[\sin(\alpha) \pm \cos(\alpha)\Big] \tag{A.10}$$

$$\cos\left(\alpha \pm \frac{\pi}{4}\right) = \cos(\alpha)\cos\left(\frac{\pi}{4}\right) \mp \sin(\alpha)\sin\left(\frac{\pi}{4}\right) = \frac{1}{\sqrt{2}}\Big[\cos(\alpha) \mp \sin(\alpha)\Big] \tag{A.11}$$

Thus, the two position vectors $\boldsymbol{x}_B$ and $\boldsymbol{x}_C$ can be rewritten as

$$\boldsymbol{x}_B = \frac{L}{2} \begin{pmatrix} \cos(\alpha) - \sin(\alpha) \\ \sin(\alpha) + \cos(\alpha) \end{pmatrix}, \; \boldsymbol{x}_C = \frac{L}{2} \begin{pmatrix} \cos(\alpha) + \sin(\alpha) \\ \sin(\alpha) - \cos(\alpha) \end{pmatrix}. \tag{A.12}$$

In order to consider a 2D system, these vectors can be inserted into Eq. (3.73) by correspondingly exchanging the tip coordinates due to the different configuration in the present case. Subsequently, the four-point resistance according to $R_{AD,BC} = -\frac{\Phi_{CB}^{AD}}{I}$ can be calculated. It follows with the prefactor $A := \frac{1}{4\pi\sqrt{\sigma_x\sigma_y}}$ that

$$R^{\text{2D}}_{\text{rh}} = -A\ln\Bigg[\frac{\sigma_y\left(\frac{L}{2}[\cos(\alpha)-\sin(\alpha)]-L\cos(\alpha)\right)^2+\sigma_x\left(\frac{L}{2}[\sin(\alpha)+\cos(\alpha)]-L\sin(\alpha)\right)^2}{\sigma_y\left(\frac{L}{2}[\cos(\alpha)-\sin(\alpha)]\right)^2+\sigma_x\left(\frac{L}{2}[\sin(\alpha)+\cos(\alpha)]\right)^2} \times\frac{\sigma_y\left(\frac{L}{2}[\cos(\alpha)+\sin(\alpha)]\right)^2+\sigma_x\left(\frac{L}{2}[\sin(\alpha)-\cos(\alpha)]\right)^2}{\sigma_y\left(\frac{L}{2}[\cos(\alpha)+\sin(\alpha)]-L\cos(\alpha)\right)^2+\sigma_x\left(\frac{L}{2}[\sin(\alpha)-\cos(\alpha)]-L\sin(\alpha)\right)^2}\Bigg] \tag{A.13}$$

$$= -A\ln\Bigg[\frac{\sigma_y\left(-\cos(\alpha)-\sin(\alpha)\right)^2+\sigma_x\left(-\sin(\alpha)+\cos(\alpha)\right)^2}{\sigma_y\left(\cos(\alpha)-\sin(\alpha)\right)^2+\sigma_x\left(\sin(\alpha)+\cos(\alpha)\right)^2} \times\frac{\sigma_y\left(\cos(\alpha)+\sin(\alpha)\right)^2+\sigma_x\left(\sin(\alpha)-\cos(\alpha)\right)^2}{\sigma_y\left(-\cos(\alpha)+\sin(\alpha)\right)^2+\sigma_x\left(-\sin(\alpha)-\cos(\alpha)\right)^2}\Bigg] \tag{A.14}$$

$$= -A\ln\Bigg[\frac{\sigma_y\left(\sin(\alpha)+\cos(\alpha)\right)^2+\sigma_x\left(\sin(\alpha)-\cos(\alpha)\right)^2}{\sigma_y\left(\sin(\alpha)-\cos(\alpha)\right)^2+\sigma_x\left(\sin(\alpha)+\cos(\alpha)\right)^2} \times\frac{\sigma_y\left(\sin(\alpha)+\cos(\alpha)\right)^2+\sigma_x\left(\sin(\alpha)-\cos(\alpha)\right)^2}{\sigma_y\left(\sin(\alpha)-\cos(\alpha)\right)^2+\sigma_x\left(\sin(\alpha)+\cos(\alpha)\right)^2}\Bigg] \tag{A.15}$$

$$\overset{\ln\left[a^2\right]=2\ln[a]}{=} -2A\ln\left[\frac{\sigma_y\left(\sin^2(\alpha)+2\sin(\alpha)\cos(\alpha)+\cos^2(\alpha)\right)+\sigma_x\left(\sin^2(\alpha)-2\sin(\alpha)\cos(\alpha)+\cos^2(\alpha)\right)}{\sigma_y\left(\sin^2(\alpha)-2\sin(\alpha)\cos(\alpha)+\cos^2(\alpha)\right)+\sigma_x\left(\sin^2(\alpha)+2\sin(\alpha)\cos(\alpha)+\cos^2(\alpha)\right)}\right] \tag{A.16}$$

$$\overset{\sin^2(\alpha)+\cos^2(\alpha)=1}{=} -2A\ln\left[\frac{\sigma_y\left(1+2\sin(\alpha)\cos(\alpha)\right)+\sigma_x\left(1-2\sin(\alpha)\cos(\alpha)\right)}{\sigma_y\left(1-2\sin(\alpha)\cos(\alpha)\right)+\sigma_x\left(1+2\sin(\alpha)\cos(\alpha)\right)}\right] \tag{A.17}$$

$$= -2A\ln\left[\frac{\sigma_y+\sigma_x-2\sin(\alpha)\cos(\alpha)\left(\sigma_x-\sigma_y\right)}{\sigma_y+\sigma_x+2\sin(\alpha)\cos(\alpha)\left(\sigma_x-\sigma_y\right)}\right] \tag{A.18}$$

$$= -2A\ln\left[\frac{\sigma_y\left[1+\frac{\sigma_x}{\sigma_y}-2\sin(\alpha)\cos(\alpha)\left(\frac{\sigma_x}{\sigma_y}-1\right)\right]}{\sigma_y\left[1+\frac{\sigma_x}{\sigma_y}+2\sin(\alpha)\cos(\alpha)\left(\frac{\sigma_x}{\sigma_y}-1\right)\right]}\right]. \tag{A.19}$$

Thus, after further rearrangement according to $\ln(a^{-1}) = -\ln(a)$, the four-point resistance for a square-shaped rhombic tip configuration on an anisotropic 2D sheet can finally be written as

$$R^{\text{2D}}_{\text{rhombic}}(\sigma_x,\sigma_y,\alpha) = \frac{1}{2\pi\sqrt{\sigma_x\sigma_y}}\ln\left[\frac{1+\frac{\sigma_x}{\sigma_y}+2\sin(\alpha)\cos(\alpha)\left(\frac{\sigma_x}{\sigma_y}-1\right)}{1+\frac{\sigma_x}{\sigma_y}-2\sin(\alpha)\cos(\alpha)\left(\frac{\sigma_x}{\sigma_y}-1\right)}\right]. \tag{A.20}$$

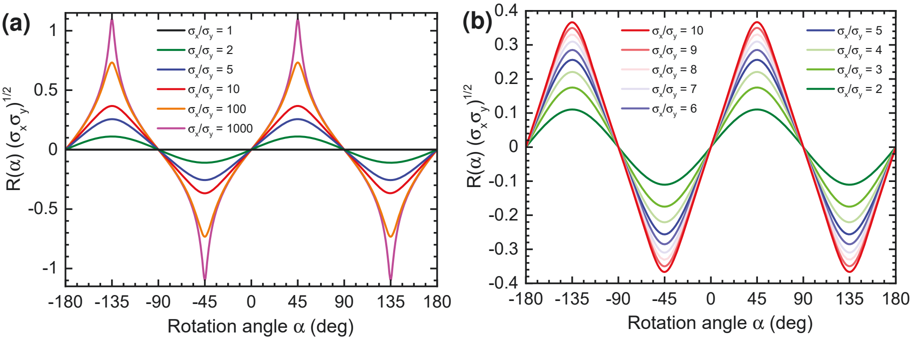

Figure A.3.: Normalized plots of the relation $R(\alpha)\sqrt{\sigma_x\sigma_y}$ for a rhombic tip configuration as function of the rotation angle α with the ratio σ_x/σ_y as additional parameter. (a) Overview for a large range of ratios σ_x/σ_y of of the π-periodic function. (b) For smaller ratios $\sigma_x/\sigma_y \leq 10$, the curve is similar to sine, but with half periodicity.

The expression only depends on the rotation α of the square and does not include any distance between the tips, i.e. the side length s, in the same way as it has been found also for the square configuration. In Fig. A.3, the angle dependence of the function is visualized by normalized plots of $R^{\text{2D}}_{\text{rhombic}}\sqrt{\sigma_x\sigma_y}$ with several different ratios $\frac{\sigma_x}{\sigma_y}$ as additional parameter. It is visible that the four-point resistance is π-periodic and point symmetric with respect to the origin. The latter is a direct consequence from the fact that already a rotation by $\frac{\pi}{2}$ basically corresponds to an exchange of the pairs of current and voltage tips (with additional exchange of the voltage polarity in order to get the minus sign), so that $|R(\alpha + \frac{\pi}{2})| = |R(\alpha)|$. This is in contrast to the square configuration, for which such an exchange is only achieved after an rotation of π. For smaller ratios $\frac{\sigma_x}{\sigma_y} < 5$ [Fig. A.3(b)], the shape of the function is similar to sine (but still with half periodicity) and also similar to the resistance of the square configuration (but shifted by $\frac{\pi}{4}$). The zero-crossings of the four-point resistance indicate the orientations of the principal axes of the anisotropic system, i.e. the directions of high (σ_x) and low (σ_y) conductivity. Thus, one advantage of the rhombic configuration is that these directions can be more precisely determined from the positions of the zero-crossings, than it is the case for the corresponding maxima in a square configuration.

A.1.3. *Van der Pauw* configuration for infinite 2D sheets

In the following, the modified *van der Pauw* equation [cf. Eq. (3.95)] will be derived for the case of an infinitely extended sheet which has an infinite number of mirror planes, thus an arbitrary placement of a linear tip setup is possible. For a general in-line tip arrangement with the spacings e, f, and g, as indicated in Fig. A.4 for the two electrical configurations (AB, CD) and (AC, DB), the position vectors of the tips can be expressed as (without

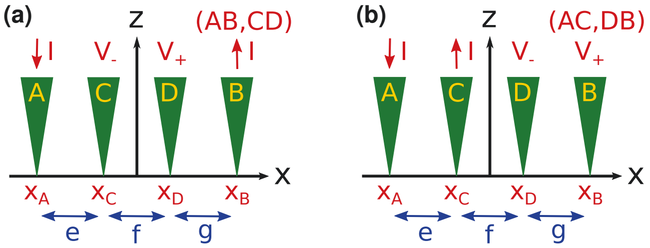

Figure A.4.: Arbitrarily spaced linear tip arrangement with spacings e, f and g as indicated for the electrical configuration (a) (AB, CD) and (b) (AC, DB).

loss of generality is $y_i = 0$)

$$\boldsymbol{x}_A = -\left(e + \frac{f}{2}\right)\hat{\boldsymbol{e}}_{\boldsymbol{x}}, \quad \boldsymbol{x}_B = \left(\frac{f}{2} + g\right)\hat{\boldsymbol{e}}_{\boldsymbol{x}}, \quad \boldsymbol{x}_C = -\frac{f}{2}\hat{\boldsymbol{e}}_{\boldsymbol{x}}, \quad \boldsymbol{x}_D = \frac{f}{2}\hat{\boldsymbol{e}}_{\boldsymbol{x}}. \tag{A.21}$$

If an infinitely extended 2D system is considered, these vectors can be inserted into Eq. (3.23). Thus, by exchanging the tip coordinates correspondingly, it follows for the four-point resistances of the two configurations (AB, CD) and (AC, DB) that

$$R^{\text{2D,lin}}_{AB,CD} = \frac{1}{4\pi\sigma_{\text{2D}}} \ln\left[\frac{g^2e^2}{(e+f)^2(f+g)^2}\right] = \frac{1}{2\pi\sigma_{\text{2D}}} \ln\left[\frac{eg}{(e+f)(f+g)}\right] \tag{A.22}$$

$$R^{\text{2D,lin}}_{AC,DB} = \frac{1}{4\pi\sigma_{\text{2D}}} \ln\left[\frac{(f+g)^2(e+f)^2}{(e+f+g)^2 f}\right] = \frac{1}{2\pi\sigma_{\text{2D}}} \ln\left[\frac{(f+g)(e+f)}{f(e+f+g)}\right], \tag{A.23}$$

respectively. It has to be ensured that both resistances in Eqs. (A.22) and (A.23) are positive, which is achieved by calculating the absolute values. For the logarithmic function $\ln(x)$ it applies that

$$\left|\ln(x)\right| = \begin{cases} \ln(x) & \text{if } x \geq 1 \\ \ln\left(\dfrac{1}{x}\right) & \text{if } x < 1. \end{cases} \tag{A.24}$$

Thus, it has to be checked first, if the arguments of the logarithms in Eqs. (A.22) and (A.23) are smaller or greater than one. So, it has to be verified or falsified that

$$\begin{aligned} &\overset{(A.22)}{\Rightarrow} \frac{eg}{(e+f)(f+g)} > 1 \Leftrightarrow eg > f^2 + fg + ef + eg \\ &\qquad \Leftrightarrow \quad 0 > f^2 + fg + ef \overset{e,f,g>0}{\Rightarrow} \text{not true} \Rightarrow R^{\text{2D,lin}}_{AB,CD} < 0 \end{aligned} \tag{A.25}$$

$$\begin{aligned} &\overset{(A.23)}{\Rightarrow} \frac{(f+g)(e+f)}{f(e+f+g)} > 1 \Leftrightarrow f^2 + fe + fg + eg > f^2 + fe + fg \\ &\qquad \Leftrightarrow \qquad eg > 0 \overset{e,g>0}{\Rightarrow} \text{true} \Rightarrow R^{\text{2D,lin}}_{AC,DB} > 0. \end{aligned} \tag{A.26}$$

Based on this information the absolute values of Eqs. (A.22) and (A.23) can be expressed as

$$\left|R_{AB,CD}^{\text{2D,lin}}\right| = \frac{1}{2\pi\sigma_{\text{2D}}}\left|\ln\left[\frac{eg}{(e+f)(f+g)}\right]\right| \overset{\substack{(A.24)\\(A.25)}}{=} \frac{1}{2\pi\sigma_{\text{2D}}}\ln\left[\frac{(e+f)(f+g)}{eg}\right] \tag{A.27}$$

$$\left|R_{AC,DB}^{\text{2D,lin}}\right| = \frac{1}{2\pi\sigma_{\text{2D}}}\left|\ln\left[\frac{(f+g)(e+f)}{f(e+f+g)}\right]\right| \overset{\substack{(A.24)\\(A.26)}}{=} \frac{1}{2\pi\sigma_{\text{2D}}}\ln\left[\frac{(f+g)(e+f)}{f(e+f+g)}\right], \tag{A.28}$$

respectively. Eqs. (A.27) and (A.28) can be rearranged, so that

$$\overset{(A.27)}{\Rightarrow} \quad -2\pi\sigma_{\text{2D}}\left|R_{AB,CD}^{\text{2D,lin}}\right| = -\ln\left[\frac{(e+f)(f+g)}{eg}\right] = \ln\left[\frac{eg}{(e+f)(f+g)}\right] \tag{A.29}$$

$$\Leftrightarrow \quad e^{-2\pi\sigma_{\text{2D}}\left|R_{AB,CD}^{\text{2D,lin}}\right|} = \frac{eg}{(e+f)(f+g)} \tag{A.30}$$

$$\overset{(A.28)}{\Rightarrow} \quad -2\pi\sigma_{\text{2D}}\left|R_{AC,DB}^{\text{2D,lin}}\right| = -\ln\left[\frac{(f+g)(e+f)}{f(e+f+g)}\right] = \ln\left[\frac{f(e+f+g)}{(f+g)(e+f)}\right] \tag{A.31}$$

$$\Leftrightarrow \quad e^{-2\pi\sigma_{\text{2D}}\left|R_{AC,DB}^{\text{2D,lin}}\right|} = \frac{f(e+f+g)}{(f+g)(e+f)}. \tag{A.32}$$

By adding Eqs. (A.30) and (A.32), it finally follows the equation

$$e^{-2\pi\sigma_{\text{2D}}\left|R_{AB,CD}^{\text{2D,lin}}\right|} + e^{-2\pi\sigma_{\text{2D}}\left|R_{AC,DB}^{\text{2D,lin}}\right|} = \underbrace{\frac{eg}{(e+f)(f+g)} + \frac{f(e+f+g)}{(f+g)(e+f)}}_{=\frac{eg+fe+f^2+fg}{eg+fe+f^2+fg}} \tag{A.33}$$

$$\Leftrightarrow \quad e^{-2\pi\sigma_{\text{2D}}\left|R_{AB,CD}^{\text{2D,lin}}\right|} + e^{-2\pi\sigma_{\text{2D}}\left|R_{AC,DB}^{\text{2D,lin}}\right|} = 1 \tag{A.34}$$

which represents the modified *van der Pauw* equation.

A.2. Supplements for $\mathbf{3}$-layer model

A.2.1. Hankel transformation

The *Hankel* transform of a function $f(t)$ is generally defined as [192, 193]

$$F_\nu(u) = \int_0^\infty dt\, f(t) t J_\nu(ut) \tag{A.35}$$

with J_ν denoting the *Bessel* function of the first kind. The inverse transformation, i.e. for retrieving $f(t)$ back, is given again by the *Hankel* transform of $F_\nu(u)$. If the definition in Eq. (A.35) is compared to Eq. (4.6a) which is considered as example in the following, then it is obvious that the left side of the equation already is the *Hankel* transform of the coefficients $a(k)-b(k)$. Thus, for separating the coefficients it is sufficient to apply another *Hankel* transformation. By extending both sides with $\rho J_0(k'\rho)$ and integrating over $\int_0^\infty d\rho$, it results that

$$\rho J_0(k'\rho)\int_0^\infty dk\,\sigma_1\left[a(k)-b(k)\right]kJ_0(k\rho) = -j_1 H(r_t-\rho)\rho J_0(k'\rho) \tag{A.36}$$

$$\Leftrightarrow \sigma_1\int_0^\infty d\rho\,\rho J_0(k'\rho)\int_0^\infty dk\left[a(k)-b(k)\right]kJ_0(k\rho) = -j_1\int_0^\infty d\rho\,H(r_t-\rho)\rho J_0(k'\rho) \tag{A.37}$$

$$\Leftrightarrow \sigma_1\int_0^\infty dk\left[a(k)-b(k)\right]k\underbrace{\int_0^\infty d\rho\,\rho J_0(k'\rho)J_0(k\rho)}_{=\frac{1}{k}\delta(k-k')} = -j_1\int_0^\infty d\rho\,H(r_t-\rho)\rho J_0(k'\rho) \tag{A.38}$$

$$\Leftrightarrow \qquad \sigma_1\int_0^\infty dk\left[a(k)-b(k)\right]\delta(k-k') = -j_1\int_0^\infty d\rho\,H(r_t-\rho)\rho J_0(k'\rho) \tag{A.39}$$

$$\Leftrightarrow \qquad \sigma_1\left[a(k')-b(k')\right] = -j_1\int_0^{r_t} d\rho\,\rho J_0(k'\rho) \tag{A.40}$$

$$\overset{k'\to k}{\Leftrightarrow} \qquad \sigma_1\left[a(k)-b(k)\right] = -j_1\int_0^{r_t} d\rho\,\rho J_0(k\rho). \tag{A.41}$$

Hereby, in Eq. (A.39) the orthogonality of the *Bessel* functions is applied, while in Eq. (A.40) the special properties of the *Delta* distribution and the *Heaviside* step function are used. In the same way, the transformation can be applied to the other Eqs. (4.6b) – (4.6e) in order to retrieve the coefficient functions.

A.2.2. Coefficients $a(k)+b(k)$

In the following, it will be shown that from Eq. (4.8) a solution for the coefficients $a(k)+b(k)$ according to Eq. (4.11) can be derived. In order to make the displayed equations clearer, the abbreviations $\sigma_{21}=\frac{\sigma_2}{\sigma_1}$ and $\sigma_{32}=\frac{\sigma_3}{\sigma_2}$ are introduced. Thus, Eq. (4.8) reads as

$$\begin{pmatrix} 1 & -1 & 0 & 0 & 0 \\ e^{kz_1} & -e^{-kz_1} & -\sigma_{21}e^{kz_1} & \sigma_{21}e^{-kz_1} & 0 \\ e^{kz_1} & e^{-kz_1} & -e^{kz_1} & -e^{-kz_1} & 0 \\ 0 & 0 & e^{kz_2} & -e^{-kz_2} & \sigma_{32}e^{-kz_2} \\ 0 & 0 & e^{kz_2} & e^{-kz_2} & -e^{-kz_2} \end{pmatrix} \cdot \begin{pmatrix} a(k) \\ b(k) \\ c(k) \\ d(k) \\ f(k) \end{pmatrix} = \begin{pmatrix} I(k,\sigma_1) \\ 0 \\ 0 \\ 0 \\ 0 \end{pmatrix}. \tag{A.42}$$

Division of the rows by common factors leads to

$$\underbrace{\begin{pmatrix} 1 & -1 & 0 & 0 & 0 \\ 1 & -e^{-2kz_1} & -\sigma_{21} & \sigma_{21}e^{-2kz_1} & 0 \\ 1 & e^{-2kz_1} & -1 & -e^{-2kz_1} & 0 \\ 0 & 0 & 1 & -e^{-2kz_2} & \sigma_{32}e^{-2kz_2} \\ 0 & 0 & 1 & e^{-2kz_2} & -e^{-2kz_2} \end{pmatrix}}_{:=\boldsymbol{A}} \cdot \underbrace{\begin{pmatrix} a(k) \\ b(k) \\ c(k) \\ d(k) \\ f(k) \end{pmatrix}}_{:=\boldsymbol{x}} = \underbrace{\begin{pmatrix} I(k,\sigma_1) \\ 0 \\ 0 \\ 0 \\ 0 \end{pmatrix}}_{:=\boldsymbol{b}}. \tag{A.43}$$

Eq. (A.43) has the form $\boldsymbol{Ax} = \boldsymbol{b}$, so that it can be solved in general by means of matrix inversion, since $\boldsymbol{x} = \boldsymbol{A}^{-1}\boldsymbol{b}$. However, as only the coefficients $a(k)$ and $b(k)$ need to be determined and the matrix exhibits several empty entries, a suitable alternative is to use *Cramer*'s rule. According to this rule the solution for the components x_i of the vector $\boldsymbol{x}$ is given by $x_i = \frac{\det(\boldsymbol{A_i})}{\det(\boldsymbol{A})}$ with the modified matrix $\boldsymbol{A_i}$ in which the i-th column is replaced by the vector $\boldsymbol{b}$, and the determinant $\det(\boldsymbol{A})$ of the matrix $\boldsymbol{A}$ [194, 195]. Thus, it can be written that

$$a(k) + b(k) = \frac{\det(\boldsymbol{A_0}) + \det(\boldsymbol{A_1})}{\det(\boldsymbol{A})}. \tag{A.44}$$

For simplifying the calculation of the determinants, the matrices have first to be rearranged by *Gaussian* elimination. Specifically, for determinants the following rules apply: (1) exchanging two rows or columns leads from $\det(\boldsymbol{A})$ to $-\det(\boldsymbol{A})$, (2) adding a multiple of a row or column to another leaves $\det(\boldsymbol{A})$ unchanged, and (3) dividing a column or row by a factor c results in $c\det(\boldsymbol{A})$. In general, determinants are not additive, i.e. $\det(\boldsymbol{A}) + \det(\boldsymbol{B}) \neq \det(\boldsymbol{A} + \boldsymbol{B})$, but if two matrices $\tilde{\boldsymbol{A}}$ and $\tilde{\boldsymbol{B}}$ (both with entries c_{ij}) differ only by the k-th column (with entries a_{ik} and b_{ik}, respectively), it is in component notation $\det(\tilde{\boldsymbol{A}}) + \det(\tilde{\boldsymbol{B}}) = \sum_{i_1,\ldots,i_n} \varepsilon_{i_1\ldots i_n} c_{i1} \cdots (a_{i_k k} + b_{i_k k}) \cdots c_{i_n n}$[1] (used in Eq. (A.48)). Also the Laplace expansion (LE) can be applied which expresses the determinant of a matrix in weighted terms of the determinants of sub-matrices with reduced size [196].

First, the numerator of Eq. A.44 is considered. With the notation $\det(\boldsymbol{A}) = |\boldsymbol{A}|$ it follows that

$$\Rightarrow \ \det(\boldsymbol{A_0}) + \det(\boldsymbol{A_1}) \tag{A.45}$$

$$= \begin{array}{c} \times\frac{1}{\underline{I(k,\sigma_1)}} \\ \left|\begin{array}{ccccc} I(k,\sigma_1) & -1 & 0 & 0 & 0 \\ 0 & -e^{-2kz_1} & -\sigma_{21} & \sigma_{21}e^{-2kz_1} & 0 \\ 0 & e^{-2kz_1} & -1 & -e^{-2kz_1} & 0 \\ 0 & 0 & 1 & -e^{-2kz_2} & \sigma_{32}e^{-2kz_2} \\ 0 & 0 & 1 & e^{-2kz_2} & -e^{-2kz_2} \end{array}\right| \end{array} + \begin{array}{c} \overbrace{\downarrow \qquad \downarrow}\ \times\frac{1}{\underline{I(k,\sigma_1)}} \\ \left|\begin{array}{ccccc} 1 & I(k,\sigma_1) & 0 & 0 & 0 \\ 1 & 0 & -\sigma_{21} & \sigma_{21}e^{-2kz_1} & 0 \\ 1 & 0 & -1 & -e^{-2kz_1} & 0 \\ 0 & 0 & 1 & -e^{-2kz_2} & \sigma_{32}e^{-2kz_2} \\ 0 & 0 & 1 & e^{-2kz_2} & -e^{-2kz_2} \end{array}\right| \end{array} \tag{A.46}$$

$$= I(k,\sigma_1) \left|\begin{array}{ccccc} 1 & -1 & 0 & 0 & 0 \\ 0 & -e^{-2kz_1} & -\sigma_{21} & \sigma_{21}e^{-2kz_1} & 0 \\ 0 & e^{-2kz_1} & -1 & -e^{-2kz_1} & 0 \\ 0 & 0 & 1 & -e^{-2kz_2} & \sigma_{32}e^{-2kz_2} \\ 0 & 0 & 1 & e^{-2kz_2} & -e^{-2kz_2} \end{array}\right| - \left|\begin{array}{ccccc} 1 & 1 & 0 & 0 & 0 \\ 0 & 1 & -\sigma_{21} & \sigma_{21}e^{-2kz_1} & 0 \\ 0 & 1 & -1 & -e^{-2kz_1} & 0 \\ 0 & 0 & 1 & -e^{-2kz_2} & \sigma_{32}e^{-2kz_2} \\ 0 & 0 & 1 & e^{-2kz_2} & -e^{-2kz_2} \end{array}\right| \tag{A.47}$$

---

[1] $\varepsilon_{i_1\ldots i_n}$ denotes the *Levi-Civita* symbol of n-th dimension

$$= I(k,\sigma_1)\begin{vmatrix} \overset{\underline{\text{LE}}}{1} & -2 & 0 & 0 & 0 \\ 0 & -e^{-2kz_1}-1 & -\sigma_{21} & \sigma_{21}e^{-2kz_1} & 0 \\ 0 & e^{-2kz_1}-1 & -1 & -e^{-2kz_1} & 0 \\ 0 & 0 & 1 & -e^{-2kz_2} & \sigma_{32}e^{-2kz_2} \\ 0 & 0 & 1 & e^{-2kz_2} & -e^{-2kz_2} \end{vmatrix} \tag{A.48}$$

$$= I(k,\sigma_1)\begin{vmatrix} \overset{\underline{\text{LE}}}{-e^{-2kz_1}-1} & -\sigma_{21} & \overset{\underline{\times\, e^{2kz_1}}}{\sigma_{21}e^{-2kz_1}} & \overset{\underline{\times\, e^{2kz_2}}}{0} \\ e^{-2kz_1}-1 & -1 & -e^{-2kz_1} & 0 \\ 0 & 1 & -e^{-2kz_2} & \sigma_{32}e^{-2kz_2} \\ 0 & 1 & e^{-2kz_2} & -e^{-2kz_2} \end{vmatrix} \tag{A.49}$$

$$\begin{aligned} &= I(k,\sigma_1)e^{-2kz_1}e^{-2kz_2}\left[\left[-e^{-2kz_1}-1\right]\begin{vmatrix} -1 & -1 & 0 \\ 1 & -e^{-2k(z_2-z_1)} & \sigma_{32} \\ 1 & e^{-2k(z_2-z_1)} & -1 \end{vmatrix}^{|\,\text{LE}}\right. \\ &\qquad\qquad\left. -\left[e^{-2kz_1}-1\right]\begin{vmatrix} -\sigma_{21} & \sigma_{21} & 0 \\ 1 & -e^{-2k(z_2-z_1)} & \sigma_{32} \\ 1 & e^{-2k(z_2-z_1)} & -1 \end{vmatrix}^{|\,\text{LE}}\right] \end{aligned} \tag{A.50}$$

$$\begin{aligned} &= I(k,\sigma_1)e^{-2k(z_2+z_1)}\left[-\left[e^{-2kz_1}+1\right]\left(-\underbrace{\begin{vmatrix} -e^{-2k(z_2-z_1)} & \sigma_{32} \\ e^{-2k(z_2-z_1)} & -1 \end{vmatrix}}_{=e^{-2k(z_2-z_1)}(1-\sigma_{32})}+\underbrace{\begin{vmatrix} 1 & \sigma_{32} \\ 1 & -1 \end{vmatrix}}_{=-1-\sigma_{32}}\right)\right. \\ &\qquad\qquad\left. -\left[e^{-2kz_1}-1\right]\left(-\sigma_{21}\underbrace{\begin{vmatrix} -e^{-2k(z_2-z_1)} & \sigma_{32} \\ e^{-2k(z_2-z_1)} & -1 \end{vmatrix}}_{=e^{-2k(z_2-z_1)}(1-\sigma_{32})}-\sigma_{21}\underbrace{\begin{vmatrix} 1 & \sigma_{32} \\ 1 & -1 \end{vmatrix}}_{=-1-\sigma_{32}}\right)\right] \end{aligned} \tag{A.51}$$

$$\begin{aligned} &= I(k,\sigma_1)e^{-2k(z_2+z_1)}\Big[\left[e^{-2kz_1}+1\right]\left(e^{-2k(z_2-z_1)}-\sigma_{32}e^{-2k(z_2-z_1)}+1+\sigma_{32}\right) \\ &\qquad\qquad +\sigma_{21}\left[e^{-2kz_1}-1\right]\left(e^{-2k(z_2-z_1)}-\sigma_{32}e^{-2k(z_2-z_1)}-1-\sigma_{32}\right)\Big] \end{aligned} \tag{A.52}$$

$$\begin{aligned} &= I(k,\sigma_1)e^{-2k(z_2+z_1)}\Big[\left[e^{-2kz_1}+1\right]\left(e^{-2k(z_2-z_1)}+1-\sigma_{32}\left[e^{-2k(z_2-z_1)}-1\right]\right) \\ &\qquad\qquad +\sigma_{21}\left[e^{-2kz_1}-1\right]\left(e^{-2k(z_2-z_1)}-1-\sigma_{32}\left[e^{-2k(z_2-z_1)}+1\right]\right)\Big] \end{aligned} \tag{A.53}$$

In the same way, the denominator of Eq. (A.44) can be calculated as

$$\Rightarrow\ \det(\boldsymbol{A}) = \begin{array}{|ccccc|} \ulcorner & \overset{+}{\downarrow} & \overset{\times\, e^{-2kz_1}}{\ulcorner} & \overset{+}{\downarrow} & \\ 1 & -1 & 0 & 0 & 0 \\ 1 & -e^{-2kz_1} & -\sigma_{21} & \sigma_{21}e^{-2kz_1} & 0 \\ 1 & e^{-2kz_1} & -1 & -e^{-2kz_1} & 0 \\ 0 & 0 & 1 & -e^{-2kz_2} & \sigma_{32}e^{-2kz_2} \\ 0 & 0 & 1 & e^{-2kz_2} & -e^{-2kz_2} \end{array} \tag{A.54}$$

$$= \begin{vmatrix} 1 & 0 & 0 & 0 & 0 \\ 1 & 1-e^{-2kz_1} & -\sigma_{21} & 0 & 0 \\ 1 & 1+e^{-2kz_1} & -1 & -2e^{-2kz_1} & 0 \\ 0 & 0 & 1 & -e^{-2kz_2}+e^{-2kz_1} & \sigma_{32}e^{-2kz_2} \\ 0 & 0 & 1 & e^{-2kz_2}+e^{-2kz_1} & -e^{-2kz_2} \end{vmatrix}\Bigg|_{\mathrm{LE}} \tag{A.55}$$

$$= \begin{vmatrix} & & & \underline{\times\, e^{2kz_2}} \\ 1-e^{-2kz_1} & -\sigma_{21} & 0 & 0 \\ 1+e^{-2kz_1} & -1 & -2e^{-2kz_1} & 0 \\ 0 & 1 & -e^{-2kz_2}+e{-}2kz_1 & \sigma_{32}e^{-2kz_2} \\ 0 & 1 & e^{-2kz_2}+e^{-2kz_1} & -e^{-2kz_2} \end{vmatrix}\Bigg|_{\mathrm{LE}} \tag{A.56}$$

$$= e^{-2kz_2}\left[\left[1-e^{-2kz_1}\right]\begin{vmatrix} -1 & -2e^{-2kz_1} & 0 \\ 1 & -e^{-2kz_2}+e^{-2kz_1} & \sigma_{32} \\ 1 & e^{-2kz_2}+e^{-2kz_1} & -1 \end{vmatrix}\Bigg|_{\mathrm{LE}} +\sigma_{21}\begin{vmatrix} \overset{\mathrm{LE}}{\overline{1+e^{-2kz_1}}} & -2e^{-2kz_1} & 0 \\ 0 & -e^{-2kz_2}+e^{-2kz_1} & \sigma_{32} \\ 0 & e^{-2kz_2}+e^{-2kz_1} & -1 \end{vmatrix}\right] \tag{A.57}$$

$$\begin{aligned} = e^{-2kz_2}\Bigg[&\left[1-e^{-2kz_1}\right]\Bigg(-\underbrace{\begin{vmatrix} -e^{-2kz_2}+e^{-2kz_1} & \sigma_{32} \\ e^{-2kz_2}+e^{-2kz_1} & -1 \end{vmatrix}}_{=e^{-2kz_2}-e^{-2kz_1}-\sigma_{32}(e^{-2kz_2}+e^{-2kz_1})} +2e^{-2kz_1}\underbrace{\begin{vmatrix} 1 & \sigma_{32} \\ 1 & -1 \end{vmatrix}}_{=-1-\sigma_{32}}\Bigg) \\ &+\sigma_{21}\left[1+e^{-2kz_1}\right]\underbrace{\begin{vmatrix} -e^{-2kz_2}+e^{-2kz_1} & \sigma_{32} \\ e^{-2kz_2}+e^{-2kz_1} & -1 \end{vmatrix}}_{=e^{-2kz_2}-e^{-2kz_1}-\sigma_{32}(e^{-2kz_2}+e^{-2kz_1})}\Bigg] \end{aligned} \tag{A.58}$$

$$\begin{aligned} = e^{-2kz_2}\Big[&\left[1-e^{-2kz_1}\right]\left(-e^{-2kz_2}+e^{-2kz_1}+\sigma_{32}e^{-2kz_2}+\sigma_{32}e^{-2kz_1}-2e^{-2kz_1}-2\sigma_{32}e^{-2kz_1}\right) \\ &+\sigma_{21}\left[1+e^{-2kz_1}\right]\left(e^{-2kz_2}-e^{-2kz_1}-\sigma_{32}e^{-2kz_2}-\sigma_{32}e^{-2kz_1}\right)\Big] \end{aligned} \tag{A.59}$$

$$
\begin{aligned}
&= e^{-2k(z_2+z_1)}\Big[\big[1-e^{-2kz_1}\big]\big(-e^{-2k(z_2-z_1)}-1+\sigma_{32}e^{-2k(z_2-z_1)}-\sigma_{32}\big)\\
&\qquad\qquad +\sigma_{21}\left[1+e^{-2kz_1}\right]\left(e^{-2k(z_2-z_1)}-1-\sigma_{32}e^{-2k(z_2-z_1)}-\sigma_{32}\right)\Big] \qquad \text{(A.60)}
\end{aligned}
$$

$$
\begin{aligned}
&= e^{-2k(z_2+z_1)}\Big[\big[e^{-2kz_1}-1\big]\big(e^{-2k(z_2-z_1)}+1-\sigma_{32}\left[e^{-2k(z_2-z_1)}-1\right]\big)\\
&\qquad\qquad +\sigma_{21}\left[e^{-2kz_1}+1\right]\left(e^{-2k(z_2-z_1)}-1-\sigma_{32}\left[e^{-2k(z_2-z_1)}+1\right]\right)\Big]. \qquad \text{(A.61)}
\end{aligned}
$$

The results from Eqs. (A.53) and (A.61) have to be inserted into Eq. (A.44). In order to simplify the fraction, the exponential functions can be expressed in terms of hyperbolic tangent which is defined as $\tanh(x)=\frac{e^x-e^{-x}}{e^x+e^{-x}}=\frac{e^{2x}-1}{e^{2x}+1}$. Thus, by factorisation of the terms inside the square brackets it results that

$$
a(k)+b(k)=\frac{\det(\boldsymbol{A_0})+\det(\boldsymbol{A_1})}{\det(\boldsymbol{A})} \qquad \text{(A.62)}
$$

$$
\overset{\substack{(A.53)\\(A.61)}}{=} I(k,\sigma_1)\,\frac{\begin{aligned}&\left(e^{-2k(z_2-z_1)}+1-\sigma_{32}\left[e^{-2k(z_2-z_1)}-1\right]\right)\\ &\qquad+\sigma_{21}\tfrac{e^{-2kz_1}-1}{e^{-2kz_1}+1}\left(e^{-2k(z_2-z_1)}-1-\sigma_{32}\left[e^{-2k(z_2-z_1)}+1\right]\right)\end{aligned}}{\begin{aligned}&\tfrac{e^{-2kz_1}-1}{e^{-2kz_1}+1}\left(e^{-2k(z_2-z_1)}+1-\sigma_{32}\left[e^{-2k(z_2-z_1)}-1\right]\right)\\ &\qquad+\sigma_{21}\left(e^{-2k(z_2-z_1)}-1-\sigma_{32}\left[e^{-2k(z_2-z_1)}+1\right]\right)\end{aligned}} \qquad \text{(A.63)}
$$

$$
= I(k,\sigma_1)\,\frac{\left(1-\sigma_{32}\frac{e^{-2k(z_2-z_1)}-1}{e^{-2k(z_2-z_1)}+1}\right)+\sigma_{21}\tanh(-kz_1)\left(\frac{e^{-2k(z_2-z_1)}-1}{e^{-2k(z_2-z_1)}+1}-\sigma_{32}\right)}{\tanh(-kz_1)\left(1-\sigma_{32}\frac{e^{-2k(z_2-z_1)}-1}{e^{-2k(z_2-z_1)}+1}\right)+\sigma_{21}\left(\frac{e^{-2k(z_2-z_1)}-1}{e^{-2k(z_2-z_1)}+1}-\sigma_{32}\right)} \qquad \text{(A.64)}
$$

$$
= I(k,\sigma_1)\,\frac{\begin{aligned}&\big(1-\sigma_{32}\tanh(-k[z_2-z_1])\big)\\ &\qquad+\sigma_{21}\tanh(-kz_1)\big(\tanh(-k[z_2-z_1])-\sigma_{32}\big)\end{aligned}}{\begin{aligned}&\tanh(-kz_1)\big(1-\sigma_{32}\tanh(-k[z_2-z_1])\big)\\ &\qquad+\sigma_{21}\big(\tanh(-k[z_2-z_1])-\sigma_{32}\big)\end{aligned}} \qquad \text{(A.65)}
$$

$$
\overset{\substack{\tanh[x]=\\-\tanh[-x]}}{=} I(k,\sigma_1)\,\frac{\begin{aligned}&\big(1+\sigma_{32}\tanh(k[z_2-z_1])\big)\\ &\qquad+\sigma_{21}\tanh(kz_1)\big(\tanh(k[z_2-z_1])+\sigma_{32}\big)\end{aligned}}{\begin{aligned}&-\tanh(kz_1)\big(1+\sigma_{32}\tanh(k[z_2-z_1])\big)\\ &\qquad-\sigma_{21}\big(\tanh(k[z_2-z_1])+\sigma_{32}\big)\end{aligned}} \qquad \text{(A.66)}
$$

$$
= -I(k,\sigma_1)\,\frac{\dfrac{1+\sigma_{32}\tanh(k[z_2-z_1])}{\tanh(k[z_2-z_1])+\sigma_{32}}+\sigma_{21}\tanh(kz_1)}{\tanh(kz_1)\dfrac{1+\sigma_{32}\tanh(k[z_2-z_1])}{\tanh(k[z_2-z_1])+\sigma_{32}}+\sigma_{21}}. \qquad \text{(A.67)}
$$

With the expression for $I(k,\sigma_1)$ given in Eq. (4.9) and the definitions for σ_{21} and σ_{32} introduced before, the result in Eq. (A.67) is equal to Eq. (4.11). In principle, the inverse of the matrix in Eq. (A.43) can also be determined numerically in order to obtain the coefficients

$a(k)+b(k)$. However, with the analytical solution from Eq. (A.67) the computational costs for calculating the *Bessel* integrals in Eq. (4.16) are much less, since the matrix inversion has not to be performed for every single value of k. Specifically, this can be of advantage, when the model is fitted to a large amount of measurement data.

A.2.3. Current density and total current

In general, the current density $\boldsymbol{j}$ inside a material is given by the conductivity σ and the gradient of the potential Φ, i.e. $\boldsymbol{j} = -\sigma\nabla\Phi$. Thus, in the framework of the 3-layer model it can be calculated by using the potential from Eq. (4.3) which reads in Cartesian coordinates

$$\Phi(\boldsymbol{x}) = \begin{cases} \Phi_1(x,y,z) = \displaystyle\int_0^\infty dk\, \underbrace{\left[a(k)e^{kz}+b(k)e^{-kz}\right]}_{:=\Phi_1(k,z)} J_0\left(k\sqrt{x^2+y^2}\right) & \text{for } 0 \le z \le z_1 \\ \Phi_2(x,y,z) = \displaystyle\int_0^\infty dk\, \underbrace{\left[c(k)e^{kz}+d(k)e^{-kz}\right]}_{:=\Phi_2(k,z)} J_0\left(k\sqrt{x^2+y^2}\right) & \text{for } z_1 \le z \le z_2 \\ \Phi_3(x,y,z) = \displaystyle\int_0^\infty dk\, \underbrace{f(k)e^{-kz}}_{:=\Phi_3(k,z)} J_0\left(k\sqrt{x^2+y^2}\right) & \text{for } z_2 \le z \le \infty, \end{cases} \tag{A.68}$$

and the layer-dependent conductivity

$$\sigma(z) = \begin{cases} \sigma_1 & \text{for } 0 \le z \le z_1 \\ \sigma_2 & \text{for } z_1 \le z \le z_2 \\ \sigma_3 & \text{for } z_2 \le z \le \infty. \end{cases} \tag{A.69}$$

As a result, the current density vector $\boldsymbol{j}(\boldsymbol{x})$ is besides the position-dependence also dependent on the parameters of the layers, i.e. σ_i and z_i. In the following, only the in-line component of the current density between two tips will be considered, since this component is relevant for lateral current transport and, e.g. is sufficient for visualizing the depth-dependence or calculating the total amount of current through one specific layer. The in-line direction of the two tips is assumed to be aligned along the x-axis (without loss of generality). If the variables inside the expression for the potential are separated for each case by introducing

$$\Phi(k,z) = \begin{cases} \Phi_1(k,z) & \text{for } 0 \le z \le z_1 \\ \Phi_2(k,z) & \text{for } z_1 \le z \le z_2 \\ \Phi_3(k,z) & \text{for } z_2 \le z \le \infty, \end{cases} \tag{A.70}$$

as indicated in Eq. (A.68), it follows for the current density component $\tilde{j}_x$ (at first arising only from one source at the origin) that

$$\tilde{j}_x(x,y,z) = -\sigma(z)\partial_x\Phi(x,y,z) \tag{A.71}$$

$$= -\sigma(z) \int_0^\infty dk\, \Phi(k,z)\, \partial_x J_0 \left(k\sqrt{x^2+y^2}\right) \tag{A.72}$$

For the derivative of *Bessel* functions it holds that $\frac{d}{dx} J_\alpha(x) = \frac{1}{2}\left[J_{\alpha-1}(x) - J_{\alpha+1}(x)\right]$. Furthermore, it is $J_{-\alpha}(x) = (-1)^\alpha J_\alpha(x) = J_\alpha(-x)$, so that $\frac{d}{dx} J_0(x) = -J_1(x)$. Thus, it follows that

$$\tilde{j}_x(x,y,z) = \sigma(z) \int_0^\infty dk\, \Phi(k,z) \frac{kx}{\sqrt{x^2+y^2}}\, J_1\left(k\sqrt{x^2+y^2}\right). \tag{A.73}$$

The same holds for a current sink, except that the sign is inverted due to the negative potential. If now two tips are considered which are positioned along the x-axis at x_A (source) and x_B (sink), respectively, it immediately results for the total component j_x by superposition (in the same way as it holds for the superimposed potential in Eq. (4.13)) that

$$j_x(x,y,z) = \tilde{j}_x(x-x_A,y,z) - \tilde{j}_x(x-x_B,y,z) \tag{A.74}$$

$$= \sigma(z) \int_0^\infty dk\, \Phi(k,z) \left[\frac{k(x-x_A)}{\sqrt{(x-x_A)^2+y^2}}\, J_1\left(k\sqrt{(x-x_A)^2+y^2}\right) - \frac{k(x-x_B)}{\sqrt{(x-x_B)^2+y^2}}\, J_1\left(k\sqrt{(x-x_B)^2+y^2}\right)\right]. \tag{A.75}$$

For an appropriately chosen coordinate system with the origin exactly in the center between the two tips which are assumed to be spaced by $|x_A - x_B| = 3s$,[2] Eq. (A.75) changes to

$$j_x(x,y,z) = \sigma(z) \int_0^\infty dk\, \Phi(k,z) \left[\frac{k\left(x+\frac{3}{2}s\right)}{\sqrt{\left(x+\frac{3}{2}s\right)^2+y^2}}\, J_1\left(k\sqrt{\left(x+\frac{3}{2}s\right)^2+y^2}\right) - \frac{k\left(x-\frac{3}{2}s\right)}{\sqrt{\left(x-\frac{3}{2}s\right)^2+y^2}}\, J_1\left(k\sqrt{\left(x-\frac{3}{2}s\right)^2+y^2}\right)\right]. \tag{A.76}$$

By integration over the yz-plane the total lateral current $I_x(x)$ in x-direction can be obtained. If the integration is performed only for one specific layer, i.e. in z-direction from z_{i-1} to z_i, then the total current $I_x^i(x)$ inside the i-th layer can be calculated (with this notation it is assumed that $z_0 = 0$ and $z_3 \to \infty$). If one starts again with one tip first, it is

$$\tilde{I}_x^i(x) = \int_{z_{i-1}}^{z_i} dz \int_{-\infty}^\infty dy\, \tilde{j}_x(x,y,z) \tag{A.77}$$

$$\overset{(A.73)}{=} \int_0^\infty dk \underbrace{\int_{z_{i-1}}^{z_i} dz\, \sigma(z)\Phi(k,z)}_{:=Z_i(k)} \underbrace{\int_{-\infty}^\infty dy\, \frac{kx}{\sqrt{x^2+y^2}}\, J_1\left(k\sqrt{x^2+y^2}\right)}_{:=Y(k,x)} \tag{A.78}$$

---

[2] With such a distance, the result is comparable to an equidistant four-point probe setup with spacing s.

While the integral $Z_i(k)$ is trivial, the integral $Y(k,x)$ can be solved by means of variable substitution with

$$\begin{aligned} a(y) &= \frac{\sqrt{x^2+y^2}}{x} & \quad\text{and}\quad && \frac{da}{dy} &= \frac{y}{x\sqrt{x^2+y^2}} = \frac{\sqrt{a^2-1}}{xa} \\ \Leftrightarrow\ y &= x\sqrt{a^2-1} & && \Leftrightarrow\ dy &= \frac{xa}{\sqrt{a^2-1}}\, da \end{aligned} \tag{A.79}$$

Thus, it follows that

$$Y(k,x) = 2\int_0^\infty dy\, \frac{kx}{\sqrt{x^2+y^2}}\, J_1\Big(k\sqrt{x^2+y^2}\Big) \tag{A.80}$$

$$= 2\int_{a(0)}^{a(\infty)} da\, \frac{xa}{\sqrt{a^2-1}}\frac{k}{a}\, J_1\left(kxa\right) \tag{A.81}$$

$$= 2kx \underbrace{\int_1^\infty da\, \frac{J_1\left(kxa\right)}{\sqrt{a^2-1}}}_{\overset{[197]}{=} -\frac{\pi}{2} \underbrace{J_{\frac{1}{2}}\left(\frac{1}{2}kx\right)}_{\overset{[197]}{=} \sqrt{\frac{4}{\pi kx}}\sin\left(\frac{kx}{2}\right)} \underbrace{N_{\frac{1}{2}}\left(\frac{1}{2}kx\right)}_{\overset{[197]}{=} -\sqrt{\frac{4}{\pi kx}}\cos\left(\frac{kx}{2}\right)}} \tag{A.82}$$

$$= 4\underbrace{\sin\left(\frac{kx}{2}\right)\cos\left(\frac{kx}{2}\right)}_{=\frac{1}{2}\sin(kx)} \tag{A.83}$$

$$= 2\sin(kx). \tag{A.84}$$

If both coefficients in Eq. (A.68) for each layer i are relabelled as $a_i(k)$ and $b_i(k)$ (with $a_3 = 0$), respectively, a general expression for the integral $Z_i(k)$ can be given as

$$Z_i(k) = \sigma_i \int_{z_{i-1}}^{z_i} dz\, \left[a_i(k)e^{kz} + b_i(k)e^{-kz}\right] \tag{A.85}$$

$$= \frac{\sigma_i}{k}\Big[a_i(k)e^{kz} - b_i(k)e^{-ikz}\Big]_{z_{i-1}}^{z_i} \tag{A.86}$$

$$= \frac{\sigma_i}{k}\Big[a_i(k)\left(e^{kz_i} - e^{kz_{i-1}}\right) - b_i(k)\left(e^{-kz_i} - e^{-kz_{i-1}}\right)\Big] \quad \text{with } i = 1,2,3. \tag{A.87}$$

Hence, the total current arising from a source at x_A and a sink at x_B is given by a superposition as

$$I_x^i(x) = \tilde{I}_x^i(x-x_A) - \tilde{I}_x^i(x-x_B) = 2\int_0^\infty dk\, Z_i(k)\Big[\sin(k[x-x_A]) - \sin(k[(x-x_B]))\Big]. \tag{A.88}$$

With a symmetric tip arrangement and a spacing $|x_A - x_B| = 3s$, it follows that

$$I_x^i(x) = 2\int_0^\infty dk\, Z_i(k)\left[\sin\left(k\left[x+\frac{3}{2}s\right]\right) - \sin\left(k\left[x-\frac{3}{2}s\right]\right)\right]. \tag{A.89}$$

If the center plane between the two current tips is considered (at $x = 0$), it holds for the current density due to symmetry that $\boldsymbol{j}(0, y, z) = j_x(0, y, z)\hat{\boldsymbol{e}}_{\boldsymbol{x}}$. Thus, the current in x-direction calculated before corresponds to the total amount of current inside the sample. Explicitly, it can be written for the total current I^i in the i-th layer that

$$I^i = I_x^i(0) = 2\int_0^\infty dk\, Z_i(k)\left[\sin\left(\frac{3}{2}ks\right) - \underbrace{\sin\left(-\frac{3}{2}ks\right)}_{=-\sin\left(\frac{3}{2}ks\right)}\right] \tag{A.90}$$

$$= 4\int_0^\infty dk\, Z_i(k)\sin\left(\frac{3}{2}ks\right). \tag{A.91}$$

Obviously, all currents I^i through the individual layers should sum up to the injected current $I = \sum_i I^i$.

A.3. Supplements for band bending calculations

In this appendix, more details about the steps for solving Poisson's equation in general and the subsequent determination of integration constants for different boundary conditions which lead to the solutions presented in section 6.4, are listed.

A.3.1. General solution

In the following, it is shown more explicitly, how the Eqs. (6.6), (6.8) and (6.10) in section 6.4.1.1 can be obtained from Poisson's equation (6.5) [88, 144].

For the derivations, the expressions for the electron and hole charge charge carrier densities specified before in Eqs. (6.43) and (6.45), and Eqs. (6.46) and (6.48) as

$$n_e(z) = n_i e^{u(z)} = n_b e^{v(z)} \tag{A.92}$$

$$p_h(z) = n_i e^{-u(z)} = p_b e^{-v(z)}, \tag{A.93}$$

respectively, have to be used. By equating Eqs. (A.92) and (A.93) for n_i, it results that

$$n_b e^{v(z)} e^{-u(z)} = p_b e^{-v(z)} e^{u(z)}, \tag{A.94}$$

and thus

$$p_b = n_b e^{2v(z)} e^{-2u(z)} \tag{A.95}$$

Starting now with the factorisation of Eq. (6.5) on the right side by $n_b + p_b$, it follows that

$$\frac{d^2v(z)}{dz^2} = -\underbrace{\frac{q^2(n_b + p_b)}{\epsilon_0\epsilon_r k_B T}}_{\overset{(6.7)}{=}\frac{1}{L^2}} \frac{n_b - p_b + p_b e^{-v(z)} - n_b e^{v(z)}}{n_b + p_b} \tag{A.96}$$

$$\overset{(A.95)}{=} -\frac{1}{L^2}\,\frac{1-e^{2v(z)}e^{-2u(z)}+e^{v(z)}e^{-2u(z)}-e^{v(z)}}{1+e^{2v(z)}e^{-2u(z)}} \tag{A.97}$$

$$= -\frac{1}{L^2}\,\frac{e^{v(z)-u(z)}\left(e^{-v(z)+u(z)}-e^{v(z)-u(z)}+e^{-u(z)}-e^{u(z)}\right)}{e^{v(z)-u(z)}\left(e^{-v(z)+u(z)}+e^{v(z)-u(z)}\right)} \tag{A.98}$$

$$= -\frac{1}{L^2}\,\frac{e^{u(z)-v(z)}-e^{-(u(z)-v(z))}-\left(e^{u(z)}-e^{-u(z)}\right)}{e^{u(z)-v(z)}+e^{-(u(z)-v(z))}}. \tag{A.99}$$

With the definitions for the hyperbolic sine and cosine functions $\sinh(x) = \frac{e^x-e^{-x}}{2}$ and $\cosh(x) = \frac{e^x+e^{-x}}{2}$, respectively, it results that

$$\frac{d^2v(z)}{dz^2} = -\frac{1}{L^2}\,\frac{\sinh[u(z)-v(z)]-\sinh[u(z)]}{\cosh[u(z)-v(z)]} \tag{A.100}$$

$$\overset{\tanh(x)=\frac{\sinh(x)}{\cosh(x)}}{=} \frac{1}{L^2}\left(\frac{\sinh[u(z)]}{\cosh[u(z)-v(z)]}-\tanh[u(z)-v(z)]\right). \tag{A.101}$$

From Eqs. (6.3) and (6.4) it is visible that $u(z) = u_b + v(z)$. Thus, Eq. (6.6) results.

For obtaining Eq. (6.8), an integration by means of separation of variables is performed. By multiplying both sides of Eq. (6.6) with $2\frac{dv}{dz}$ it can be written that

$$\underbrace{2\frac{dv}{dz}\frac{d^2v}{dz^2}}_{=\frac{d}{dz}\left[\frac{dv}{dz}\right]^2} = \frac{2}{L^2}\frac{dv}{dz}\left(\frac{\sinh[u_b+v(z)]}{\cosh(u_b)}-\tanh(u_b)\right) \tag{A.102}$$

$$\int dz\left[\frac{d}{dz}\left(\frac{dv}{dz}\right)^2\right] = \frac{2}{L^2}\int dv\left(\frac{\sinh[u_b+v(z)]}{\cosh(u_b)}-\tanh(u_b)\right) \tag{A.103}$$

$$\left(\frac{dv}{dz}\right)^2 = \frac{2}{L^2}\left(\frac{\cosh[u_b+v(z)]}{\cosh(u_b)}-v(z)\tanh(u_b)+c\right) \tag{A.104}$$

$$\frac{dv}{dz} = \operatorname{sgn}[-v(z)]\frac{\sqrt{2}}{L}\underbrace{\sqrt{\frac{\cosh[u_b+v(z)]}{\cosh(u_b)}-v(z)\tanh(u_b)+c}}_{=:\,D(v(z),c)}. \tag{A.105}$$

The introduction of the sign function in Eq. (A.105) is owed to the definition of the band bending given before in Eq. (6.3) which implies that $v(z\to\infty) = 0$. Thus, it holds for the derivative that $\frac{dv}{dz} < 0$ for $v(z) > 0$ and $\frac{dv}{dz} > 0$ for $v(z) < 0$. The integration constant c has to be determined from boundary conditions. Another integration of Eq. (A.105) by separation of variables yields

$$\operatorname{sgn}[-v(z)]\frac{L}{\sqrt{2}}\int_{v(0)}^{v(z)} dv'\,\frac{1}{D(v'(z),c)} = \int_0^z dz = z(v). \tag{A.106}$$

The value for $v(0)$ has to be determined from a second boundary condition. Eq. (A.106) defines implicitly the band bending $v(z)$.

A.3.2. Infinite bulk material

The case of an infinite bulk material is considered by the boundary conditions given in Eq. (6.9). Applied to Eq. (A.105), it immediately results for the constant c that

$$\left.\frac{dv}{dz}\right|_{z\to\infty} = 0 \quad \overset{v(z\to\infty)=0}{\Leftrightarrow} \quad D(0,c) = 0 \quad \Leftrightarrow \quad 1 + c = 0 \quad \Leftrightarrow \quad c = -1 \tag{A.107}$$

Thus, it follows that

$$D(v(z),-1) = \sqrt{\frac{\cosh[u_b + v(z)]}{\cosh(u_b)} - v(z)\tanh(u_b) - 1} \tag{A.108}$$

$$= \sqrt{\frac{\cosh[u_b + v(z)] - v(z)\sinh(u_b) - \cosh(u_b)}{\cosh(u_b)}} \tag{A.109}$$

$$= \sqrt{\frac{e^{u_b+v(z)} + e^{-(u_b+v(z))} - v(z)e^{u_b} + v(z)e^{-u_b} - e^{u_b} - e^{-u_b}}{e^{u_b} + e^{-u_b}}} \tag{A.110}$$

$$= \sqrt{\frac{e^{u_b}\left(e^{v(z)} - v(z) - 1\right) + e^{-u_b}\left(e^{-v(z)} + v(z) - 1\right)}{e^{u_b} + e^{-u_b}}}. \tag{A.111}$$

By inserting Eq. (A.111) into Eq. (A.106), the solution from Eq. (6.10) is obtained.

A.3.3. Thin film with symmetric approach

For a thin film within the symmetric approach, the boundary conditions are given by Eq. (6.12). It follows for the constant c_{sym} that

$$\left.\frac{dv}{dz}\right|_{z=\frac{d}{2}} = 0 \quad \Leftrightarrow \quad D\left(v\left(\frac{d}{2}\right), c_{\text{sym}}\right) = 0 \tag{A.112}$$

$$\Leftrightarrow c_{\text{sym}} = v\left(\frac{d}{2}\right)\tanh(u_b) - \frac{\cosh\left[u_b + v\left(\frac{d}{2}\right)\right]}{\cosh(u_b)} \tag{A.113}$$

Thus, it results that

$$D(v(z), c_{\text{sym}}) = \sqrt{\frac{\cosh[u_b+v(z)] - \cosh\left[u_b+v\left(\frac{d}{2}\right)\right] - \left[v(z)-v\left(\frac{d}{2}\right)\right]\sinh(u_b)}{\cosh(u_b)}} \tag{A.114}$$

$$= \sqrt{\frac{e^{u_b+v(z)} + e^{-(u_b+v(z))} - e^{u_b+v\left(\frac{d}{2}\right)} - e^{-\left(u_b+v\left(\frac{d}{2}\right)\right)} - \left[v(z)-v\left(\frac{d}{2}\right)\right]\left(e^{u_b}-e^{-u_b}\right)}{e^{u_b}+e^{-u_b}}} \tag{A.115}$$

$$= \sqrt{\frac{e^{u_b}\left(e^{v(z)} - e^{v\left(\frac{d}{2}\right)} - v(z) + v\left(\frac{d}{2}\right)\right) + e^{-u_b}\left(e^{-v(z)} - e^{-v\left(\frac{d}{2}\right)} + v(z) - v\left(\frac{d}{2}\right)\right)}{e^{u_b}+e^{-u_b}}}. \tag{A.116}$$

Inserting Eq. (A.116) into Eq. (A.106) leads to Eq. (6.13).

A.3.4. Thin film with asymmetric approach

A.3.4.1. Case A

The boundary conditions for case A can be found in Eqs. (6.18) and (6.20). It is obvious that the constant c^A_{asym} is equal for both branches, since

$$\left.\frac{dv_1}{dz_1}\right|_{z=z_0} = -\left.\frac{dv_2}{dz_2}\right|_{z_2=d-z_0} = 0 \quad \overset{v_1(z_0)=v_2(d-z_0)=v_0}{\Leftrightarrow} \quad D\left(v_0, c^A_{\text{asym}}\right) = 0. \tag{A.117}$$

From a comparison with Eq. (A.112), it is immediately visible that

$$c^A_{\text{asym}} = v_0 \tanh(u_b) - \frac{\cosh[u_b + v_0]}{\cosh(u_b)} \tag{A.118}$$

Thus, it is

$$D\big(v(z), c^A_{\text{asym}}\big) = \sqrt{\frac{e^{u_b}\big(e^{v(z)} - e^{v_0} - v(z) + v_0\big) + e^{-u_b}\big(e^{-v(z)} - e^{-v_0} + v(z) - v_0\big)}{e^{u_b} + e^{-u_b}}}. \tag{A.119}$$

With the arguments for the two branches discussed in section 6.4.3.1, Eq. (A.119) can be inserted into Eq. (A.106), thus resulting in Eq. (6.22) for $v_i(z_i)$. The auxiliary condition for v_0 specified in Eq. (6.23) can be obtained from Eq. (A.106) as

$$v_1(z_0) = v_0 \quad \Leftrightarrow \quad z_0 = \underbrace{\text{sgn}[-v_1(z_1)]}_{=\text{sgn}(-v_{\text{top}})} \frac{L}{\sqrt{2}} \int_{v_{\text{top}}}^{v_0} dv' \, \frac{1}{D(v'(z), c^A_{\text{asym}})} \tag{A.120}$$

$$v_2(d - z_0) = v_0 \quad \Leftrightarrow \quad d - z_0 = \underbrace{\text{sgn}[-v_2(z_2)]}_{=\text{sgn}[-v_1(z_1)]} \frac{L}{\sqrt{2}} \int_{v_{\text{bottom}}}^{v_0} dv' \, \frac{1}{D(v'(z), c^A_{\text{asym}})}. \tag{A.121}$$

Thus, by inserting Eq. (A.120) into Eq. (A.121), it directly follows Eq. (6.23).

A.3.4.2. Case B

For case B the boundary conditions are given by Eq. (6.21). As no specific condition for $\frac{dv}{dz}$ exists, the integration constant c^B_{asym} cannot be expressed explicitly. Thus, it follows directly from Eq. (A.105) that

$$D\big(v(z), c^B_{\text{asym}}\big) = \sqrt{\frac{e^{u_b}\big(e^{v(z)} - v(z) + c^B_{\text{asym}}\big) + e^{-u_b}\big(e^{-v(z)} + v(z) + c^B_{\text{asym}}\big)}{e^{u_b} + e^{-u_b}}}. \tag{A.122}$$

The constant c^B_{asym} is implicitly defined for each branch by the conditions

$$v_1(d) = v_{\text{bottom}} \quad \Leftrightarrow \quad d = \underbrace{\text{sgn}[-v_1(z_1)]}_{=\text{sgn}[-v_{\text{top}}]} \frac{L}{\sqrt{2}} \int_{v_{\text{top}}}^{v_{\text{bottom}}} dv' \, \frac{1}{D(v'(z), c^B_{\text{asym}})} \tag{A.123}$$

$$v_2(d) = v_{\text{top}} \quad \Leftrightarrow \quad d = \underbrace{\operatorname{sgn}[-v_2(z_2)]}_{=\operatorname{sgn}[-v_{\text{top}}]} \frac{L}{\sqrt{2}} \underbrace{\int_{v_{\text{bottom}}}^{v_{\text{top}}} dv' \, \frac{1}{D(v'(z), c^{B}_{\text{asym}})}}_{= -\int_{v_{\text{top}}}^{v_{\text{bottom}}} dv' \, \frac{1}{D(v'(z), c^{B}_{\text{asym}})}} \; . \tag{A.124}$$

It is visible that Eqs. (A.123) and (A.124) differ only in the sign which can be expressed by $\operatorname{sgn}(|v_{\text{top}}| - |v_{\text{bottom}}|)$. Thus, both conditions can be condensed to the expression given by Eq. (6.26).

A.3.4.3. Case C

The boundary conditions for case C are given by the Eqs. (6.19) and (6.20). Again, no explicit condition for $\frac{dv}{dz}$ exists, however, it can be concluded from Eq. (A.105) that the integration constant c^{C}_{asym} is equal for both branches, since

$$\left.\frac{dv_1}{dz_1}\right|_{z_0} = -\left.\frac{dv_2}{dz_2}\right|_{d-z_0} \overset{\substack{v_1(z_0)=0 \\ =v_2(d-z_0)}}{\Leftrightarrow} \quad \operatorname{sgn}[-v_1(z_1)] D\big(0, c^{C1}_{\text{asym}}\big) = -\underbrace{\operatorname{sgn}[-v_2(z_2)]}_{=-\operatorname{sgn}[-v_1(z_1)]} D\big(0, c^{C2}_{\text{asym}}\big) \tag{A.125}$$

$$\Leftrightarrow \quad c^{C1}_{\text{asym}} = c^{C2}_{\text{asym}} =: c^{C}_{\text{asym}}. \tag{A.126}$$

Thus, $D\left(v(z), c^{C}_{\text{asym}}\right)$ is given in analogy to Eq. (A.122). The constant c^{C}_{asym} can be obtained from the two conditions

$$v_1(z_0) = 0 \quad \Leftrightarrow \quad z_0 = \underbrace{\operatorname{sgn}[-v_1(z_1)]}_{=\operatorname{sgn}(-v_{\text{top}})} \frac{L}{\sqrt{2}} \int_{v_{\text{top}}}^{0} dv' \, \frac{1}{D(v'(z), c^{C}_{\text{asym}})} \tag{A.127}$$

$$v_2(d - z_0) = 0 \quad \Leftrightarrow \quad d - z_0 = \underbrace{\operatorname{sgn}[-v_2(z_2)]}_{=-\operatorname{sgn}[-v_1(z_1)]} \frac{L}{\sqrt{2}} \underbrace{\int_{v_{\text{bottom}}}^{0} dv' \, \frac{1}{D(v'(z), c^{C}_{\text{asym}})}}_{= -\int_{0}^{v_{\text{bottom}}} dv' \, \frac{1}{D(v'(z), c^{C}_{\text{asym}})}} \; . \tag{A.128}$$

Eq. (A.127) has to be inserted into Eq. (A.128). Since it holds for case C by construction that $\operatorname{sgn}(v_{\text{top}}) = -\operatorname{sgn}(v_{\text{bottom}})$, both integrals can be combined, resulting in the condition given by Eq. (6.27).

Appendix B. Measurement data

In this second part of the appendix, supplementary measurement data can be found.

- Composed large-size STM image showing all of the step edges below the Si(111)-(7×7) surface reconstruction in the sample region used for the angle-dependent four-point measurement from Fig. 4.13 in section 4.4.2 [Fig. B.1].
- dI/dV measurement of a double-layered step edge on the $\mathrm{Bi_{14}Rh_3I_9}$ surface. [Fig. B.2].
- Enlarged dI/dV measurement of the same step edges on the $\mathrm{Bi_{14}Rh_3I_9}$ surface as depicted in Fig. 7.7 in section 7.3.2 [Fig. B.3].
- dI/dV measurement of a scratch on the $\mathrm{Bi_{14}Rh_3I_9}$ surface [Fig. B.4].

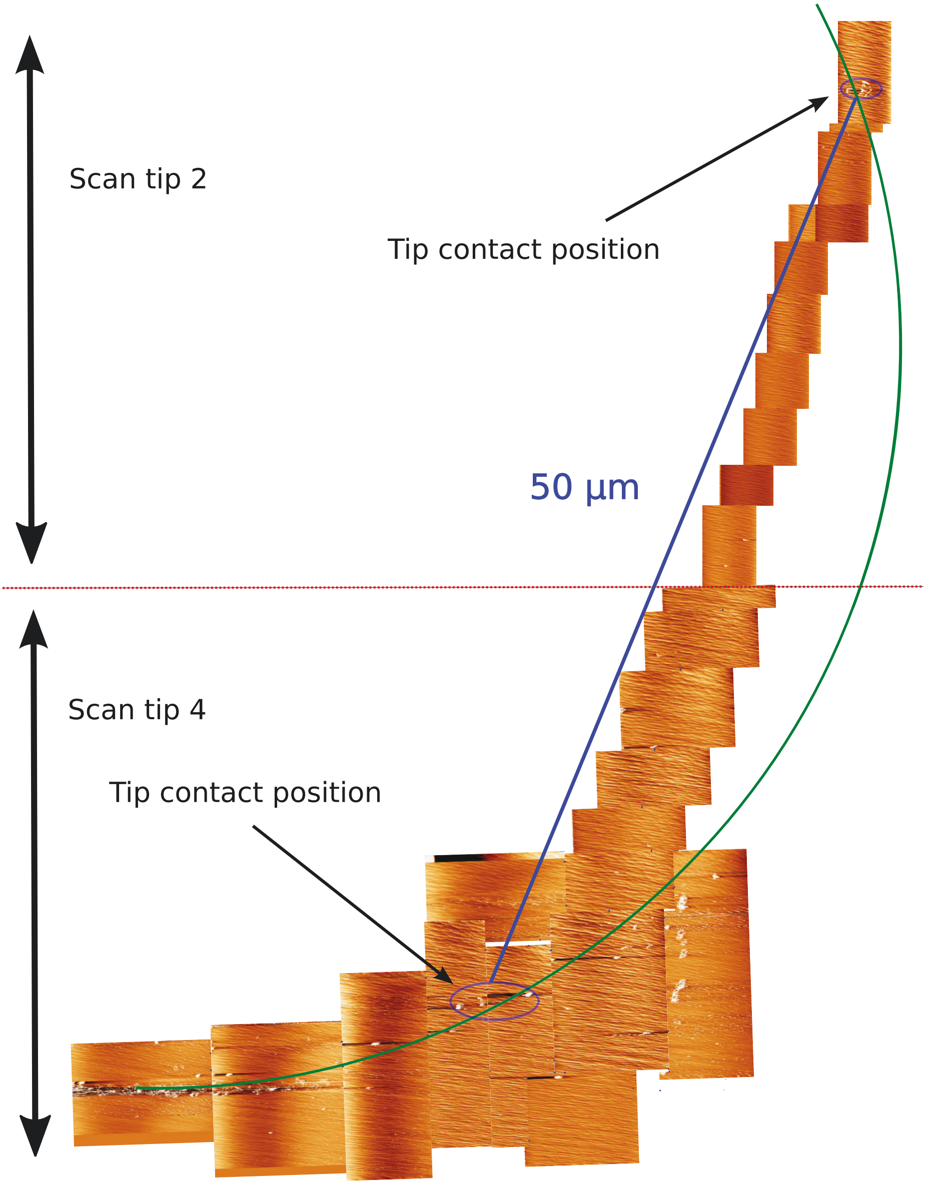

Figure B.1.: Composed large-size STM scan depicting a part of the substrate region, on which the angle-dependent four-point measurement in Fig. 4.13 (section 4.4.2) has been performed. The complete (7×7) surface in between the tips (distance of $50\,\mu$m along the blue line) is imaged, which enables to count all of the involved step edges. The individual STM images are aligned according to the shape of the step edges. The green circle indicates the envelope formed by the differently orientated squares of each angle-dependent measurement. Along the circle the distinct tip positions, i.e. the tip indentations, are partially visible. During acquisition of the individual STM images the tip has been changed, as indicated.

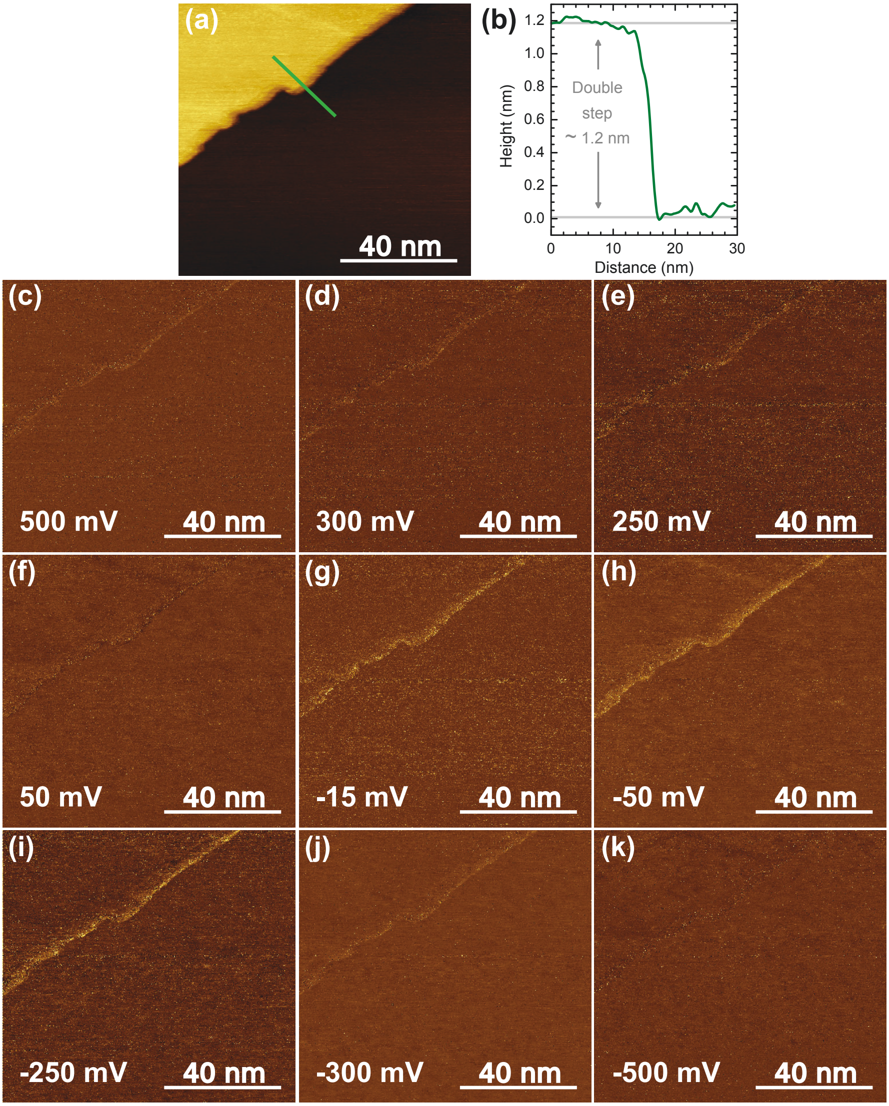

Figure B.2.: Spectroscopic dI/dV measurement of a double-layered step edge on the $\mathrm{Bi_{14}Rh_3I_9}$ surface, as discussed for similar data in section 7.3.2. Measurement parameters are: $U = 500\,\mathrm{mV}$ (a), $I_\mathrm{stab} = 86\,\mathrm{pA}$, $V_\mathrm{mod,RMS} = 9\,\mathrm{mV}$, $f_\mathrm{mod} = 980\,\mathrm{Hz}$.

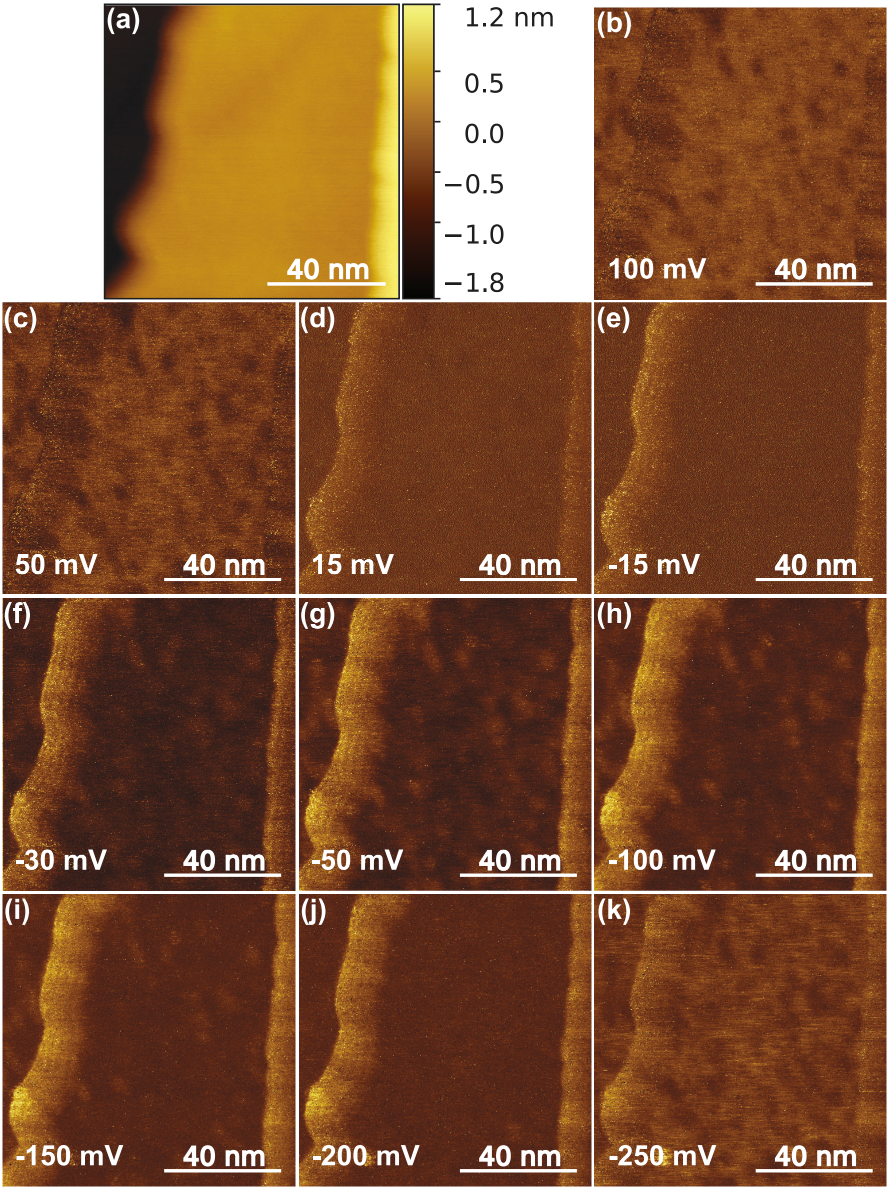

Figure B.3.: Enlarged spectroscopic dI/dV measurement of the same step edges on the $Bi_{14}Rh_3I_9$ surface as depicted in Fig. 7.7 in section 7.3.2. Measurement parameters are: $U = 100\,\mathrm{mV}$ (a), $I_{\mathrm{stab}} = 350\,\mathrm{pA}$, $V_{\mathrm{mod,RMS}} = 9\,\mathrm{mV}$, $f_{\mathrm{mod}} = 980\,\mathrm{Hz}$.

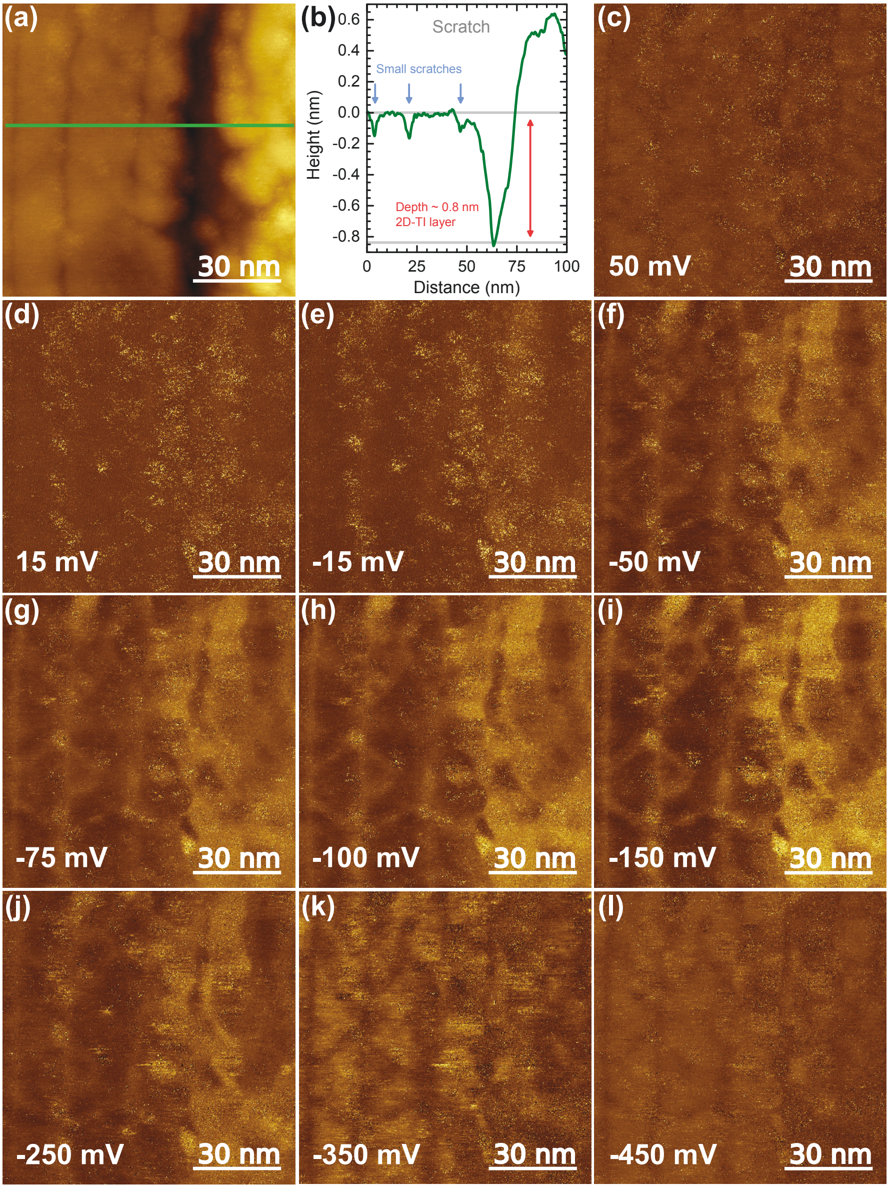

Figure B.4.: Spectroscopic dI/dV measurement of a scratch on the $Bi_{14}Rh_3I_9$ surface, as discussed for similar data in section 7.3.3. Measurement parameters are: $U = 50\,\mathrm{mV}$ (a), $I_{\mathrm{stab}} = 300\,\mathrm{pA}$, $V_{\mathrm{mod,RMS}} = 7\,\mathrm{mV}$, $f_{\mathrm{mod}} = 980\,\mathrm{Hz}$.

Appendix C. Technical information

In this third part of the appendix, further technical information about the experimental setup are provided.

C.1. Technical documents

In the following, several technical documents are listed:

- Drawing of the annealing station used for cleaning silicon substrates by direct current heating [Fig. C.1].
- Screenshot of the *Createc* software used for operating the multi-tip STM [Fig. C.2].

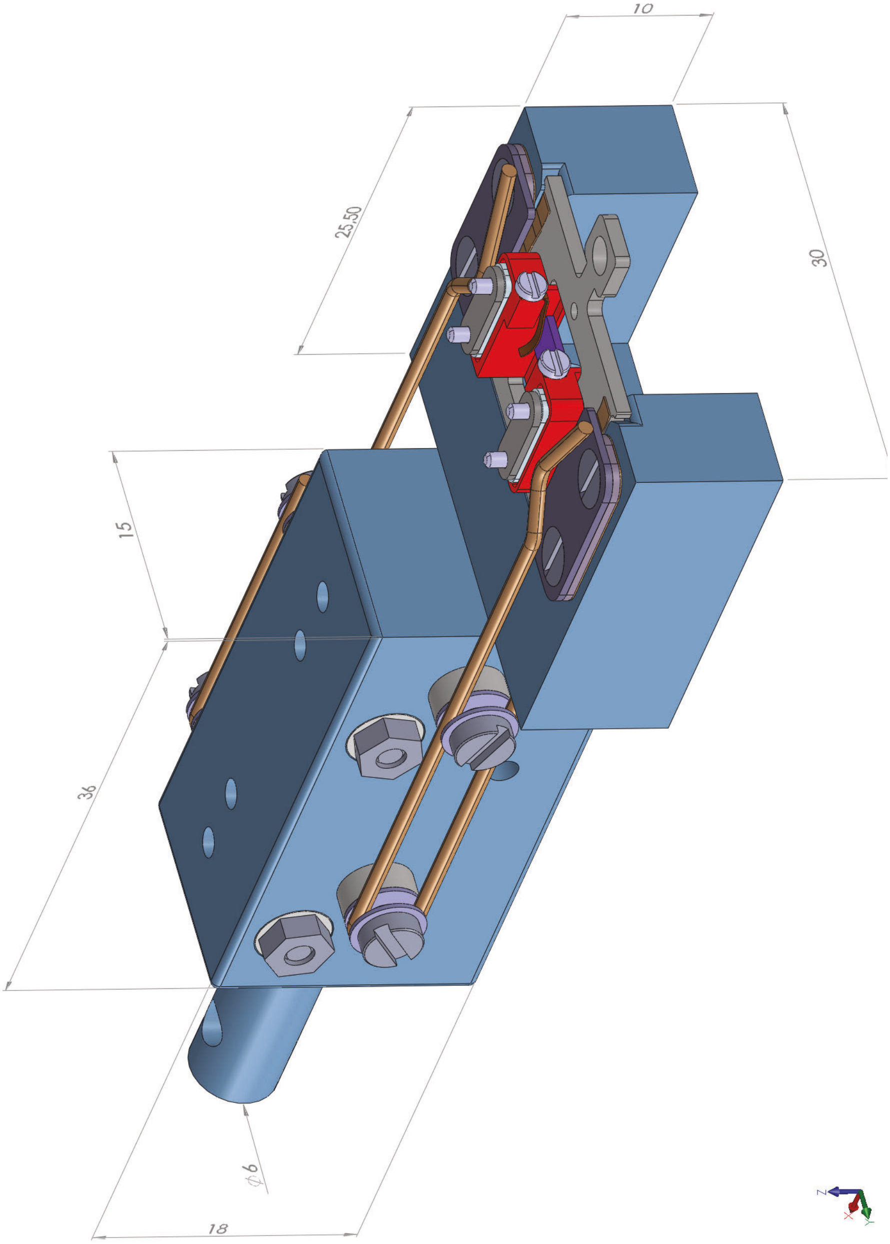

Figure C.1.: Drawing of the direct current annealing station for silicon samples mounted on a standard *Omicron* sample holder. The annealing station is attached to a transfer rod inside the UHV chamber. All dimensions in mm.

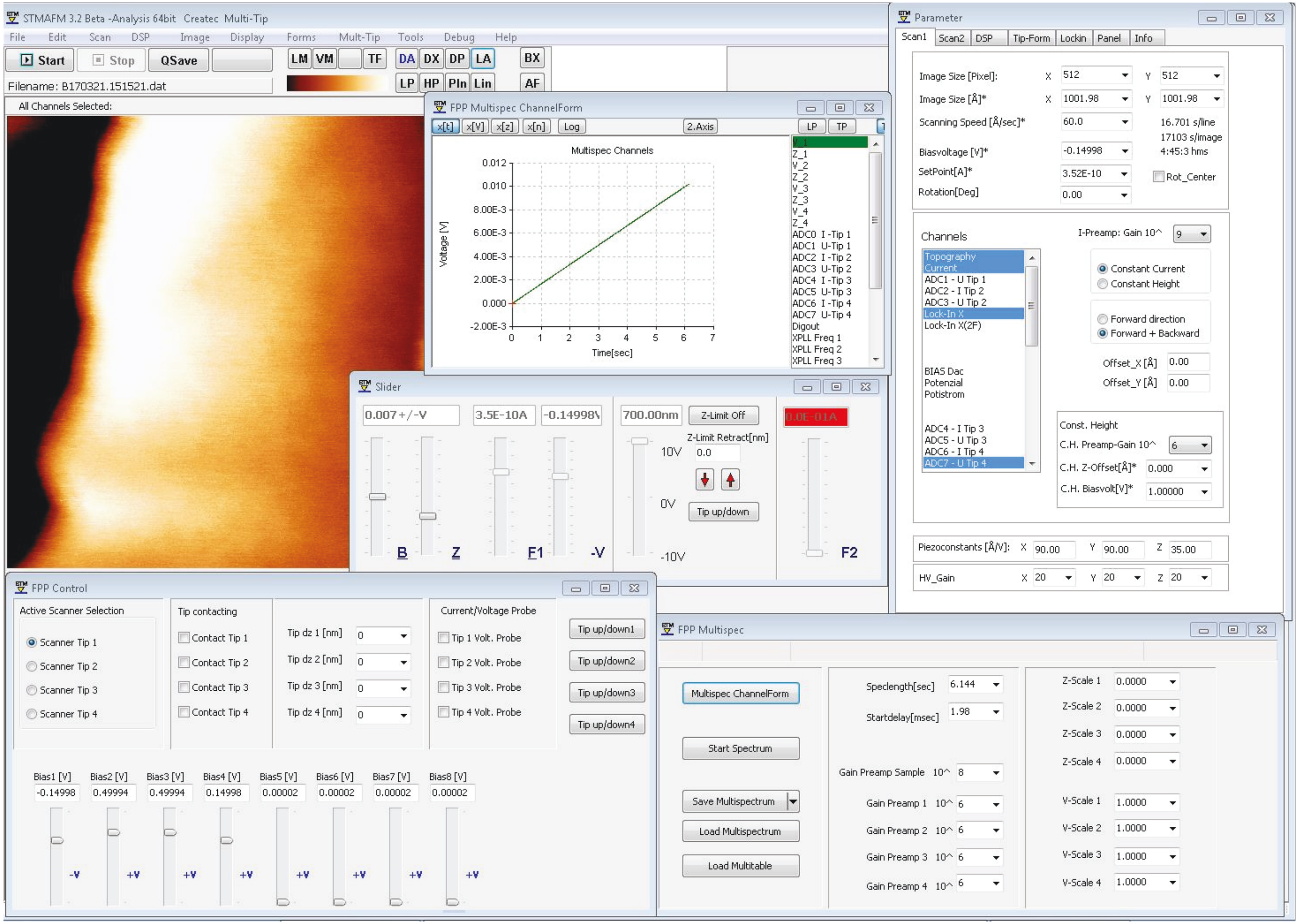

Filename: B170321.151521.dat

All Channels Selected:

0.007+/-V
3.5E-10A
-0.14998V
700.00nm
0.0E-01A
Z-Limit Retract[nm] 0.0

Image Size [Pixel]: X 512 Y 512
Image Size [Å]* X 1001.98 Y 1001.98
Scanning Speed [Å/sec]* 60.0
16.701 s/line
17103 s/image
4:45:3 hms
Biasvoltage [V]* -0.14998
SetPoint[A]* 3.52E-10
☐ Rot_Center
Rotation[Deg] 0.00

I-Preamp: Gain 10^ 9
● Constant Current
○ Constant Height
○ Forward direction
● Forward + Backward
Offset_X [Å] 0.00
Offset_Y [Å] 0.00

Const. Height
C.H. Preamp-Gain 10^ 6
C.H. Z-Offset[Å]* 0.000
C.H. Biasvolt[V]* 1.00000

Piezoconstants [Å/V]: X 90.00 Y 90.00 Z 35.00
HV_Gain X 20 Y 20 Z 20

● Scanner Tip 1
○ Scanner Tip 2
○ Scanner Tip 3
○ Scanner Tip 4

☐ Contact Tip 1
☐ Contact Tip 2
☐ Contact Tip 3
☐ Contact Tip 4

Tip dz 1 [nm] 0
Tip dz 2 [nm] 0
Tip dz 3 [nm] 0
Tip dz 4 [nm] 0

☐ Tip 1 Volt. Probe
☐ Tip 2 Volt. Probe
☐ Tip 3 Volt. Probe
☐ Tip 4 Volt. Probe

Bias1 [V]	Bias2 [V]	Bias3 [V]	Bias4 [V]	Bias5 [V]	Bias6 [V]	Bias7 [V]	Bias8 [V]
-0.14998	0.49994	0.49994	0.14998	0.00002	0.00002	0.00002	0.00002

Speclength[sec] 6.144
Startdelay[msec] 1.98
Gain Preamp Sample 10^ 8
Gain Preamp 1 10^ 6
Gain Preamp 2 10^ 6
Gain Preamp 3 10^ 6
Gain Preamp 4 10^ 6

Z-Scale 1 0.0000
Z-Scale 2 0.0000
Z-Scale 3 0.0000
Z-Scale 4 0.0000
V-Scale 1 1.0000
V-Scale 2 1.0000
V-Scale 3 1.0000
V-Scale 4 1.0000

Figure C.2.: Screenshot of the *Createc* software used for operating the multi-tip STM.

C.2. Coordinate systems for tip positioning

For movement of the four tips in the plane of the sample surface, basically two different types of coordinate systems have to be distinguished, i.e. the (four) tip coordinate systems and the scan coordinate system, as it is depicted in Fig. C.3.

Each of the four tips has its own individual tip coordinate system, whose y-axis is basically aligned always along the projection of the tip axis onto the sample surface. More general, it is pointing along the radial direction from the corresponding slider of the tip to the center of the STM, but in practice this typically coincides with the orientation of the tips. The origin of each tip coordinate system is located at the idle position of the corresponding tip. Thus, in total four tip coordinate systems exist, each of them rotated by an angle of $90°$. All (manual) coarse movements of a tip are based on its tip coordinate system. The control buttons inside the STM software for slip-stick movement (*Ramp controller*) and piezo offset (*Pan view*) are controlling the x- and y- direction within the coordinate system of the currently selected tip.

Furthermore, for scanning a global scan coordinate system exists which applies to all four tips. The alignment of this scan coordinate system corresponds to the orientation of the tip coordinate system of tip 1, as visualized in Fig. C.3. All tips are scanning within this global coordinate system, whereby the x-direction always points along the fast scan direction. This fact is particularly important, when scanning with all four tips at the same time. Within the scan coordinate system, the idle positions of each of the four tips are distinguished, as this allows for a control of the scanned area for each tip with respect to its idle position. In a more strict sense, even four different scan coordinate systems exist, but which differ solely by a translation of their respective origins to the corresponding tip idle positions.

The control of the scanned area for a specific tip inside the software during data acquisi-

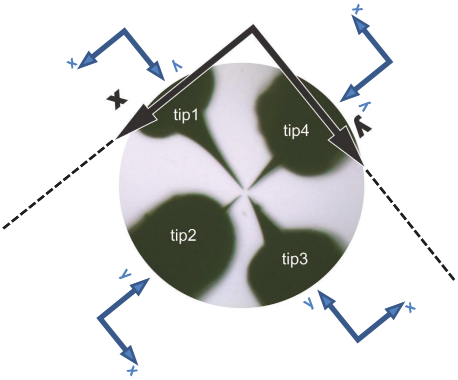

Figure C.3.: Arrangement of the individual coordinate systems of the four tips (blue) which are used for positioning, and the commonly used scan coordinate system (black). In the center, an optical microscope image is depicted showing the four tips in front of the sample surface.

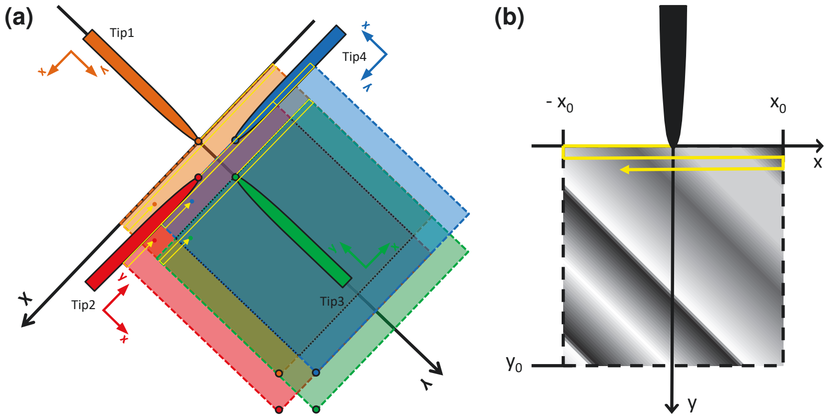

Figure C.4.: (a) Scan areas (colored) of the four tips on the sample surface. The individual tip coordinate systems are indicated by color next to the tips, as well as the common scan coordinate system (black). The yellow lines mark the scan directions (line-by-line) of the individual tips, when scanning over the surface. If the four tips are initially placed at the colored points, as indicated, then their relative positions do not change during collective scanning. Thus, after the scans, they end up at the correspondingly colored points at the bottom. The overlap of the commonly scanned area of the surface is indicated by the surrounding dotted black line. (b) View of the scanned image as it appears in the STM software during data acquisition. The scanning direction of the tip (line-by-line) is marked by the yellow line. The scan coordinate system (black), and thus the image is mirrored at the x-axis with respect to the sample surface as it appears in the optical microscope.

tion (functions *SetXYOffset-Top*, *SetXYOffset-Center*, *SetXYOffset-Zoom*) takes place with respect to the scan coordinate system. Also, the values for the x- and y-offset of the piezos which are controllable by the two boxes in the *Parameter/Scan*-window in the software, refer to the scan coordinate system, and thus control immediately the position of the corresponding tip in the scanned image. A conversion of the entered offset-values to the tip coordinate system of the currently active tip in order to actuate the proper piezocontacts occurs internally by the software.

A rotation of the scan coordinate system is adjustable by the box *Rotation* within the *Parameter/Scan*-window. A positive value causes a clockwise rotation of the scan coordinate system around the idle position of the active tip (origin). Within the rotated state, the x-direction is still pointing along the fast scanning direction. Only if the control button *RotCenter* is active, the rotation occurs around the center of the currently chosen scan area. While doing so, the idle position of the tip is changed automatically by selecting proper values for the piezo offsets. However, an important point is that the numbers for x- and y-offset within the *Parameter/Scan*-window still refer to the not rotated scan coordinate system, i.e. *Rotation*-value set to zero. Thus, these values do not correspond to the directions of the rotated scan coordinate system and particularly, not to the orientation of the acquired scan image.

A collective scanning of all four tips at the same time is possible, since the tips are moving within the common scan coordinate system. Thus, the relative position between the four tips stays the same during scanning, as it is visualized in Fig. C.4(a) by the correspondingly colored points at the indicated tip positions and at the expected end position of the scans. Each tip scans its individually selected area (colored) line-by-line (yellow arrows), but cannot collide with another tip, as no crossing of the tip movements occurs. Hence, this allows to image an specific area of the sample with four tips at the same time, as indicated in Fig. C.4(a) by the colored segment surrounded by the dotted black line. For example, this can be very useful, when it is desired to contact specific small features on the sample surface by multiple tips, or when the distances between the tips should be determined based on the shift of the individual scan images with respect to each other. Nevertheless, from the point of view of one specific tip, the scan orientation appears to be rotated for each tip. This has to be taken into account, when looking at the visualization of the tip positions inside the software (*PanView*). Here, the scan area seems to be rotated for each tip, as it is depicted within the tip coordinate system for each tip individually.

Within the acquired scan image, the scan coordinate system is mirrored along the x-axis. Thus, the y-axis is always pointing downwards, as shown in Fig. C.4(b). This implies that also the image of the sample surface is mirrored when appearing on the screen. If the piezo-offset of a tip is disregarded for a moment, the tip idle position before a scan is located at $(0, 0)$ [Fig. C.4(b)]. When starting the measurements, the tip moves initially to $(-x_0, 0)$ and then starts scanning in x-direction line-by-line over the surface. The final position of the tip after the scan is at (x_0, y_0). Afterwards, the tip returns to the initial position.

C.3. Setup of an *in situ* electromagnet for switching the tip spin polarisation

In order to prepare for spin-polarized transport measurements with the four-tip STM, a small electromagnet was developed with the aim to enable an *in situ* switching of the spin-polarization of one ferromagnetic nickel tip in the four tip setup by a strong short-time pulse of magnetic field. Such a method is favourable, since in this case the tip has not to be unmounted in order to change polarisation outside the UHV environment, and thus the currently chosen measurement region on the sample surface will not be lost. Hence, this enables to measure subsequently with different spin-polarisation at the same position and therefore allows for exclusion of any influence of position-dependent sample properties when comparing the results. For this purpose, an electromagnetic coil with a ferrite core has been constructed which is attached to a standard sample holder, as it is depicted in Fig. C.5. In this way, the coil can be handled similar to a standard sample, as shown in Fig. C.5(a), so that no modifications of the UHV chamber are necessary. Moreover, the coil can be positioned on top of the multi-tip STM by usage of the adjustable heating stage which at the same time provides the electrical contacts [Fig. C.5(b)].

A cross-sectional view of the coil setup with dimensions is depicted in Fig. C.5(c). The ferrite core at the lower end is made out of *Armco* iron which has a high degree of purity

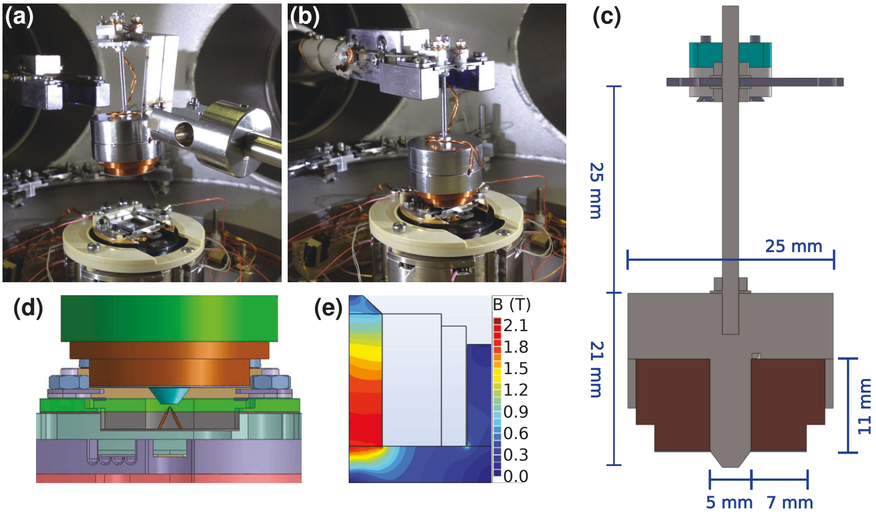

Figure C.5.: (a),(b) View of the electromagnetic coil inside the UHV environment. The handling is similar to a standard sample (a) and for operation the heating stage is used in order to enable contacting and positioning above the multi-tip STM (b). (c) Cross-sectional view of the setup with dimensions. The ferromagnetic core coil (core in grey, copper wire in brown) is attached to a standard sample holder (at top) with electrical contacts (cyan). (d) Front view of the coil positioned above the multi-tip STM. The lower end of the ferrite core has a distance of $\sim 1\,\mathrm{mm}$ from the STM tips with the sample in between (not drawn). (e) Simulation of the magnetic field strength inside the ferrite core (colored area) for a current density of $22\,\mathrm{A/mm^2}$, a wire diameter of $0.5\,\mathrm{mm}$ and 500 turns. The cross section of the coil (wire) is indicated by the rectangles. The simulation has been performed by *Dr. Helmut Soltner* (*ZEA-1*, *Research Center Jülich*).

and, thus, a high permeability. The core is attached to the sample holder at the top by a threaded rod made out of stainless steel. Moreover, the sample holder provides two isolated electrical contacts (depicted in cyan color), in the same way as used for the direct current annealing of silicon samples, which are connected to the ends of the wire of the coil in the present setup. The coil itself (depicted in brown color) consists out of 480 turns of a *Kapton* coated copper wire with outer diameter of $0.47\,\mathrm{mm}$ (copper diameter $0.4\,\mathrm{mm}$) with a total length of about $20\,\mathrm{m}$. During fabrication a UHV compatible glue was used in order to fix the wire. Due to the limited space in the direct vicinity of the STM, the wire is coiled with a step at the lower end which allows to approach the ferrite core as close as possible towards the STM tips. This is necessary for achieving a sufficient high magnetic field at the position of the STM tips in order to switch the spin polarization. When approached, the apex of the core (diameter $3\,\mathrm{mm}$) is spaced by about $1\,\mathrm{mm}$ from the end of the tips, as it is visualized in Fig. C.5(d). This minimal distance is necessary, since during STM measurements the sample is placed in between tips and ferrite core, whereby the sample surface is pointing downwards towards the tips and the ferrite core is positioned very closely ($\sim 100\,\mu\mathrm{m}$) above the backside of the sample. Here, a direct touch of core and sample should be avoided in

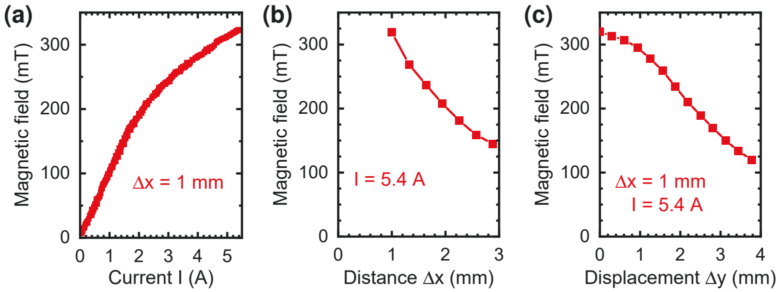

Figure C.6.: Measurements of the magnetic field strength of the coil with a *Hall* sensor under ambient conditions. (a) Magnetic field as function of the current inside the coil measured at a distance of $\Delta x = 1\,\mathrm{mm}$ apart from the core apex. (b) Magnetic field as function of the distance Δx from the core apex along the symmetry axis of the coil (current $5.4\,\mathrm{A}$). (c) Magnetic field as function of lateral displacement Δy perpendicular to the symmetry axis of the coil (at a distance $\Delta x = 1\,\mathrm{mm}$, current $5.4\,\mathrm{A}$). The measurements have been performed by *Arthur Leis*.

order to prevent an enhanced disturbance of the STM measurements by vibrations.

The shape of the ferrite core is on the one hand chosen in such a way that for a close distance to the core, where the tip position is expected, the strength of the magnetic field is as high as possible, but on the other hand a fast decrease is achieved for larger distances in order to prevent undesired stray fields and a coupling to the magnets of the tip holders. Particularly, the latter point is important, since such a magnetic coupling could induce a movement of the tips which has to be absolutely avoided. For this reason, the ferrite core has a large lateral extend on the upper end of the coil and additionally covers also partly the outside of the coil. Furthermore, a $1\,\mathrm{mm}$ thin iron plate is spot-welded to the inner pin of the core at the lower side, thus covering the open bottom side of the coil (not visible in Fig. C.5). With such a shape the magnetic field lines are guided in lateral direction and thus, do not have such a large extent in z-direction. A simulation of the magnetic field strength inside the core, as depicted in Fig. C.5(e), shows that besides a very dense field directly in the center, the field at the core apex (here at the top side) is about $400\,\mathrm{mT}$, while on the outer side of the core a substantial decrease of the field occurs. Another fact, which is advantageous at multi-tip STMs is that the tips are usually longer than in standard STM due to the fact that they are arranged under an angle towards the surface. Thus, longer tips can be utilized in order to increase the distance between the ferrite core and the tip holders even more.

In order to characterize the electromagnet, the magnetic field distribution in z- and lateral direction as function of current has been measured under ambient conditions by a *Hall* sensor. The results are shown in Fig. C.6. For a distance of $1\,\mathrm{mm}$ below the apex of the core (on the symmetry axis of the coil), a magnetic field of about $310\,\mathrm{mT}$ can be achieved by using a current of $5.4\,\mathrm{A}$ [Fig. C.6(a)]. Such a current strength corresponds to a current density of $45\,\mathrm{A/mm^2}$ inside the copper wire, and thus is way too high for a stable continuous operation of the coil, since the thermal heating would damage the wire. However, for a pulsed operation for pulses below $10\,\mathrm{s}$ with a sufficient large time in between for cooling down, this high current density is tolerated by the coil. Inside an UHV environment, the pulse duration has to be reduced a bit more, since otherwise the thermal heating leads to a substantial increase in pressure. For a current of $5.4\,\mathrm{A}$, the magnetic field as function of distance in z-direction is depicted in Fig. C.6(b) showing a quite fast decrease in field strength. The lateral distribution for a displacement Δy perpendicular to the symmetry axis (at a distance of $1\,\mathrm{mm}$ in z-direction) is depicted in Fig. C.6(c), exhibiting a slightly reduced decrease compared to the z-direction.

Band / Volume 55
Organic-Metal Hybrid Interfaces at the Mesoscopic Scale
G. Zamborlini (2018), xi, 133 pp
ISBN: 978-3-95806-328-0

Band / Volume 56
Configurable frequency synthesizer for large scale physics experiments
N. Parkalian (2019), xxi, 114 pp
ISBN: 978-3-95806-393-8

Band / Volume 57
Resistive switching phenomena in stacks of binary transition metal oxides grown by atomic layer deposition
H. Zhang (2019), ix, 196 pp
ISBN: 978-3-95806-399-0

Band / Volume 58
Element-Selective Investigation of Femtosecond Spin Dynamics in Ni_xPd_{1-x} Magnetic Alloys using Extreme Ultraviolet Radiation
S. Gang (2019), 93, xx pp
ISBN: 978-3-95806-411-9

Band / Volume 59
Defect engineering in oxide thin films
F. V. E. Hensling (2019), 10, 164 pp
ISBN: 978-3-95806-424-9

Band / Volume 60
Chemical control of the electrical surface properties of *n*-doped transition metal oxides
M. Andrä (2019), X, 150, XXXVIII pp
ISBN: 978-3-95806-448-5

Band / Volume 61
Digital Signal Processing and Mixed Signal Control of Receiver Circuitry for Large-Scale Particle Detectors
P. Muralidharan (2020), xv, 109 pp
ISBN: 978-3-95806-489-8

Band / Volume 62
Development of Electromagnetic Induction Measurement and Inversion Methods for Soil Electrical Conductivity Investigations
X. Tan (2020), ix, 124 pp
ISBN: 978-3-95806-490-4

Band / Volume 63
Novel System Approach for a mm-range Precision Indoor Positioning System
R. Xiong (2020), xi, 144 pp
ISBN: 978-3-95806-517-8

Band / Volume 64
Quantitative investigation of group III-nitride interfaces by a combination of scanning tunneling microscopy and off-axis electron holography
Y. Wang (2021), 102 pp
ISBN: 978-3-95806-534-5

Band / Volume 65
Scalable Control Electronics for a Spin Based Quantum Computer
L. Geck (2021), xiv, 114, xv-xxxiii
ISBN: 978-3-95806-540-6

Band / Volume 66
DNA-capped silver nanoparticles for stochastic nanoparticle impact electrochemistry
L. Nörbel (2021), VI, 142 pp
ISBN: 978-3-95806-541-3

Band / Volume 67
Development, characterization, and application of intraretinal implants
V. Rincón Montes (2021), XII, 173 pp
ISBN: 978-3-95806-553-6

Band / Volume 68
Optogenetic and electrical investigation of network dynamics in patterned neuronal cultures
T. J. J. Hondrich (2021), x, 177 pp
ISBN: 978-3-95806-555-0

Band / Volume 69
Disentangling parallel conduction channels by charge transport measurements on surfaces with a multi-tip scanning tunneling microscope
S. Just (2021), xii, 225 pp
ISBN: 978-3-95806-574-1

Weitere ***Schriften des Verlags im Forschungszentrum Jülich*** unter
http://wwwzb1.fz-juelich.de/verlagextern1/index.asp

Information
Band / Volume 69
ISBN 978-3-95806-574-1

Mitglied der Helmholtz-Gemeinschaft

JÜLICH
Forschungszentrum